

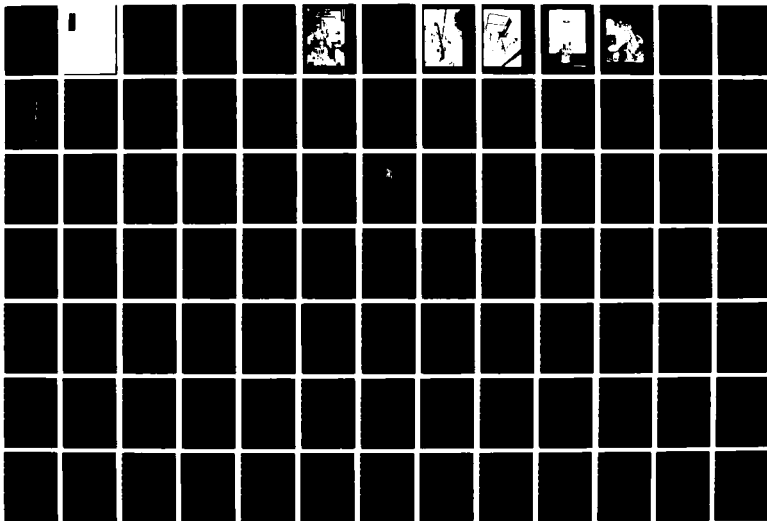
UNCLASSIFIED

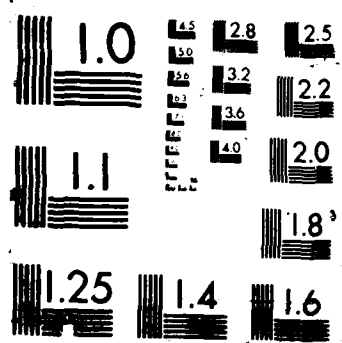
K M LAKIN 10 JUL 87 AFOSR-TR-87-1393 AFOSR-84-0300

14

F/G 13/8

NL





AD-A187 335

Table of Contents

1. Introduction

2. Thin Film Facility

2.1 ICB Systems

2.2 Sputter Deposition System

2.3 Electron Energy Loss Spectroscopy

2.4 Auger Spectroscopy

2.5 High Speed Ellipsometry

3. Film Deposition Studies

3.1 Aluminum on Silicon

3.2 Germanium Film Deposition

3.3 Sputter Deposition of LiNbO_3

4. Invited Talks, Contributed Papers, and Publications

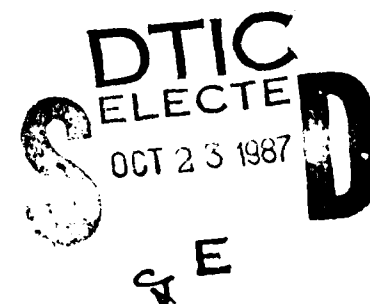
Appendix A. "Construction of two very-high-speed photometric ellipsometers," M. Fleshner, M.S. Thesis

Appendix B. "Germanium thin films deposited by the ionized-cluster beam method," J.S. McCalmont, M.S. Thesis

Appendix C. "The deposition and characterization of lithium niobate thin films," J. Martin, M.S. Thesis



Accession For	
NTIS GRA&I	<input checked="" type="checkbox"/>
DTIC TAB	<input type="checkbox"/>
Unannounced	<input type="checkbox"/>
Justification	
By	
Distribution/	
Availability Codes	
Dist	Avail and/or Special
A-1	



This document has been approved for public release and sale; its distribution is unlimited.

1. INTRODUCTION

This final report covers the period 9-1-84 to 11-30-86. During this time the program involved a research effort on ionized cluster beam deposition (ICB), an effort to synthesize LiNbO_3 films by sputter deposition, and the development of a high speed ellipsometer for in situ film deposition monitoring.

The work on ICB has mainly involved the installation and operation of a single source ICB system and the design and installation of a triple source ICB system. The purchase of the ICB systems were the result of successive 1983 and 1984 University Research Instrumentation Program (URIP) grants.

2. THIN FILM FACILITY

A 1983 DoD University Research Instrumentation Program Grant to ISU was used for construction of the first phase of a major thin film facility for research on film growth. Specifically, the grant was to provide funding for purchase of a single source ultrahigh vacuum (UHV) ionized cluster beam (ICB) deposition system which would be coupled by a UHV transistor system to film diagnostics chambers and other deposition systems. One of the other deposition system, a UHV sputtering system had been constructed previously as part of a research program on deposition of AlN thin films supported by AFOSR. A high resolution electron energy loss spectrometer with LEED and UPS capability was constructed with support from DoD, DoE, and ISU.

A 1984 DoD URIP grant provided for construction of a three source ICB system and a scanning Auger spectrometer. Figure 1 shows the layout of the thin film facility and Figure 2 provides an overview of the facility at the current time.

This grant provided support for much of the detailed design and for installation of the equipment as well as for initial film growth research in the facility. All systems in the facility were custom designed and custom

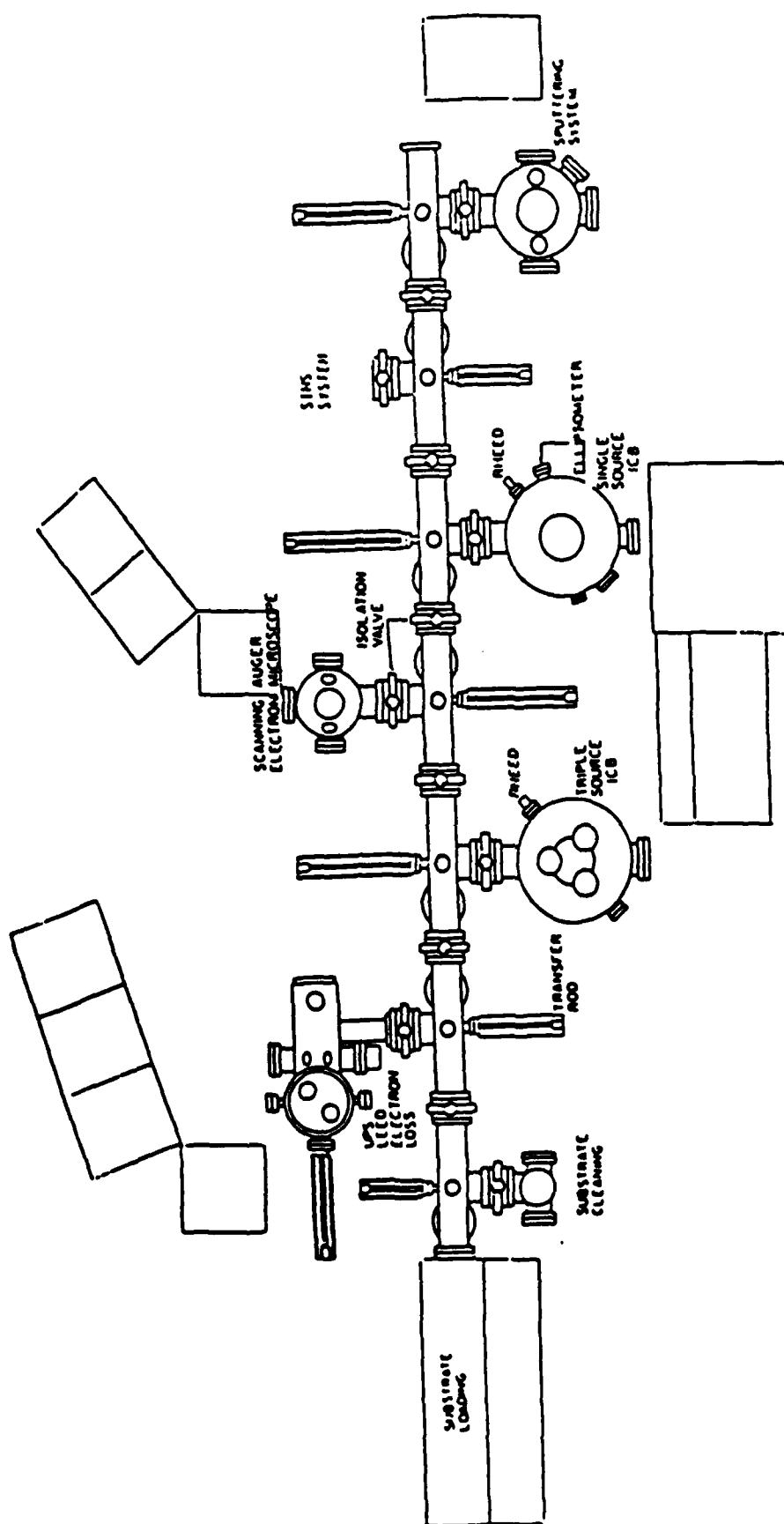


Figure 1 I.S.U. thin film facility



Figure 2 Overview of thin film facility with Scanning Auger in foreground.

built to be compatible with a central transfer system (Figure 3) and UHV environmental conditions.

2.1 ICB Systems

Two identical UHV chambers were built to house either one or three ICB sources, with ports for RHEED, ellipsometry and sample transfer. The initial ICB source, purchase from Eaton Corporation, the vacuum chamber and the control system are shown in Figure 4. This source was found to be very unreliable and discussions with Eaton Corporation resulted in a second generation source. This source was modified for UHV use and mounted on an 8 inch OD UHV flange for convenient insertion and removal from the vacuum chamber. Figure 5 shows this second generation source with the necessary ceramic insulators so that it could be biased up to 10 kV relative to the chamber walls. The single second generation source has been used for several deposition studies reported in other sections of this report.

With reasonably satisfactory performance by the single source system, a three source system was designed and built using the same chamber configuration but modifying the base plate to allow for three sources and shutters. Figure 6 shows two of the sources in place on the base plate.

2.2 Sputter Deposition System

Our group has been very successful in the preparation of oriented piezoelectric films by DC magnetron sputtering. As part of the thin film facility, an UHV compatible sputtering system was designed and constructed. Initially a commercially available magnetron sputtering head was purchased and installed in the chamber. The UHV chamber compatibility resulted in a significant reduction in impurities in the deposited films such as oxygen in AlN. By transferring substrates into the system from the load lock, the sputtering chamber remains evacuated between depositions.



Figure 3 Section of transfer line with magnetic cross-transfer manipulator.

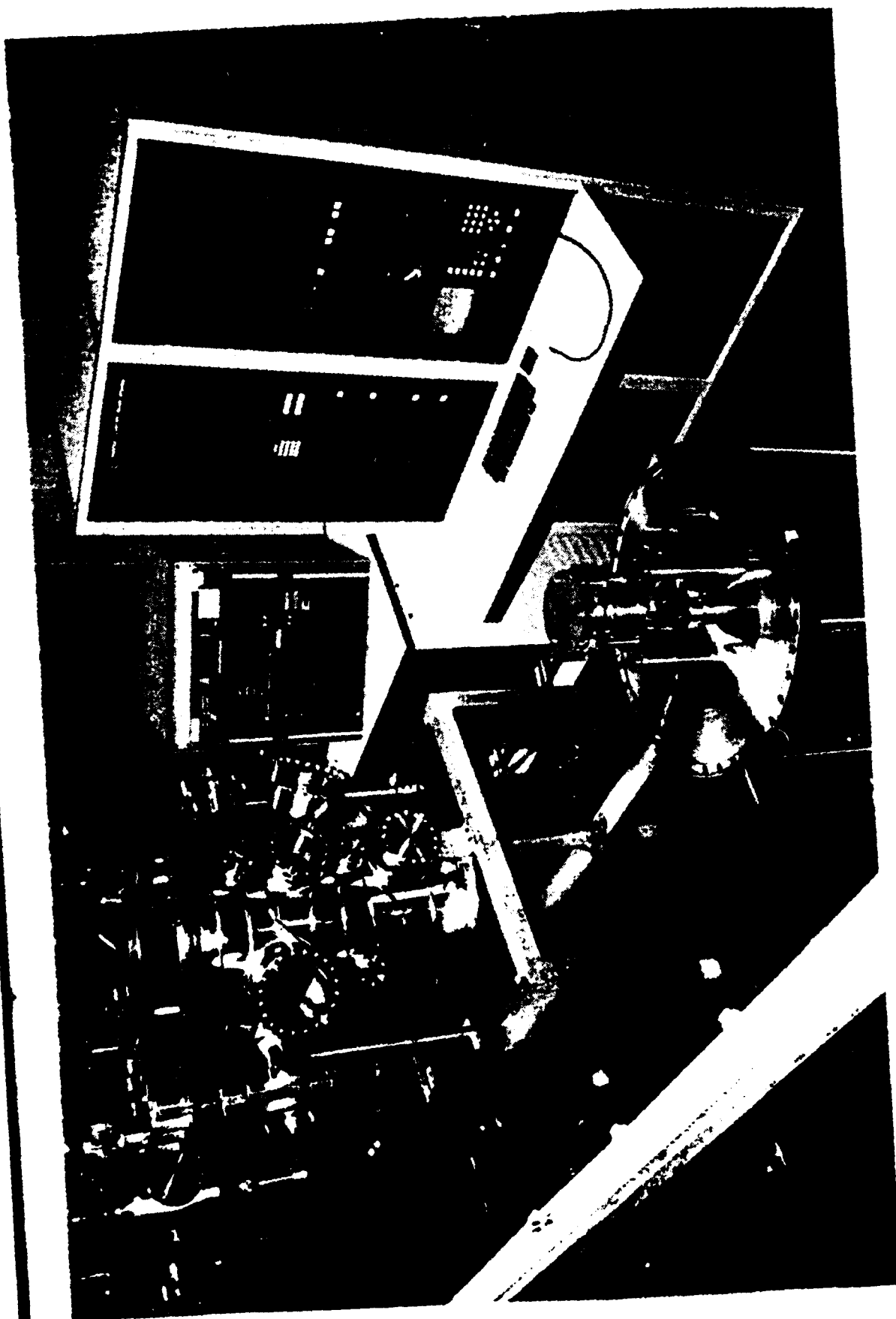


Figure 4 Single source ionized cluster beam deposition system during initial states of construction. The source shown on the baseplate has been replaced by a second generation source.

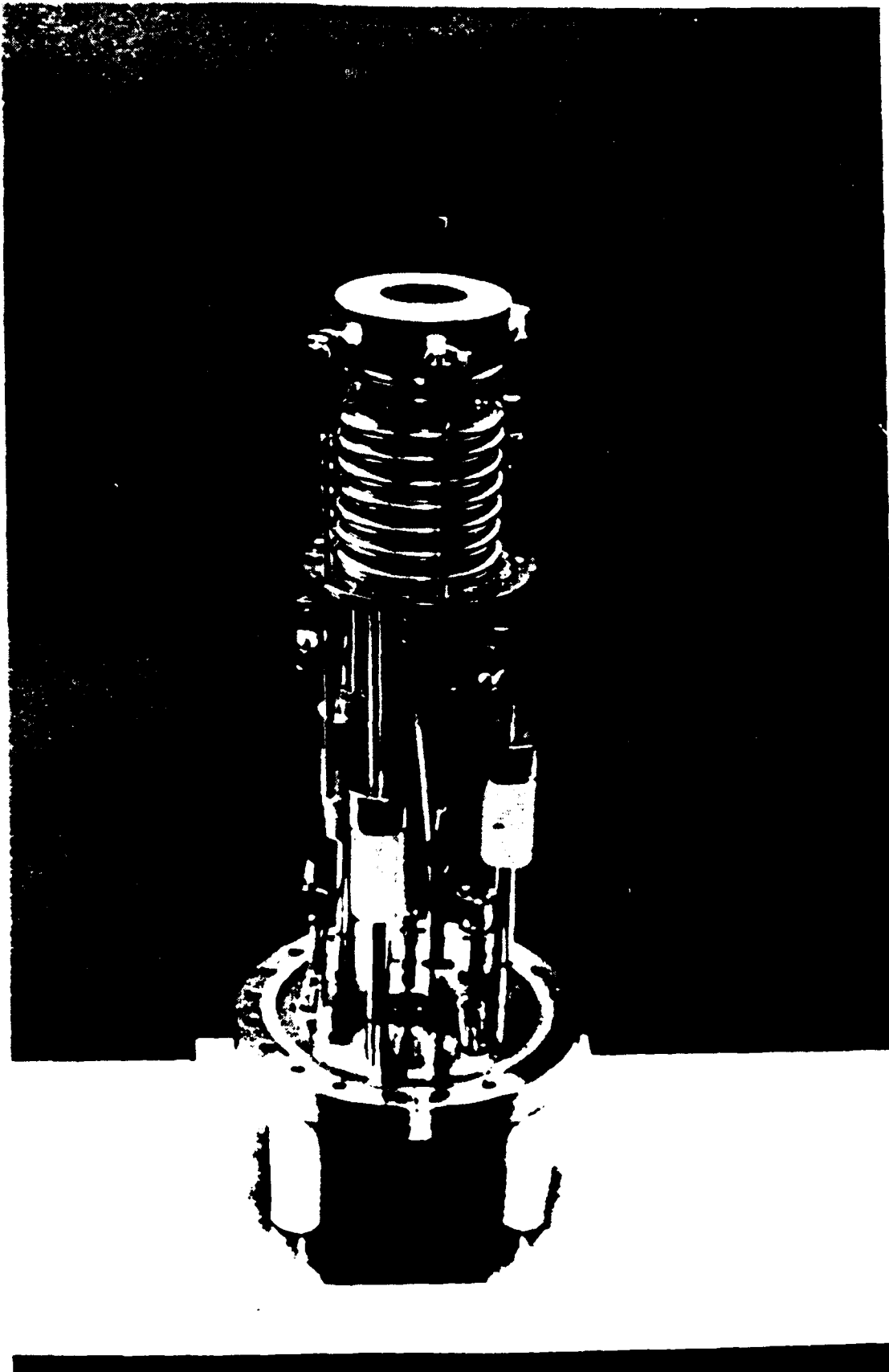


Figure 5 Second generation ionized cluster beam source mounted on an ultrahigh vacuum flange.

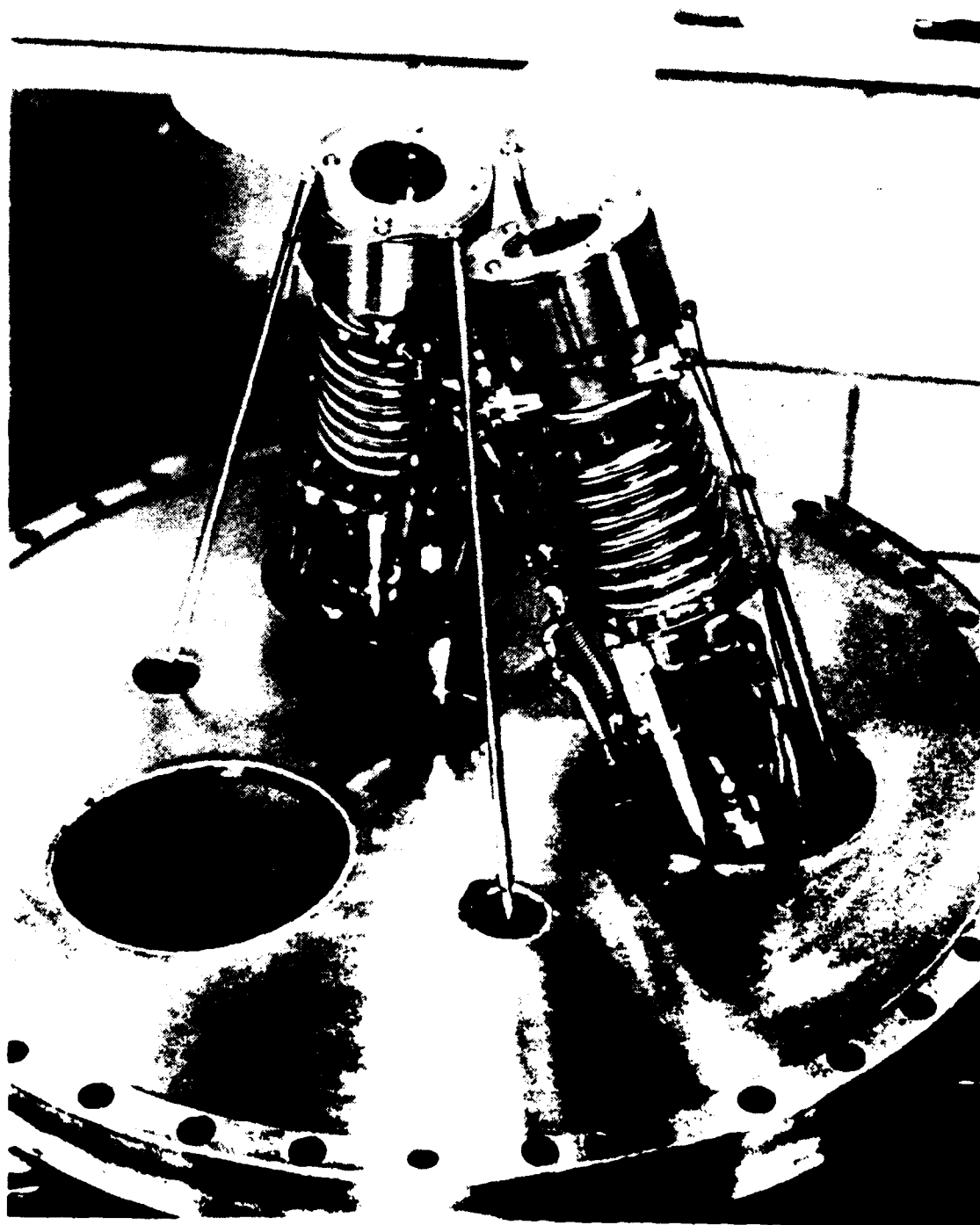


Figure 6 Base plate of three source ionized cluster beam deposition chamber. Two of the second generation sources are shown along with the shutter mechanism.

The commercial sputtering head, however, was totally unsatisfactory for deposition of oriented piezoelectric films. Previous experience with small locally built sputtering heads indicated that such designs could be used successfully to prepare such oriented films. A large scale head compatible with UHV conditions was therefore built for the thin film facility. The new 10 inch head has successfully produced oriented AlN films with very low oxygen concentrations.

2.3 Electron Energy Loss Spectroscopy

The High Resolution Electron Energy Loss Spectrometer (HREELS) is designed to detect vibrational modes on surfaces. A commercial unit was purchased from Leybold Heraeus (EELS 22 system) and placed in a locally designed vacuum system.

Because of the low energies of the electrons probing the surface, very low magnetic fields are required. Netic and Co-Netic alloy sheets were employed to reduce the magnetic fields to acceptable levels.

Since sample cleanliness is essential to the detection of surface modes, recent work has concentrated on sample preparation. This includes the installation of a differentially pumped ion gun, a sample heater, and a sample holder that will eventually be used in conjunction with a load lock. Figure 7 shows the typical loss spectra for an amorphous Si film.

Valence band and core level Electron Energy Loss Spectroscopy (EELS) were used to study r.f. sputter deposited hydrogenated amorphous germanium carbide films ($a\text{-Ge}_{1-x}\text{C}_x\text{H}$; $0 \leq x \leq 1$). The optical gap of the films ranged from 0.8 - 1.0 eV in $a\text{-Ge:H}$ to 1.2 - 2.3 eV in $a\text{-C:H}$. Valence band EELS of clean sputter etched $a\text{-Ge}$ and $a\text{-Ge:H}$ films ($x=0$), as compared to that of Ar^+ sputter etched $\text{Ge}(111)$ and hydrogen covered single crystals of Ge , respectively, indicated preferential sputtering of hydrogen by Ar ions, in contrast to recent observations on r.f. sputter deposited $a\text{-Si:H}$, where Ar^+

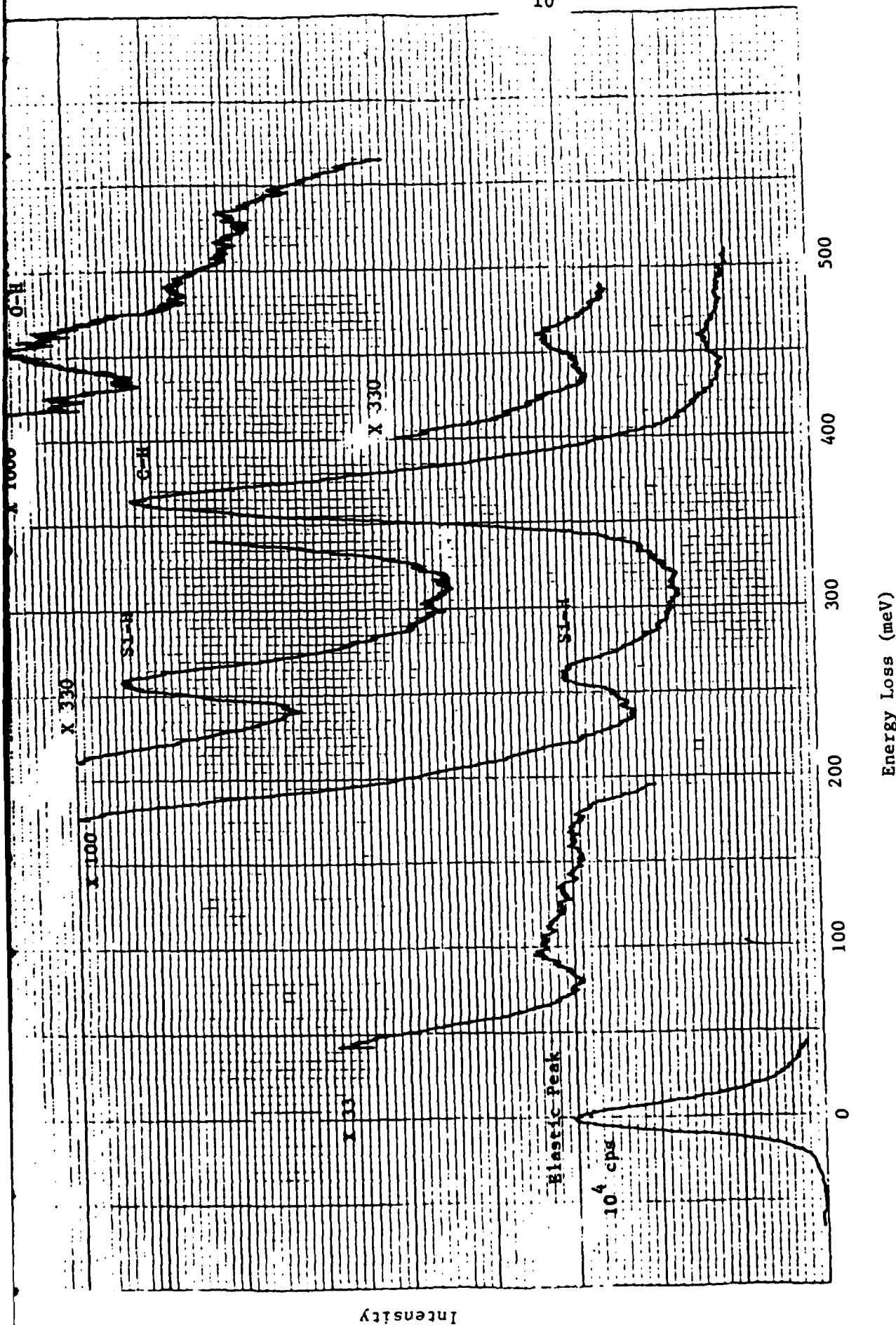


Figure 7 Loss spectra for a typical aSi:H thin film. Clearly shown are C and O contaminant on the surface.

etching did not cause complete depletion of hydrogen from the surface. In $a\text{-Ge}_{1-x}\text{C}_x\text{:H}$ alloy films ($0 < x < 1$) loss peaks related to carbon and Ge-C bonds were identified. Auger analysis of as prepared a-C and a-C:H films ($x=1$) indicated relatively clean surfaces. Typically, only 1 - 2% oxygen was found on the surfaces. EELS experiments indicated graphite-like surface structures. In addition, the hydrogen bulk content had no influence on the spectra, suggesting that the surfaces of the a-C:H films were hydrogen depleted. The Auger carbon lineshape further confirmed this assumption.

2.4 Auger Spectroscopy

A scanning Auger based on the Perkin Elmer 545 system has been constructed. It incorporates a Kratos rasterable ion gun for depth profiling. Lateral resolution for imaging and Auger mapping is about $1\text{ }\mu\text{m}$. A depth profile of a Ge film on Si is shown in Figure 8. Routine depth profiles and Auger maps showing lateral distribution of elements can be made on all the films being grown.

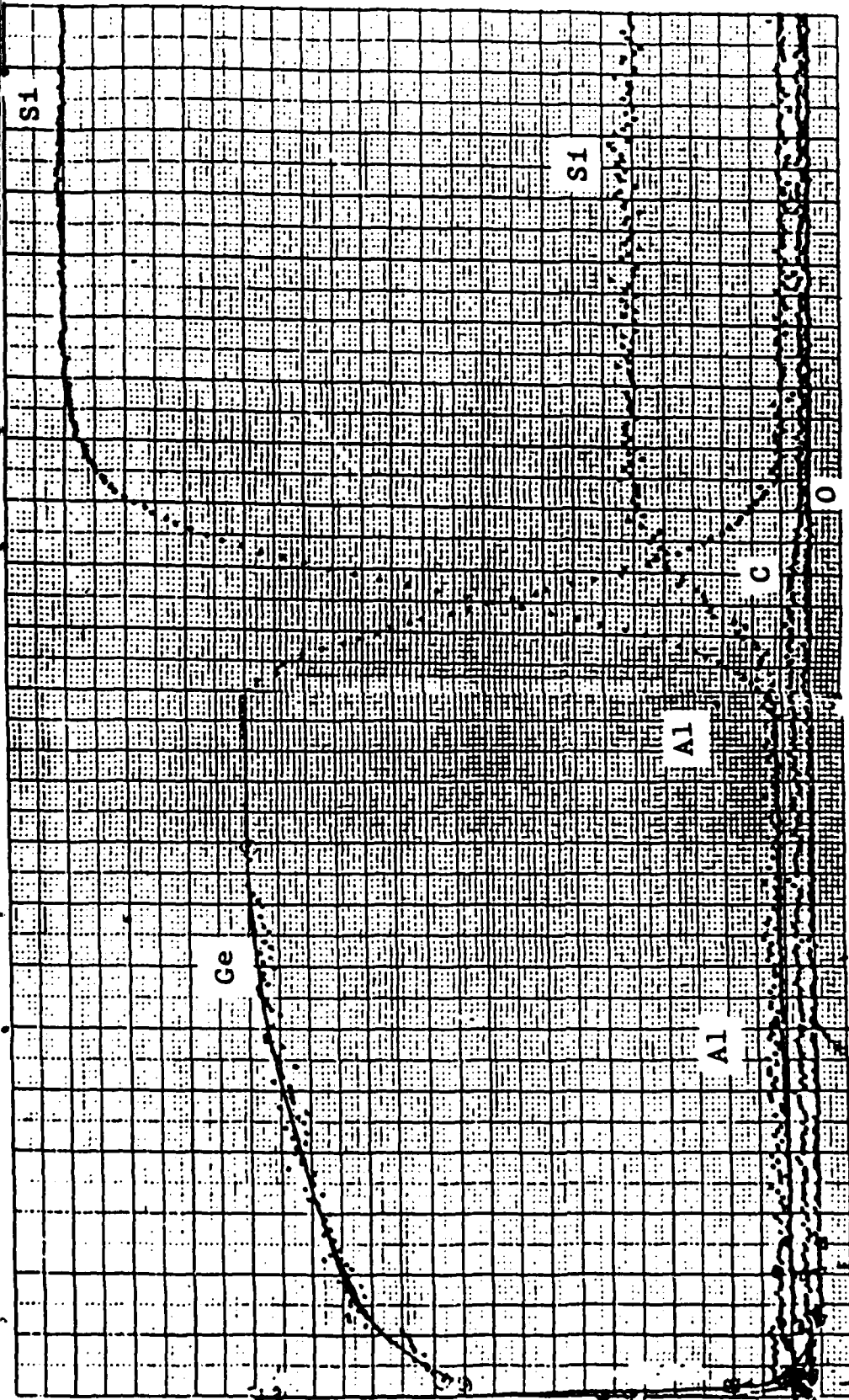
The Auger chamber makes use of differential pumping of the ion gun and a load lock to maintain a low pressure at all times in the analysis chamber. A base pressure of $< 2 \times 10^{-10}$ Torr is routine.

2.5 High Speed Ellipsometry

The use of RHEED to monitor film growth during deposition is not practical with ICB because of the high electric fields in the system. For this reason ellipsometry is being investigated as an alternate probe. Commercially available systems are, however, too slow to provide the desired time resolution for film nucleation studies. We, therefore, elected to construct a system with < 0.1 sec/data point resolution.

Two different very high speed ellipsometers have been constructed as part of a thesis project (see the M.S. thesis by M. Fleshner included in the

Relative Concentration



Sputter Time

Figure 8 Auger depth profile of a Ge film on Si. In addition to the Ge Auger line and the high and energy Si lines, the Al, C and O lines were monitored. Little or no C or O was observed in the film or at the interface but there appeared to be a small increase in the Al dopant at the interface.

appendix). Using a Jones matrix formalism, generalized expressions for the intensity of light were calculated for these designs. Based on these expressions, unique alignment procedures were developed for the two ellipsometers. An electronics feedback mechanism also had to be developed. A software package was written such the ellipsometers could be operated by a Hewlett Packard 9836 computer. The software included a complex math module, procedures to calculate a discrete Fourier transform, the value of any Bessel function with any argument, a digitizer control package, procedures to reduce the raw data to (Ψ, Δ) and a program which interprets (Ψ, Δ) to provide film thickness, index of refraction, and the reflectivity of the unknown film.

Special adapters are now being designed such that one of the ellipsometers can be mounted on the three source ICB system for film growth studies.

3. FILM DEPOSITION STUDIES

As the deposition equipment became operational several film growth studies were initiated. The growth of aluminum on silicon and germanium epitaxy on silicon were used to obtain experience with ICB deposition in preparation for more detailed studies on cluster size and acceleration voltage effects on film growth.

Studies were also started on the reactive r.f. magnetron sputter deposition of LiNbO_3 films on silicon and sapphire substrates for device applications.

3.1 Aluminum on Silicon

We have applied the ICB technique to the growth of Aluminum films on (001) silicon substrates. Details of the growth are given in the McCalmont thesis attached to this report.

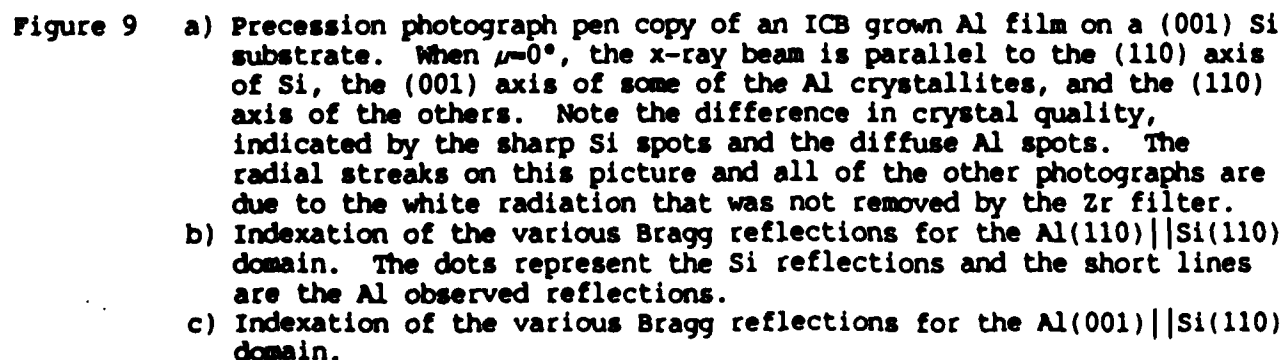
Crystal quality and orientation of the films were determined by x-ray diffraction. A low resolution θ - 2θ scan yielded only one Al reflection, indexed as (220). The question naturally arose as to whether or not the film was epitaxial. Figure 9 shows a pen copy of the precession photograph of this system together with sketches to visualize the spots from the various domains. The pen copy has been substituted for the photograph because the Al reflections were quite weak and did not reproduce well. The θ - 2θ scan probes only the central, vertical line on the picture.

The Al (220) reflection is easily visible. About ten other reflections can be seen from the Al film; they are weak, extended, and diffuse, indicating that the film is polycrystalline, but with very highly preferred orientations. It is interesting to note the indices of these reflections. Aluminum is face-centered cubic, and it is impossible in a cubic cell to have a (111) and a (020) plane only about 10° apart as is observed. Similarly, the ($\bar{2}20$) and (002) reflections cannot both lie on the same line. Thus, there are two preferred orientations. Both have the (110) direction perpendicular to the surface.

This domaining is simple to understand. The ($\bar{2}20$) Al to (400) Si d-spacing mismatch is about 5%. The two energetically equivalent orientations available to the aluminum during the growth place the ($1\bar{1}0$) direction of Al parallel to either the (100) or (010) directions of the Si substrate surface.

A third, less likely, orientation is indicated by another very weak pair of {200} reflections. Inokawa and Takagi (1985) show electron diffraction patterns of Al also grown by ICB on (001) Si. The major two preferred orientations were identified, but this third one was not observed by them.

To summarize, the investigated ICB Al films are polycrystalline, but with most of the crystallites epitaxially grown on the Si substrate. A final interesting observation is the presence of diffuse streaks, parallel to the $\langle 111 \rangle$ axes of Si and connecting the Si reflections. These are presumably due to a straining of the substrate or thermal diffuse scattering.



As more experience is obtained with ICB deposition, it may prove a useful technique for metallization of silicon substrates for ohmic contacts.

3.2 Ge Film Deposition

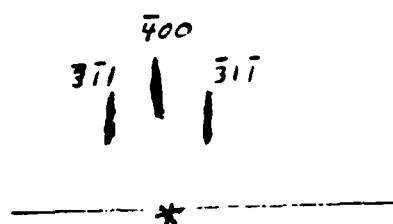
Although our initial efforts in the growth of Al films by ICB provided interesting results, there were considerable problems with the crucible nozzle plugging. To avoid the crucible problem, we chose to use Ge deposition as a method to evaluate the ICB system. Also, epitaxial Ge films on silicon substrates provide the first step toward the growth of GaAs on Si.

A series of Ge films have been deposited in the single source ICB. Details of the depositions are included in the McCalmont thesis and associated paper attached at the end of this report. A typical RHEED pattern for (100) Ge on (100) Si is shown in Figure 10.

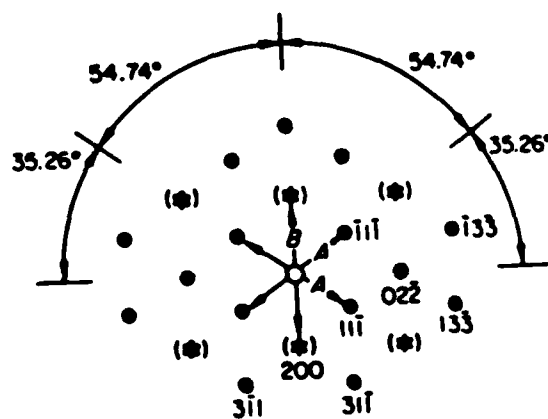
Figure 7.3 in the attached thesis by McCalmont is a precession photograph of a 0.5 μm thick (001) Ge epitaxial layer on a (001) Si substrate grown by ICB. Each spot in the photograph is doubled: the inner spot is a Ge reflection and the outer one is from the Si crystal. The intensities of the Ge reflections are usually weaker than those of Si because of the thinness of the layer. The lattice mismatch between Ge and Si is about 4%, yet the epitaxial quality is excellent.

As capabilities for deposition of GaAs are not yet available locally, several of the Ge coated silicon substrates have been sent to another laboratory for CVD growth of GaAs.

Epitaxial Ge films have also been obtained on (100) GaAs substrates. These films were deposited during the ICB source checkout procedure so extensive evaluation of the films has not been done.



a)



$$\frac{2}{\sqrt{3}} \cdot 1.155 \text{ } \theta \cdot \lambda \cdot [011]$$

b)

Figure 10

RHEED pattern of (100) Ge film on (100) Si: substrate with electron beam parallel to (110).

- a) Observed RHEED pattern. Streaking due to very flat film surface. The center streak is the spectral reflection.
- b) General electron diffraction pattern for the diamond structure with the electron beam parallel to the (110). The asterisks indicate positions of possible double diffraction reflections.

3.3 Sputter Deposition of LiNbO_3

Lithium niobate films have been sputter deposited and analyzed to determine their suitability for transducer or resonator material. A set of sputtering parameters was determined as the most relevant variables in the r.f. sputter deposition of LiNbO_3 thin films. The parameters were then optimized with respect to each other to obtain the best quality (in regard to crystallinity) thin films. The optimized parameters were:

An applied radio-frequency power of 300 watts.

A target-substrate separation of 8 cm.

A sputtering pressure of 3m Torr.

An oxygen content of 50% in the sputtering gas.

A substrate temperature of 550°C - 600°C .

A sapphire substrate.

Details of this work are given in the thesis by J. Martin in Appendix C.

With these optimized parameters in effect, the resulting films were deposited with a deposition rate of approximately 1300 Å/hour. The DC bias during the deposition was around 350 volts. Infrared scans of the films revealed a definite LiNbO_3 crystalline curve with distinctive peaks. X-ray diffraction patterns and RHEED photos demonstrated that the films were highly oriented polycrystalline LiNbO_3 . Auger electron spectroscopy on these films indicated an almost identical stoichiometry as bulk single crystal LiNbO_3 , with little contamination. The relative permittivity of these films was determined to be 15-16. No piezoelectric effect was observed using the composite resonator structure.

Several possible explanations were supplied concerning this lack of piezoelectric response. While LiNbO_3 deposited on p+ membranes appears unsuitable for use as a composite resonator, very possibly due to the p+ membrane, sputtered LiNbO_3 could be used for other piezoelectric devices which require thinner films and do not demand a substrate with a poor lattice match or p+ doping. SAW devices on sapphire would be an example.

Further work will be done. A better sputtering system (more automated) will be used so that slower deposition rates, and thus possibly better films can be produced. An applied DC bias can be added to the sputtering system so as to more likely pole the sputtered films. Another possibility would be to try an entirely different method of sputtering lithium niobate, such as completely reactive sputtering.

4. INVITED TALKS, CONTRIBUTED PAPERS AND PUBLICATIONS

Invited Talks

- "Ionized Cluster Beam Deposition of Thin Films," H.R. Shanks, University of Sherbrooke, Sherbrooke, Quebec, Canada, May 1985.
- "Ionized Cluster Beam Growth of Electronic Materials," H.R. Shanks, American Association on Crystal Growth Conference, Lake Tahoe, California, June 1985.
- "Ionized Cluster Beam Growth of Materials," H.R. Shanks, 3M Research Center, St. Paul, Minnesota, August 1985.
- "Design of ICB Sources," H.R. Shanks, Perkin-Elmer, Minneapolis, Minnesota, January 1986.
- "Ionized Cluster Beam Deposition of Thin Films," H.R. Shanks, NRL, Washington, D.C., March 1986.
- "Aluminum and Germanium Thin Films Deposited in an Ultrahigh-Vacuum Ionized Cluster Beam System," J.S. McCalmont, H.R. Shanks, and K.M. Lakin, International Workshop on Ionized Cluster Beam Techniques, Tokyo, Japan, June 1986.

Contributed Papers

- "New ISU Thin Film Facility," H.R. Shanks, AVS Illinois Sectional Meeting, Chicago, October 1984.
- "Germanium Thin Films Deposited by the Ionized Cluster Beam Technique," J.S. McCalmont, H.R. Shanks and K.M. Lakin, 33 National Symposium of the AVS, Baltimore, October 1986.

Publications

- J.L. Staudenmann, R.D. Horning and R.D. Knox, "Buerger Precession Camera and Overall Characterization of Thin Films and Flat-Plate Crystals," Journal of Applied Crystals 20 210 (1987).
- R. Shinar, J. Shinar, H.S. Wu, and H.R. Shanks, "Electron Energy Loss Studies on RF Sputtered $a\text{Ge}_{1-x}\text{C}_x\text{:H}$ Films." To be published in Journal of Vacuum Science and Technology.
- J.S. McCalmont, H.R. Shanks and K.M. Lakin, "Aluminum and Germanium Thin Films Deposited in an Ultrahigh-Vacuum Ionized Cluster Beam System," Proceedings, International Conference on the Ionized Cluster Beam Techniques (1986).
- J.S. McCalmont, H.R. Shanks and K.M. Lakin, "Germanium Thin Films Deposited by the Ionized Cluster Beam Technique." To be published as extended abstract, Journal of Vacuum Science and Technology.

APPENDIX A

Construction of two very-high-speed
photometric ellipsometers

Construction of two very-high-speed
photometric ellipsometers

by

Mark L. Fleshner

A Thesis Submitted to the
Graduate Faculty in Partial Fulfillment of the
Requirements for the Degree of
MASTER OF SCIENCE

Department: Physics
Major: Applied Physics

Approved:

In Charge of Major Work

For the Major Department

For the Graduate College

Iowa State University
Ames, Iowa

1986

TABLE OF CONTENTS

	page
INTRODUCTION	1
1. THEORY OF ELLIPSOMETRY	3
1.1. Representations of Polarized Light	3
1.1.1. The ellipse of polarizations	4
1.1.2. The Stokes vector and Poincare sphere	5
1.1.3. The Jones vector	7
1.2. The Jones Matrix Formalism	9
1.2.1. The relative intensity	10
1.2.2. The rotation matrix	11
1.2.3. The Jones matrix	12
1.3. Using the Jones Matrix Formalism in Ellipsometry	18
1.3.1. The Relationship of ψ and Δ with the Jones Matrix	18
1.3.2. The PCSA/PSCA Arrangements	20
2. OVERVIEW OF ELLIPSOMETER SYSTEMS	25
2.1. The Manual Null Ellipsometer	25
2.2. Automatic Ellipsometers	27
2.2.1. Automatic null ellipsometers	28
2.2.2. Automatic photometric ellipsometers	29
2.2.2.1. Static photometric ellipsometers	29
2.2.2.2. Dynamic photometric ellipsometers	30
2.2.2.2.1. Rotating polarizer/analyzer ellipsometer	30
2.2.2.2.2. Photoacoustic modulated ellipsometer	32
3. CONSTRUCTION OF A DYNAMIC PHOTOMETRIC ELLIPSOMETER (A POLARIZATION MODULATED ELLIPSOMETER)	37
3.1. The Optical Setup	37
3.1.1. The Rochon prisms	40
3.1.2. The photoacoustic modulator	42
3.1.3. The sample mount	43
3.1.4. Other mounts	43
3.2. The Electrical Setup	46
3.2.1. The photomultiplier tube	46
3.2.2. The feedback mechanism	48
3.2.3. The signal processing	54
3.3. Alignment	54
3.3.1. The initial setup	55
3.3.2. The final setup	57

3.4. Data Reduction	60
3.4.1. The discrete Fourier transform	61
3.4.2. Obtaining the optimal signal	66
3.4.2.1. Relationship of the Fourier coefficients with the Bessel functions	67
3.4.2.2. The gain of the PMT as a function of the voltage at the cathode	68
3.5. Calculation of ψ and Δ	71
4. CONSTRUCTION OF A VERY-HIGH-SPEED STATIC PHOTOMETRIC ELLIPSOMETER (THE DUAL ANALYZER ELLIPSOMETER)	75
4.1. The Ellipsometer Setup	76
4.1.1. The optical setup	76
4.1.2. Alignment	76
4.1.3. The electrical setup	79
4.2. Theory of the Ellipsometer	81
4.2.1. Static vs. dynamic photometric measurements	82
4.2.2. A particular setup	89
5. INTERPRETATION OF ψ AND Δ	91
5.1. The Bare Substrate System	91
5.1.1. Implementation	94
5.2. The Ambient-Film-Substrate System	94
5.2.1. Solving for the film thickness	101
5.2.2. Implementation	105
ACKNOWLEDGMENTS	106
APPENDIX A. SCHEMATIC DIAGRAM: THE HP 6516A POWER SUPPLY	109
APPENDIX B. PASCAL PROGRAM: THE DATA REDUCTION TESTS	112
APPENDIX C. PASCAL PROGRAM: FOR THE PHOTOACOUSTIC MODULATED ELLIPSOMETER	116
APPENDIX D. PASCAL PROGRAM: FOR THE DUAL ANALYZER ELLIPSOMETER	124
APPENDIX E. PASCAL PROGRAM: FOR THE INTERPRETATION OF ψ AND Δ	134

INTRODUCTION

Recently, scientists and engineers from the fields of surface physics and integrated device fabrication have focused much attention on the area of thin films research. As a result, a renewed interest has developed in the nondestructive experimental technique called ellipsometry, first introduced over a century ago. For many years, the slow and laborious technique of null ellipsometry was used to characterize the surfaces of filmed and non-filmed materials. However, the introduction of many new deposition techniques has inspired new questions as to exactly what takes place in the first moments a film is put down. Hence, an interest has arisen to develop very high speed ellipsometers, which can observe and even monitor the growth of thin films in situ.

With the advent of high speed small computers and digital devices, it is now possible to perform ellipsometric measurements at rates in the micro-second regime. This paper deals with the construction of two such very high speed ellipsometers. Chapter 1 discusses the general theory of ellipsometry. Chapter 2 gives an overview of the ellipsometer systems currently available, and detailed descriptions of how some of these ellipsometers function. Chapter 3 describes, in detail, the photoacoustic modulated ellipsometer, developed for this work. Chapter 4 discusses a new type of ellipsometer, (which will be called the dual analyzer ellipsometer), developed for this work. This ellipsometer can acquire a set of ellipsometric data at speeds over 10 times faster than

the fastest photoacoustic modulated ellipsometers currently available. Also, Chapter 4 includes a discussion as to precisely where this new type of ellipsometer system fits in the general categories outlined in Chapter 2. Finally, Chapter 5 deals with the interpretation of the raw data obtained by ellipsometers. The interpretation of ellipsometric data is a vast subject. Therefore, the two most commonly used methods of interpretation were implemented here.

1. THEORY OF ELLIPSOMETRY

Ellipsometry can be generally defined as the measurement of the state of polarization of a polarized vector wave¹. In particular, optical ellipsometry deals only with polarized vector waves of light. Ellipsometry is generally conducted in order to acquire information about a particular optical system, which somehow modifies the state of polarization. Measurement of the initial and final states of polarization describes the type of modification that the polarization has undergone. From this information, it is possible to determine the complex index of refraction of a planar interface or a single thin film, the thickness of the film, or even such things as the stoichiometry of the surface. In addition, ellipsometry is a nondestructive technique, and therefore, has a wide range of applications from measurements on metals to measurements on cell-surface materials.

In order to understand how the initial and final states of polarization are measured, it is necessary to understand the various methods of representing polarized light. Three representations of polarization will be discussed: the ellipse of polarizations, the Stokes vector (and Poincare sphere), and finally the Jones vector.

1.1. Representations of Polarized Light

Polarization is a property that all vector waves have in common. Polarization refers to the time development at a fixed point in space of a field vector. The electric field vector E is usually chosen to define the state of polarization for light, since the electrons in

matter interacting with electromagnetic radiation in the visible region experience a much greater force due to the electric field than the magnetic field.

1.1.1. The ellipse of polarizations

The following discussion is based on a similar discussion in Ref.

2. Consider the case of a monochromatic plane wave of electromagnetic radiation, where the electric field vector, E , is harmonic in time and is transverse to the direction of propagation (the z axis). E can then be written

$$E_x = a_1 \cos(\tau + \delta_1) \quad 1.1$$

$$E_y = a_2 \cos(\tau + \delta_2) \quad 1.2$$

$$E_z = 0, \quad 1.3$$

where τ is the variable part of the phase, namely $\tau = \omega t - kz$,

a_1 and a_2 are spacial functions but time independent, and δ_1 and δ_2 are constant phase factors.

The factor τ can be eliminated from equations 1.1 and 1.2 yielding

$$\frac{E_x^2}{a_1^2} + \frac{E_y^2}{a_2^2} - 2 \frac{E_x}{a_1} \frac{E_y}{a_2} \cos \delta = \sin^2 \delta \quad 1.4$$

where $\delta = \delta_2 - \delta_1$. This is the equation of an ellipse. Notice that the equation of an ellipse degenerates into the equation of a line when $\delta = m\pi$, and into an equation of a circle when $E_{0x} = E_{0y}$ and $\delta = (2m+1)\pi/2$, $m = 0, \pm 1, \pm 2, \pm 3, \dots$

A graph of locust of points solving equation 1.4 is shown figure

1.1. The ellipse is inscribed into a rectangle whose sides are parallel

to the coordinate axes and whose lengths are $2a_1$ and $2a_2$. The principal semi-axes a and b of the ellipse and the angle ψ , which the major axis makes with x , are specified by the formulae

$$a^2 + b^2 = a_1^2 + a_2^2 \quad 1.5$$

$$\tan 2\psi = \tan 2\alpha \cos \delta \quad 1.6$$

$$\sin 2\chi = -\sin 2\alpha \sin \delta \quad 1.7$$

where $\tan \chi = \pm b/a$ and $\tan \alpha = a_2/a_1$. Note that $-90^\circ \leq \chi \leq 90^\circ$ specifies the shape and orientation of the ellipse and ψ characterizes the ellipticity and the sense in which the ellipse is being described. Therefore, to completely characterize the polarization ellipse, three independent quantities are necessary, either the amplitudes a_1 and a_2 and the phase difference δ or the major and minor axes a, b at the angle χ , which specifies the orientation of the ellipse.

1.1.2. The Stokes vector and Poincare sphere

It is convenient to characterize the state of polarization by certain parameters first introduced by G. G. Stokes in 1852 called Stokes parameters². The Stokes parameters of a plane monochromatic wave are the four quantities

$$s_0 = a_1^2 + a_2^2 \quad 1.8$$

$$s_1 = a_1^2 - a_2^2 \quad 1.9$$

$$s_2 = 2a_1a_2\cos\delta \quad 1.10$$

$$s_3 = 2a_1a_2\sin\delta \quad 1.11$$

where a_1 , a_2 and δ are defined above. Since an ellipse can be characterized by three independent variables, the four Stokes parameters must be related by an identity, namely

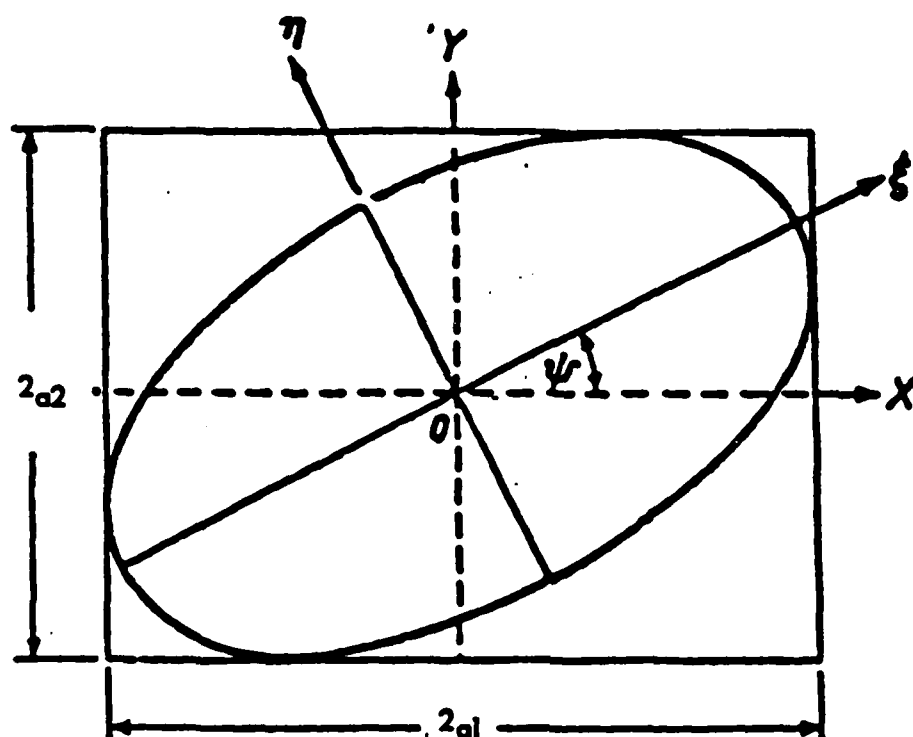


Figure 1.1. Elliptically polarized wave. The vibrational ellipse for the electric field vector

$$s_0^2 = s_1^2 + s_2^2 + s_3^2. \quad 1.14$$

The parameter s_0 is proportional to the intensity of the wave. s_1 , s_2 and s_3 are related to the angles χ and ψ defined above in the following way

$$s_1 = s_0 \cos 2\chi \cos 2\psi \quad 1.13$$

$$s_2 = s_0 \cos 2\chi \sin 2\psi \quad 1.14$$

$$s_3 = s_0 \sin 2\chi. \quad 1.15$$

The relations 1.13-1.15 indicate a simple geometric representation of the states of polarization, i.e., s_1 , s_2 , and s_3 may be regarded as the Cartesian coordinates of a point on a sphere \mathcal{E} of radius s_0 , such that 2χ and 2ψ are the spherical angular coordinates of this point. See figure 1.2. To every possible state of polarization of a plane monochromatic wave of a given intensity ($s_0 = \text{a constant}$), there corresponds one point on \mathcal{E} . The sphere \mathcal{E} is called the Poincare sphere. The set (s_0, s_1, s_2, s_3) is commonly called the Stokes vector of the polarization.

1.1.3. The Jones vector

A more concise representation of polarization than those described previously is the Jones vector representation. Assume a single monochromatic, uniform, transverse electric travelling plane wave of arbitrary polarization. If such a wave travels in the direction of the z axis, then the electric field vector can be written as,

$$\mathbf{E}(z, t) = [E_x \cos(\omega t - \frac{2\pi z}{\lambda} + \delta_x)]\mathbf{i} + [E_y \cos(\omega t - \frac{2\pi z}{\lambda} + \delta_y)]\mathbf{j} \quad 1.16$$

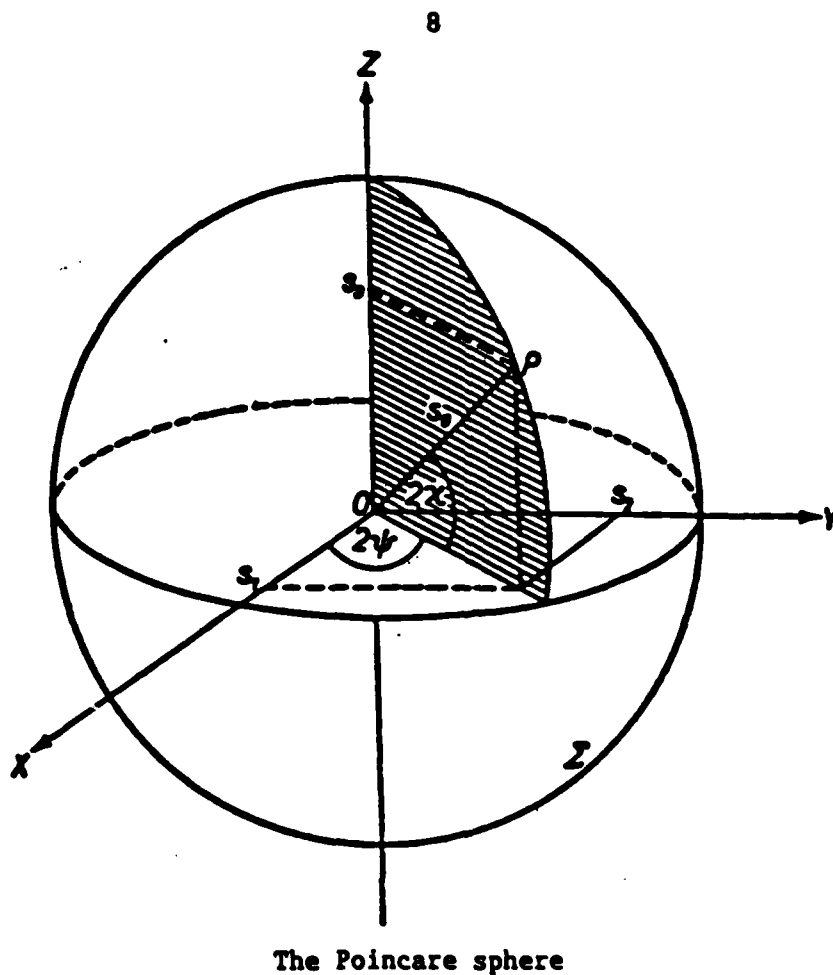


Figure 1.2. Poincare's representation of the state of polarization of a monochromatic wave

where E_x and E_y represent the amplitudes of the linear, simple harmonic oscillations of the electric field components along the x and y axes, and δ_x and δ_y represent the respective phases of these oscillations. $E(z,t)$ can be written in the form of a 2×1 column vector as follows

$$E(z,t) = \begin{bmatrix} E_x \cos(\omega t - 2\pi z/\lambda + \delta_x) \\ E_y \cos(\omega t - 2\pi z/\lambda + \delta_y) \end{bmatrix}. \quad 1.17$$

Suppressing the temporal and z spatial dependence and using phasor notation equation (1.17) can be replaced by

$$E = \begin{bmatrix} E_x \\ E_y \end{bmatrix} \quad 1.18$$

where $\dots E_x = IE_x Ie^{i\delta_x}$ and $E_y = IE_y Ie^{i\delta_y}$.

Equation 1.18 is the desired concise representation of polarized light mentioned above and is known as the Jones vector of the wave¹. As was the case with the previous representations of polarized light, the Jones vector contains complete information about the polarization of the wave i.e., it contains complete information of the amplitudes and phases of the field components. The Jones vector is a complex vector because its elements are phasors. The components of the Jones vector represent two sinusoidal linear oscillations along two mutually perpendicular directions.

1.2. The Jones Matrix Formalism

The intensity of light incident on the photodetector is the fundamental quantity measured at the photodetector of any ellipsometer.

Therefore, it is necessary to obtain an expression for the intensity of the light. The Jones matrix formalism is often used to obtain this expression.

1.2.1. The relative intensity

The intensity of the wave represented by equation (1.18) can be written to within a multiplicative constant as

$$I = \mathbf{E}^T \mathbf{E} = |E_x|^2 + |E_y|^2 \quad 1.20$$

where \mathbf{E}^T is the Hermitian adjoint of the Jones vector \mathbf{E} .

In most applications of ellipsometry, one is interested in a relative intensity and not the absolute intensity. A wave is said to be normalized and its Jones vector is said to be normal. Such a wave satisfies the condition

$$\mathbf{E}^T \mathbf{E} = 1 \quad 1.21$$

Figure 1.3 gives some examples of Jones vectors for various states of polarization¹.

1.2.2. The rotation matrix

Figure 1.4 shows the resolution of the electric field vector \mathbf{E} along two coordinate systems (x, y) and (x', y') . The law of transformation of the Jones vector under the effect of a coordinate rotation can be written in matrix as

$$\mathbf{E} = \begin{bmatrix} E_x' \\ E_y' \end{bmatrix} = \begin{bmatrix} \cos \alpha & \sin \alpha \\ -\sin \alpha & \cos \alpha \end{bmatrix} \quad 1.22$$

or more concisely,

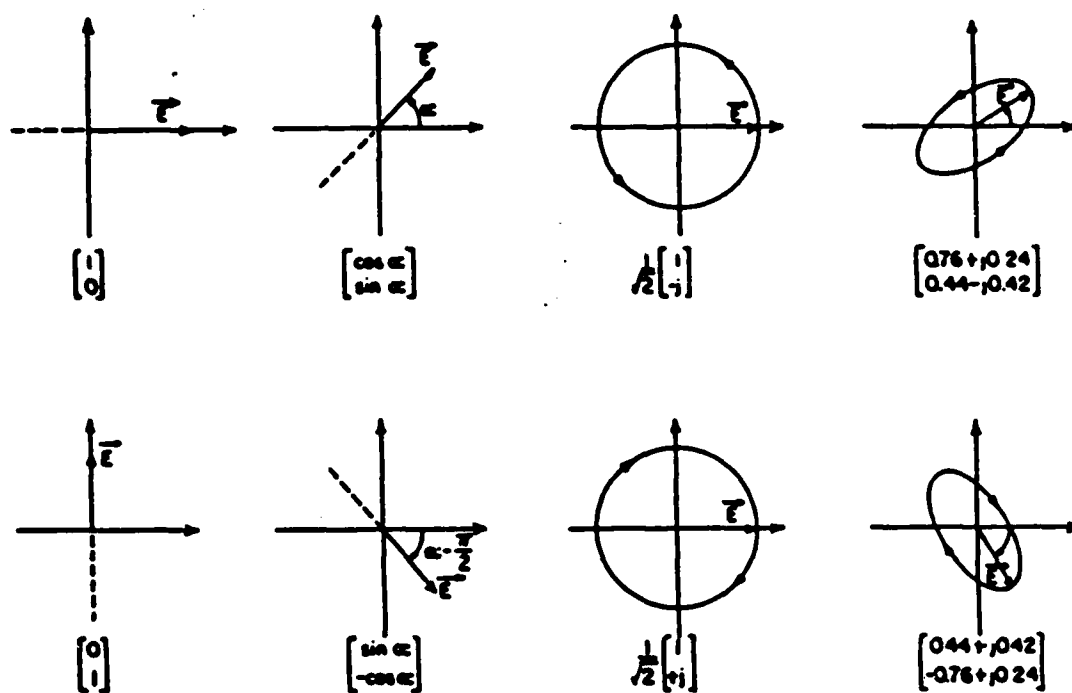


Figure 1.3. The Jones vectors of some states of polarization

$$E_{x'y'} = R(\alpha)E_{xy} , \quad 1.23$$

where

$$R(\alpha) = \begin{bmatrix} \cos\alpha & \sin\alpha \\ -\sin\alpha & \cos\alpha \end{bmatrix} . \quad 1.24$$

$R(\alpha)$ is called the rotation matrix. Similarly, $R(-\alpha)$ is called the antirotation matrix. $R(\alpha)$ and $R(-\alpha)$ are extremely useful in determining the relative intensity of the light measured in an ellipsometer.

1.2.3. The Jones matrix

Recall that the fundamental principal in ellipsometry is the measurement of the modification of the initial and final states of polarization of light interacting with some sort of optical system. Consider a uniform monochromatic transverse electric plane wave incident on a nondepolarizing optical system. Figure 1.5 shows a schematic diagram of the optical system.

In the absence of non-linearity and other frequency-changing processes, the pair of oscillations, $E_{0x'}$ and $E_{0y'}$, at the output of the optical system are related to the pair of oscillations, E_{ix} and E_{iy} , at the input of the optical system by the following linear equations

$$E_{0x'} = T_{11}E_{ix} + T_{12}E_{iy} \quad 1.25$$

$$E_{0y'} = T_{21}E_{ix} + T_{22}E_{iy} . \quad 1.26$$

Equations 1.25 and 1.26 can be written in matrix form as

$$\begin{bmatrix} E_{0x'} \\ E_{0y'} \end{bmatrix} = \begin{bmatrix} T_{11} & T_{12} \\ T_{21} & T_{22} \end{bmatrix} \begin{bmatrix} E_{ix} \\ E_{iy} \end{bmatrix} \quad 1.27$$

or more concisely,

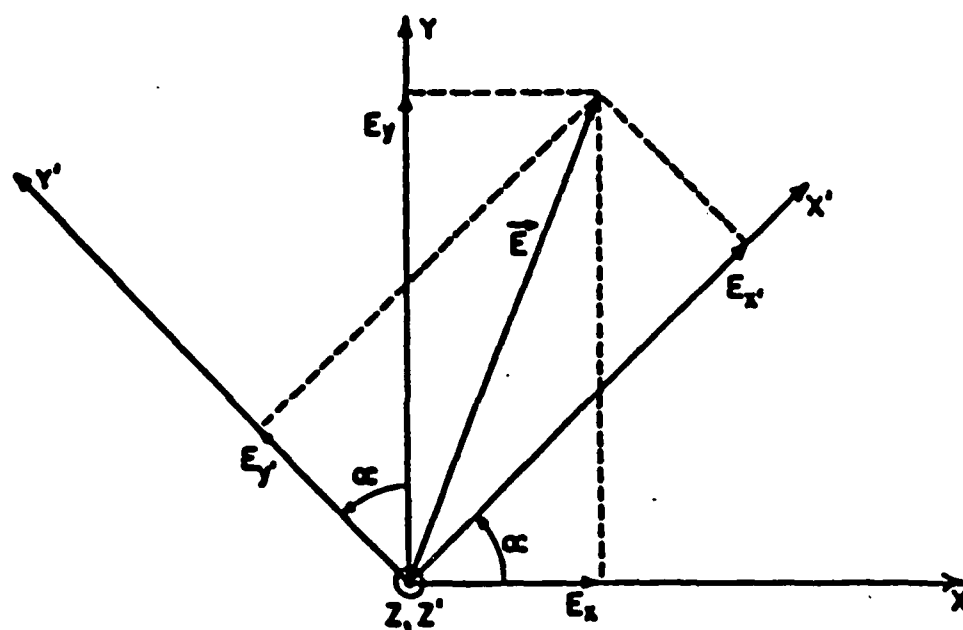


Figure 1.4. Resolution of the electric vector \vec{E} along two non-coincident coordinate systems (x, y) and (x', y')

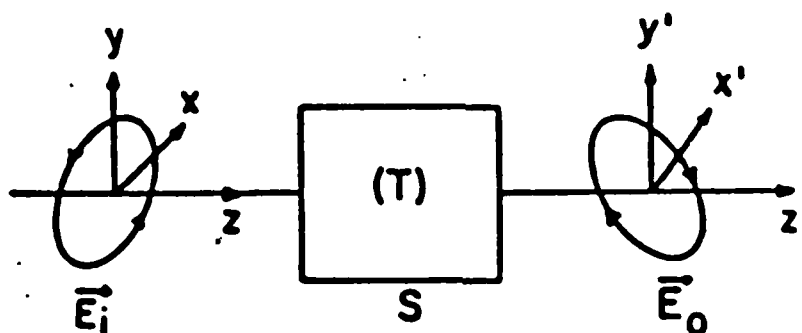


Figure 1.5. Incident on and emergent from the optical system S are plane waves of Jones vectors \vec{E}_i and \vec{E}_o referenced to Cartesian coordinate systems (x, y, z) and (x', y', z') , at the input and output of S , respectively. $\vec{E}_o = (T)\vec{E}_i$ where (T) is the Jones matrix of S

$$E_o = TE_i, \quad 1.28$$

where

$$T = \begin{bmatrix} T_{11} & T_{12} \\ T_{21} & T_{22} \end{bmatrix} \quad 1.29$$

Equation 1.29 expresses the Jones vector representation of the polarization of the output wave as a linear matrix transformation. The 2×2 matrix T is called the Jones matrix of the optical system. T describes the overall effect of the optical system on the incident wave.

The effect of N optical systems is demonstrated in figure 1.6. The Jones matrices of the N systems are T_1, T_2, \dots, T_N . The combined effect of the N systems on the output Jones vector can be written

$$E_o = T_N T_{N-1}, \dots, T_1 E_i \quad 1.30$$

or more concisely,

$$E_o = T_{\text{comb}} E_i \quad 1.31$$

where

$$T_{\text{comb}} = T_N T_{N-1}, \dots, T_1. \quad 1.32$$

T_{comb} is the Jones matrix of the combined system.

The following are examples of Jones matrices of optical systems commonly used in ellipsometry¹.

The isotropic retarder

$$T = e^{-2\pi k/\lambda} \begin{bmatrix} e^{-j2\pi nd/\lambda} & 0 \\ 0 & e^{-j2\pi nd/\lambda} \end{bmatrix}. \quad 1.33$$

An isotropic retarder is a plane parallel section of an isotropic medium of refractive index $N = n - jk$. The Jones matrix T for this device

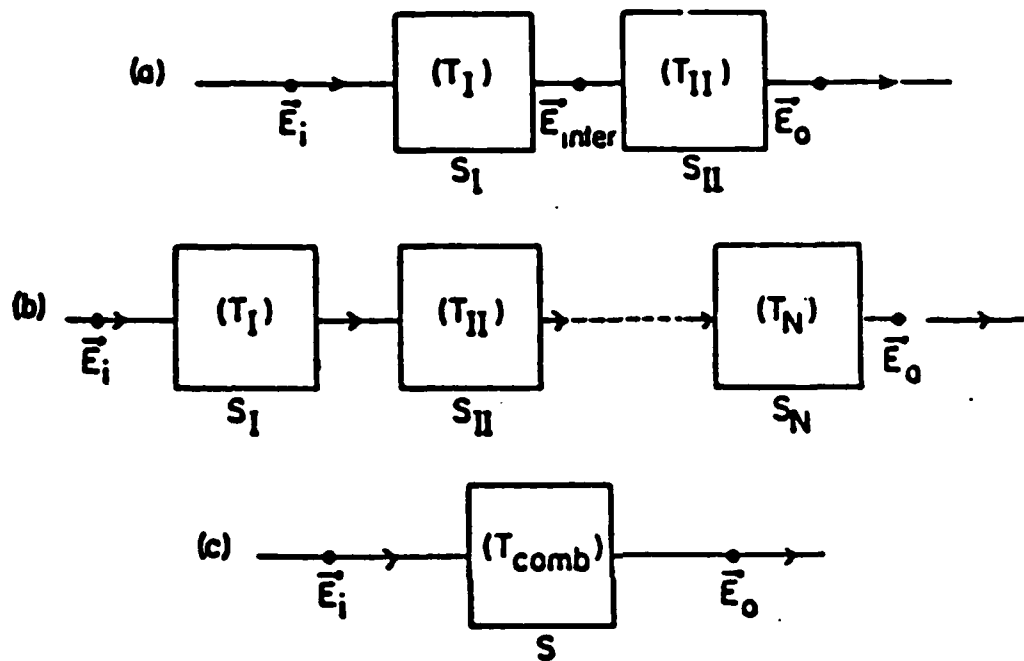


Figure 1.6. The combined effect of N optical systems S_I, S_{II}, \dots, S_N , of Jones matrices $(T_I), (T_{II}), \dots, (T_N)$ is equivalent to one system with Jones matrix $(T_{comb}) = (T_N)(T_{N-1}) \dots (T_{II})(T_I)$

expresses the fact that the wave whose wavelength in a vacuum is λ has been retarded by $2\pi nd/\lambda$.

The linear retarder (compensator)

$$T = \begin{bmatrix} e^{-j2\pi n'd/\lambda} & 0 \\ 0 & e^{-j2\pi n''d/\lambda} \end{bmatrix}. \quad 1.34$$

Here, n' is the ordinary refractive index and n'' is the extraordinary refractive index. The Jones matrix T for this device expresses the fact that the electric field vector along the two privileged directions parallel and perpendicular to the optic axis are retarded by different amounts, $2\pi n'd/\lambda$ and $2\pi n''d/\lambda$, respectively. T can be rewritten as

$$T = e^{2\pi ndn'/\lambda} \begin{bmatrix} 1 & 0 \\ 0 & e^{-j\delta} \end{bmatrix} = K_C \begin{bmatrix} 1 & 0 \\ 0 & e^{-j\delta} \end{bmatrix} \quad 1.35$$

where $\delta = (2\pi d/\lambda)(n'' - n')$ and K_C is a complex number that accounts for the equal amplitude and phase shift along the privileged directions.

The ideal polarizer

$$T = e^{-j2\pi d/\lambda} \begin{bmatrix} 1 & 0 \\ 0 & 0 \end{bmatrix} = K_P \begin{bmatrix} 1 & 0 \\ 0 & 0 \end{bmatrix}. \quad 1.36$$

The ideal polarizer does not allow any component of E_0 perpendicular to the transmission axis. Again, K_P is a complex number containing information on the equal amplitude and phase shift the light has undergone.

The simple reflector

$$R = \begin{bmatrix} r_p & 0 \\ 0 & r_p \end{bmatrix}. \quad 1.36$$

A simple reflector here will be defined to be a system with a single planar interface. The elements of R are the famous Fresnel coefficients and will be discussed in detail in a later chapter.

1.3. Using the Jones Matrix Formalism in Ellipsometry

As was mentioned earlier, Jones matrix formalism is used to obtain an expression of the intensity of light incident on the photodetector of the ellipsometer. Since the Jones matrix of the sample is not yet known, parameters must be introduced, which characterize the Jones matrix of this optical system. These parameters are commonly referred to as the ellipsometric angles ψ and δ . Maintaining ψ and Δ as two unknowns, it is then possible to determine the desired expression for the relative intensity of the light at the photodetector.

1.3.1. The relationship of ψ and Δ to the Jones matrix of an arbitrary optical system

In general, the Jones matrix T describes the overall effect of the optical system on the incident wave, where

$$T = \begin{bmatrix} T_{11} & T_{12} \\ T_{21} & T_{22} \end{bmatrix}. \quad 1.38$$

Examining equations 1.25 and 1.26 it can be seen that if the incident wave is linearly polarized in the x direction (i.e., $E_{iy} = 0$), then, in general, the output of the system will have two orthogonal linear

oscillations E_{ox} , and E_{oy} , and similarly for $E_{ix} = 0$. Hence, the presence of off-diagonal elements produces electric field oscillations in two perpendicular directions.

In most cases, the optical sample can be oriented so that the off-diagonal elements are zero. Then T in equation 1.38 reduces to the Jones matrix of a simple reflector, equation 1.37. The ellipsometric parameters can then be defined as

$$r_p/r_s = |r_p|/|r_s|e^{(\delta_p - \delta_s)} = \tan\psi e^{i\Delta}, \quad 1.39$$

where

$$\tan\psi = |R_p|/|R_s| \text{ and} \quad 1.40$$

$$\Delta = \delta_p - \delta_s. \quad 1.41$$

ψ and Δ are the ellipsometric parameters currently used in most ellipsometric applications.

In an ellipsometer, a beam of polarized light is propagated through a succession of optical devices, each of which produces a specific change in the state of polarization. Usually the Jones matrices of all but one of the optical systems in the ellipsometer are known before a measurement has been made. The optical system under investigation can modify the state of polarization of the light in one or a combination of the following basic processes: reflection or refraction, transmission, and scattering. As explained above (in the absence of depolarization) the optical system can be described in terms of its corresponding 2×2 Jones matrix. Therefore, the purpose of an ellipsometer is to determine the Jones matrix of the one optical system in question.

In the absence of depolarization by the optical system, the initial and final states will both be completely polarized. The

eigenpolarizations of an optical system can then be defined as the two polarization states that pass through the optical system unchanged (to within a multiplicative constant). In this case, the off-diagonal elements of the Jones matrix of the optical system are zero. Therefore, when light is reflected at the interface between two isotropic (non-optically-active) media, the linear polarizations of the electric field parallel (p) and perpendicular (s) to the plane of incidence are reflected with their polarization unchanged. The discussion that follows deals with the case where the linear eigenpolarizations of an optical system are known, i.e., the Jones matrix can be written as a diagonal matrix.

1.3.2. The PCSA/PSCA ellipsometer arrangements

A common ellipsometric arrangement is shown in figure 1.7. The following description is from Ref. 1. The optical system S under investigation has orthogonal linear eigenpolarizations (χ_{ex} and χ_{ey}) along orthogonal coordinate axes x and y. The optical system modifies the state of polarization of the incident light beam when that state is different from either one of its eigenpolarizations, χ_{ex} or χ_{ey} . The modified state of polarization of the light beam outgoing from the optical system is analyzed by the analyzing section of the instrument that consists of a linear analyzer (A) followed by a photodetector or photomultiplier tube (PMT). The photodetector measures the light flux after the beam has travelled through the polarizer-compensator-system-analyzer (PCSA) sequence of elements. The orientations of the polarizer, compensator, and analyzer around the beam axis are specified

by the azimuth angles P, C, and A, respectively. For the polarizer and analyzer, the azimuths P and A define the orientation of their transmission axes (i.e., the directions of the transmitted linear eigenpolarizations). For the compensator, the azimuth C defines the orientation of its fast axis (i.e., the direction of the fast linear eigenpolarization). All azimuths P, C, and A are measured from the direction of the x linear eigenpolarization of the optical system under measurement and are taken positive in a counterclockwise sense when looking against the direction of propagation of the beam.

With the help of the Jones matrix formalism discussed previously, it is straightforward to calculate the electric field vector and consequently, the relative intensity at the photodetector. As was discussed in Chapter 1, the resultant of N optical components is the 2×2 matrix obtained by matrix multiplication. Hence, the resultant electric field vector at the photodetector is

$$E_{A0}^{te} = T_A^{te} R(A) T_S^{xy} R(-C) T_C^{fs} R(P-C) E_{P0}^{te}, \quad 1.42$$

where T_A^{te} , T_S^{xy} , and T_C^{fs} are the Jones matrices of the analyzer, sample, and compensator, respectively (the notation used will be that used in Ref. 1). The diagonal Jones matrix representing the unknown optical system is written

$$T^{xy} = \begin{bmatrix} V_{ex} & 0 \\ 0 & V_{ey} \end{bmatrix}, \quad 1.43$$

where V_{ex} and V_{ey} are the complex eigenpolarizations of the system.

Expanding equation 1.42 yields

$$E_{A0}^{te} = A_C K_C K_A L, \quad 1.44$$

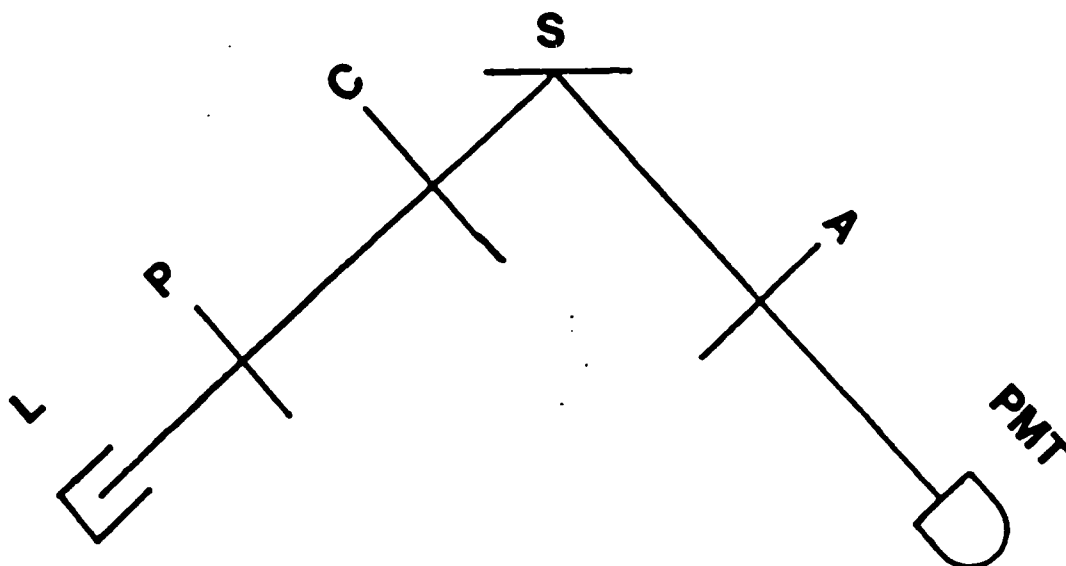


Figure 1.7. The PCSA arrangement. The elements are: the laser (L), polarizer (P), compensator (C), sample (S), analyzer (A), and photomultiplier tube (PMT)

where

$$L = V_{ex} \cos A [\cos C \cos(P-C) - \rho_c \sin C \sin(P-C)] + V_{ey} \sin A [\sin C \cos(P-C) + \rho_c \cos C \sin(P-C)] . \quad 1.45$$

If the photodetector response is a linear function of the total light flux that impinges on it, its output will be proportional to the intensity of the light emergent from the analyzer. From equations 1.43 and 1.44 as well as equation 1.20 for the relative intensity, the detected signal P_d is given by

$$P_d = K_D (E_{AO}^{te})^T (E_{AO}^{te}) , \quad 1.46$$

where K_D is a real factor that depends on the intensity profile of the light beam and the nature of the photodetector. Equation 1.46 can be written as

$$P_D = GLL^* = G|L|^2 , \quad 1.47$$

where L is defined in equation 1.45 and

$$G = K_D |A_c|^2 |K_c|^2 |K_A|^2 . \quad 1.48$$

Notice that $P_D = f(P, C, A, \rho_c, V_{ex}, V_{ey})$.

The PSCA arrangement is identical to the PCSA arrangement, except that the compensator is placed before the optical sample rather than after it. Analysis of the state of polarization of the light beam as it passes through the sequence of elements can be carried out in a step-by-step fashion as was done in the PCSA arrangement. If this is done it is found that the expression for L is identical to equation 1.45 with A interchanged with P . Hence, the PCSA and the PSCA are not fundamentally different and equation 1.47 represents both the PCSA and the PSCA arrangements.

Equation 1.47 is the basis of most ellipsometers now in existence,

including the ellipsometers constructed for this work (with some modifications). The expanded form of P_D will be written out completely in Chapter 2, after some modifications have been made. Finally, the assumption that the photodetector is linear is basically incorrect. However, it can be made nearly linear as will be discussed later. The following chapter gives a brief discussion of several types of ellipsometers based on equation 1.47.

2. OVERVIEW OF ELLIPSOMETER SYSTEMS

A schematic classification of the ellipsometers currently available is shown in figure 2.1. Due to its historical significance, the manual null ellipsometer will be examined. In addition, automatic null (mechanical and electro-optic) and photometric (both rotating polarizer/analyzer and photoacoustic modulated) ellipsometers will be discussed.

2.1. The Manual Null Ellipsometer

The manual null ellipsometer was the first ellipsometer constructed. Null ellipsometry is based on finding a set of azimuth angles P , C , and A such that P_D (from equation 1.45) is zero. The following nulling scheme is from Ref. 1. Note that if $P_D = 0$ and $L = 0$ then

$$V_{ex}/V_{ey} = -\tan A[(\tan C + \rho_c \tan(P-C))/(1 - \rho_c \tan C \tan(P-C))]. \quad 2.1$$

If we have a perfect quarter-wave-plate, (QWP) then

$\rho_c = T_c = -j$. If in addition, the fast axis of the QWP is oriented at an azimuth of $C = \pi/4$ with respect to the x eigenpolarization axis, then

$$V_{ex}/V_{ey} = -\tan A' \exp[-j2(P' - \pi/4)], \quad 2.2$$

where (P', A') is the set of angles which causes a null condition.

Similarly, if $C = -\pi/4$ then

$$V_{ex}/V_{ey} = \tan A'' \exp[-j2(P'' + \pi/4)], \quad 2.3$$

where (P'', A'') is the set of angles which causes a null condition.

As was mentioned in Chapter 1, the ratio V_{ex}/V_{ey} can be written in terms of the ellipsometric parameters ψ and Δ as

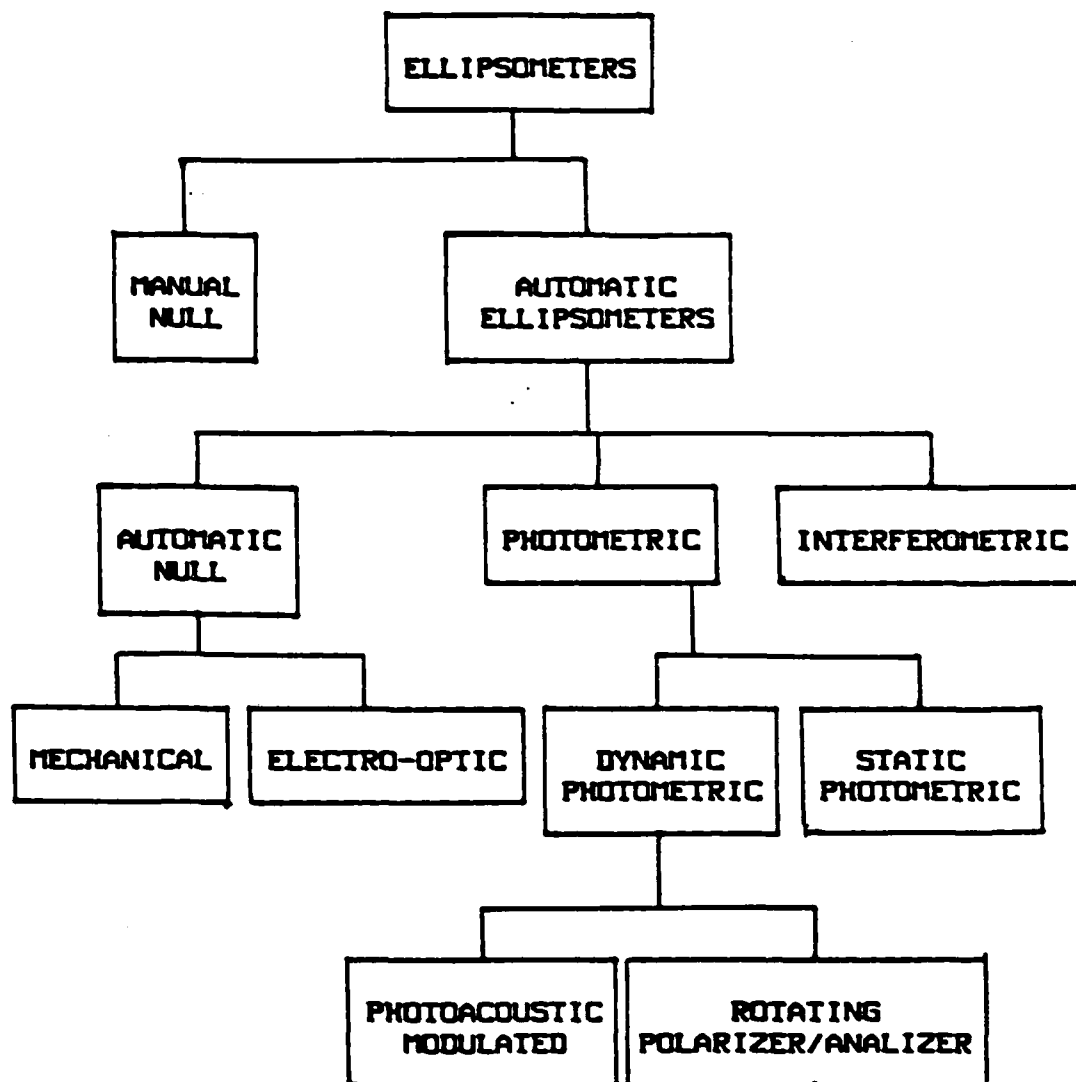


Figure 2.1. Schematic classification of ellipsometers in existence today

$$\rho = V_{ex}/V_{ey} = \tan \psi e^{i(\Delta)} . \quad 2.4$$

Hence, the above null conditions, equations 2.2 and 2.3 correspond to

$$\tan \psi = |\tan A'| \quad 2.5$$

$$\Delta = -2P' \pm \pi/2 \quad 2.6$$

and

$$\tan \psi = |\tan A''| \quad 2.7$$

$$\Delta = 2P'' \pm \pi/2 . \quad 2.8$$

Combining these equations we find that

$$\Delta = P'' - P' \quad 2.9$$

$$\text{and} \quad \psi = \tan^{-1} |\tan A| , \quad 2.10$$

where $A = A'$ or A'' .

It should be noted that this is just one of many types of nulling schemes that could be used with a PCSA arrangement. Also, the response of the phototube does not need to be linear for the null ellipsometer. This in itself makes the null ellipsometer a very accurate and precise instrument. Manual nulling, however, is an extremely slow process (on the order of minutes) and therefore not suitable for many insitu applications. In such circumstances automation of the ellipsometer becomes essential.

2.2. Automatic Ellipsometers

Automation of ellipsometers has become an extremely effective method for increasing the rate at which a set of ellipsometric parameters can be acquired. This automation is mostly due to the introduction of microprocessors and small computers. The design of automatic ellipsometers has progressed along three distinct lines: those

that adhere to the concept of null measurement, those that use interferometric methods, and those that use photometric methods. Of the three methods, the second method is the only one which is not based on the PCSA/PSCA arrangement. It is, however, based on an extremely interesting concept and will be excluded here only because it does not implement the PCSA/PSCA arrangement. Hence, figure 1.7 (the PCSA arrangement) represents the optical setups that follow.

2.2.1. Automatic null ellipsometers

Automatic null ellipsometers are of two different kinds: (1) those that employ motors to drive the polarizing elements to null, and (2) those that are entirely electro-optic with no moving parts.

Motor driven self-nulled ellipsometers use feedback signals to actuate servo-motors which, in turn, rotate the analyzer and polarizer, respectively. The feedback signals are ac signals generated by small modulation of the light beam.³ The servo-motors can be replaced by stepping motors. This permits on-line data acquisition and on-line data reduction.⁴ Motor driven self-nulled ellipsometers can acquire one set of ellipsometric data in about one second, with a high, 0.01° resolution.

Electro-optic self-nulled ellipsometers adhere to the concept of null measurement but with no moving parts. One method is to use Faraday cells to magneto-optically rotate the azimuth angles of the polarizer and analyzer, instead of doing it manually or by motors.⁵ Another method is to use two KDP Z-cut crystals employed as variable phase plates, whose retardations are controlled by dc voltages.⁶ Small ac

voltages, used as control signals, are superimposed on the dc voltage and used in feedback loop to achieve null condition. The total response time and resolution for these types of ellipsometers is about equal to those of the motordriven self-nulled ellipsometer.

2.2.2. Automatic photometric ellipsometers

Photometric ellipsometers are based on analysis of the variation of the detected light flux in a known fashion. Again, the equation of the light flux impinging on the photodetector is equation 1.45. The raw data from photometric ellipsometers are intensity signals obtained with prescribed conditions.

There are two fundamentally distinct photometric ellipsometers, dynamic and static. The distinction between static and dynamic photometric ellipsometers lies in the manner in which the raw data from the photodetector are analyzed. In a static photometric ellipsometer, the detected signal (usually dc) is recorded at predetermined fixed settings of the components of the ellipsometer. In a dynamic photometric ellipsometer, one or more of the parameters P , C , A , and δ_c is periodically varied with time and the detected signal is Fourier analyzed.

2.2.2.1. Static photometric ellipsometers The equation of the light flux (equation 1.46) is a function of A , P , and possibly C and δ_c if a compensator is present. If no compensator is present, then $C = 0$ and $\delta_c = 0$. If $P_D(j)$ represents the detected signals at n different sets (P_j, A_j) of polarizer-analyzer angles, substitution of this data

into equation 2.10 yields n equations in $G' = G(V_{ex}^2 + V_{ey}^2)$, ψ and Δ . Hence, a minimum of three independent equations are necessary to determine ψ and Δ .

The Gaertner L116A automatic ellipsometer acquired for use here at the Microelectronics Research Center is an example of a static photometric ellipsometer.⁷ During automatic operation, the analyzer rotates at a frequency of about 1 Hz. Intensity readings of the reflected light, as sensed by the photodetector, are taken every 5° during one rotation of the analyzer, beginning at 0° and ending at 355° . This gives $n = 72$ equations with 3 unknowns. Of course, n need only be 3 to solve for ψ and Δ , but a larger n yields more consistent results. It should be noted that ψ and Δ are assumed constant during the 72 readings, hence, the minimum time required for one set of ellipsometric parameters is one second. If only three equations had been used, then one set of parameters could be obtained in about 0.83 seconds. Hence, speed is sacrificed in return for accuracy.

2.2.2.2. Dynamic photometric ellipsometers As mentioned earlier, a dynamic photometric ellipsometer is characterized by the fact that one or more of the optical parameters, (A, P, ρ_c) is modulated and the detected signal is Fourier analyzed. There are many ways to obtain this modulation. Two methods have, however, received more attention recently. These are the rotating analyzer/polarizer ellipsometer and the photoacoustic modulated ellipsometer.

2.2.2.2.1. Rotating analyzer/polarizer Starting with the

PCSA arrangement, if the polarizer and analyzer are rotated at different speeds and the transmitted flux is linearly detected, then this periodic waveform can be Fourier analyzed. The optical arrangement is again the PCSA arrangement (without a compensator), thus equation 1.47 gives the intensity of the light at the photodetector with $C = 0$ and $Te^{j\Delta}_c = 1$. Now, $A = \omega_A t$ and $P = \omega_P t$, where ω_P , ω_A are the angular frequencies of the polarizer and the analyzer, respectively, and the intensity becomes a function of time, which can be Fourier analyzed.

As an example if $\omega = \omega_A = 3\omega_P$, then the intensity can be written in terms of nine Fourier amplitudes a_0 and (a_n, b_n) , $n = 1, 2, 3, 4$ where

$$I = a_0 + \sum (a_n \cos n\omega_f t - b_n \sin n\omega_f t) \quad 2.11$$

and $\omega_f = 2\omega$.⁸

The nine Fourier amplitudes can be obtained by performing a Discrete Fourier Transform (DFT) of the signal I . If the optical system (sample) under measurement is nondepolarizing, it can be completely described by a complex 2×2 Jones matrix T , and this Jones matrix gives the ellipsometric parameters ψ and Δ as explained in section 1.3.1. The components of the Jones matrix can then be written in terms of the nine Fourier amplitudes a_0 , (a_n, b_n) .

The rate in which ψ and Δ can be obtained is limited here by the angular frequency, ω , since a Fourier transform of the signal requires at least one complete cycle of the signal. An upper limit for the frequency of rotation is about 10,000 rpm (about 130 Hz). Therefore, the minimum time interval necessary to obtain one set of ellipsometric data is about 5 ms. This is significantly faster than the manual and automatic null systems, as well as the static photometric system

described earlier.

2.2.2.2.2. The photoacoustic modulated ellipsometer The photoacoustic modulated ellipsometer (PME) is based on the ellipsometer first constructed by Jaspersen.⁹ The optical arrangement is basically the PCSA arrangement with the compensator replaced by the modulator. The modulator designed by Jaspersen is at the heart of the ellipsometer.

Figure 2.2 is a diagram of the modulator head. A uniaxial sinusoidal standing strain wave is established in a rectangular block of fused quartz by means of an ac-driven piezoelectric crystal quartz transducer cemented to one end of the block. The oscillating strain is accompanied by an oscillating induced birefringence, such that the fused quartz block acts as a linear retarder with an alternating (time-varying) relative retardation. The direction of the strain determines the direction of the fast axis of the modulated retarder; the amplitude of the sinusoidal retardation is proportional to that of the strain and consequently, to the voltage applied to the transducer.

The relative phase shift has the form

$$\delta(t) = R \sin \omega t, \quad 2.12$$

where ω is the resonant angular frequency of the modulator unit, and R is the peak relative phase shift. It can be shown (see Ref. 2) that the peak retardation, R , is directly proportional to the voltage applied to the transducer and inversely proportional to the wavelength of the light, i.e., $R \propto V/\lambda$.

The expression for the relative intensity of the light impinging on the photodetector can be obtained from equation 1.45 by substituting M

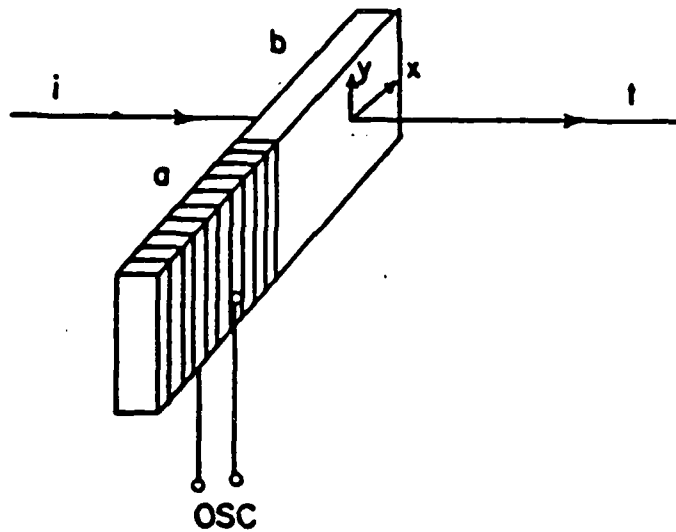


Figure 2.2. A piezobirefringence polarization modulator is composed of cemented crystal and fused-quartz blocks, a and b, respectively. Under the action of an ac voltage from an oscillator (OSC), a stress standing wave is established in block b and the associated oscillating birefringence modulates the state of polarization of a light beam as it passes through the block. x and y indicate the principal strain directions

for C and $\delta(t)$ for δ_c , where M is the angle that the stress axis makes with the x eigenpolarization and $\delta(t)$ is the relative phase shift as given in equation 2.12. With these modifications, the expression for the intensity becomes

$$I(t) = I_0 + I_s \sin \delta(t) + I_c \cos \delta(t), \quad 2.13$$

where

$$I_0 = G(V_{ex}^2 + V_{ey}^2)/4[1 - \cos 2\psi \cos 2A + \cos 2M \cos 2(P-M) \cdot (\cos 2A - \cos 2\psi) + \sin 2A \cos 2(P-M) \sin 2M \sin 2\psi \cos \Delta] \quad 2.14$$

$$I_s = G(V_{ex}^2 + V_{ey}^2)/4[\sin 2(P-M) \sin 2A \sin 2\psi \sin \Delta] \quad 2.15$$

$$I_c = G(V_{ex}^2 + V_{ey}^2)/4[\sin 2(P-M)(\sin 2M(\cos 2\psi - \cos 2A) + \cos 2M \sin 2A \sin 2\psi \cos \Delta)]. \quad 2.16$$

Again, V_{ex} and V_{ey} are the diagonal elements of the Jones matrix for the optical sample and G is identical to the G introduced in Section 1.3.2 on the PCSA arrangement, but with K_c replaced by K_m .

The $\cos \delta(t)$ and $\sin \delta(t)$ can be expanded in a Jacobi series,

$$\cos \delta(t) = \cos(R \sin \omega t) = J_0(R) + 2\sigma J_{2m}(R) \cos 2m\omega t \quad 2.17$$

$$\sin \delta(t) = \sin(R \sin \omega t) = 2\sigma J_{2m+1}(R) \sin(2(m+1)\omega t), \quad 2.18$$

where the $J_m(R)$ s are Bessel functions of the first kind of order m and argument R .

Finally, if the voltage applied to the modulator is adjusted so that $J_0(R) = 0$, the flux the light incident on the photodetector becomes

$$I(t) = I_0 + I_\omega \sin \omega t + I_{2\omega} \cos 2\omega t + \dots, \quad 2.19$$

where

$$I_0 = G(V_{ex}^2 + V_{ey}^2)/4 \quad 2.20$$

$$I_\omega = G(V_{ex}^2 + V_{ey}^2)/4 \cdot 2J_1(R)I_s \quad \text{and} \quad 2.21$$

$$I_{2\omega} = G(V_{ex}^2 + V_{ey}^2)/4 \cdot 2J_2(R)I_c. \quad 2.22$$

The fundamental (ω) and second harmonic (2ω) components of the detected signal can be isolated and measured. Their ratios to the dc component are defined as R_ω and $R_{2\omega}$

$$R_\omega = I_\omega/I_{dc} = 2J_1(R)I_s \quad 2.23$$

$$R_{2\omega} = I_{2\omega}/I_{dc} = 2J_2(R)I_c, \quad 2.24$$

can be determined. The explicit equations relating ψ and δ to R_ω and $R_{2\omega}$ can be determined once a particular set of azimuths P , M , and A are known.

Finally, it should be pointed out that the expressions I_0 , I_s , and I_c in equations 2.15, 2.16 and 2.17 respectively, were calculated for this work. The expression for I_0 does not agree with the only other source which had calculated the explicit form of $I(t)$, namely Ref. 10. In that work, I_0 was calculated to be

$$I'_0 = ((r_p^2 + r_s^2)/4)[1 + \cos 2A \cos 2M \cos 2(M-P) - (\cos 2A + \cos 2M \cos 2(M-P) \cos 2\psi)] \quad 2.25$$

Here r_p and r_s are the diagonal elements of the Jones matrix for the optical sample. The two expressions for I_0 agree in the particular sets of azimuths implemented by Ref. 10. However, the following argument shows that equation 2.25 cannot possibly be correct.

If the retardation $R = 0$, then the modulator no longer effects the intensity of the light (except for a multiplicative constant) so $I \neq I(t, M)$. If, however, $R = 0$ is substituted into the entire expression by Ref. 7, then $I = I(t, M)$. Hence Ref. 10 does not have the correct explicit general form for $I(t)$. On the other hand, substituting $R = 0$ into equations 2.15 - 2.17 and using some trigonometric identities yields

$$I = (G(V_{ex}^2 + V_{ey}^2)/4)[1 - \cos 2\psi \cos 2A + \cos 2P(\cos 2A - \cos 2\psi) + \sin 2P \sin 2A \sin 2\psi \cos \Delta] , \quad 2.26$$

which is independent of M and t and is the correct expression for a polarizer, sample, and analyzer (PSA) arrangement.

3. CONSTRUCTION OF A HIGH SPEED DYNAMIC PHOTOMETRIC ELLIPSOMETER (A PHOTOACOUSTIC MODULATED ELLIPSOMETER)

A schematic diagram of the ellipsometer is shown in figure 3.1. The ellipsometer can be divided into the optical setup and the electronic setup.

3.1. The Optical Setup

The polarizer and analyzer are crystal quartz Rochon prisms with a 2 degree beam separation. The modulator has a fused silica optical element with a 1.65 cm aperture and a wavelength transmittance range of 0.18-2.6 μm . The resonant frequency is 50 kHz. The light source is a low power (1 mW) HeNe laser, $\lambda = 632.8 \text{ nm}$. The laser head contains a quarter wave depolarizer to achieve maximum circular polarization of the beam. An optical interference filter between the analyzer and the photodetector blocks out all wavelengths other than that of the laser beam, reducing the effects of ambient illumination. The sample holder has two translational and one rotational degree of freedom. The sample itself is held vertical by a small vacuum. The mounts for the prisms, modulator, laser, and sample were specially constructed out of a piece of 0.5" thick aluminum slab. Apertures were placed between all optical components to allow only the desired beam to be transmitted. All mounts were painted black to reduce reflections and were secured on a stainless steel optical bench, which has predrilled holes separated by 1". The entire optical bench is secured on a table which has mechanically absorbing rubber pads placed under all four legs.

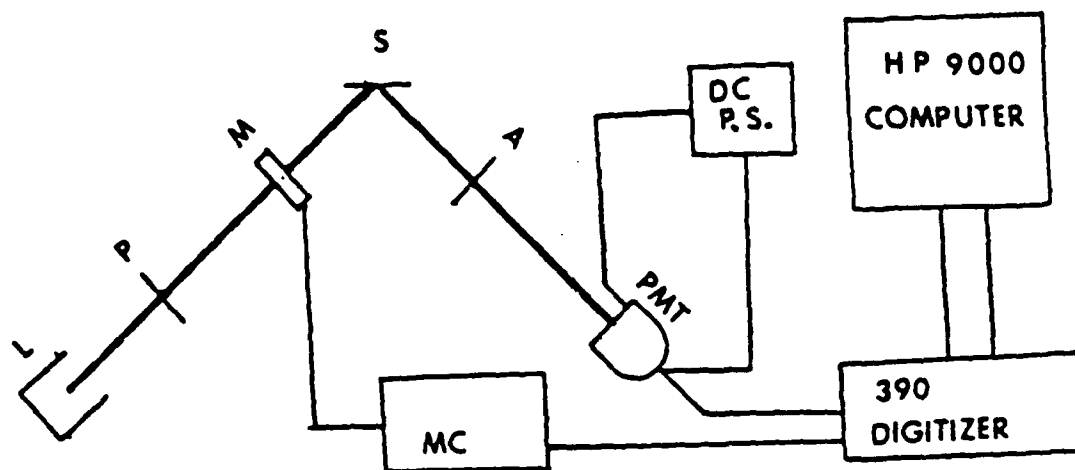


Figure 3.1. The photoacoustic modulated ellipsometer. The elements are: the laser (L), polarizer (P), modulator (M), sample (S), analyzer (A), photomultiplier tube (PMT), modulator controller (MC), digitizer and computer

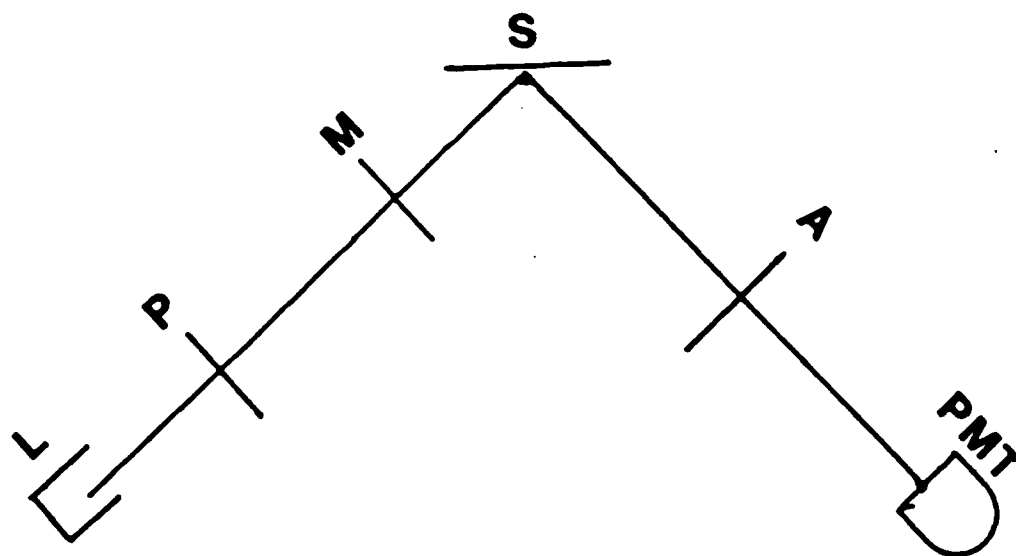


Figure 3.2. The optical setup for the photoacoustic modulated ellipsometer. The elements are: the laser (L), polarizer (P), photoacoustic modulator (M), sample (S), analyzer (A), and photomultiplier tube. This is the PCSA arrangement with the compensator replaced by a photoacoustic modulator

3.1.1. The Rochon prisms

Rochon prisms are birefringent polarizers. With unpolarized incident light they produce two transmitted beams with mutually perpendicular polarization directions and different directions of propagation. The prisms are made of quartz and have their optic axes as shown in figure 3.3.

In the first part of the Rochon prism both waves have the ordinary index of refraction n_o . In the second part the o wave (ordinary wave) vibrating in the plane of the paper continues to have index n_o and is not deviated. The e wave vibrating perpendicular to the plane of the paper has index n_e and is deviated up or down according to whether $n_e > n_o$ or $n_e < n_o$. Hence, the polarization of the undeviated beam is easily determined by observing the two spots of the transmitted beams as shown in figure 3.3.

Prism polarizers are the highest quality polarizers having the least absorption loss and the greatest degree of polarization. In general, the quality of a polarizer is determined as follows.

The total transmittance through a polarizing element is

$$K\lambda = (k_1 + k_2)/2, \quad 3.1$$

where k_1 is the transmittance of light which is polarized along the transmission axis, k_2 is the transmittance of light polarized perpendicular to the transmission axis, and λ is used to denote that the transmittance is wavelength dependent. For a perfect polarizer, $k_1 = 1.0$ and $k_2 = 0.0$, resulting in $K\lambda = 0.5$. For a pair of identical polarizers with their transmission axes parallel, the transmittance of light is

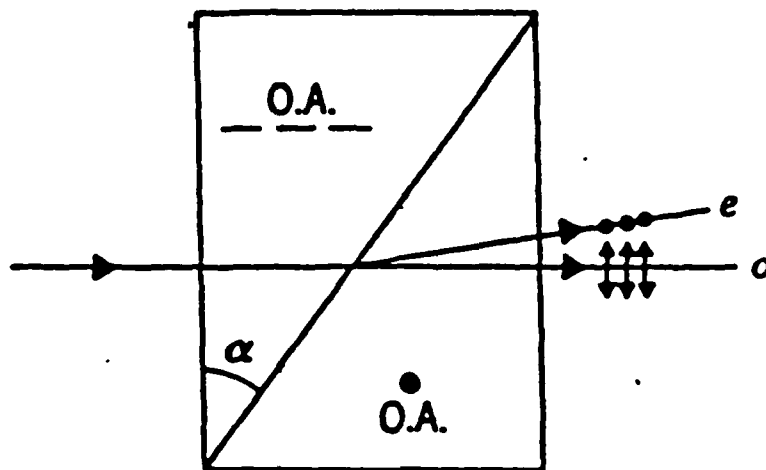


Figure 3.3. The Rochon prism. The extraordinary wave is indicated by e, the ordinary wave by o and the optic axis by O.A.

$$H_0 = (k_1^2 + k_2^2)/2 \quad 3.2$$

and the transmittance with the transmission axes perpendicular is

$$H_{90} = k_1 \cdot k_2 \quad 3.3$$

The extinction ratio, $E\lambda$ is defined as the ratio of H_{90} to H_0 ,

$$E\lambda = H_{90}/H_0 = 2k_1k_2/(k_1^2 + k_2^2) \quad 3.4$$

The Rochon prisms are high quality prism polarizers. For such polarizers, H_0 approaches 0.45 and $E\lambda$ is between 10^{-5} and 10^{-6} .

3.1.2. The photoacoustic modulator

The modulator used is a Hinds PEM-80 photoelastic modulator system. The system consists of a modulator head and the corresponding controller. The modulator head contains a rectangular-shaped fused silica photoelastic optical element set into mechanical vibration by a bonded-on piezoelectric transducer made of crystal quartz. The wavelength transmittance range is 0.18-2.6 micron, with a 1.65 cm aperture and resonant frequency of 50 kHz. The separately housed controller has a 10-turn peak-to-peak retardation control which sets the modulator's oscillation amplitude. The controller also provides two square wave reference outputs at 50 and 100 kHz. These reference outputs can be used as oscilloscope triggers or phase references for lock-in amplifiers.

3.1.3. The sample mount

A schematic diagram of the sample mount is shown in figure 3.4. A mount with rotational freedom about the z axis (which determines the angle of incidence) was secured on a mount with translational freedom about the xy plane. All three degrees of freedom could be controlled by micrometers. The rotational micrometer provides precision to within 0.1° and the translational micrometers provides precision to within 0.1mm. The hand-made top section of the sample mount provides two additional rotational degrees of freedom with somewhat less precision. Here, the sample is held down by vacuum created by a small forepump. The sample mount was carefully grooved and O-ring sealed to maintain vacuum, which allows the vacuum pump to be turned off during measurements reducing any mechanically induced noise it may produce. The five small 1mm diameter holes eliminate all detectable strain on the sample.

3.1.4 Other mounts

The polarizer and analyzer mounts have high precision rotational freedom along the direction of the laser beam. In addition, both mounts, as well as the commercial laser mount, are themselves mounted on platforms which can be roughly adjusted, using three bolts with heads that have been lathed smooth as indicated in figure 3.5.

The modulator mount also has an adjustable platform like that shown in figure 3.5. Once the modulator has been secured, it cannot be moved without realigning the ellipsometer. The photomultiplier tube mount was constructed similar to that of the polarizer and analyzer mounts, but without the rotational adjustment about the beam. Its design is also

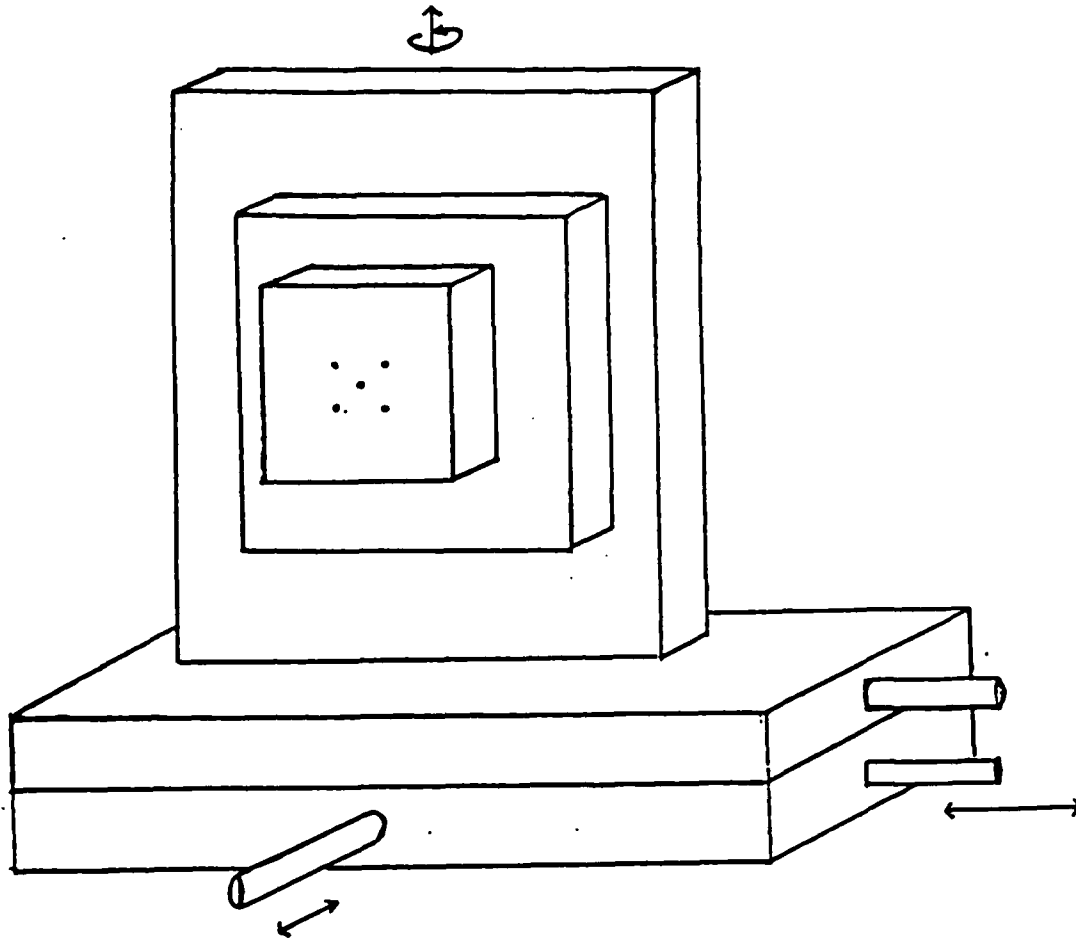


Figure 3.4. The sample mount

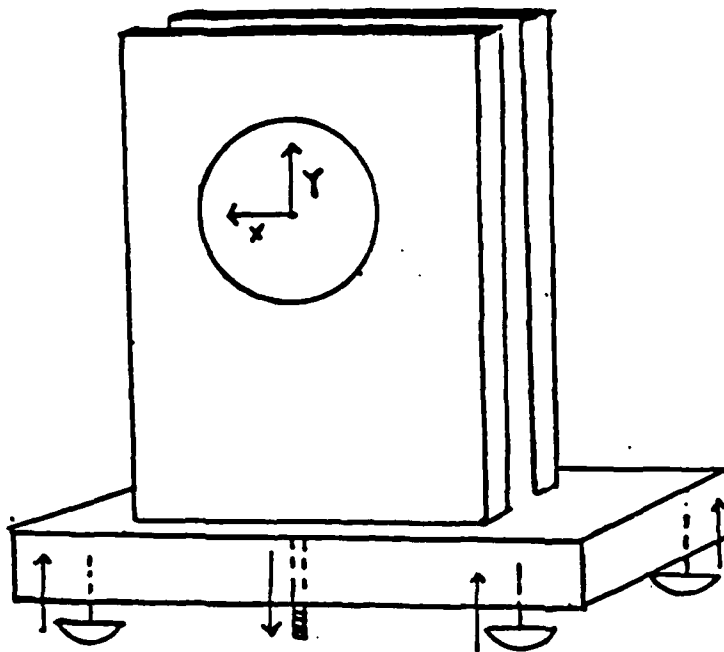


Figure 3.5. The polarizer, analyzer, and photomultiplier tube mount

basically that of figure 3.5.

3.2. The Electrical Setup

A schematic diagram of the electrical setup is shown in figure 3.6. The light incident on the Centronics P4283 broad spectral response photomultiplier tube (PMT) is converted into a current at the anode. The current is then read as a voltage at a load resistor. A capacitor serves as a dc block allowing the ac portion of the signal to be measured at channel 1 of a Tektronix 390AD programable digitizer, which converts the analog signal to a digital signal using a 10 bit A/D converter. The digitizer is controlled by a Hewlett Packard 9000 computer. The digital signal is then sent via an HP-IB interface bus to a Hewlett Packard 9000 computer for further data reduction. Finally, the dc portion of the signal is fed back into a Hewlett Packard model 6516A high voltage dc power supply forcing the dc current at the anode to remain constant for all incident light intensities.

3.2.1. The photomultiplier tube

The photomultiplier tube, PMT, (in fact phototubes in general) is an inherently nonlinear device. Due to the recent increase in photometric ellipsometers a lot of attention has been paid to this subject, e.g., see Ref. 11 and Ref. 12. To understand the inherent nonlinearity of the PMT, refer to figure 3.7. Assume that we have a phototube which provides a constant output current for when the incident light flux is constant. The resistor R provides the voltage difference between the anode and the cathode. The phototube acts as a gain stage

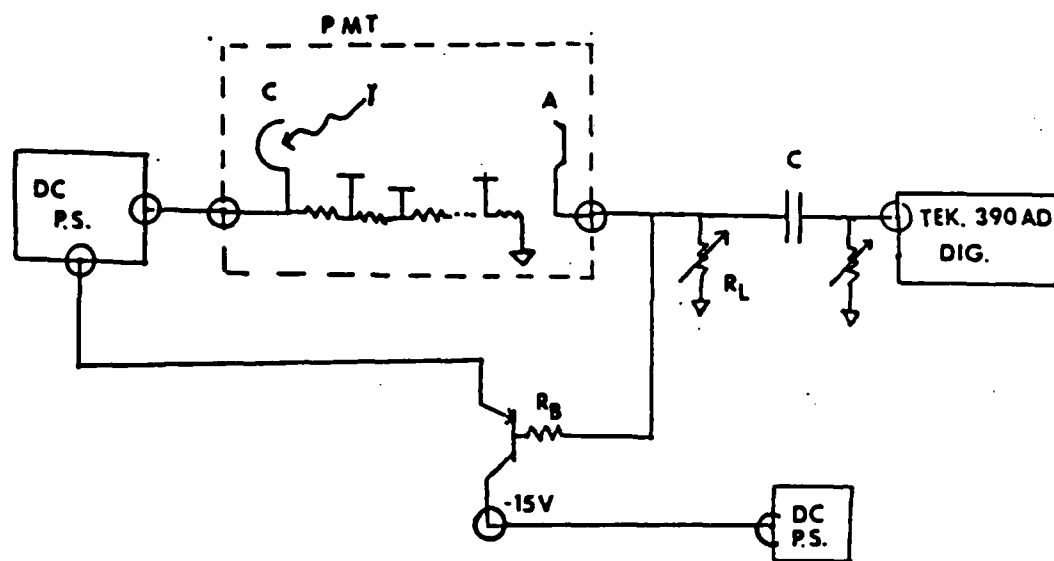


Figure 3.6. The electrical setup

for the light incident on it. Now, if the light flux increases, there will be an increase in the current through the phototube, i_p . This is equivalent to reducing the load resistance, R_L . Since the voltage at X remains constant due to the regulated dc power supply, the current through R is reduced, which reduces the gain of the PD. Hence, criterion necessary to obtain a linear response is to have $i_d \gg i_p$.

In the case of a photomultiplier tube, R_d is replaced by a voltage divider network shown below.¹³ A 150V Zener diode was placed between the cathode and the first dynode to maintain their difference at the recommended 150V value. The voltage of the cathode is $500 \pm 100V$, which corresponds to an i_d of about 385 ± 80 mA. Using the 1 mW HeNe laser, i_p was found to be about 1mA. In this case, i_p/i_d is about $2.5 \cdot 10^{-3}$, which satisfies the above criterion. It should be pointed out that initially an 8 mW HeNe laser was used yielding an i_p/i_d ratio about 10-20 times larger. The linearity of the PMT was indeed noticeably reduced.

3.2.2. The feedback mechanism

The model 6516A is a series regulated power supply. A simplified schematic diagram of the internal feedback mechanism is given in figure 3.9, and a complete schematic diagram is provided in Appendix A.

Ordinarily, Q16 detects an error voltage that is proportional to the voltage at the base of Q16 and ground. The error signal is amplified by Q10 and applied to the series regulator, Q11. The series regulator increases or decreases the output current as required to maintain a constant dc output voltage that is equal to the programmed

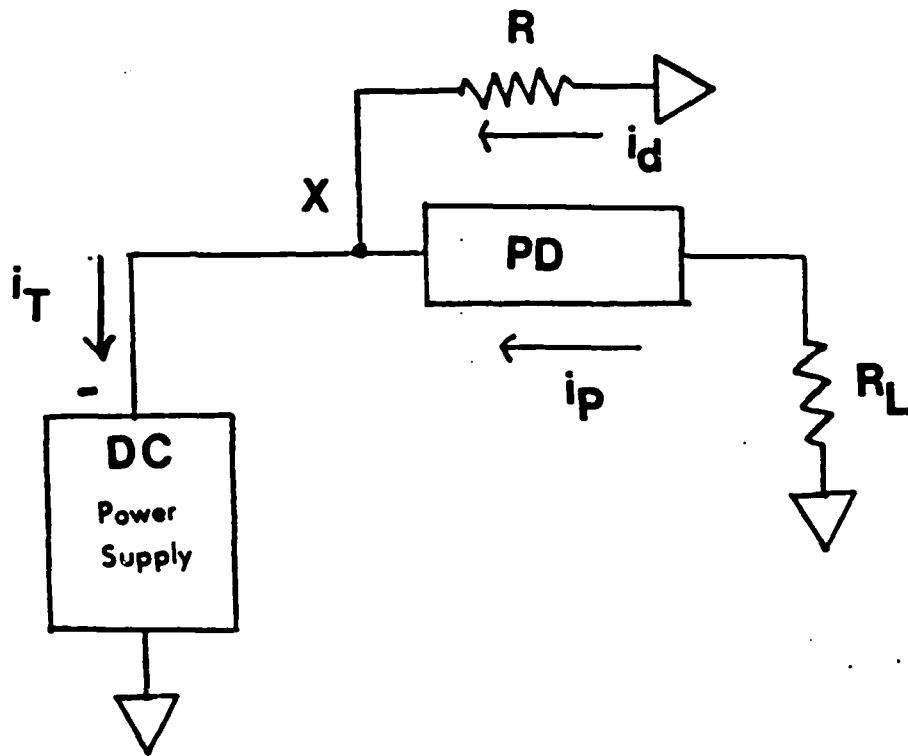


Figure 3.7. Simplified schematic diagram of a photodetector circuit. Here, R is the resistance of the dynode chain between the anode and the cathode, R_L is the load resistance, i_d is the current through R , i_p is the current from the light flux and i_T is the total current supplied by the dc power supply

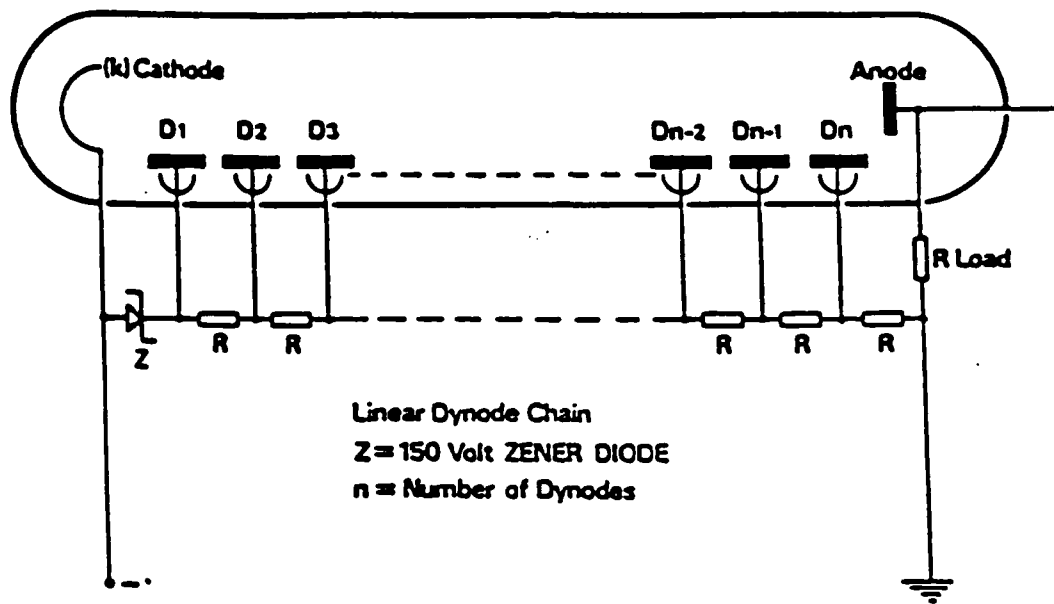


Figure 3.8. Schematic of the voltage divider network of the photomultiplier tube

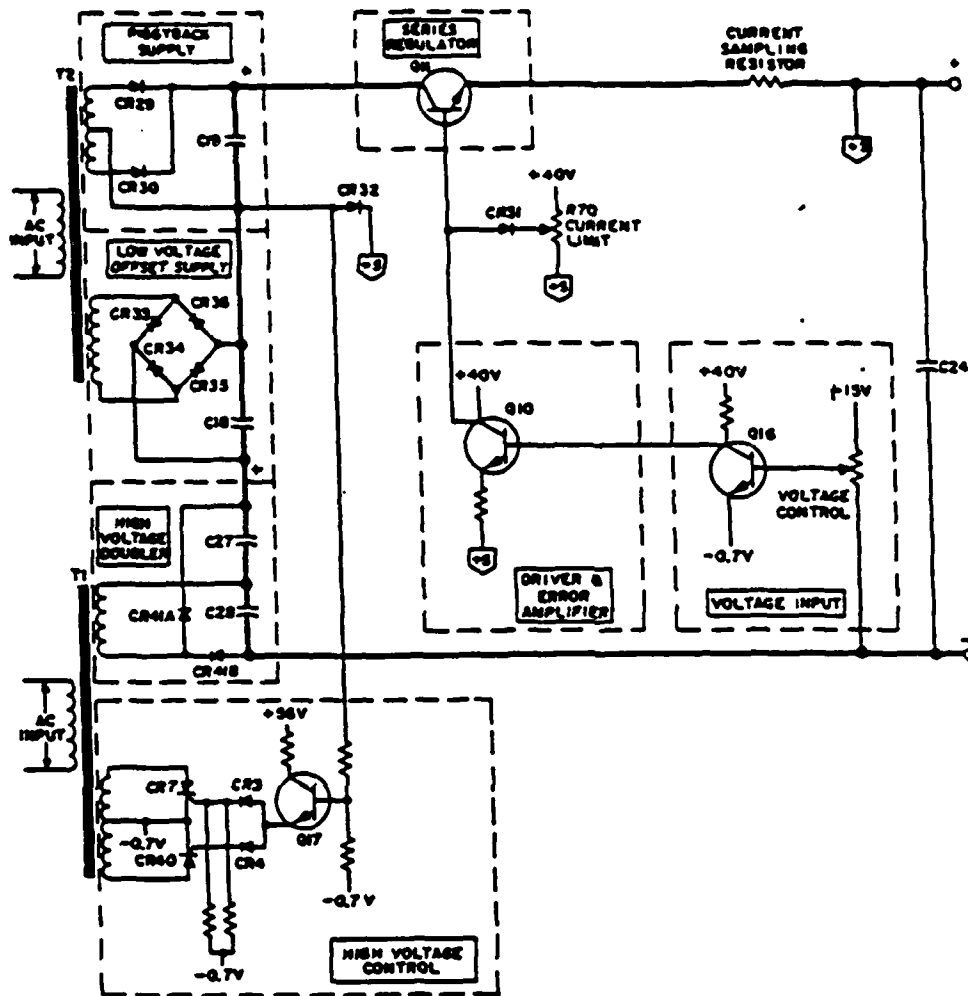


Figure 3.9. A simplified schematic diagram of the internal feedback mechanism of the 6516A power supply¹⁴

voltage. More precisely, the error voltage changes the conduction of the series regulator which, in turn, alters the output voltage so that the difference between the two input voltages applied to the Q16 is reduced to zero. This maintains the output voltage constant.¹⁴

The above feedback mechanism can be altered so that the voltage, and therefore the current at the anode of the PMT, remains constant. A schematic diagram of this altered feedback mechanism is shown in figure 3.10. Light incident on the cathode of the PMT is converted into a current at the anode. The dc portion of the current is run into Q_{fb} , a PNP transistor, which amplifies the current. This amplified current is then applied to the base of Q16. The load resistor R_L controls the dc current fed into the base of Q_{fb} . If the flux of light incident on the PMT changes, an error voltage appears at Q16 and is amplified and fed back into the series regulator. Then the conduction of the series regulator is changed, which alters the output voltage so that the voltage, and hence, the current at the anode, is constant. A switch located on the chassis of the 6516A power supply allows for the altered feedback mechanism to be turned off and the internal feedback mechanism to be restored.

Finally, the feedback mechanism results in a constant dc current at the anode of the PMT for all samples, regardless of the total reflectivity of the light at the sample. For example, the feedback mechanism functioned correctly, using a gold sample (highly reflective), a silicon sample with an SiO_2 film (moderately reflective), and a glass sample (slightly reflective).

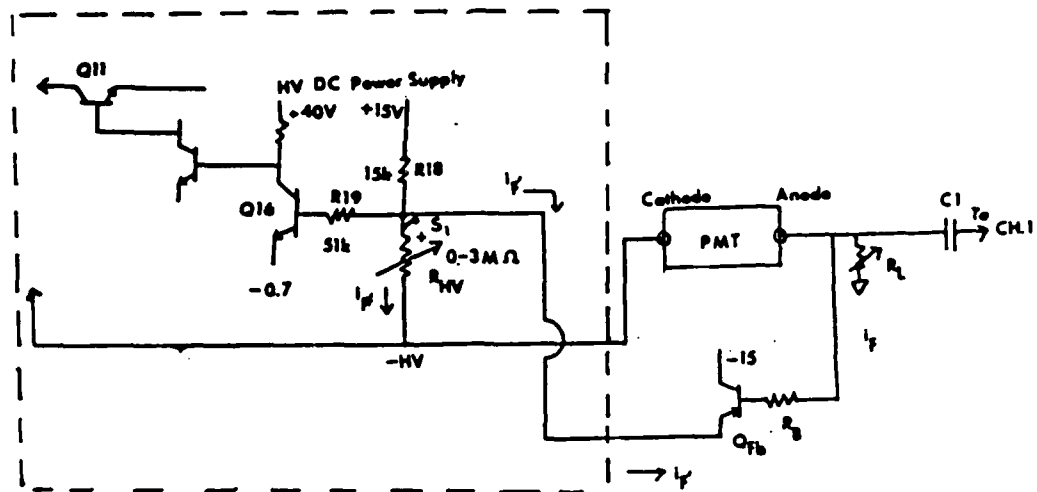


Figure 3.10. A diagram of the altered feedback mechanism

3.2.3. The signal processing

The ac signal can be adjusted independently of the dc feedback by adjusting R'_L . The resulting signal is then measured at channel 1 of the 390AD digitizer. The commands to initialize the 390AD are all received via the HPPIB bus from the 9000 computer. The commands are either resident in previously written software or are directly entered through the keyboard. The initialization commands include; the input voltage range, the type of arming and triggering, the delay time for trigger, and the sampling frequency.

An external trigger signal is provided by the photoacoustic modulator controller at 50 kHz. The signal at the anode of the PMT is not in phase with this 50 kHz reference signal, but using the correct delay time after the trigger, it is possible to obtain a signal with the proper phase. Once triggered the signal is then read into the 9000 computer. The signal, consisting of either 1024 or 2048 words (2 bytes each), is read via a fast-hand-shake block transformation into a buffer, created in the memory of the 9000. The 390AD provides an end of file, EOF signal on one of the control lines of the HPPIB bus to end data transfer. In addition, the software has been written to allow for a direct memory transfer, DMA if such hardware is available.

3.3. Alignment

The proper alignment of the optical components of the ellipsometer means that the following will be true;

$$\phi = 70^\circ, P-M = 45^\circ, M = 0^\circ, \text{ and } A = 45^\circ.$$

Here, ϕ is the angle of incidence and P, M, A are the angles that the

polarizer, modulator, and analyzer make with respect to the x eigenpolarization of the optical system. The x eigenpolarization (the plane of incidence) is perpendicular to the normal of the plane of the optical bench, i.e., the light beam travels parallel to the optical bench. The alignment procedure centers on using a precisely cut prism as the initial sample.

3.3.1. The initial setup

Figure 3.11 is a schematic diagram of the initial setup. Here, a_1 , a_2 , a_3 , and a_4 are all specially constructed circular apertures with a 1mm diameter. Figure 3.12 provides a closer view of the prism sample.

When properly aligned, the beam is normally incident on surface s_1 , totally internally reflected at s_2 , and normally incident on s_3 . The following steps were used for this initial alignment.

1. The prism was placed so that the laser beam was totally internally reflected.
2. The orientation of the prism was adjusted so that the reflected beam passed through a_2 , then a_1 .
3. The sample mount was finely adjusted so that the reflection at s_2 occurred at the center of the prism. (At this point, the plane of incidence is parallel to the optical bench and the angle of incidence is 70° .)
4. Apertures a_3 and a_4 were positioned so that the reflected beam passed through them.
5. Finally, the PMT was positioned so that a maximum dc reading was obtained.

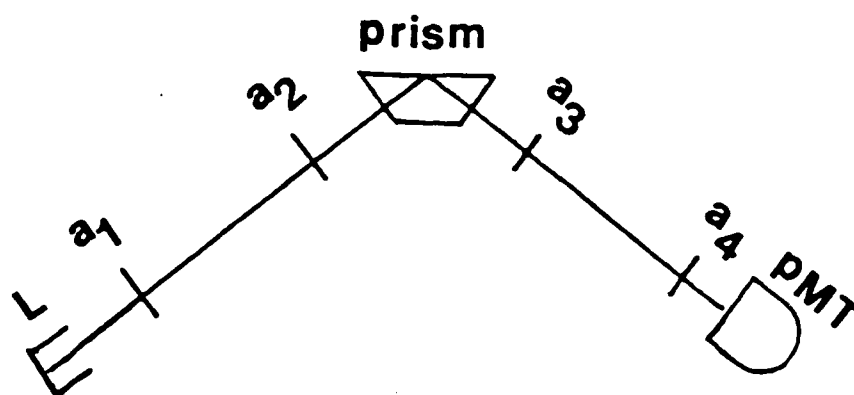


Figure 3.11. The initial setup for alignment

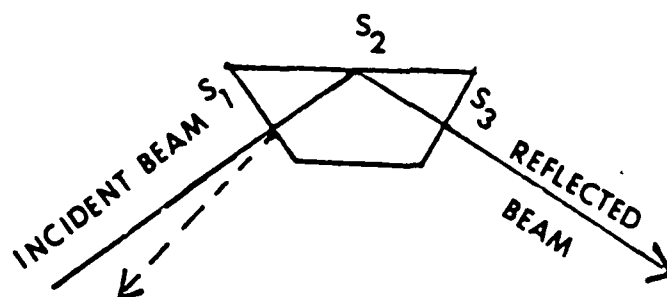


Figure 3.12. A closer view of the prism sample

The uncertainty to which ϕ and the x eigenpolarization are known can be determined as follows. Defining the uncertainty in h (the distance from the center of the laser beam to the optical bench) as δh and using the small angle approximation

$$\sin \delta \theta \approx \delta \theta , \quad 3.5$$

it can be seen that

$$\delta \theta \approx \delta h / l . \quad 3.6$$

A safe approximation for δh is $\delta h \approx 1\text{mm}$, which along with $l \approx 500\text{mm}$ yields an uncertainty in ϕ and the x eigenpolarization of about 10^{-4}° .

3.3.2. The final setup

Figure 3.13 shows the final alignment setup. Here the modulator, polarizer and analyzer have been inserted. The following steps were used for this final alignment.

1. Starting from the initial setup, insert the analyzer A and adjust so that the light beam passes undeviated through the center of the Rochon prism for all analyzer angles.
2. Insert the modulator ($M \approx 0$) and adjust so that the light beam reflected at the surface closest to a_1 nearly, but not exactly overlaps the laser aperture.
(Overlapping causes undesirable interference.)

At this point, all optical components are in place, but their angles with respect to the x eigenpolarization still have to be determined. Recalling figure 3.12, normal incidence on s_1 and s_3 , as

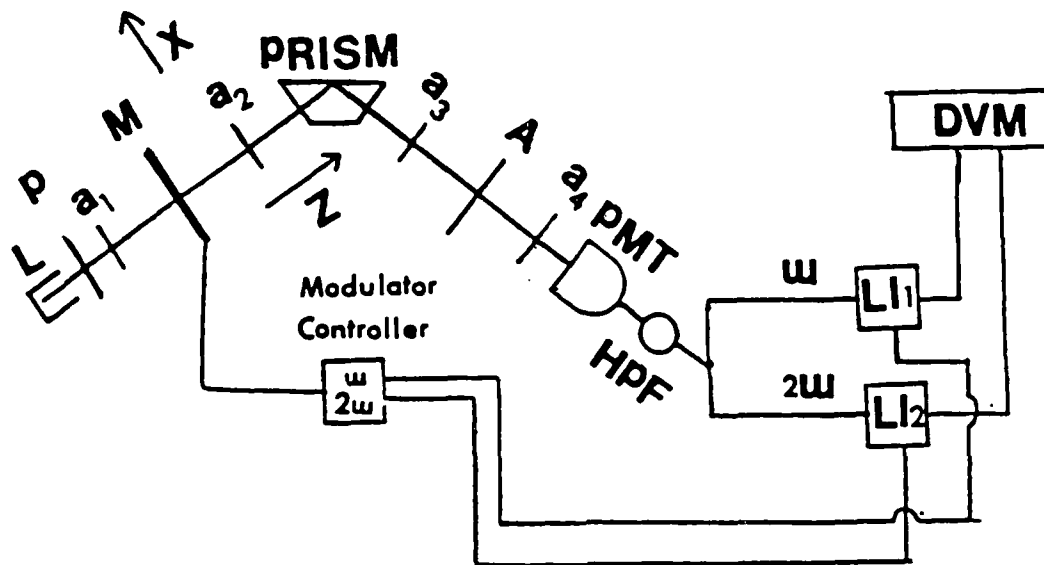


Figure 3.13. The final alignment setup. Here, a high pass filter, HPF allows the ac portion of the signal to be measured by two lock-in amplifiers, LI1 and LI2. A dc signal from the lock-in amplifiers proportional to the rms of the ω and 2ω signal is then measured by a digital voltmeter, DVM

well as total internal reflection at s_2 , implies that the net ψ for this optical system is 45° . Substituting, $\psi = 45^\circ$ into the general equation of the intensity of light, equations 2.13 - 2.16 the ac component of the signal is

$$I^{ac} = (I_c - J_0(R))\cos\delta(t) + I_s\sin\delta(t) \quad 3.7$$

where,

$$I_c = (G(V_{ex}^2 + V_{ey}^2)/4)\sin 2(P-M)\sin 2A \quad 3.8$$

$$I_s = (G(V_{ex}^2 + V_{ey}^2)/4)\sin 2(P-M)[\sin 2M\cos 2A + \cos 2M\sin 2A\cos\Delta] \quad 3.9$$

and where $J_0(R)$ is the 0th order Bessel function with argument R (all other terms are defined as in equations 2.13 - 2.16). Recall from equations 2.23 and 2.24 that I_s corresponds to odd harmonics and I_c corresponds to even harmonics. The following steps are based on equations 3.7 - 3.9.

3. Set the peak-to-peak retardation of the modulator to the value to be used in subsequent measurements. If the desired retardation is 2.4048 radians, then the peak-to-peak should be set at 248.
4. Using lock-in amplifiers, lock in on the 50 kHz and 100 kHz signals and adjust P until both are maximum. From equation 3.7, this corresponds to $P - M = 45^\circ$.
5. Adjust A until the 50 kHz signal is 0. From the equation for I this corresponds to $A = 0$.
6. With $A = 0$, adjust M until the 100 kHz signal is 0. From the equation for I , this corresponds to $M = 0$.

7. Set $A = 45^\circ$ and adjust P until both the 50 and 100 kHz signals are 0. From equations 3.8 and 3.9 this corresponds to $P = 0$.

At this point, $M = 0$, and P and A are known with respect to the x eigenpolarization. A note should be made as to the ordering of step 3. It was found that the stress axis for this particular modulator was slightly dependent on the peak-to-peak retardation, i.e., on the voltage applied to the piezoelectric crystal. This could be due to slight strains within the fused silicon block. The largest variation in M for the entire range of retardations was found to be about 0.05° . This was found by repeating step 5. By setting the retardation in step 3, the error in M can be eliminated. Recall that R is proportional to V/λ , where V is the voltage applied to the piezoelectric transducer and λ is the wavelength of the light. Hence, this error could not be eliminated for a spectroscopic ellipsometer.

Finally, since the x eigenpolarization has been determined with respect to A and P , it is not necessary to construct an entirely new set of alignment procedures after changing M . Rather, M can be rotated and P adjusted until the ac signal at the PMT is 0 (or more realistically a minimum). At this point $P = M$, so M is determined.

3.4. Data Reduction

The operating system of the HP 9800 computer is a Pascal operating system, and all programs were written in Pascal. The data transfer as well as many other aspects of the data reduction required extensive use of HP modules. With the aid of these modules, the Pascal programs were

every bit as powerful as BASIC programs and in some cases even more powerful. A modified system library was created using selected commercial modules as well as a complex numbers module. The programs and modules written for this work are located in Appendices B-E. It was necessary to write a small routine which is embedded in the larger "READ_CH1" procedure. This routine converts the data received from the 390AD into ASCII characters which would then be printed on the screen or undergo further data reduction. Otherwise, the data would be interpreted as control characters by the operating system. It should be noted that any BASIC operating system (for which the 390AD was designed to be used) takes care of this in the transfer routine.

3.4.1. The discrete Fourier transform

A procedure which calculates the Digital Fourier Transform or DFT of a set of data was written. The procedure calculates the amplitudes and the phases of the first n Fourier coefficients where n is an integer. It is not necessary to take a Fast Fourier Transform or FFT of the data, since it does not provide any more useful information, yet it requires the calculation of all N Fourier coefficients. The DFT procedure, called DFT_50 is based on the following mathematical discussion.^{15,16,17}

Any periodic function, which is least square integrable can be written in a Fourier series as

$$f(x) = \sum_{-\infty}^{\infty} a_n \phi_n(x) , \quad 3.10$$

where ϕ_n is an infinite set of orthonormal functions and a_n are the Fourier amplitudes of $f(x)$ given by the inner product

$$a_n = (\phi_n, f) . \quad 3.11$$

In particular, if the period of the function is $2L$ then the orthonormal set

$$\phi_n(x) = \frac{e^{in\pi x/L}}{\sqrt{2L}} \quad 3.12$$

where, $n = 0, \pm 1, \pm 2, \dots$. The inner product is then defined as

$$a_n = \frac{1}{2L} \int_x^{x+2L} f(x) e^{-in\pi x/L} dx . \quad 3.13$$

If the function is time dependent with period T , then it is standard to write

$$\sum_{-\infty}^{\infty} a_n e^{i2n\pi t/T} , \quad 3.14$$

where

$$a_n = \frac{1}{T} \int_t^{t+T} f(t) e^{-2n\pi t/T} dt \quad 3.15$$

The set of functions $e^{i2n\pi t/T}$ is no longer normalized. This set of a_n s are referred to as the finite Fourier transform of $f(t)$ and are actually the correct Fourier coefficients for a signal of period of T

In practice, we can only use a finite number of measured values of $f(t)$. The signal, $f(t)$ is measured at $t = k\Delta t$, where Δt is the time interval between two sampled values of f and is called the sampling

interval. If NMAX samples are obtained in a time interval T, then $T = NMAX\Delta t$. Substituting these for t and T in equation 3.15 and going from continuous to discrete variables yields

$$a_n = \frac{1}{NMAX\Delta t} \sum_{k=0}^{NMAX-1} f(k\Delta t) \exp \left[\frac{-j2\pi nk\Delta t}{NMAX\Delta t} \right], \quad 3.16$$

which can be reduced to

$$a_n = \frac{1}{NMAX} \sum_{k=0}^{NMAX-1} f(k\Delta t) \exp \left[\frac{-j2\pi nk}{NMAX} \right], \quad 3.17$$

where the set of a_n s are referred to as the N point discrete Fourier transform¹⁶ of $f(t)$.

If f is a real function then

$$a_n = a_{n-NMAX},$$

i.e., the a_n s are periodic. Therefore, it is only necessary to calculate half of the Fourier coefficients, and it is desirable to have NMAX odd. Also, the NMAX within the argument of the exponential can be varied, yielding different sets of DFTs. However, the total number of points in the DFT must remain the total number of points sampled. For example, if NMAX is doubled, the range of Fourier components is divided in half but the number of Fourier components within this range remains the total number of data points.

If a signal contains frequency components less than or equal to a frequency f_{MAX} where

$$f_{MAX} = 2/(NMAX\Delta t) = f_{SAMPLING}/2,$$

then f can be exactly reconstructed from the NMAX sampled values taken

at $t = k\Delta t$, where $\Delta t = 1/N_{MAX}$. This is known as the sampling theorem.¹⁶ Hence, changing N_{MAX} in evaluating a_n s does yield correct results as long as the signal has no frequency components greater than $f_{SAMPLING}/2$.

Finally, the complex Fourier coefficients can be converted to a magnitude and a phase. Setting an amplitude, A_n to be two times the magnitude of a_n (except A_0 which is set equal to $|a_0|$) and a phase, δ_n to be the phase of a_n , equation 3.18 can be written as

$$f(k) = \sum_{n=0}^{\infty} A_n \cos \left[\frac{2\pi nk}{N_{MAX}} + \delta_n \right] . \quad 3.18$$

The amplitudes, A_n , are the Fourier components.

Recall that the general form of the intensity of light incident on the PMT is

$$I_0 = I_0 + I_c \cos \delta(t) + I_s \sin \delta(t) \quad 3.19$$

and $\cos \delta(t)$ and $\sin \delta(t)$ can be expanded in a Jacobi series as was shown in Chapter 2. This would seem to indicate that a DFT would not yield correct results according to the sampling theorem, since the series includes an infinite number of harmonics. However, the higher order Bessel functions are nearly zero for the retardations in question. Hence, since the Fourier amplitudes are proportional to the Bessel functions, for all frequency components greater than 500 kHz will be zero, and the sampling frequency can be chosen such that

$$f_{SAMPLING} \geq 500 \text{ kHz} .$$

Finally, it should be mentioned that the DFT produces the best results if an integral number of 20 μs intervals are used. This is obvious if one recalls that the Fourier transform actually reproduces a signal with

a period T (see equation 3.15).

With the above information in mind, the DFT for the photometric ellipsometer was constructed in the following manner.

1. The sampling frequency was chosen to be 60 MHz, well above the 500 kHz limit.
2. N_{MAX} was chosen to be the nearest odd integer to $f_{SAMPLING}/f_{OSCILLATOR}$, where $f_{OSCILLATOR}$ is the modulator's frequency (50 kHz).
3. The complex coefficients, a_n , were then converted into A_n and δ_n as defined in equation 3.19.

A program was written called "spectral_analysis", located in Appendix B, which thoroughly tested the DFT procedure. In this program, it was possible to create two different types of signals;

1. $f(t) = A_0 + A_n \cos(n\omega t + \delta_n)$
2. $f(t) = I_c \cos(\omega t) + I_s \sin(\omega t)$.

Arbitrary A_n , δ_n , and ω could be entered in (1), and arbitrary azimuth and ellipsometric angles could be entered in (2). Then, a discrete Fourier transform (DFT) is performed on the resulting data and compared to the expected values.

The DFT procedure worked correctly in (1) and (2) for all situations in which $f_{SAMPLING}$ was an integral multiple of $f_{OSCILLATOR}$. If, however, the ratio of the two frequencies was not an integer, then an error of about 0.05% was introduced, which could be further reduced if more than 1 period of data were Fourier analyzed. Hence, it is important to choose a sampling frequency which is an integral multiple of the modulator frequency to insure the best possible DFT results when

observing 1 period of data.

The next step involved reading a signal with known Fourier amplitudes into the 390AD digitizer and perform a DFT on it. The modulator provides a 50 kHz modulating frequency. This was checked by sending the 50 kHz square wave reference signal into the 390AD and performing DFTs on the resulting data using an $f_{\text{OSCILLATOR}}$ in the "DFT_50" procedure between 49 and 51 kHz, increasing by 1 Hz each time. Since the Fourier transform of a square wave has only nonzero odd frequency components, the best $f_{\text{OSCILLATOR}}$ frequency for the DFT could then be determined by observing when the even components were minimized. This did indeed occur at $f_{\text{OSCILLATOR}} = 50$ kHz, but the minima were not zero as they would be in the ideal case. Rather, they were about 0.1% of the corresponding odd magnitudes. The fact that zeros were not obtained plays an important role when the data are further reduced to obtain ψ and Δ , i.e., the data reduction itself, introduces an error of about .1% for ψ and Δ .

3.4.2. Obtaining the optimal signal

Before actually calculating ψ and Δ , it was necessary to adjust the load resistance in order to obtain the optimal signal at the PMT. Varying the load resistance can significantly change the signal at the anode, resulting in large variations in the Fourier coefficients, and consequently the resulting ψ and Δ . As far as is known, these signal analyzing procedures have not been done before.

3.4.2.1. Relationship of the Fourier Coefficients to the Bessel

Functions From the general equation of light flux, $I(t)$, and the Jacobi expansion of $I(t)$ in terms of sines and cosines and Bessel functions, it can be seen that (excluding the dc component) the ratio of odd or even magnitudes of Fourier coefficients are equal to the corresponding ratio of odd or even Bessel functions for all ψ and Δ . Therefore, independent of the settings of the optical components as well as optical properties of the particular sample, a comparison of ratios of the magnitudes of Fourier components with the ratios of the Bessel functions gives an indication of the quality of the signal being processed. The program, "DFT_ellipsometer", which controls the acquisition and reduction of data for this ellipsometer is located in Appendix C. The program displays the first seven Fourier coefficients and their corresponding phases, as well as, the resulting values of ψ and Δ . In addition, the procedure "Gain_Calibration" compares the ratios of these Fourier coefficients to the corresponding ratios of Bessel functions. The two lowest order Bessel functions are calculated from the following series relation

$$J_n(x) = \sum_{k=0}^{\infty} \frac{(-1)^k (x/2)^{n+2k}}{k! \Gamma(n+k+1)} \quad 3.20$$

and the higher order Bessel functions are obtained using the recursion relation

$$J_{n+1}(x) = \frac{2n}{x} J_n(x) - J_{n-1}(x) \quad 3.21$$

If I_s is zero, then the even ratios must be used to determine the quality of the signal. If I_c is zero, then the odd ratios must be used.

It is also possible to solve for the retardation as a function of the magnitudes of the Fourier coefficients. Combining recursion relation 3.21 and the fact that the ratio of Fourier coefficients is equivalent to the ratio of corresponding Bessel functions gives

$$R = \left[\frac{24A_2A_3}{(A_1+A_3)(A_2+A_4)} \right]^{1/2} \quad 3.22$$

Equations similar to 3.22 but using higher order Fourier coefficients can also be obtained, e.g.,

$$R = \left[\frac{48A_3A_4}{(A_2+A_4)(A_3+A_5)} \right]^{1/2} \quad 3.23$$

The procedure "RETARDATION_CALIBRATION" calculates the two lowest order retardations, i.e., from the two lowest sets of Fourier amplitudes. Unlike the "GAIN_CALIBRATION" procedure, both I_c and I_s must be nonzero, (which will often be the case), in order to obtain good results.

3.4.2.2. The gain of the PMT as a function of the voltage at the cathode

The actual voltage measured by the digitizer is a function of the load resistance and the voltage of the high voltage power supply. Variations in either one of these causes variations in both the magnitudes and phases of the Fourier coefficients as expected. Note, however, that the capacitor used as the dc block is so large, that the

capacitive reactance is nearly zero for the 50 kHz signal. Hence, it is expected that the ratios of the Fourier amplitudes, (as discussed in the previous section), remain constant for all values of the load resistance and high voltage power supply. It was found, however, that the ratios of the Fourier amplitudes is dependent on the voltage at the cathode of the PMT. Hence, the gain of the PMT at different frequencies are different functions of the voltage at the cathode of the PMT.

Figure 3.14 shows the relationship of the ratios of the Fourier coefficients as a function of the voltage of at the cathode of the high voltage power supply. The sample used for this case was a silicon wafer, which has a moderate reflectivity. (Recall that the odd or even ratios of the Fourier coefficients is independent of the ellipsometric angles, ψ and Δ , as well as, the azimuth angles P , M , and A of the ellipsometer.) As can be seen, the ratios of the Fourier components is extremely dependent on the voltage at the cathode. Higher order Fourier coefficients have magnitudes on the order of 1% of A_1 and A_2 . These coefficients are even more sensitive to the voltage at the cathode of the PMT.

If the feedback mechanism described above is used, then this does not present a significant problem. The gain of the PMT changes several orders of magnitude, if the voltage at the cathode of the PMT varies from -475V to -675. Hence, although the total reflectivity of the sample may vary over one order of magnitude, the high voltage at the cathode of the PMT need vary only slightly to maintain the dc current at the anode constant.

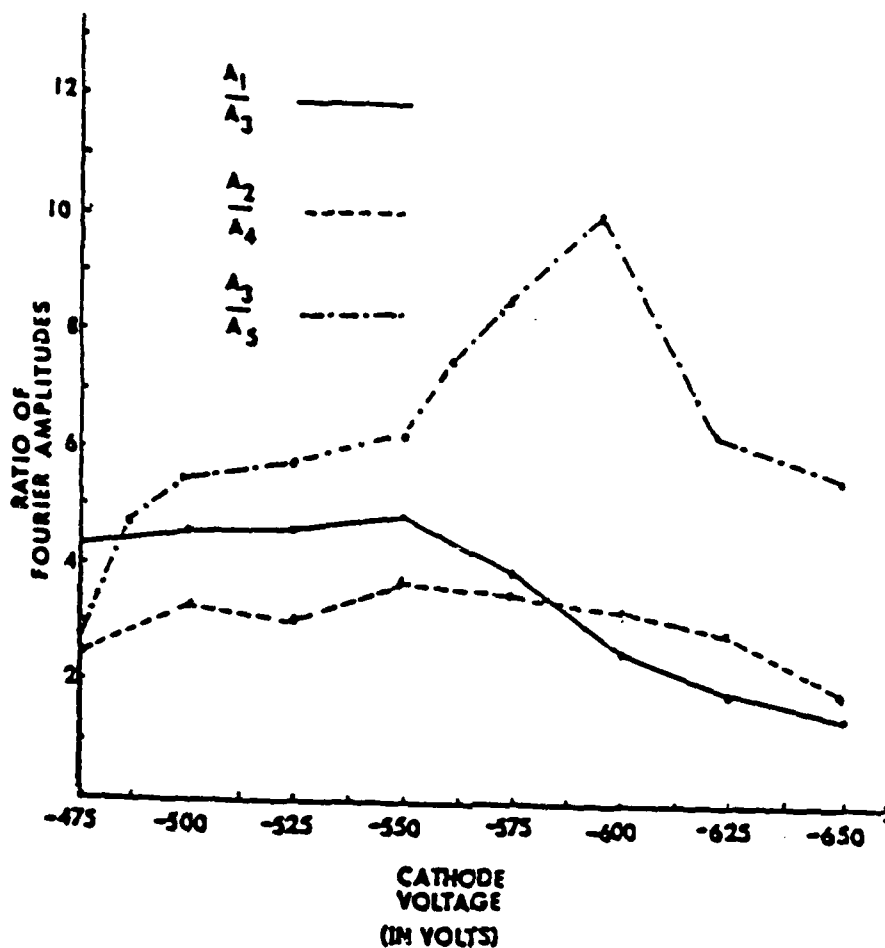


Figure 3.4. A plot of the ratios of the Fourier amplitudes verses the voltage at the cathode of the photomultiplier tube. Here, $A_1 - A_5$ are the amplitudes of the first five fourier coefficients, obtained by performing a discrete Fourier transform, DFT on the signal at the anode of the PMT. The sample used was a 1000Å film of SiO_2 on Si, and the load resistance is 2500 k Ω

AD-A187 335

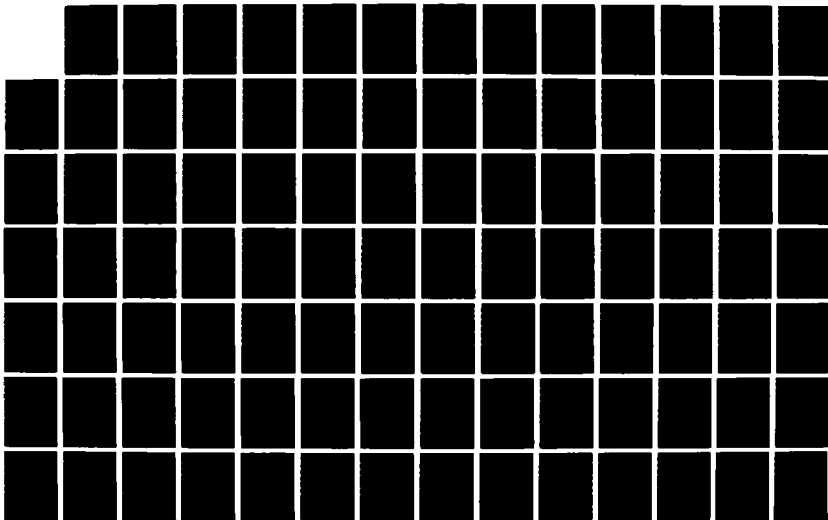
SYNTHESIS AND CHARACTERIZATION OF THIN FILMS(U) IOWA
STATE UNIV AMES MICROELECTRONICS RESEARCH CENTER
K M LAKIN 10 JUL 87 AFOSR-TR-87-1393 AFOSR-84-0388

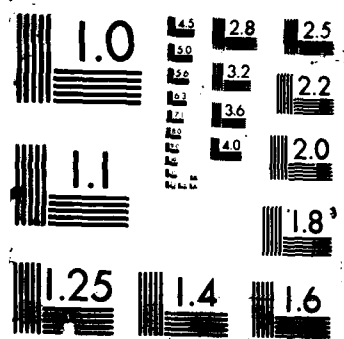
2/4

UNCLASSIFIED

F/G 13/8

NL





3.5. Calculation of ψ and Δ

Recall that the general equation for the signal at the anode of the PMT (provided that the PMT has a linear response to the light flux) was calculated to be

$$I(t) = I_0 + I_c \cos \delta(t) + I_s \sin \delta(t), \quad 3.24$$

where,

$$I_0 = G' [1 - \cos 2\psi \cos 2A + \cos 2M \cos 2(P-M)(\cos 2A - \cos 2\psi) + \sin 2A \cos 2(P-M) \sin 2M \sin 2\psi \cos \Delta], \quad 3.25$$

$$I_s = G' [\sin 2(P-M) \sin 2A \sin 2\psi \sin \Delta], \quad 3.26$$

$$I_c = G' [\sin 2(P-M) [\sin 2M (\cos 2\psi - \cos 2A) + \cos 2M \sin 2A \sin 2\psi \cos \Delta]], \text{ and} \quad 3.27$$

$$G' = G(V_{ex}^2 + V_{ey}^2)/4. \quad 3.28$$

Here, G is the proportionality constant defined in Section 1.3.2, M , P , and A are the angles that the modulator, polarizer and analyzer make with respect to the x eigenpolarization, ψ and Δ are the ellipsometric parameters, and V_{ex} and V_{ey} are the diagonal components of the Jones matrix of the unknown optical system.

As was mentioned in the alignment section, Section 3.3, the above signal can be written as the sum of an ac and a dc component, namely

$$I(t) = I_{ac} + I_{dc} \quad 3.29$$

where

$$I_{ac} = I_s \sin \delta(t) + I_c (1 - J_0(R)) \cos \delta(t), \quad 3.30$$

$$I_{dc} = I_0 + J_0(R)I_c \quad \text{and} \quad 3.31$$

R is the retardation in radians. The feedback mechanism presented earlier forces a constant dc current for all samples and retardations.

Setting the parameters M , P , and A so that

$$P = 45^\circ$$

$$M = 0^\circ, \text{ and}$$

$$A = 45^\circ,$$

the equations I_0 , I_c and I_s become

$$I_0 = G', \quad 3.32$$

$$I_s = G' \sin 2\psi \sin \Delta, \text{ and} \quad 3.33$$

$$I_c = G' \sin 2\psi \cos \Delta. \quad 3.34$$

Solving for $\sin 2\psi$ and $\tan \Delta$ in terms of I_s , I_c , and I_0 yields

$$\sin 2\psi = [I_s^2 + I_c^2]^{1/2} / I_0 \quad 3.35$$

$$\text{and} \quad \tan \Delta = I_s / I_c. \quad 3.36$$

Expanding $\sin \delta(t)$ and $\cos \delta(t)$ according to the Jacobi expansion as introduced in Chapter 2 it can be shown that

$$2I_s J_j(R) = A_j \quad j = 1, 3, 5, \dots \quad 3.37$$

$$2I_c J_k(R) = A_k \quad k = 2, 4, 6, \dots \quad 3.38$$

and

$$I_0 + I_c J_0 = a_0, \quad 3.39$$

where the A_n s are the amplitudes of the Fourier coefficients as defined in the section describing the DFT procedure.

Substituting for I_s , I_c , and I_0 in equations 3.35 yields

$$\sin 2\psi = [(A_j/J_j(R))^2 + (A_k/J_k(R))^2]^{1/2} / (2A_0 - A_k(J_0(R)/J_k(R))) \quad 3.40$$

which reduces to

$$\sin 2\psi = [(A_j/J_j)^2 + (A_k/J_k)^2]^{1/2} / 2A_0, \quad 3.41$$

when $R = 2.4048$, the first root of $J_0(R)$.

At this point, forcing the dc current at the anode of the PMT forces A_0 constant for all samples. Introducing the constant dc_cal as $dc_cal = 2A_0$, equation 3.41 becomes

$$\sin 2\psi = [(A_j/J_j(R_0))^2 + (A_k/J_k(R_0))^2]^{1/2} / dc_cal. \quad 3.42$$

This equation is the basis of the "FOURIER_PSI" procedure located in the DFT_ELLIPSOMETER program in the Appendix.

The equation for $\tan \Delta$ becomes

$$\tan \Delta = J_k(R_0)A_j / (J_j(R_0)A_k) \quad \text{for } j < k \quad 3.43$$

and

$$\cot \Delta = J_j(R_0)A_k / (J_j(R_0)A_k) \quad \text{for } j > k. \quad 3.44$$

Since all amplitudes and Bessel functions used above are positive, it would seem that Δ is restricted to the range

$$0^\circ \leq \Delta \leq 90^\circ.$$

However, the actual range of Δ is

$$0^\circ \leq \Delta \leq 180^\circ.$$

To determine which quadrant Δ is in, it is necessary to refer to the phases of the Fourier coefficients obtained from the DFT procedure.

Once again, referring to equation 3.24 for the intensity of light at the PMT we see that

$$I_s > 0 \text{ for all } \Delta,$$

but $I_c > 0$ whenever $0^\circ \leq \Delta \leq 90^\circ$

and $I_c < 0$ whenever $90^\circ \leq \Delta \leq 180^\circ$

Hence, with $M = 0^\circ$, $P = A = 45^\circ$ and the phases of the odd Fourier coefficients are 270° (corresponding to positive sine waves), the following equations are true;

$$0^\circ \leq \Delta \leq 90^\circ \text{ whenever } \delta_k = 0^\circ$$

and $90^\circ \leq \Delta \leq 180^\circ$ whenever $\delta_k = 180^\circ$,

where $k = 2, 4, 6 \dots$, and the δ_k s are the phases of the Fourier coefficients obtained from the DFT procedure. The actual phases of the odd components are not exactly 0° or 180° , but rather are within 15° of these, if the phases of the odd components are within 15° of 270°

It should be noted that $\tan \Delta$ turns out to be independent of the dc current, due to the symmetry of the experimental setup, namely $M = 0$. This is why this particular configuration was chosen. Hence, any errors resulting from unequal amplification of the dc verses the ac portions of the signal by the PMT will not effect the accuracy of the Δ measurement. On the other hand, the unequal amplification of the various ac components does effect the accuracy of the ψ measurement.

The best results for ψ and Δ were obtained, using the lowest order terms $j = 1$ and $j = 2$. This is expected, since the analysis of the higher order frequencies, as discussed earlier, showed that the gain of the PMT is indeed frequency-dependent.

4. CONSTRUCTION OF A VERY-HIGH-SPEED ELLIPSOMETER (THE DUAL ANALYZER ELLIPSOMETER)

This ellipsometer is capable of acquiring a set of ellipsometric parameters (ψ, Δ) at rates over 10 times those of the fastest ellipsometers currently available. The ellipsometer utilizes a photoacoustic modulator. Only the ac portions of the signals are used. This eliminates errors due to depolarization caused by imperfect optical components, as well as, errors due to extraneous sources of light. The ellipsometer does not require a high-speed power supply to respond to fluctuations in the flux of the light source in a feedback loop. Rather, these fluctuations automatically cancel themselves out. Finally, the ellipsometer retains the advantage of no mechanically moving parts.

Ordinarily, photoacoustic modulators are used to construct dynamic photometric ellipsometers, i.e., ellipsometers based on Fourier analysis of the output signal. This forces the minimum time necessary for the acquisition of ψ and Δ to the period of the modulator signal (usually about 20 microseconds). Also, Fourier analysis takes several seconds for most minicomputers. This means that the data reduction usually must be performed after the ellipsometric measurements have been made. This eliminates the possibility of using the dynamic photometric ellipsometer in any sort of feedback mechanism for precise observation and control of thin film growth under vacuum. This new ellipsometer is a static photometric ellipsometer, so its signal, is not Fourier analyzed, and therefore, the above restrictions would no longer exist.

4.1. The Ellipsometer Setup

Once again, the ellipsometer setup can be divided into an optical and an electrical setup. As in Chapter 3, a discussion of each of these setups, as well as the alignment procedure follows.

4.1.1. The Optical Setup

A schematic diagram of the ellipsometer is shown in figure 4.1. An obvious major difference in the setup is the dual analyzing arms. The ellipsometer can be called a dual analyzer ellipsometer (DAE). The laser beam is split into two beams using a piece of fused silicon.

Figure 4.2 shows how the beam is split. The beam reflected from the first planar interface is analyzed by one arm of the ellipsometer and the transmitted beam is analyzed by the other arm of the ellipsometer. The resulting signals at the PMT are then read simultaneously.

4.1.2. Alignment

The alignment procedure discussed in the last chapter is used here to align the transmitted section of the ellipsometer. After this was completed, the beam splitter is placed between the sample and analyzer, A_T . Then the following steps are performed with the modulator off.

1. The beam splitter is rotated about its z axis until the beam of light is reflected at the principal angle and passes through an aperture.
2. The analyzer, A_R , is placed so that the beam passes

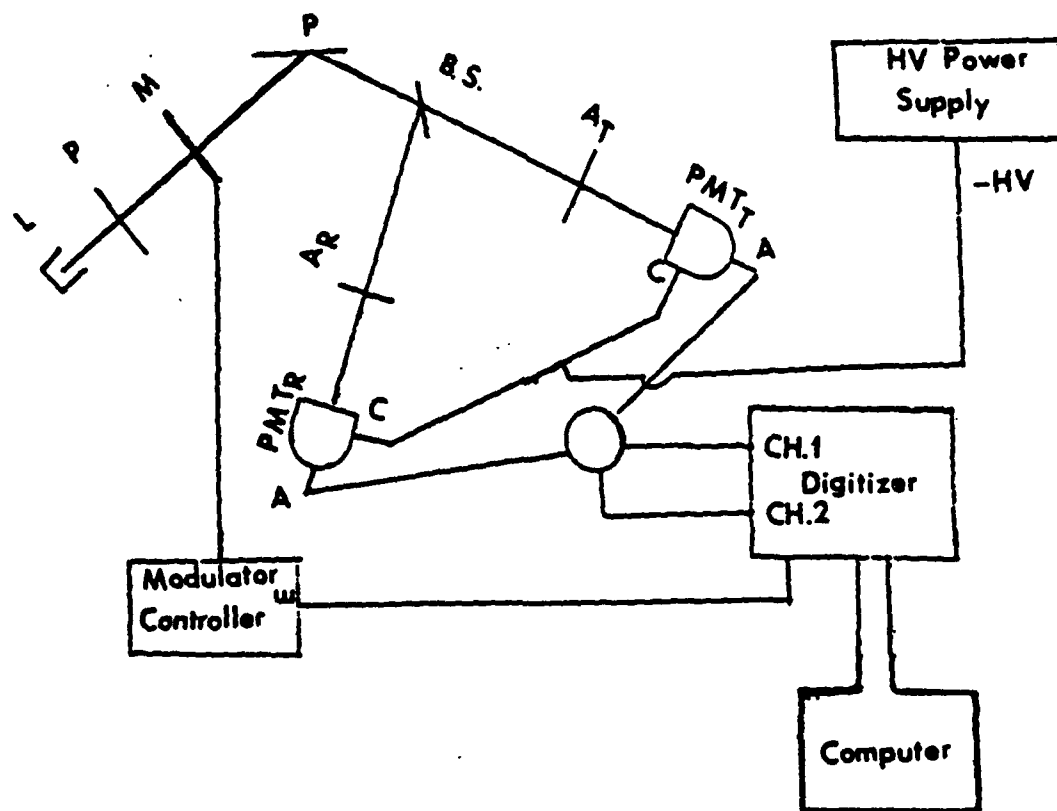


Figure 4.1. The dual analyzer ellipsometer (DAE). The elements are: the laser (L), polarizer (P), modulator (M), sample (S), beam splitter (BS), analyzers, (A_R) and (A_T), photomultiplier tube (PMT), modulator controller, dc power supply, digitizer and mini-computer

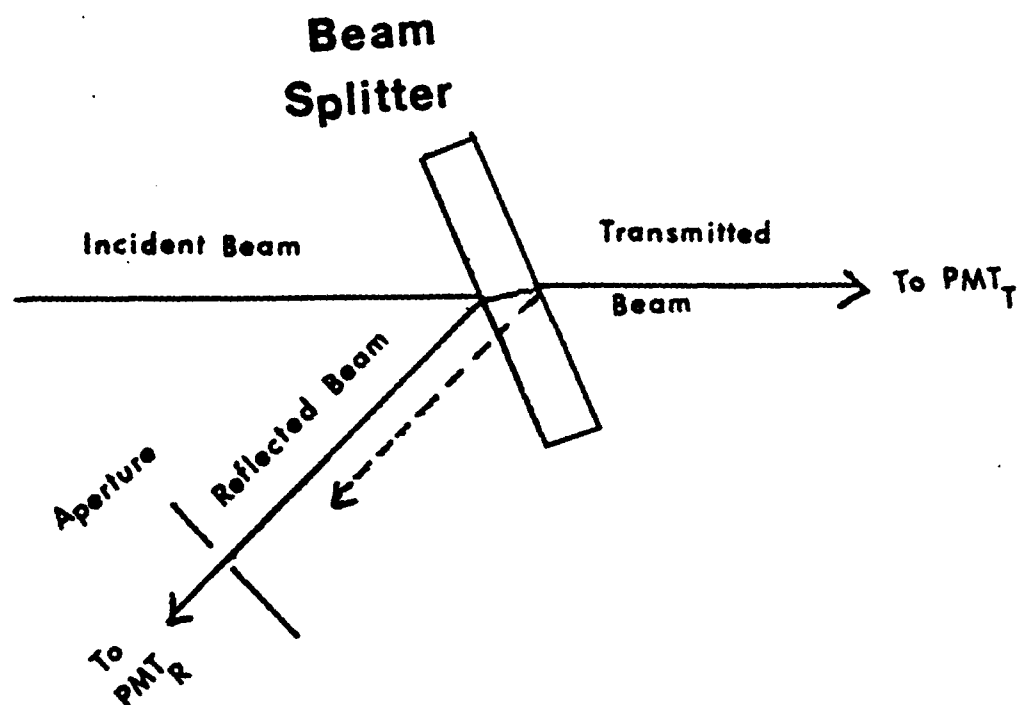


Figure 4.2. The beam splitter

undeviated through it to PMT_R .

3. The polarizer is set at 90° and A_R is adjusted for a null. This corresponds to $A_R = 0^\circ$.
4. Finally, since the transmitted beam has been slightly deviated by the beam splitter as indicated in figure 4.2, A_T and PMT_T are translated so that the beam once again passes through them.

The modulator is then turned on and adjusted (as explained in the previous chapter) so that $M = 45^\circ$. The dual analyzer is now aligned.

4.1.3. The electrical setup

The figure below shows the electrical setup. The same power supply, computer, and digitizer used in the previous photoacoustic modulated ellipsometer were used here as well. Hence, only those aspects of the DAE which are different from the previous ellipsometer or which have a fundamentally different role will be discussed here.

Two Centronics P4283 broad spectral response photomultiplier tubes with identical voltage divider networks are connected to the same high voltage power supply, so that the voltage at the cathodes of both PMTs remains the same. It is not necessary that the gains of the two PMTs be the same (indeed, they probably are not the same). Nevertheless, it must be assumed that their ratio remains the same at any given voltage. This is true as long as the current resulting from the light incident on both cathodes is much smaller than the current through either voltage divider network. This was already discussed in Section 3.2.1 for the case of a single phototube. The corresponding discussion in Section

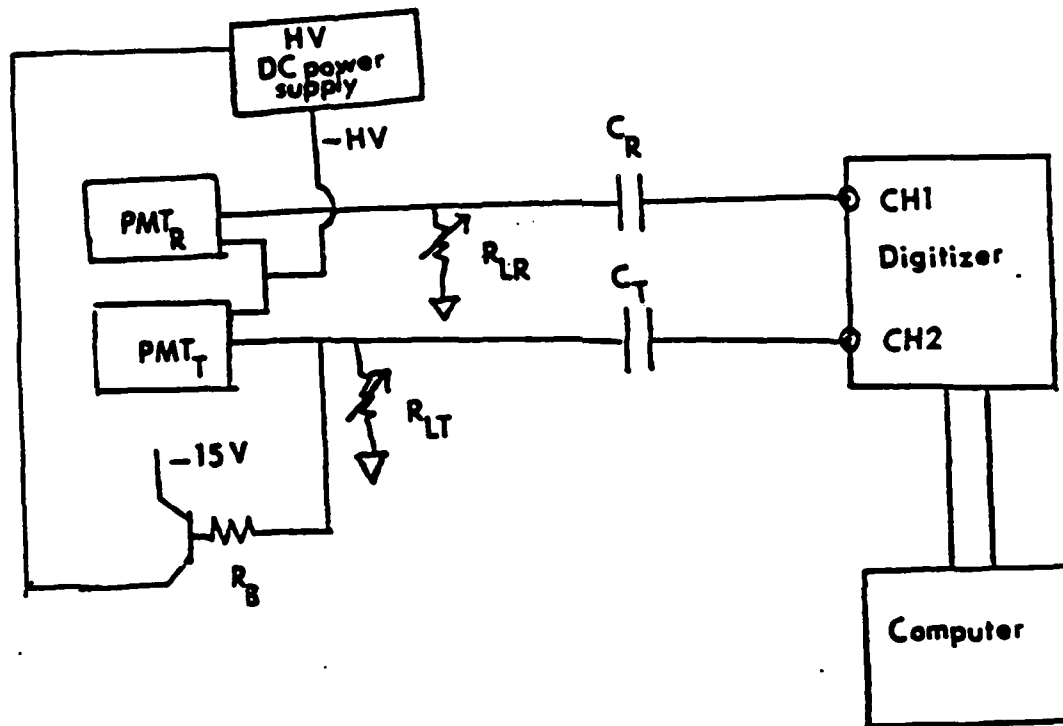


Figure 4.3. The electrical setup for the DAE

3.2.2 for the HP 6516A power supply demonstrates that the criterion, $i_d \gg i_p$, would still be satisfied when using two PMTs.

The dc portion of the current from PMT_T is incorporated in a feedback loop in the same fashion as that of the ellipsometer from the previous chapter. The dc portion from PMT_R is allowed to flow through R_{LR} . R_{LR} and R_{LT} can be varied independently of each other. C_R and C_T act as dc blocks allowing the ac signals to be A/D converted by the Tektroniks 390AD.

4.2. Theory of the Ellipsometer

The Jones matrix formalism, introduced in the earlier chapters, was used to calculate the intensity of the light at the two PMT's. The Jones matrix of the beam splitter will be written

$$X = \begin{bmatrix} X_{ex} & 0 \\ 0 & X_{ey} \end{bmatrix}, \quad 4.1$$

where X_{ex} and X_{ey} are the eigencoefficients for either the transmitted or reflected beams, i.e.,

$$X_{ex} = R_{ex} \text{ and } X_{ey} = R_{ey} \text{ for the reflected beam, and}$$

$$X_{ex} = T_{ex} \text{ and } X_{ey} = T_{ey} \text{ for the transmitted beam.}$$

As is standard in reflection or transmission ellipsometry, one can introduce the ellipsometric parameters ψ and Δ ,

$$R_{ex}/R_{ey} = \tan \psi_R e^{i\Delta_R}$$

$$\text{or} \quad T_{ex}/T_{ey} = \tan \psi_T e^{i\Delta_T}.$$

Hence, using the Jones matrix formalism, the intensity of the light at either of the PMTs is

$$I^X(t) = I_0^X + I_S^X \sin \delta(t) + I_C^X \cos \delta(t) \quad 4.2$$

where

$$I_0^X = (G_X \alpha \beta_X / 8) [(1 + \cos 2\psi_X) - (\cos 2\psi_X + \cos 2\psi) + \cos 2M \cos 2(P-M) \cdot \quad 4.3$$

$$[\cos 2A(1 + \cos 2\psi_X \cos 2\psi) - (\cos 2\psi_X + \cos 2\psi)] + \\ \sin 2A \cos 2(P-M) \sin 2M \sin 2\psi \sin 2\psi_X \cos(\Delta + \Delta_X)]$$

$$I_S^X = (G_X \alpha \beta_X / 8) [\sin 2(P-M) \sin 2A \sin 2\psi \sin 2\psi_X \sin(\Delta + \Delta_X)] \quad 4.4$$

$$I_C^X = (G_X \alpha \beta_X / 8) [\sin 2(P-M) [\sin 2M ((\cos 2\psi_X + \cos 2\psi) - \cos 2A \cdot \quad 4.5 \\ (1 + \cos 2\psi_X \cos 2\psi)) + \cos 2M \sin 2A \sin 2\psi \sin 2\psi_X \cos(\Delta + \Delta_X)]]$$

and where

$$\alpha = V_{ex}^2 + V_{ey}^2 \quad 4.6$$

$$\beta_X = X_{ex}^2 + X_{ey}^2, \quad 4.7$$

and the X coefficients are those defined above.

4.2.1. Static vs. dynamic photometric measurements

As was mentioned earlier, the major difference between static and dynamic photometric ellipsometers is that the latter is Fourier analyzed and the former is not. Nevertheless, a time interval, called the "resolution time", can be attributed to both types of ellipsometers. Resolution time will be defined later.

Figures 4.4a, 4.4b, and 4.4c demonstrate three different situations that could be encountered by a dynamic photometric ellipsometer. Note that in the general case $\psi = \psi(t)$, $\Delta = \Delta(t)$ and $\alpha = \alpha(t)$. The minimum time interval, Δt , necessary to obtain 1 set of ellipsometric data by Fourier analysis is the period of modulation, Δt . The value Δt can be defined as the resolution time of the ellipsometer. Note, Δt can vary

from μs to hundreds of ms depending on the type of modulation used, e.g., photoacoustic, rotating/analyzer, etc. ...

In figure 4.4a, it is assumed that ψ , Δ , and α are slowly varying functions of t . If, on the other hand, ψ , Δ and α vary on a time scale approximately that of Δt as in figure 4.4b, then Fourier analysis of the signal yields a sort of average ψ and Δ . Finally, if ψ , Δ , and α vary significantly within Δt , as in figure 4.4c, then an average set of parameters, ψ and Δ obtained from Fourier analysis tells very little about the types of optical changes that have actually occurred.

The situations encountered in figures 4.a, 4.b, and 4.e for dynamic photometric ellipsometers can also be considered within the realm of static photometric ellipsometers. Namely, a resolution time can be attributed to this type of ellipsometer. Again, ψ , Δ , and α can vary with time. Most often, however, ψ and Δ are independent of time when static photometric ellipsometers are used. The resolution time, Δt is the time required to obtain three independent equations of $I(t)$. The Δt usually ranges from several seconds to several minutes, depending on the method of measurement. Again, the information that the resulting ellipsometric parameters, ψ and Δ , provide depends on the relationship between $\psi(t)$, $\Delta(t)$, $\alpha(t)$, and Δt .

For both the dynamic and static photometric ellipsometers, the sample being measured is a function of ψ , Δ , and α (defined above). Hence, it is necessary to obtain 3 linearly independent equations in order to calculate one set of ellipsometric parameters.

In the case of the photoacoustic modulated ellipsometer previously discussed (a dynamic photometric ellipsometer), the quantity $K = G\alpha/4$ is

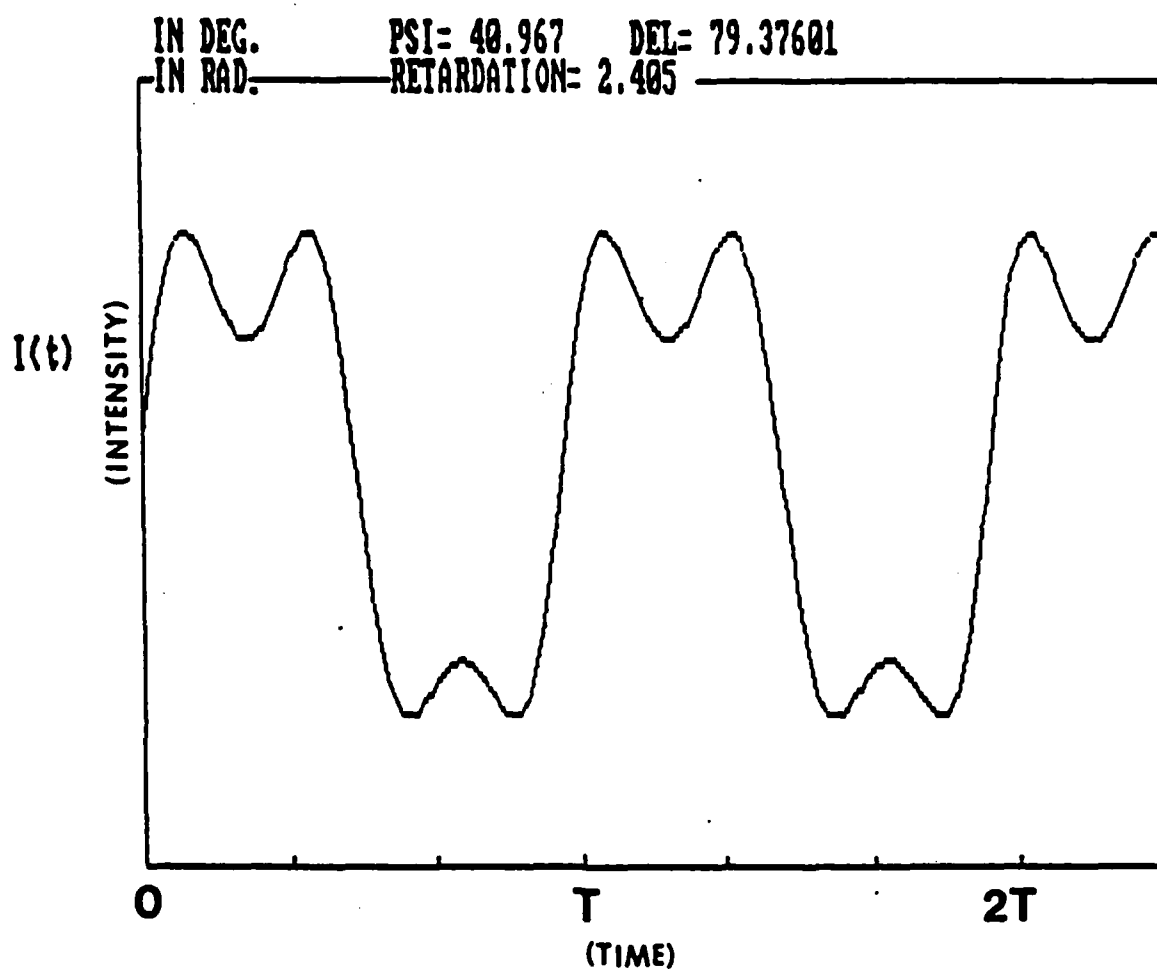


Figure 4.4a. The light intensity, $I(t)$, as a function of time. Here, Ψ and Δ are constant over one modulation period, T

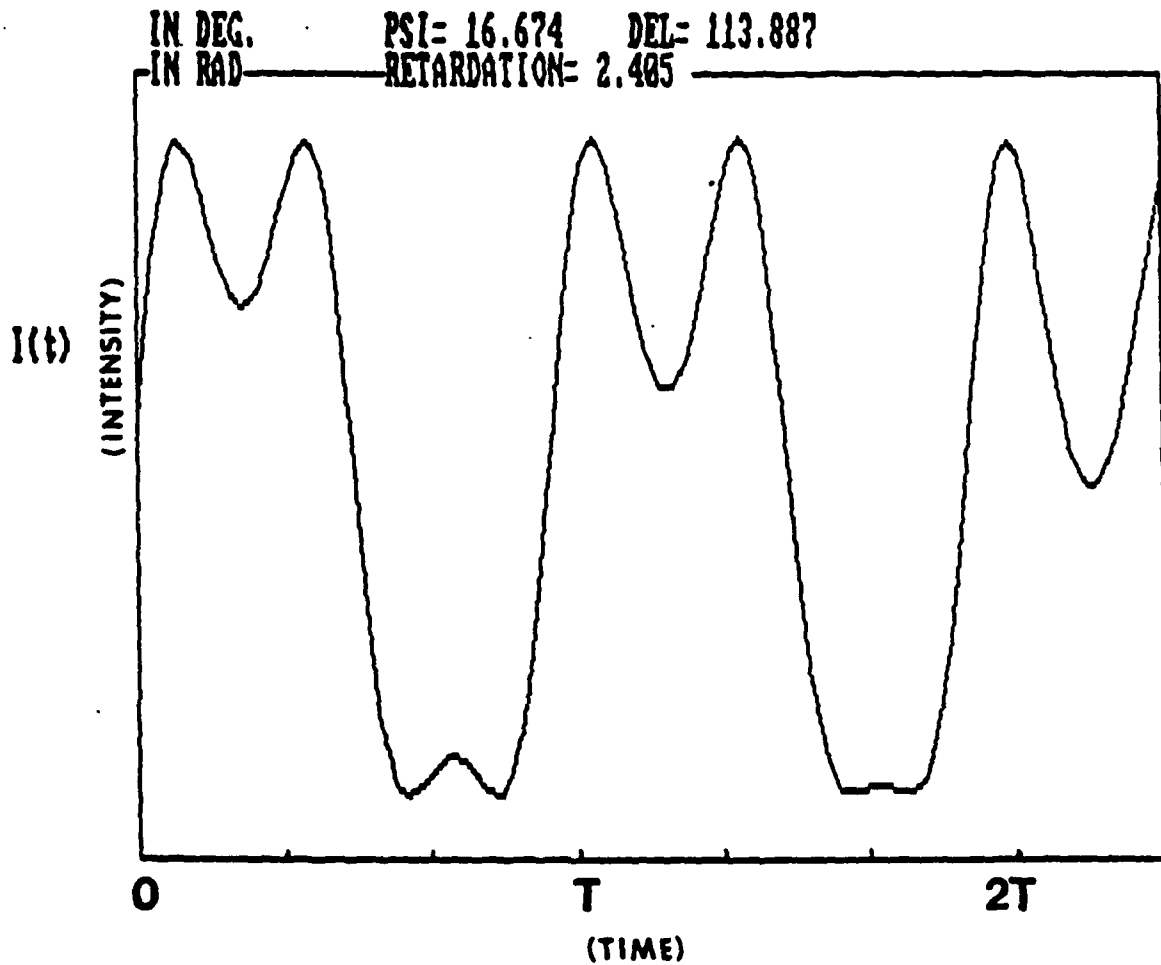


Figure 4.4b. The light intensity, $I(t)$, as a function of time. Ψ and Δ vary linearly with respect to time. Here, Ψ varies from 40.97° to 16.67° and Δ varies from 79.38° to 113.89° over 2.334 modulation periods, i.e., $2.334 T_s$

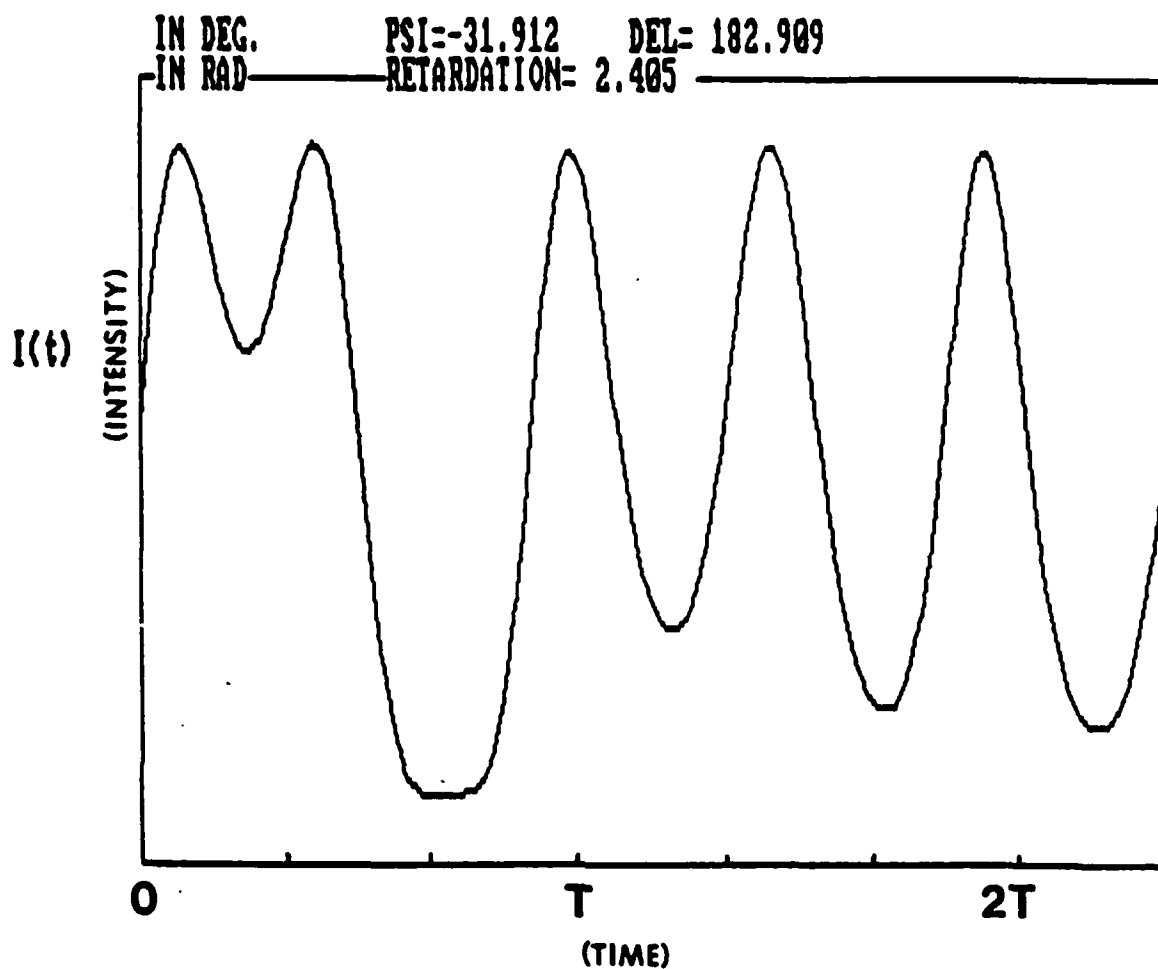


Figure 4.4c. The light intensity, $I(t)$, as a function of time. Here, Ψ and Δ vary linearly, Ψ varies from 40.97° to 16.67° and Δ varies from 79.38° to 113.89° over one modulation period, T .

held constant by incorporating the dc output of the PMT in a feedback loop. Also, note that both G and α can be functions of time, but their product K remains constant. Hence, one independent variable was effectively eliminated as an unknown. Therefore, it is possible to obtain the two independent parameters ψ and Δ from two independent equations. (The Bessel function recursion relation introduced in Chapter 3 necessarily reduces the number of independent parameters which can be obtained from Fourier analyzing the signal to two.)

In the case of a static photometric ellipsometer, three independent equations are obtained from three different sets of measurements as was shown in Section 2.2.2.1. The three sets of equations are usually obtained by mechanically changing polarizer or analyzer settings, either automatically or manually.

In the case of the DAE introduced here, each measurement yields two simultaneous equations for ψ and Δ . β_x , ψ_x , and Δ_x in equations 4.2-4.5 are constants for both the reflected and transmitted signals at all times. Therefore, the proportionality factor K' for the (DAE), defined as

$$K'_x = G_x \alpha \beta_x / 8 \quad 4.8$$

corresponds to K in the discussion for a modulated ellipsometer.

However, in order to obtain information within very short time intervals (e.g. in situ measurements under high vacuum), K' can no longer be maintained constant using the feedback loop described in Chapter 3, i.e., $K'_x = K'_x(t)$. Note, if somehow a very high speed dc power supply existed and were incorporated in such a feedback loop, the power supply would respond to the modulated ac signal producing a dc output at the

anode containing no ellipsometric information.

The DAE automatically takes care of this problem. Since two signals are analyzed simultaneously, the ratio of K_R/K_T remains fixed and eliminates the third independent variable as is seen below,

$$p_k = \frac{I_T^{ac}(k)}{I_R^{ac}(k)} = \gamma_1 \left[\frac{I_S^T s_k + I_C^T c_k}{I_S^R s_k + I_C^R c_k} \right] \quad k=1,2,3, \dots \quad 4.9$$

where $t = t_k = k/f_s$ is written as k , (f_s is the sampling frequency)

$$s_k = \sin(R \sin \omega t_k), \quad 4.10$$

$$c_k = \cos(R \sin \omega t_k) \text{ and} \quad 4.11$$

$$\gamma_1 = K_T/K_R \quad 4.12$$

Equation 4.9 is one equation with two unknowns (ψ, Δ). Hence, it is necessary to sample at two different times, t_k and t_{k+1} , in order to obtain two independent equations. A crucial point to be made here is that it is assumed that ψ and Δ remained constant over the interval $t_{k+1}-t_k$. Note, in this case, the modulation of the polarization of the signal is totally analagous to mechanically adjusting the polarizer or analyzer in a static photometric ellipsometer as explained earlier. Therefore, $t_{k+1}-t_k$ is the resolution time, Δt , of the ellipsometer. The value Δt should be chosen large enough so that significant changes in the modulation of the polarized light have occurred, yet small enough so that ψ and Δ remain essentially constant over that time interval. Unlike dynamic photometric ellipsometers, the resolution of the DAE is not a definite minimum time interval and can be varied for a given set of data to obtain optimal results.

In general, the two linearly independent equations necessary to

calculate ψ and Δ are obtained from equation 4.9 for the k and $k+1$ points, p_k and p_{k+1} . In order to solve these for ψ and Δ , it is necessary at this point to introduce the explicit forms of I_s^x and I_c^x . These depend on the particular arrangement of azimuths for the various optical components in the ellipsometer.

4.2.2. A particular setup

The following was chosen as the setup for the ellipsometer;

1. $M = 45^\circ$
2. $P = 90^\circ$
3. $A_R = 90^\circ$ and $A_T = 45^\circ$
4. $\psi_R = 0^\circ$ and $\psi_T = 45^\circ$ (the principal angle of a dielectric).

Substituting these values into the general equation of the intensity of light at the two PMTs, equations 4.2-4.5, it is found that

$$I_s^R = 0 \quad 4.13$$

$$I_c^R = 2K'^R \sin 2M (1 + \cos 2\psi) \quad 4.14$$

$$I_s^T = K'^T \sin 2\psi \sin \Delta \quad 4.15$$

$$I_c^T = K'^T \cos 2\psi \quad 4.16$$

where K'^x is defined in equation 4.8. Note, the reflected beam only has even harmonic terms, because the beam splitter was placed at its principal angle. This configuration was chosen because it produces an extremely high quality reflected signal, independent of Δ , with an amplitude comparable to that of the transmitted signal. It also provides convenient points, t_k , for sampling as will be discussed shortly.

Substitute the values of I_s^x and I_c^x acquired for the particular setup given above into equation 4.9. Using the two resulting equations when $t = t_k$ and $t = t_{k+1}$, expressions for ψ and Δ are found to be,

$$\psi = \frac{1}{2} \cos^{-1} \left[\frac{p_k c_k s_{k+1} - p_{k+1} c_{k+1} s_k}{[s_k(p_{k+1} c_{k+1} - \gamma_1 c_{k+1}) - s_{k+1}(p_k c_k - \gamma_1 c_k)]} \right] \quad 4.17$$

$$\Delta = \sin^{-1} \left[\frac{p_k c_k + \cos \psi (p_k c_k - \gamma_1 c_k)}{\gamma_1 \sin 2\psi s_k} \right] \quad 4.18$$

where all terms are defined as in equations 4.10-4.12.

5. INTERPRETATION OF ψ AND Δ

In order to interpret ellipsometric data taken when polarized light is refracted from or transmitted by bare or filmed substrates, the electromagnetic theory of light should be used to derive an expression for the complex valued reflection and transmission coefficients in terms of macroscopic optical properties that characterize the particular structure under measurement. Two ideal situations, the bare substrate and the single filmed substrate, will be discussed here. The notation for the complex index of refraction in a homogeneous, isotropic, linear-absorbing medium will be denoted by $N = n - jk$, where n is the index of refraction and k is the extinction coefficient of the medium. The time dependence of all harmonic fields will be chosen to be $e^{j\omega t}$. This is the notation decided on at the 1968 International Conference on Ellipsometry.¹⁸

5.1. The Bare Substrate System

The following discussion is similar to that of Ref 1. Figure 5.1 shows the oblique reflection and transmission of an optical plane wave at the planar interface between two semi-infinite homogeneous optically isotropic media, 0 and 1, with complex indices of refraction N_0 and N_1 . The change in index of refraction is assumed to be abrupt at the interface. Since the media are isotropic, the eigenpolarizations are the linear vibrations parallel (p) and perpendicular (s) to the plane of incidence.

Let (E_{ip}, E_{is}) and (E_{rp}, E_{rs}) represent the complex amplitudes of the

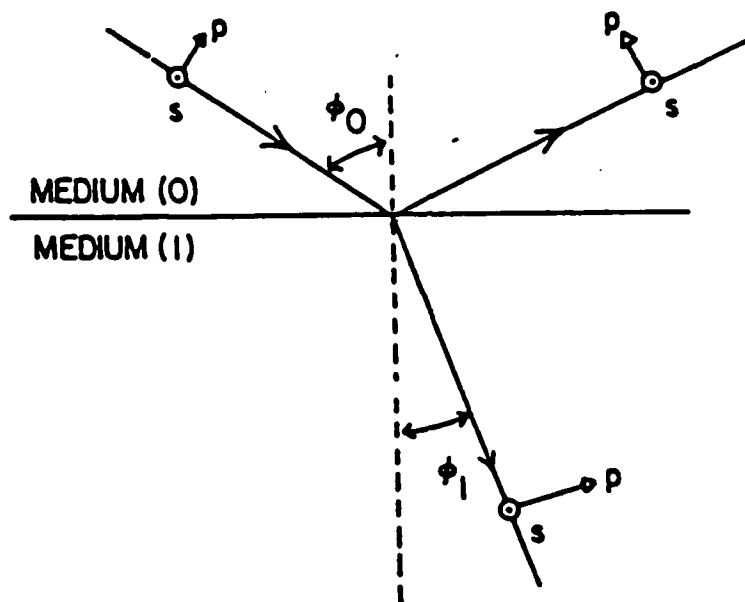


Figure 5.1. Oblique reflection and transmission of a plane wave at the planar interface between two semi-infinite media, 0 and 1. The angles of incidence are ϕ_0 and ϕ_1 , respectively. The axes parallel and perpendicular to plane of incidence are p and s , respectively

components of the electric field vectors of the incident and reflected waves, respectively, at opposite points directly above and below the interface. Matching the tangential E and H fields across the interface yields

$$\frac{E_{rp}}{E_{ip}} = r_p = \frac{N_1 \cos \phi_0 - N_0 \cos \phi_1}{N_1 \cos \phi_0 + N_0 \cos \phi_1} \quad 5.1$$

$$\frac{E_{rs}}{E_{ip}} = r_s = \frac{N_0 \cos \phi_0 - N_1 \cos \phi_1}{N_0 \cos \phi_0 + N_1 \cos \phi_1}, \quad 5.2$$

which are the Fresnel complex-amplitude reflection coefficients. Recall from Chapter 1 that reflection ellipsometry is based on measuring ψ and Δ , where

$$\rho = V_{ex}/V_{ey} = \tan \psi e^{i\Delta}. \quad 5.3$$

For a bare substrate, $V_{ex} = r_p$ and $V_{ey} = r_s$. Substituting equations 5.1 and 5.2 into equation 5.3 leads to

$$N_1 = N_0 \tan \phi_0 \left[1 - \frac{4\rho}{(1+\rho)^2} \sin^2 \phi_0 \right]. \quad 5.4$$

Equation 5.4 shows that the complex index of refraction can be determined from one set of ellipsometric parameters (ψ, Δ) if the complex index of refraction of medium 0, N_0 , and the angle of incidence of the light, ϕ_0 are known.

The reflectances, R_p and R_s , are defined as

$$R_p = |r_p|^2 \quad 5.5$$

$$R_s = |r_s|^2. \quad 5.6$$

R_p and R_s give the fraction of the total intensity in the p and the s

directions which is reflected at the interface of the two media.

The following figures obtained from Ref. 1 show the variation of the phase shifts, δ_{rp} and δ_{rs} , the reflectances, R_p and R_s , and the ellipsometric parameters, ψ and Δ , as the angle of incidence, ϕ , is changed. The samples are a dielectric, a semiconductor, and a metal. In all three cases, the wavelength of light, λ , is 5461Å.

5.1.1. Implementation

The Pascal program "Data_analysis" located in Appendix has been written which includes procedures to calculate N_1 , R_p , and R_s based on equation 5.4. In addition, the same program is written in HPL, Hewlett Packard Language, because a Hewlett Packard 9558 calculator was originally used as a controller for the ellipsometer. Inspection of the two programs should reveal the great advantage of record declaration, that a computer language such as Pascal offers, as opposed to non-record languages such as BASIC and HPL. This is one of the overriding reasons Pascal was chosen.

5.2. The Ambient-Film-Substrate System

The figure below illustrates reflection of a plane wave by an ambient(1)-film(1)-substrate(2) system. The film has abrupt parallel-plane boundaries separated by the film thickness, d_1 , and is located between semi-infinite ambient and substrate media. All three media are homogeneous and optically isotropic, with complex indices of refraction N_0 , N_1 , and N_2 , respectively.

The following procedure was originally presented by Drude.¹⁹ A

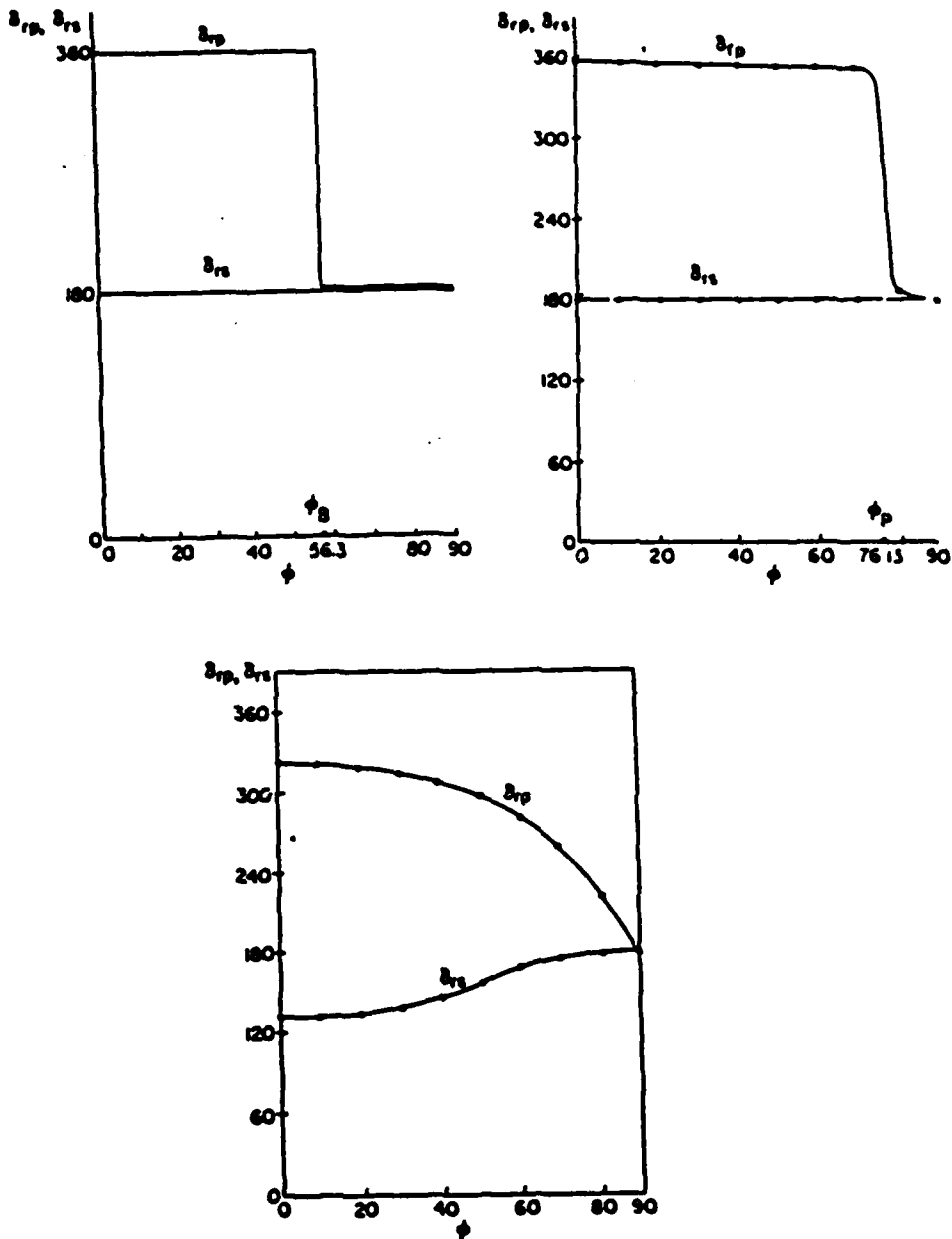


Figure 5.2a. The reflection phase shifts, δ_{rp} and δ_{rs} , for the p and s polarizations as functions of the angle of incidence ϕ (degrees) for an air/glass interface $N_{\text{glass}} = 1.50$ (top), an air/silicon interface $N_{\text{Si}} = 4.05 - j0.028$ (middle), and an air/gold interface $N_{\text{Au}} = 0.35 - j2.45$ (bottom). In all cases $\lambda = 5461 \text{ \AA}$.

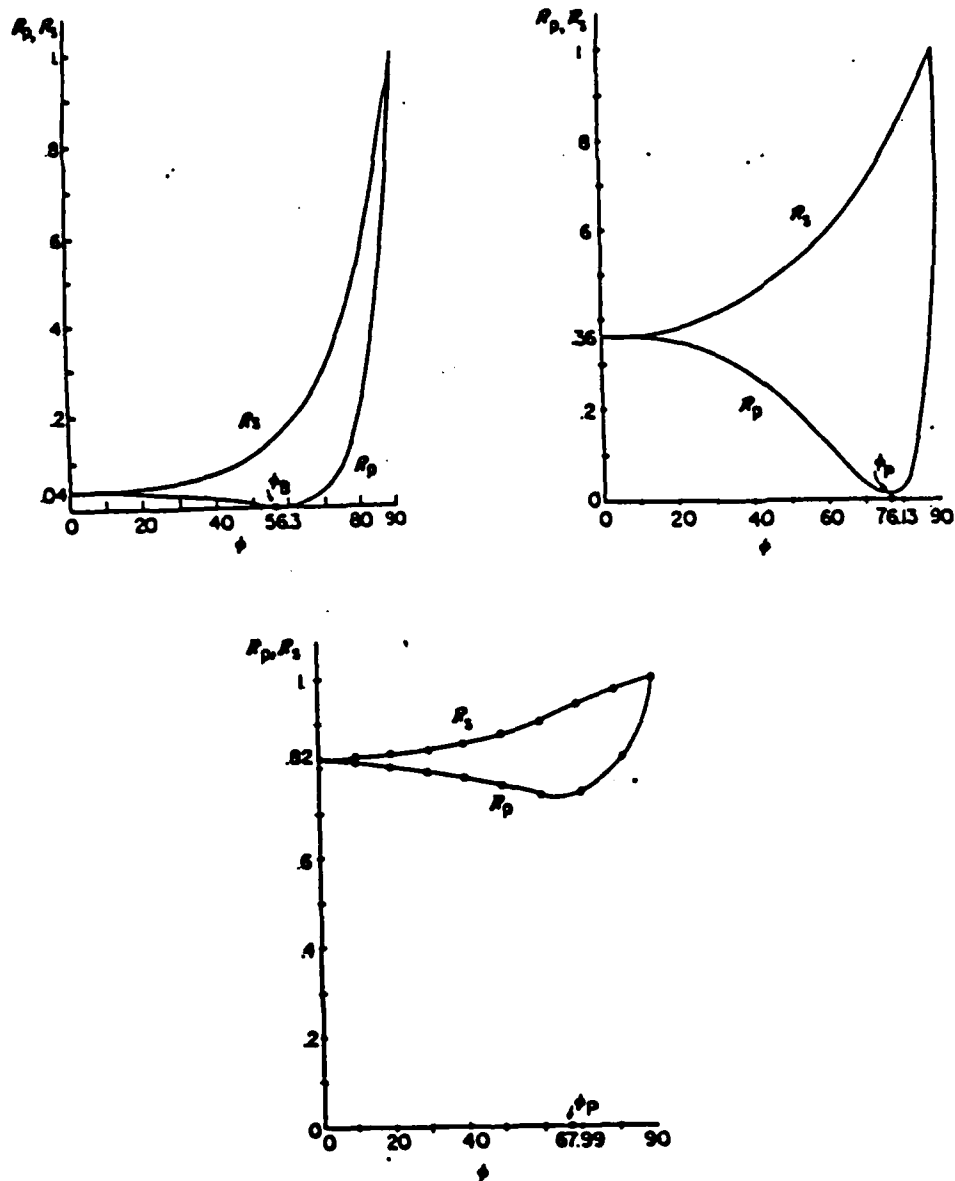


Figure 5.2b. The intensity reflectances, R_p and R_s , for the p and s polarizations as functions of the angle of incidence ϕ (degrees) for an air/glass interface $N_{\text{glass}} = 1.50$ (top), an air/silicon interface $N_{\text{Si}} = 4.05 - j0.028$ (middle), and an air/gold interface $N_{\text{Au}} = 0.35 - j2.45$ (bottom). In all cases $\lambda = 5461\text{\AA}$.

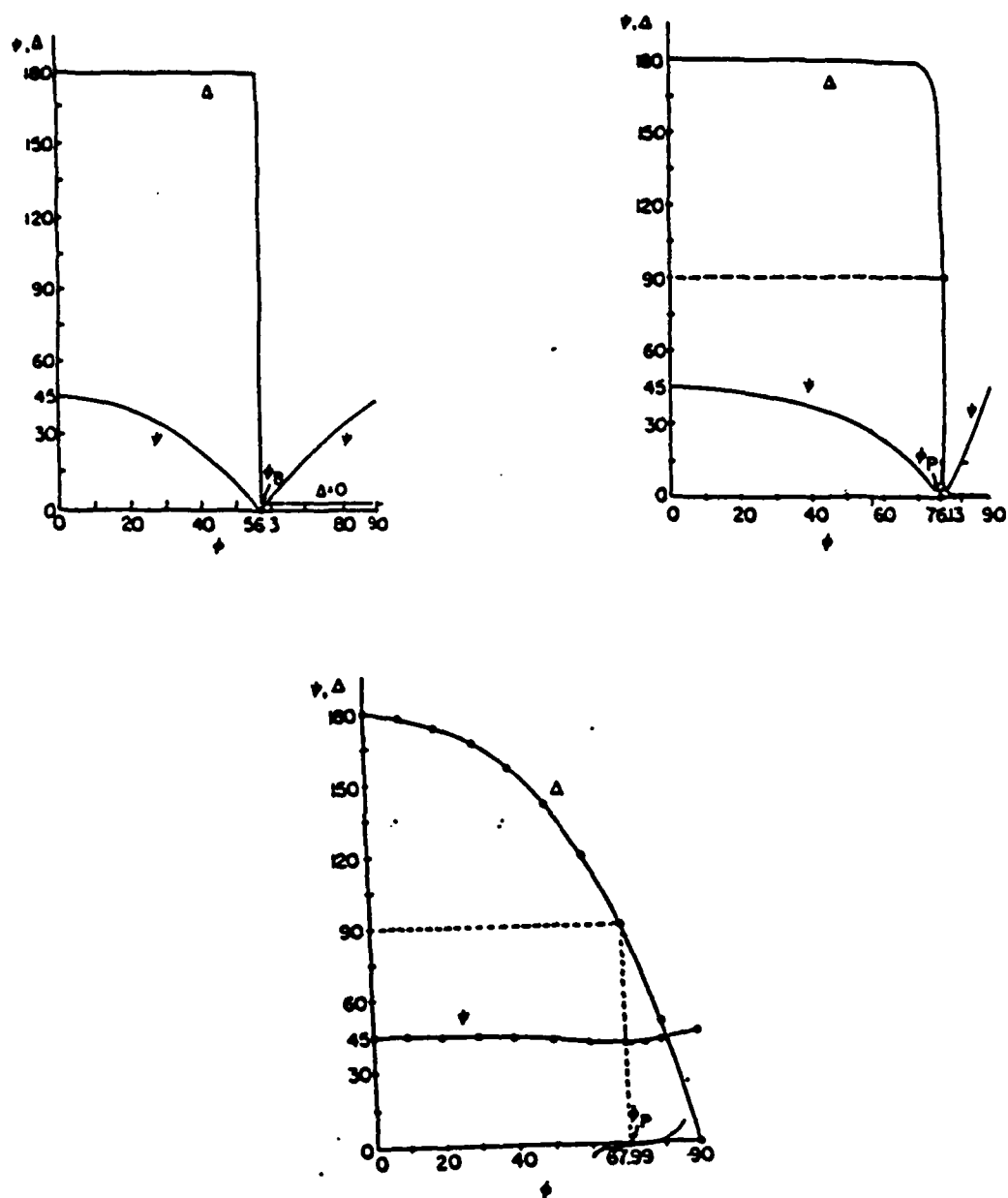


Figure 5.2c. The ellipsometric angles, ψ and Δ , as functions of the angle of incidence ϕ (degrees) for reflection at an air/glass interface $N_{\text{glass}} = 1.50$ (top), an air/silicon interface $N_{\text{Si}} = 4.05 - j0.028$ (middle), an air/gold interface $N_{\text{Au}} = 0.35 - j2.45$ (bottom). In all cases $\lambda = 5461\text{\AA}$.

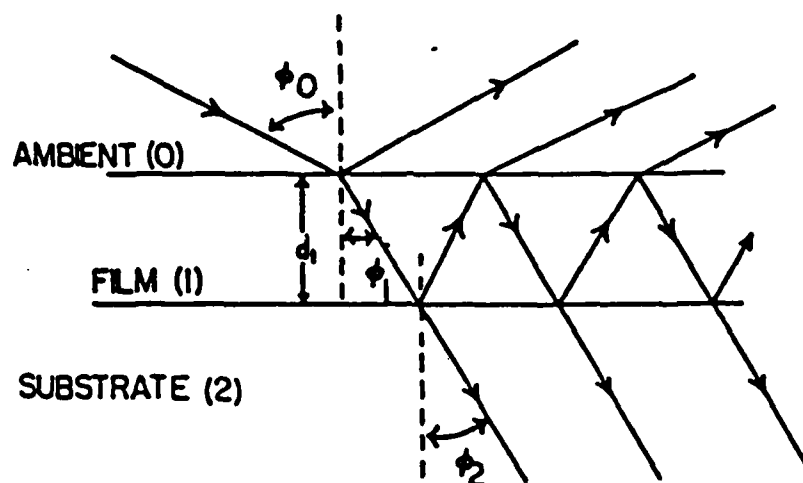


Figure 5.3. Oblique reflection and transmission of a plane wave by an ambient(0)-film(1)-substrate(2) system with parallel-plane boundaries. d_1 is the film thickness. ϕ_0 is the angle of incidence in the ambient and ϕ_1 , ϕ_2 are the angles of refraction in the film and substrate, respectively

plane wave incident at an angle of ϕ_0 on medium 1 will give rise to resultant or "net" reflected and transmitted waves at angles ϕ_1 and ϕ_2 , respectively. The Fresnel reflection and transmission coefficients at the 0-1 and 1-2 interfaces are denoted by r_{01} , t_{01} , r_{12} , and t_{12} , respectively. The complex amplitudes of the successive partial plane waves that make up the resultant reflected wave are

$$r_{01}, t_{01}t_{10}r_{12}e^{-j2\beta}, t_{01}t_{10}r_{10}r_{12}^2e^{-j4\beta}, \dots$$

where

$$\beta = (2\pi d_1/\lambda)N_1\cos\phi_1 \quad 5.7$$

and

λ is the vacuum wavelength,

d_1 is the film thickness,

N_1 is the film complex index of refraction and

ϕ_1 is the complex angle of refraction of the film.

Addition of the partial waves leads to an infinite geometric series for the resulting reflected wave of

$$R = r_{01} + t_{01}t_{10}\sum r_{10}^{n-1}r_{12}^ne^{-j2n\beta}, \quad 5.8$$

whose summation gives

$$R = \frac{r_{01} + r_{12}e^{-j2\beta}}{1 + r_{01}r_{12}e^{-j2\beta}}. \quad 5.9$$

Equation 5.9 is valid for a linearly polarized plane wave in any direction. In particular, if the incident wave is polarized in the p or s direction, then

$$R_p = \frac{r_{01p} + r_{12p}e^{-j2\beta}}{1 + r_{01p}r_{12p}e^{-j2\beta}} \quad 5.10$$

$$R_s = \frac{r_{01s} + r_{12s}e^{-j2\beta}}{1 + r_{01s}r_{12s}e^{-j2\beta}} \quad 5.11$$

The Fresnel reflection and transmission coefficients at the 0-1 and 1-2 interfaces that appear in the above equations are

$$r_{j,j+1,p} = \frac{N_{j+1}\cos\phi_j - N_j\cos\phi_{j+1}}{N_{j+1}\cos\phi_j + N_j\cos\phi_{j+1}} \quad 5.12$$

$$r_{j,j+1,s} = \frac{N_j\cos\phi_j - N_{j+1}\cos\phi_{j+1}}{N_j\cos\phi_j + N_{j+1}\cos\phi_{j+1}} \quad 5.13$$

where, $j = 0$ or 1 . The three angles ϕ_0 , ϕ_1 and ϕ_2 are interrelated by Snell's Law

$$N_0\sin\phi_0 = N_1\sin\phi_1 = N_2\sin\phi_2. \quad 5.14$$

Finally, to relate ψ and Δ to the ambient film substrate system above, recall that

$$\rho = R_p/R_s = |R_p|/|R_s| = \tan\psi e^{i\Delta}. \quad 5.15$$

where R_s and R_p are given in equations 5.10 and 5.11, respectively.

When applying the above theory to practical film-substrate systems, the following conditions²⁰ must be met.

1. The lateral dimensions of the film must be many times its thickness so that the infinite summation of partial waves is valid.
2. The light sources bandwidth, beam diameter, and degree of collimation as well as film thickness must be all such that the multiple reflected and transmitted waves combine coherently.
3. The film material must not be amplifying.

These conditions are satisfied in many practical applications of ellipsometry.

Finally, before solving equation 5.15 for the film thickness, it is constructive to examine ρ as a function of thickness. The figure below shows a family of nonintersecting curves called constant angle of incidence contours, CAICs.¹ Each closed curve is for a fixed angle of incidence, ϕ_0 . These were obtained by increasing the film thickness in the equation for ρ . The $\phi_0 = 0^\circ$ and $\phi_0 = 90^\circ$ collapse at the null points $\rho = -1$ and $\rho = 1$, respectively. The curves are for a SiO_2 -Si system at $\lambda = 6328 \text{ \AA}$. As can be seen, the sensitivity of ρ (and therefore, ψ and Δ) to changes in film thickness is extremely dependent on the angle of incidence. In general, the highest sensitivity occurs when ϕ_0 is near ϕ_s , the angle at which the system acts as an s-suppressing reflection polarizer. ϕ_s is about 62° for SiO_2 -Si with $\lambda = 6328 \text{ \AA}$.

5.2.1. Solving for the film thickness

Equation 5.15 shows that $\rho = \rho(N_0, N_1, N_2, d_1, \phi_0, \lambda) = \tan \psi e^{j\Delta}$. If N_0 , N_1 , N_2 , and λ are known, then $\rho = \rho(\phi_0, d_1)$. This allows one to examine ρ as a function of film thickness d for various angles of incidence ϕ_0 . It can be shown¹ that an expression for the thickness, d_1 , in terms of N_0 , N_1 , N_2 , ϕ_0 , λ , ψ and Δ is obtained by inverting equation 5.15. The expression is

$$d_1 = [j(4\pi)^{1/2}(N_1^2 - N_0^2 \sin^2 \phi_0)^{-1/2} \ln X] \lambda, \quad 5.16$$

$$\text{where } X = \frac{-(B - \rho E) \pm [(B - \rho E)^2 - 4(C - \rho F)(A - \rho D)]^{1/2}}{2(C - \rho F)} \quad 5.17$$

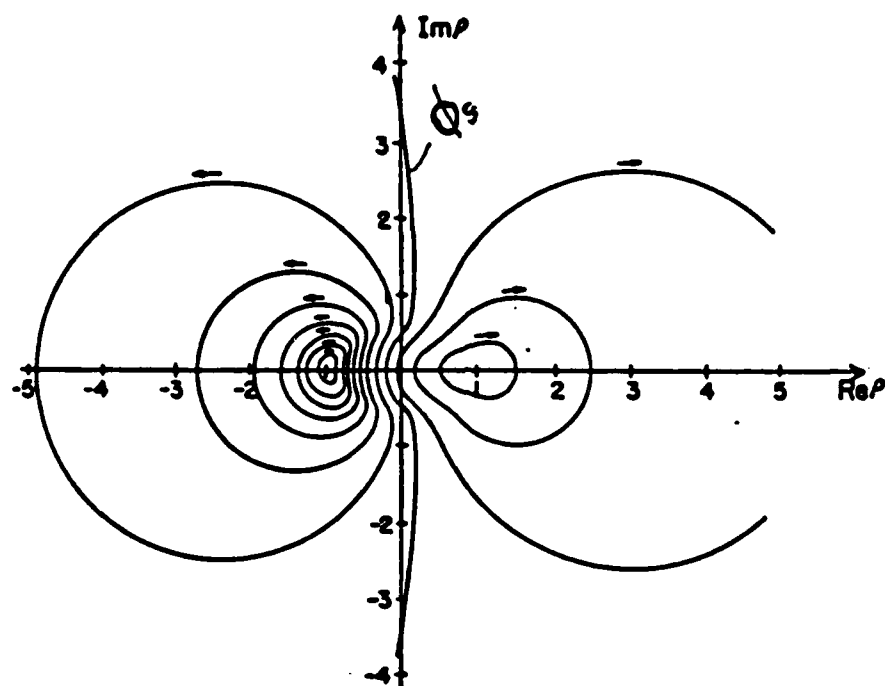


Figure 5.4. Constant-angle-of-incidence contours (CAICs) in the complex ρ -plane for the air-SiO₂ system at $\lambda = 6328\text{\AA}$. The arrows indicate the direction in which the film thickness increases

and

$$A = r_{01p}, \quad B = r_{12p} + r_{01p}r_{01s}r_{12s}, \quad C = r_{12p}r_{01s}r_{12s},$$

$$D = r_{01s}, \quad E = r_{12s} + r_{01p}r_{12p}r_{01s}, \quad F = r_{01p}r_{12p}r_{12s},$$

and the reflection coefficients are given in equations 5.12 and 5.13.

Note, X has two values corresponding to the positive or negative solution of a quadratic. The appropriate root should be chosen such that it leads to a positive real calculated film thickness, d_1 , or in the presence of errors, to a complex value with the smaller imaginary part and non-negative real part. In the latter, the film thickness can be chosen to be the real part and the error is of the order of magnitude of the imaginary part.

Defining D_ϕ , called the film thickness parameter, by

$$D_\phi = (N_1^2 - N_0^2 \sin^2 \phi)^{-1/2}, \quad 5.18$$

it can be seen that, if d_1 is a solution of equation 5.14, then

$$d_1^m = d_1 + mD_\phi \quad m = 0, \pm 1, \pm 2, \dots \quad 5.19$$

is also a solution. Hence, equation 5.15 does not give a unique thickness. The figure below shows a plot of the thickness period, D_ϕ , as a function of the angle of incidence, ϕ_0 . Here, $\lambda = 6328\text{\AA}$, $N_0 = 1$, and $N_1 = 1.46$ (which corresponds to a SiO_2 film). The minimum value of D_ϕ occurs at $\phi = 0^\circ$ ($D_\phi = 2167.13\text{ \AA}$), while the maximum value occurs at $\phi = 90^\circ$ ($D_\phi = 2974.34\text{ \AA}$).

Hence, the indeterminacy of film thickness indicated by equation 5.19 represents no difficulty when the range of film thicknesses is known a priori from other considerations or from additional nonellipsometric (e.g., reflectance) measurements.

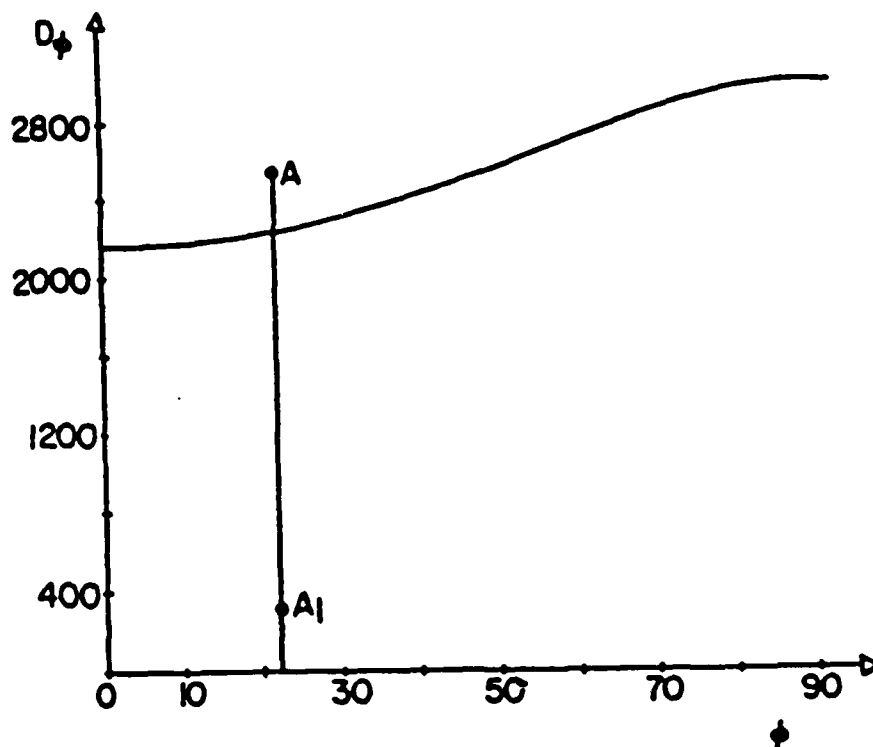


Figure 5.5. Film-thickness period, D_ϕ , in angstroms, when $N_0 = 1$, $N_1 = 1.46$ (SiO_2) and $\lambda = 6328 \text{ Å}$, as a function of the angle of incidence ϕ in degrees. The ellipsometric function ρ has the same value at points A (ϕ, d) and A₁ ($\phi, d - D_\phi$)¹

5.2.2. Implementation

The program located in Appendix E contains an option to solve equations 5.16 and 5.17. Extensive use of the complex number module "complexmath" was made. The program calculates the thickness, d_1 , as well as the thickness period, D_ϕ , for any λ , N_0 , N_1 , N_2 , and ϕ .

ACKNOWLEDGEMENTS

I would like to thank Professor Howard Shanks for providing leadership and guidance in my research. Thanks also go to the other committee members for their participation. They are Dr. Stan Burns and Dr. Bruce Harmon. I would also like to thank Mark Albers, Andy Burkland, and Rich Ketcham for many interesting discussions. Finally, special thanks go to my wife, Raz, my parents, and my brothers and sisters, whose support and encouragement helped me through this project.

REFERENCES

1. R. A. M. Azzam and N. M. Bashara, Ellipsometry and Polarized Light (North-Holland, Amsterdam, 1977).
2. M. Born and E. Wolf, Principles of Optics (Pergamon, New York, 1975).
3. H. Takasaki, Appl. Opt. 5, 759 (1966)
4. L. Ord and B. L. Wills, Appl. Opt. 6, 16273 (1967); ref. 1, p. 155.
5. H. J. Mathieu, D. E. McClure, and R. H. Muller, Rev. Sci. Instrum. 45, 798 (1974).
6. T. Yamauchi and H. Hasunuma, Sci. Light (Japan) 16, 64 (1967).
7. Gaertner Scientific Corp., Dual Mode Automatic Ellipsometer L116A User Manual, (Gaertner, Chicago, Il.).
8. R. M. A. Azzam, Opt. Com. 25, 137 (1978).
9. S. N. Jaspersen and S. E. Schnatterly, Rev. Sci. Instrum. 40, 761 (1969).
10. B. Drevillon et. al, Rev. Sci. Instrum. 53(7), 769 (1982).
11. D. L. Redhead, PMTS: A Realistic Look at What's Available, Photonics Spectra, 93 (1986).
12. D. E. Aspnes and A. A. Studna, Rev. Sci. Instrum. 49(3), 291 (1982).
13. Centronic Inc., Photomultipliers, (Centronic House, New Addington, England).
14. Hewlett Packard, DC Power Supply HVB Series Model 6516A Operating and Service Manual, (Hewlett Packard, 1967).
15. C. K. Yuen, and D. Fraser, Digital Spectral Analysis, (CSIRO, East Melbourne, Australia, and Pitman Pub. Ltd., London, 1979).
16. R. V. Churchill and J. W. Brown, Fourier Series and Boundary Value Problems, (McGraw-Hill, Inc., New York, 1978).
17. H. F. Weinberger, A First Course in Partial Differential Equations, (John Wiley & Sons, New York, 1965).

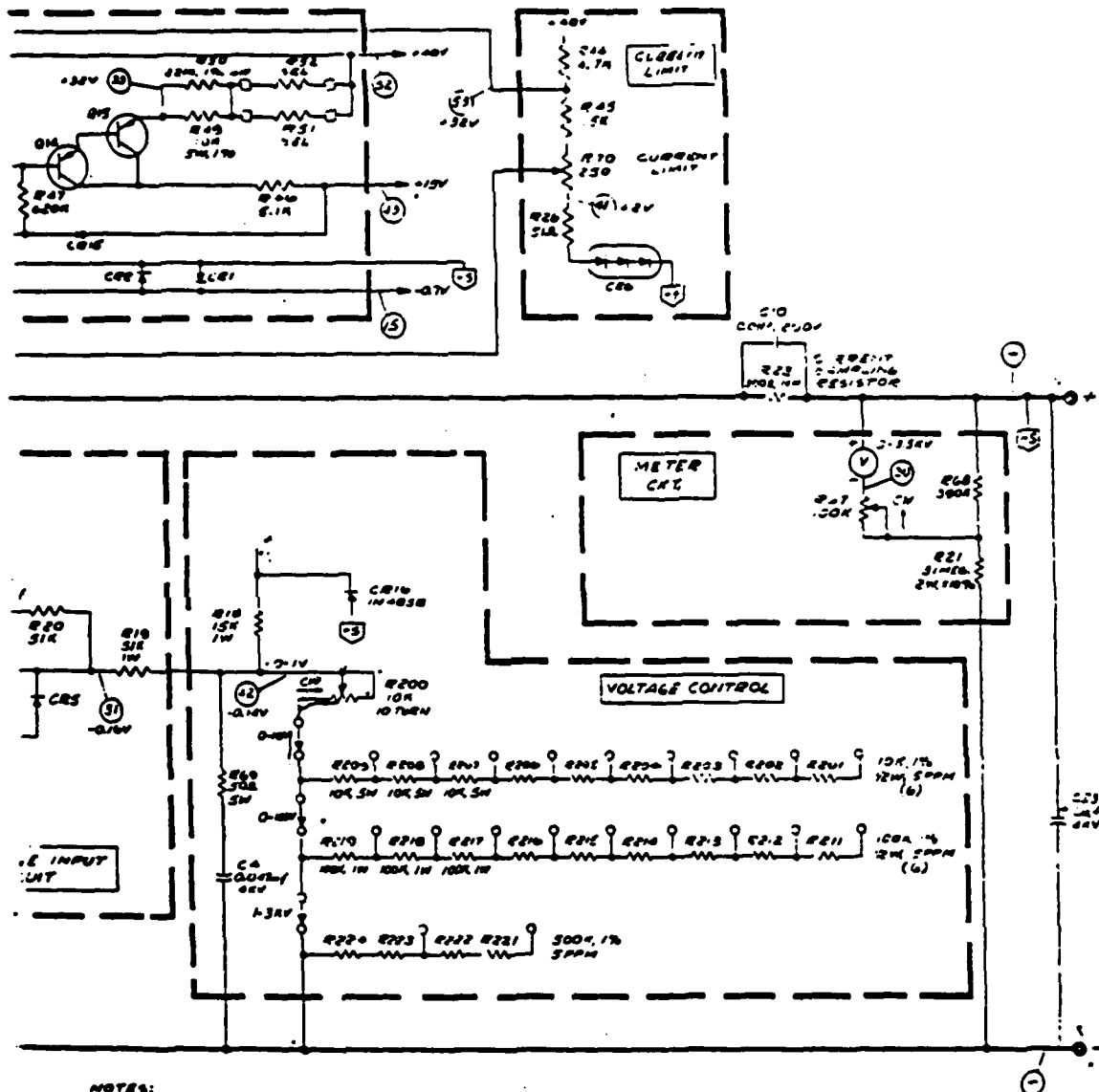
18. N. M. Bashara, A. B. Buckman and A. C. Hall, Eds., Proceedings of the Symposium on Recent Developments in Ellipsometry, (North-Holland, Amsterdam, 1969); Surface Sci. 16, (1969).
19. P. Drude, Ann. Phys. Chem. 39, 481 (1890).
20. O. S. Heavens, Optical Properties of Thin Solid Films, (Dover, New York, 1965).

APPENDIX A.

SCHEMATIC DIAGRAM

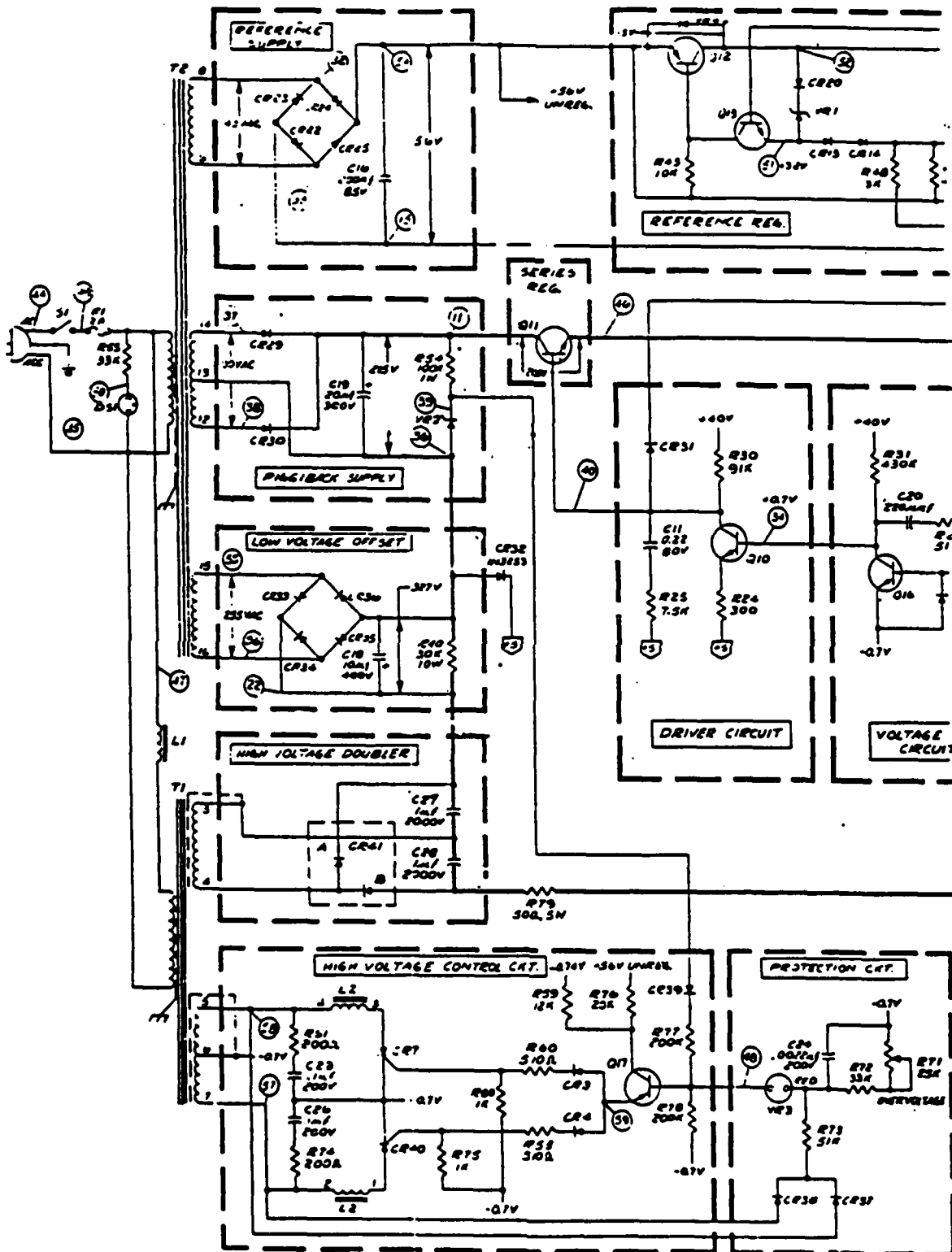
OF THE

6516A POWER SUPPLY



NOTES:

1. ALL RESISTORS ARE 2W 5% UNLESS OTHERWISE NOTED.
2. ALL 10W 10W RESISTORS ARE 1% IN TOLERANCE.
3. ———— DENOTES VOLTAGE FEEDBACK SIGNAL.
4. ———— DENOTES CURRENT FEEDBACK SIGNAL.
5. DC VOLTAGES WERE MEASURED UNDER THE FOLLOWING CONDITIONS:
 - A. SIMON MODEL P-6 IS EQUIVALENT.
 - B. NEGATIVE INPUT.
 - C. VOLTAGES REFERENCED TO -5 UNLESS OTHERWISE NOTED.
 - D. VOLTAGES ARE TYPICAL ±10% UNLESS OTHERWISE NOTED.
 - E. ALL READINGS TAKEN WITH OUTPUT VOLTAGE LIMITED SET TO 500V AND NO LOAD CONNECTED.



APPENDIX B.

PASCAL PROGRAM
THE DATA REDUCTION TESTS

```

program spectral_analysis(input,output);
import complexmath;
const
  pi = 3.141592654;

type
  symarray = array [0..1200] of real;
var
  i,nmax           :integer;
  data             :symarray;
  magc,phase       :symarray;
  option           :string[1];

{-----}
procedure DFT(data:symarray;nmax:integer;var magc,phase:symarray);
const pi = 3.141592654;
var
  j,i,k           :integer;
  num_fourier_pts,num_DFTs :integer;
  tempcos,temp sin,carg,delta_arg :real;
  fudge           :real;
  c               :complex;

begin
  num_DFTs := 1;
  num_fourier_pts := 500;
  delta_arg := 0.0;
  writeln('enter fudge factor ');
  readln(fudge);
  carg := 2*pi/(fudge*nmax);

  for j := 0 to (num_DFTs - 1) do
    begin
      for i := 0 to (nmax div 2) do
        begin
          tempcos := 0.0;
          temp sin := 0.0;

          for k := 0 to (nmax - 1) do
            begin
              tempcos := tempcos + cos(carg*k*i + delta_arg*j)*data[k];
              temp sin := temp sin - sin(carg*k*i + delta_arg*j)*data[k];
            end;

            c.re      := tempcos/nmax;
            c.im      := temp sin/nmax;
            magc[i]   := mag(c);
            phase[i]  := arg(c)*180/pi;

            if abs(magc[i]) < 1E-6 then
              begin
                magc[i] := 0;
                phase[i] := 0;
              end;
            if (i) = 0 then
              begin
                writeln('i = ',i,' magc = ',2*magc[i],' phase = ',phase[i]);
              end;

            if (i) = 0 and (magc[i] < 0) then
              begin

```

```

        writeln('i = ',i,' magc = ',c*magc[i], ' phase = ',phase[i]);
    end;}

    end; {end i loop}

    end; {end j loop}

end; {end DFT procedure}
(-----)
procedure COS_SERIES(nmax:integer;var data:symarray);
const
    pi = 3.141592654;
var
    num_fourier_pts,i,j,k          :integer;
    freq_comp                      :array [0..20] of integer;
    A,phase,carg                   :array [0..20] of real;
begin
    writeln('enter num_fourier_pts');
    readln(num_fourier_pts);
    for j := 0 to (num_fourier_pts - 1) do
        begin
            writeln('enter number of freq component 1 to--',nmax div 2);
            readln(freq_comp[j]);
            writeln('enter amplitude of this component');
            readln(A[j]);
            writeln('enter phase of this component');
            readln(phase[j]);
            phase[j] := phase[j]*pi/180;
        end; {end j loop}

        for k := 0 to (nmax - 1) do
            begin
                data[k] := 0.0;
                for i := 0 to (num_fourier_pts - 1) do
                    begin
                        carg[i] := (2*freq_comp[i]*k*pi/nmax)+phase[i];
                        data[k] := data[k] + A[i]*cos(carg[i]);
                    end;
                end; {end k}
            for k := 0 to (nmax - 1) do
                begin
                    writeln('data ',k,' ',data[k]);
                end;
            end; {end COS_SERIES procedure}
        (-----)

    procedure PMT_OUTPUT(nmax:integer;var data:symarray);
    const
        pi = 3.141592654;
    var
        x,t,Is,Ic,retardation      :real;
        osc_freq,sampl_freq         :real;
        k                           :integer;
        deg_angle                   :real;
        P,M,A,psi,delta             :real;

    function rad(deg_angle:real):real;
    begin
        rad := (deg_angle*pi)/180;
    end;

```

```

begin
  writeln('enter osc_freq and sampling_freq');
  readln(osc_freq,sampl_freq);
  t := 2*pi*osc_freq/sampl_freq;

  writeln('enter Ic and Is');
  readln(Ic,Is);

  retardation := 2.405;

  (writeln('enter psi and del');
  readln(psi,del));

  P := 45;
  A := 45;
  M := 0.0;

  P := rad(P);
  A := rad(A);
  M := rad(M);
  (psi := rad(psi);
  del := rad(del));

  (Is := sin(2*P-2*M)*sin(2*A)*sin(2*psi)*sin(del);
  Ic := sin(2*P-2*M)*(sin(2*M)*(cos(2*psi)-cos(2*A)) +
  cos(2*M)*sin(2*A)*sin(2*psi)*cos(del));

  for k := 0 to (nmax - 1) do
    begin
      x := k*t;
      x := retardation*sin(x);
      data[k] := Ic*cos(x) + Is*sin(x);
      (writeln('data ',k,' ',data[k]));
    end;

end;

(-----)

begin

  writeln('enter nmax ');
  readln(nmax);
  writeln('option 0 -- end program');
  writeln('option 1 -- create & fourier analyze PMT output');
  writeln('option 2 -- create & fourier analyze a sinusoidal series');

  writeln('enter number of option and hit (enter)');
  readln(option);

  if option = chr(48) then
    begin
      halt;
    end
  else if option = chr(49) then
    begin
      PMT_OUTPUT(nmax,data);
      DFT(data,nmax,magc,phase);
    end
  else if option = chr(50) then
    begin
      COS_SERIES(nmax,data);
      DFT(data,nmax,magc,phase);
    end;

```

APPENDIX C.

PASCAL PROGRAM
FOR THE DYNAMIC PHOTOMETRIC
PHOTOACOUSTIC MODULATED ELLIPSOMETER

```

program AUTO_DFT_ELLIPSOMETER(input,output);
import complexmath,
       iodeclarations,
       hpib_0,
       hpib_1,
       hpib_2,
       general_2,
       general_4;

const
  pi                = 3.141592654;
  addr_390ad        = 708;
  addr_scanner      = 709;
  pme_freq          = 50251.3;
  nmax              = 2050;
  lastk             = 25;
  phase_error       = 30;  (this is in deg.)

  (lastk is num of terms in bessell fn expansion)
  (8th term is on the order of 1E-10)

type
  realarray  = array [0..2050] of real;
  mediumarray = array [0..2050] of real;
  shortarray = array [0..20] of real;

var
  i,n,k                :integer;
  sampling_freq,retardation :real;
  retardation1,retardation2 :real;
  dc_offset,dc_check,x  :real;
  data_chi              :realarray;
  magc,phase,dcl,psi    :shortarray;
  j                      :shortarray;
  option                :string[1];
  rpsi,rdcl,RL,HV       :real;
  delay_cnt,pp          :real;

  ----->
function factorial(k:integer):real;
var
  i                :integer;
  temp_factorial   :real;
begin
  temp_factorial := 1;
  if k < 0 then
    begin
      for i:= 1 to k do
        begin
          temp_factorial := i*temp_factorial;
        end;
      end;
    factorial := temp_factorial;
  end;

function J0(x:real):real;
var
  temp J0.term      :real;

```

```

k                                :integer;

begin
  temp_J0 := 0;
  for k := 0 to lastk do
    begin
      term := (exp(2*k*ln(x/2)))/sqr(factorial(k));
      if odd(k) then
        begin
          temp_J0 := temp_J0 - term;
        end
      else
        begin
          temp_J0 := temp_J0 + term;
        end;
      end;
    J0 := temp_J0;
  end;

function J1(x:real):real;
var
  temp_J1,term                    :real;
  k                                :integer;

begin
  temp_J1 := 0;
  for k := 0 to lastk do
    begin
      term := (exp((2*k+1)*ln(x/2)))/(sqr(factorial(k))*(k+1));
      if odd(k) then
        begin
          temp_J1 := temp_J1 - term;
        end
      else
        begin
          temp_J1 := temp_J1 + term;
        end;
      end;
    J1 := temp_J1;
  end;

procedure Jn(n:integer;x:real;var J:shortarray);
var
  i,nmax                            :integer;

begin
  J[0] := J0(x);
  J[1] := J1(x);
  if n < nmax then
    begin
      nmax := n;
    end
  else
    begin
      nmax := 15;
    end;
  for i := 2 to nmax do
    begin
      J[i] := 2*(i-1)*J[i-1]/x - J[i-2];
    end;
  end;

function odd_factorial (x:real):real;
var
  temp,temp1                        :real;

```



```

i                                     :integer;

begin
  if trunc(x) = 0 then
    begin
      odd_factorial := 1;
    end
  else
    begin
      temp1 := 1;
      for i := 1 to trunc(x) do
        begin
          temp := 2*i-1;
          temp1 := temp*temp1;
        end;
        odd_factorial := temp1;
      end;
    end;
end;

function time_delay(n:integer;phase:shortarray):real;
begin
  time_delay := 1 - (phase[n]/2*pi*n);
end;

(-----)
procedure DFT_50(data_ch1:realarray;sampling_freq:real;
var magc,phase:shortarray);

var
  j,i,k,nnmax                                     :integer;
  num_fourier_pts                                :integer;
  tempcos,temp sin,carg                           :real;
  nfudge                                           :real;
  c                                                 :complex;

begin
  num_fourier_pts := 8;
  nfudge := sampling_freq/pme_freq;
  carg := 2*pi/nfudge; {this gives interval btwn fourier coef}
  if (odd(trunc(nfudge))) then {this insures odd num data pts used}
    begin {an odd num of data pts gives best results}
      nnmax := trunc(nfudge);
    end
  else
    begin
      nnmax := trunc(nfudge) + 1;
    end;
  writeln('nnmax =',nnmax);
  for i := 0 to (num_fourier_pts - 1) do
    begin
      tempcos := 0.0;
      temp sin := 0.0;
      for k := 0 to (nnmax - 1) do {here is where odd num of data pts used}
        begin
          tempcos := tempcos + (cos(k*i*carg))*data_ch1[k];
          temp sin := temp sin - (sin(k*i*carg))*data_ch1[k];
        end;

        c.re      := tempcos/nnmax; {dvd by nnmax since that is}
        c.im      := temp sin/nnmax; {num of terms summed in k loop}
                                     {corresponds to division by T (period)}

        if i <> 0 then
          begin

```

```

        magc[i] := 2*mag(c); (for cosine series this is the amp)
        phase[i] := arg(c)*180/pi;
    end
else
    begin
        phase[0] := arg(c)*180/pi;
        magc[0] := mag(c);
    end;
if abs(magc[i]) < 1E-5 then
    begin
        magc[i] := 0;
        phase[i] := 0;
    end;
if abs(phase[i]) < 1E-5 then
    begin
        phase[i] := 0.0;
    end;
if abs(phase[i]-180) < 1E-5 then
    begin
        phase[i] := 180;
    end;

    writeln(' i = ',i,' magc = ',magc[i],' phase = ',phase[i]);
end; {end i loop}
end; {end DFT procedure}

```

<----->

```

procedure INITIALIZE_CH1(var sampling_freq:real);
var
    samp_freqstr, ch1_mode                :string(5);
    input_range_1, delay_count, dc_offset_str :string(5);
begin
    clear(7);

    samp_freqstr := '60E6';
    sampling_freq := 60000000;
    ch1_mode := 'AC';

    {now write this information to 390ad}
    {-----}

    writestring(addr_390ad, 'CLR CH1;CAL;OVER OFF;WRI OFF;REM OFF');
    writestring(addr_390ad, 'ML1 OFF;');

    writestring(addr_390ad, 'VMO CH1;');
    writestring(addr_390ad, 'C2: ');
    writestring(addr_390ad, ch1_mode);
    writestring(addr_390ad, ';');

    writestring(addr_390ad, 'OF1 0;ARM EXT;TMO NOR;TSR EXT;');
    writestring(addr_390ad, 'TB A;');

    writestring(addr_390ad, 'SFA ');
    writestring(addr_390ad, samp_freqstr);
    writestring(addr_390ad, ';');
    writestring(addr_390ad, 'SFB ');
    writestring(addr_390ad, samp_freqstr);
    writestring(addr_390ad, ';');

    writeln('enter input_range');
    readln(input_range_1);

```

```

writestring(addr_390ad,'111 ');
writestring(addr_390ad,input_range_1);
writestring(addr_390ad,'');

dc_offset_str := '0';
dc_offset      := 0;

writestring(addr_390ad,'OF1 ');
writestring(addr_390ad,dc_offset_str);
writestring(addr_390ad,'');

delay_count := '1110';
writestring(addr_390ad,'DLY ');
writestring(addr_390ad,delay_count);
writestring(addr_390ad,'');

end;

procedure TRIG_390AD_CH1(var dc_offset:real);
var
  anything          :string[1];
begin
  dc_offset := 0;
  writeln('hit (ent) to TRIGGER 390ad');
  writeln('type q to HALT program');
  readln(anything);
  if anything = 'q' then halt;

  writestring(addr_390ad,'RES;');

  writestring(addr_390ad,'CLR CH1;');

  writestring(addr_390ad,'DT ON;');

  clear(7);
end;
{-----}

procedure READ_CH1(addr_390ad:integer;dc_offset:real;var data_chi:realarray);
var
  chi_buffer          :buf_info_type;
  i,b1,b2             :integer;
  c0,c1,c2            :char;

  {read data into the buffer}
begin
  iobuffer(chi_buffer,4096);
  buffer_reset(chi_buffer);

  writestring(addr_390ad,'READ CH1;');
  transfer_end(addr_390ad,OVERLAP_FASTEST,to_MEMORY,chi_buffer);
  while buffer_busy(chi_buffer) do
    writeln('transferring chl data');
    clear(7);
    {data is in the buffer}
    dc_offset := dc_offset+5.115;

    i := 1;
    readbuffer (chi_buffer,c0); {sets pointer to correct byte}
    while buffer_data (chi_buffer) > 2 do
      begin
        readbuffer (chi_buffer, c1);
        readbuffer (chi_buffer, c2);
        i := i + 1;
        b1 := ord (c1);

```

```

        b2 := ord (c2);
        data_chi[i] := b1 * 256 + b2 - 512 + abs(dc_offset);
    end;
    (clear(7);
    writestring(addr_390ad,'ARM NOR; TMO NOR; TSR EXT;');
    writestring(addr_390ad,'RES;'));
```

end;

----->

```

procedure RETARDATION_MEASUREMENT(magc:shortarray;
var retardation1,retardation2:real);
var
denom1,denom2          :real;
i                      :integer;
```

```

begin
    for i := 1 to 5 do
        begin
            if magc[i] = 0.0 then
                begin
                    halt;
                end;
            end;
            denom1 := (magc[1] + magc[3])*(magc[2] + magc[4]);
            retardation1 := sqrt(24*(magc[3]*magc[2])/denom1);
            denom2 := (magc[2] + magc[4])*(magc[3] + magc[5]);
            retardation2 := sqrt(48*(magc[3]*magc[4])/denom2);
            writeln('retardation1 = ',retardation1);
            writeln('retardation2 = ',retardation2);
        end;
    end;
```

----->

```

procedure GAIN_CALIBRATION(retardation:real;magc:shortarray);
var
    even_ratio_magc,odd_ratio_magc          :shortarray;
    even_ratio_J,odd_ratio_J,J              :shortarray;
    i,imax,k                                 :integer;
    dc_check                                 :real;
```

```

begin
    imax := 1;
    Jn(10,retardation,J);

    writeln('ampl ratio  ','  '  'bessel fn ratio');
    for i := 0 to imax do
        begin
            even_ratio_magc[i] := magc[2*(i+1)]/magc[2*(i+2)];
            even_ratio_J[i]    := J[2*(i+1)]/J[2*(i+2)];
            odd_ratio_magc[i]  := magc[2*i+1]/magc[2*i+3];
            odd_ratio_J[i]     := J[2*i+1]/J[2*i+3];

            writeln(even_ratio_magc[i],'  ',even_ratio_J[i],'  ',2*(i+1),'/',2*(i+2))
            writeln(odd_ratio_magc[i],'  ',odd_ratio_J[i],'  ',2*i+1,'/',2*i+3)
        end;
    end;
```

----->

```

procedure FOURIER_PSI(retardation:real;magc:shortarray;var psi:real);
var
    temp,tan_2psi,fudge_dc          :real;
    cos_2psi,sin_2psi               :real;
    k                                :integer;
```

```

temp_psi, x                               :real;
J                                           :shortarray;

begin
  Jn(15, retardation, J);
  {writeln('enter temp_psi');
  readln(temp_psi);
  temp_psi := pi*temp_psi/180;}
  x := sqrt(sqr(magc[1]/(2*J[1])) + sqr(magc[2]/(2*J[2])));
  {fudge_dc := x/sin(2*temp_psi);}

  {writeln('fudge_dc = ', fudge_dc);}
  fudge_dc := 404.085;

sin_2psi := (sqrt(sqr(magc[1]/(2*J[1])) + sqr(magc[2]/(2*J[2]))))/fudge_dc;
cos_2psi := sqrt(abs(1-sqr(sin_2psi)));

tan_2psi := sin_2psi/cos_2psi;
psi := (arctan(tan_2psi)*180/pi)/2;

  writeln('psi = ', psi);
end;

procedure FOURIER_DEL(retardation:real;magc:shortarray;var del:real);
var
  psi, tan_del                               :real;
  sin_del, cos_del, tan_2psi                 :real;
  J                                           :shortarray;

begin
  Jn(15, retardation, J);
  tan_del := magc[1]*J[2]/(magc[2]*J[1]);
  del := arctan(tan_del);
  if abs(phase[2]-180) < 90 then
    begin
      del := 180 - del;
    end;
  del := 180*del/pi;
  writeln('del = ', del);
end;

{-----}

begin
  INITIALIZE_CH1(sampling_freq);
  for i := 1 to 1000 do
    begin
      TRIG_390AD_CH1(dc_offset);
      READ_CH1(addr_390ad, dc_offset, data_ch1);
      DFT_50(data_ch1, sampling_freq, magc, phase);
      RETARDATION_MEASUREMENT(magc, retardation1, retardation2);
      retardation := 2.4048;
      GAIN_CALIBRATION(retardation, magc);
      FOURIER_PSI(retardation, magc, rpsi);
      FOURIER_DEL(retardation, magc, rdel);
      writeln('pme_freq = ', pme_freq);
    end;
  end;
  {end for loop}

```

APPENDIX D.

PASCAL PROGRAM
FOR THE STATIC PHOTOMETRIC
DUAL ANALYZER
PHOTOACOUSTIC MODULATED ELLIPSOMETER

```

program DAE(input, output);
import complexmath,
       iodeclarations,
       hpib_0,
       hpib_1,
       hpib_2,
       general_2,
       general_4;

const
    pi                = 3.141592654;
    addr_390ad        = 708;
    addr_scanner       = 709;
    pme_freq           = 50376.0;
    nmax               = 2050;
    lastk              = 25;
    phase_error        = 30; {this is in deg.}

    {lastk is num of terms in bessell fn expansion}
    {8th term is on the order of 1E-10}

type
    realarray = array [0..1100] of real;
    mediumarray = array [0..1100] of real;
    shortarray = array [0..20] of real;
    buf         = buf_info_type;

var
    i, n, k                : integer;
    sampling_freq, retardation : real;
    retardation1, retardation2 : real;
    dc_offset, dc_check, x  : real;
    data_ch1, data_ch2      : realarray;
    magc, phase, del, psi   : shortarray;
    j                        : shortarray;
    option                  : string[1];

{-----}
function pp_retardation(peak_to_peak:real):real;

begin
    pp_retardation := 5.1356 - (504-peak_to_peak)/97.3478
end;

function factorial(k:integer):real;
var
    i                : integer;
    temp_factorial   : real;

begin
    temp_factorial := 1;
    if k () 0 then
        begin
            for i:= 1 to k do
                begin
                    temp_factorial := i*temp_factorial;
                end;
            end;
            factorial := temp_factorial;
        end;
end;

```

```

function J0(x:real):real;
var
  temp_J0, term      :real;
  k                  :integer;

begin
  temp_J0 := 0;
  for k := 0 to lastk do
    begin
      term := (exp(2*k*ln(x/2)))/sqr(factorial(k));
      if odd(k) then
        begin
          temp_J0 := temp_J0 - term;
        end
      else
        begin
          temp_J0 := temp_J0 + term;
        end;
      end;
    J0 := temp_J0;
  end;

function J1(x:real):real;
var
  temp_J1, term      :real;
  k                  :integer;

begin
  temp_J1 := 0;
  for k := 0 to lastk do
    begin
      term := (exp((2*k+1)*ln(x/2)))/(sqr(factorial(k))*(k+1));
      if odd(k) then
        begin
          temp_J1 := temp_J1 - term;
        end
      else
        begin
          temp_J1 := temp_J1 + term;
        end;
      end;
    J1 := temp_J1;
  end;

procedure Jn(n:integer; x:real; var J:shortarray);
var
  i, nmax            :integer;

begin
  J[0] := J0(x);
  J[1] := J1(x);
  if n < nmax then
    begin
      nmax := n;
    end
  else
    begin
      nmax := 15;
    end;
  for i := 2 to nmax do
    begin
      J[i] := 2*(i-1)*J[i-1]/x - J[i-2];
    end;
  end;
end;

```



```

function odd_factorial (x:real):real;
var
  temp,temp1      :real;
  i               :integer;

begin
  if trunc(x) = 0 then
    begin
      odd_factorial := 1;
    end
  else
    begin
      temp1 := 1;
      for i := 1 to trunc(x) do
        begin
          temp := 2*i-1;
          temp1 := temp*temp1;
        end;
      odd_factorial := temp1;
    end;
  end;

function arcsin(x:real):real;
var
  temp,temp1      :real;
  i               :integer;

begin
  if x >= 1 then
    begin
      arcsin := 90;
    end
  else if x <= -1 then
    begin
      arcsin := 270;
    end
  else
    begin
      temp1 := 0;
      for i := 2 to 100 do
        begin
          temp := exp((2*i-1)*ln(abs(x)));
          temp := odd_factorial(i-1)*temp/(2*i-1);
          temp := temp/(2*factorial(i-1));
          temp1 := temp + temp1;
          if i = 40 then writeln('temp = ',temp);
        end;
      temp1 := temp1 + x;
      arcsin := 180*temp1/pi;
    end;
  end;

{-----}
procedure DFT_50(data_chi:realarray;sampling_freq:real;
var magc,phase:shortarray);

var
  j,i,k,nnmax      :integer;
  num_fourier_pts  :integer;
  tempcos,temp sin,carg :real;
  nfudge           :real;
  c                :complex;

begin

```

```

num_fourier_pts := 3;
nfudge := sampling_freq/pme_freq;
carg := 2*pi/nfudge; {this gives interval btwn fourier coef}
if (odd(trunc(nfudge))) then {this insures odd num data pts used}
begin {an odd num of data pts gives best results}
  nnmax := trunc(nfudge);
end
else
begin
  nnmax := trunc(nfudge) + 1;
end;

for i := 0 to (num_fourier_pts - 1) do
begin
  tempcos := 0.0;
  tempsin := 0.2;

  for k := 0 to (nnmax - 1) do {here is where odd num of data pts used}
  begin
    tempcos := tempcos + (cos(k*i*carg))*data_chi[k];
    tempsin := tempsin - (sin(k*i*carg))*data_chi[k];
  end;

  c.re := tempcos/nnmax; {dvd by nnmax since that is}
  c.im := tempsin/nnmax; {num of terms summed in k loop}
                                {corresponds to division by T (period)}

  if i < 0 then
  begin
    magc[i] := 2*mag(c); {for cos series this is the amp}
    phase[i] := arg(c)*180/pi;
  end
  else
  begin
    phase[0] := arg(c)*180/pi;
    magc[0] := mag(c);
  end;

  if abs(magc[i]) < 1E-5 then
  begin
    magc[i] := 0;
    phase[i] := 0;
  end;
  if abs(phase[i]) < 1E-5 then
  begin
    phase[i] := 0.0;
  end;
  if abs(phase[i]-180) < 1E-5 then
  begin
    phase[i] := 180;
  end;

  writeln(' i = ',i, ' magc = ',magc[i], ' phase = ',phase[i]);
end; {end i loop}
end; {end DFT procedure}

```

←—————→

```

procedure INITIALIZE(var sampling_freq,retardation:real);
var
  samp_freqstr,chi_mode,ch2_mode      :string[7];
  input_range_1,input_range_2        :string[7];
  pp                                   :real;

begin
  clear(7);

  writeln('possible choices for sampling freq are :');

```

```

writeln('5,10,20,50,100,200,500,1E3');
writeln('2E3,5E3,10E3,20E3,50E3,100E3');
writeln('200E3,500E3,1E6,2E6,5E6,10E6');
writeln('20E6,30E6');
writeln('ENTER samp_freqstr');
readln(samp_freqstr);
writeln('enter sampling_freq');
readln(sampling_freq);
writeln('ENTER input_range_1 IN VOLTS');
readln(input_range_1);
writeln('ENTER input_range_2');
readln(input_range_2);

{now write this information to 390ad}
{-----}

writestring(addr_390ad,'CLR CH1;CLR CH2;CAL;OVER OFF;WRI OFF;REM OFF');
writestring(addr_390ad,'ML1 OFF;ML2 OFF');
writestring(addr_390ad,'CP1 AC;CP2 AC');

writestring(addr_390ad,'VMO DUA;');

writestring(addr_390ad,'IR1 ');
writestring(addr_390ad,input_range_1);
writestring(addr_390ad,';');

writestring(addr_390ad,'IR2 ');
writestring(addr_390ad,input_range_2);
writestring(addr_390ad,';');

writestring(addr_390ad,'OF1 0;ARM EXT;TMO NOR;TSR EXT;');
writestring(addr_390ad,'TB A;');

writestring(addr_390ad,'SFA ');
writestring(addr_390ad,samp_freqstr);
writestring(addr_390ad,';');
writestring(addr_390ad,'SFB ');
writestring(addr_390ad,samp_freqstr);
writestring(addr_390ad,';');

writeln('enter peak to peak retardation');
readln(pp);
retardation := pp_retardation(pp);
writeln('the retardation is ',retardation);

end;

procedure TRIG_390AD;
var
  anything           :string[1];
  delay_count       :string[7];
begin
  {at this pt the 390ad is ready to be triggered}
  writeln('enter delay count');
  readln(delay_count);
  writestring(addr_390ad,'DLY ');
  writestring(addr_390ad,delay_count);
  writestring(addr_390ad,';');

  writeln('hit (ent) to TRIGGER 390ad');
  writeln('type q to HALT program');
  readln(anything);
  if anything = 'q' then halt;

  writestring(addr_390ad,'SES;');

```

```

        writestring(addr_390ad,'CLR CH1;');
        writestring(addr_390ad,'DT ON;');
        clear(7);
    end;
    {-----}

    procedure READ_1(addr_390ad:integer;var data_ch1:realarray);
    var
        buffer_ch1           :buf;
        i,b1,b2              :integer;
        c0,c1,c2             :char;

        {read data into the buffer}
    begin
        iobuffer(buffer_ch1,2100);
        buffer_reset(buffer_ch1);

        writestring(addr_390ad,'READ CH1;');

        transfer_end(addr_390ad,OVERLAP_FASTEST,TO_MEMORY,buffer_ch1);
        while buffer_busy(buffer_ch1) do
            begin
                writeln('transferring data1');
            end;

            {data is in the buffer}

            i := 1;
            readbuffer (buffer_ch1,c0); {sets pointer to correct byte}
            while buffer_data (buffer_ch1) > 2 do
                begin
                    readbuffer (buffer_ch1, c1);
                    readbuffer (buffer_ch1, c2);
                    i := i + 1;
                    b1 := ord (c1);
                    b2 := ord (c2);
                    data_ch1[i] := b1*256 + b2 - 512;
                end;
            end;

        procedure READ_2(addr_390ad:integer;var data_ch2:realarray);
        var
            buffer_ch2           :buf;
            i,b1,b2              :integer;
            c0,c1,c2             :char;

            {read data into buffer}
        begin
            iobuffer(buffer_ch2,2100);
            buffer_reset(buffer_ch2);

            writestring(addr_390ad,'READ CH2;');

            transfer_end(addr_390ad,OVERLAP_FASTEST,TO_MEMORY,buffer_ch2);
            while buffer_busy(buffer_ch2) do
                begin
                    writeln('transferring data2');
                end;
            end;
            clear(7);

            {data is in buffer}

```

```

i := 1;
readbuffer(buffer_ch2,c0);
while buffer_data(buffer_ch2) > 2 do
begin
  readbuffer (buffer_ch2,c1);
  readbuffer (buffer_ch2,c2);
  i := i + 1;
  b1 := ord(c1);
  b2 := ord(c2);
  data_ch2[i] := b1*256 + b2 - 512;
end;
end;

```

----->

```

procedure RETARDATION_MEASUREMENT (magc:shortarray;
var retardation1,retardation2:real);
var
denom1,denom2
i
:real;
:integer;

```

```

begin
  for i := 1 to 5 do
  begin
    if magc[i] = 0.0 then
    begin
      halt;
    end;
  end;
  denom1 := (magc[1] + magc[3])*(magc[2] + magc[4]);
  retardation1 := sqrt(24*(magc[3]*magc[2])/denom1);
  denom2 := (magc[2] + magc[4])*(magc[3] + magc[5]);
  retardation2 := sqrt(48*(magc[3]*magc[4])/denom2);
  writeln('retardation1 = ',retardation1);
  writeln('retardation2 = ',retardation2);
end;

```

```

(procedure COMPARE(data_ch1,data_ch2:intarray);
var
bigsum,i,sum
:integer;

```

```

begin
  bigsum := 0;
  for i := 1 to 2048 do
  begin
    sum := data_ch1[i] - data_ch2[i];
    bigsum := sum + bigsum;
    writeln('CH1 - CH2 = ',sum);
  end;
  writeln('bigsum = ',bigsum);
end;

```

```

IF num_of_runs mod 2 = 1 then
begin
  rewrite(ch1_ref);
  for i := 1 to 2048 do
    WRITE(ch1_ref,data_ch1[i]);
  end;

```

```

IF num_of_runs mod 2 = 0 then
begin
  reset(ch1_ref);
  tot_diff := 0;
  for i := 1 to 2048 do
    begin

```

```

        read(ch1_ref, ref1);
        diff := abs(data_ch1[i] - ref1);
        writeln('THE DIFFERENCE IS ', diff);
        tot_diff := diff + tot_diff;
    end;
    writeln('THE TOT DIFF IS ', tot_diff);

end;}

(-----)
procedure AVE_DATA_12(data_ch1:realarray;var data_ave_ch1:realarray);
var
    i,j,k                                     :integer;
    samples_per_pt,total_num_of_pts         :integer;
    y,x1                                     :real;

begin
    {average the pts here}
    writeln('enter number of pts to be averaged into 1');
    readln(samples_per_pt);
    y := 2048/samples_per_pt;
    total_num_of_pts := trunc(y);

    writeln('total number of pts is',total_num_of_pts);

    for j := 1 to total_num_of_pts do
        begin
            x1 :=0;

            for i := 1 to samples_per_pt do
                begin
                    k := samples_per_pt*(j-1) +i;
                    x1 := x1 + data_ch1[k];
                end;
            data_ave_ch1[j] := x1/samples_per_pt;
            writeln(j,' CH1 ',data_ave_ch1[j]);

        end; {end j loop}
    end; {end procedure AVE_PTS}

    procedure GAIN_CALIBRATION(retardation:real;magc:shortarray);
    var
        even_ratio_magc,odd_ratio_magc       :shortarray;
        even_ratio_J,odd_ratio_J,J           :shortarray;
        i,imax,k                             :integer;
        dc_check                             :real;

    begin
        imax := 2;
        Jn(10,retardation,J);
        writeln('dc components ','fourier components');
        for k := 0 to imax do
            begin
                dc_check :=(sqr(magc[2*k+1]/J[2*k+1])+sqr(magc[2*(k+1)]/J[2*(k+1)]))/4;
                writeln(sqr(magc[0]),' ',dc_check);
            end;
        writeln('ampl ratio ','bessel fn ratio');
        for i := 0 to imax do
            begin
                even_ratio_magc[i] := magc[2*i]/magc[2*(i+1)];
                even_ratio_J[i] := J[2*i]/J[2*(i+1)];
                odd_ratio_magc[i] := magc[2*i+1]/magc[2*i+3];
                odd_ratio_J[i] := J[2*i+1]/J[2*i+3];
            end;
        end;
    end;
end;

```

```

      writeln(even_ratio_magc[i], ' ', even_ratio_j[i], ' ', 2*i, ' / ', 2*(i+1));
      writeln(odd_ratio_magc[i], ' ', odd_ratio_j[i], ' ', 2*i+1, ' / ', 2*(i+3));
    end;
  end;

procedure DAE_PSI(data_ch1:realarray;data_ch2:realarray;retardation:real;
                  sampling_freq:real);
var
  gamma,arg,delta1,delta2                :real;
  b_ratio1,b_ratio2,ratio1,ratio2        :real;
  num_cos_2psi,den_cos_2psi,psi           :real;
  delta_gamma,delta_arg,ddelta_arg,ggamma,temp :real;
  sin_2psi,cos_2psi,sin_del,cos_del,dell  :real;
  k,i,j,start,sstart,max_int             :integer;
  option                                  :char;

begin
  start := 0;
  for k := start to 500 do
    begin
      if (data_ch2[2*k] < 0) and (data_ch2[2*k+1] < 0) then
        begin
          ratio1 := data_ch1[2*k]/data_ch2[2*k];      {this is pk}
          ratio2 := data_ch1[2*k+1]/data_ch2[2*k+1];  {this is pk+1}

          arg := 2*pi*pme_freq/sampling_freq;

          delta1 := retardation*sin(arg*2*k);
          delta2 := retardation*sin(arg*(2*k+1));

          b_ratio1 := cos(delta1)/sin(delta1);
          b_ratio2 := cos(delta2)/sin(delta2);

          num_cos_2psi := -(ratio1*b_ratio1 - ratio2*b_ratio2);
          den_cos_2psi := b_ratio2*(ratio2-gamma) - b_ratio1*(ratio1-gamma);
          cos_2psi := num_cos_2psi/den_cos_2psi;

          sin_2psi := sqrt(1-sqr(cos_2psi));
          psi := (arctan(sin_2psi/cos_2psi))/2;
          sin_del := data_ch1[2*k]*cos(2*psi)/(sin(2*psi)*data_ch2[2*k]);
          cos_del := sqrt(1-sqr(sin_del));
          dell := arctan(sin_del/cos_del);
          dell := 180*dell/pi;
          psi := 180*psi/pi;
          writeln(' psi = ',psi,' del = ',dell);
          if k > j then
            begin
              j := 20 + j;
              readln;
            end;
          end; {end if condition}
        end; {end for k loop}
      end;
    }-----}

  begin
    for i := 1 to 500 do
      begin
        INITIALIZE(sampling_freq,retardation);
        TRIG_390AD;
        READ_1(addr_390ad,data_ch1);
        READ_2(addr_390ad,data_ch2);
        DAE_PSI(data_ch1,data_ch2,retardation,sampling_freq);
      end;
    end;
  end;
end;

```

APPENDIX E.

PASCAL PROGRAM
FOR THE INTERPRETATION OF Ψ AND Δ


```

program film (input,output);
import complexmath;

var
  i                      :integer;
  option                 :string[1];

function cxcos (a:complex): complex;
var tempcnum :complex;
begin
  tempcnum := mul(a,a);
  tempcnum := scmul(-1,tempcnum);
  tempcnum := add(one,tempcnum);
  cxcos := sq_rt(tempcnum);
end;

function rp (a,b,c,d:complex): complex;
var cnumtemp      :array [1..5] of complex;
begin
  cnumtemp[1] := mul(c,b);
  cnumtemp[2] := mul(a,d);
  cnumtemp[3] := scmul(-1,cnumtemp[2]);
  cnumtemp[4] := add(cnumtemp[1],cnumtemp[3]);
  cnumtemp[5] := add(cnumtemp[1],cnumtemp[2]);
  rp      := dvd(cnumtemp[4],cnumtemp[5]);
end;

function rs (a,b,c,d:complex): complex;
var cnumtemp      :array [1..5] of complex;
begin
  cnumtemp[1] := mul(a,b);
  cnumtemp[2] := mul(c,d);
  cnumtemp[3] := scmul(-1,cnumtemp[2]);
  cnumtemp[4] := add(cnumtemp[1],cnumtemp[3]);
  cnumtemp[5] := add(cnumtemp[1],cnumtemp[2]);
  rs      := dvd(cnumtemp[4],cnumtemp[5]);
end;

{-----}
procedure ABCDEF(n0,n1,n2:complex;phi0:real;var A,B,C,D,E,F:complex);
var
  cxsin0,cxsin1,cxsin2      :complex;
  cxcos0,ccos1,ccos2      :complex;
  r0ip,r12p,r0is,r12s      :complex;
  tempB,tempC,tempE,tempF   :complex;
  i                          :integer;

begin
  cxsin0 := scmul(sin(phi0),n0);
  cxsin1 := dvd(cxsin0,n1);
  cxsin2 := dvd(cxsin0,n2);
  cxcos0 := cxcos(cxsin0);
  cxcos1 := cxcos(cxsin1);
  cxcos2 := cxcos(cxsin2);

  r0ip := rp(n0,cxcos0,n1,cxcos1);
  r12p := rp(n1,cxcos1,n2,cxcos2);
  r0is := rs(n0,cxcos0,r1,cxcos1);

```

```

r12s := rs(n1,cxcos1,n2,cxcos2);

A := add(zero,r0:p);
tempB := mul(r01p,r01s);
tempB := mul(r12s,tempB);
B := add(r12p,tempB);
tempC := mul(r12p,r01s);
C := mul(r12s,tempC);
D := add(zero,r01s);
tempE := mul(r01p,r12p);
tempE := mul(r01s,tempE);
E := add(r12s,tempE);
tempF := mul(r01p,r12p);
F := mul(r12s,tempF);
end;

{-----}
function Dphi(a,b:real;c,d:complex): complex;
var tempcnum :array [1..8] of complex;
begin
  tempcnum[1] := scmul(sin(a),c);
  tempcnum[2] := mul(tempcnum[1],tempcnum[1]);
  tempcnum[3] := scmul(-1,tempcnum[2]);
  tempcnum[4] := mul(d,d);
  tempcnum[5] := add(tempcnum[3],tempcnum[4]);
  tempcnum[6] := dvd(one,tempcnum[5]);
  tempcnum[7] := sq_rt(tempcnum[6]);
  Dphi := scmul(b/2,tempcnum[7]);
end;

{-----}
function XX(a:complex;b:real): complex; {a=dphi_lambda,b=thickness}
const pi = 3.141592654;
var
  tempcnum,cxarg :complex;
begin
  tempcnum.re := 0.0;
  tempcnum.im := -2*pi*b;
  cxarg := dvd(tempcnum,a);
  XX.re := (exp(cxarg.re))*cos(cxarg.im);
  XX.im := (exp(cxarg.re))*sin(cxarg.im);
end;

{-----}
function altarg(a:complex):real;
const pi = 3.14159265;
begin
  if arg(a) > pi then
    begin
      altarg := -abs(2*pi - arg(a));
    end
  else if arg(a) <= pi then
    begin
      altarg := arg(a);
    end;
end;

{-----}

procedure FILM_PSI_DEL;
const
  pi = 3.141592654;

var
  psi,del,phi0,lambda,thickness :real;
  x,n0,n1,n2,dphi_lambda :complex;
  A,B,C,D,E,F :complex;
  row :complex;
  tempcnum :array [1..8] of complex;

```

```

begin
  (writeln('enter n0,n1,n2');
  readln(n0.re,n0.im,n1.re,n1.im,n2.re,n2.im);}

  writeln('enter phi0 in degrees and thickness in angstroms');
  readln(phi0,thickness);

  phi0 := phi0*pi/180;

  n0.re := 1;
  n0.im := 0;
  n1.re := 1.46;
  n1.im := 0;
  n2.re := 3.85;
  n2.im := 0.03;
  lambda := 6328;

  ABCDEF(n0,n1,n2,phi0,A,B,C,D,E,F);

  dphi_lambda := Dphi(phi0,lambda,n0,n1);
  writeln('Dphi0 = ',dphi_lambda.re,' + j ',dphi_lambda.im);

  x := XX(dphi_lambda,thickness);

  tempcnum[1] := mul(x,x);
  tempcnum[2] := mul(C,tempcnum[1]);
  tempcnum[3] := mul(B,x);
  tempcnum[4] := add(tempcnum[2],tempcnum[3]);
  tempcnum[5] := add(A,tempcnum[4]);
  tempcnum[6] := mul(F,tempcnum[1]);
  tempcnum[7] := mul(E,x);
  tempcnum[8] := add(tempcnum[6],tempcnum[7]);
  tempcnum[9] := add(D,tempcnum[8]);
  row := dvd(tempcnum[5],tempcnum[9]);

  writeln('row = ',row.re,' + j ',row.im);

  psi := arctan(mag(row));
  psi := 180*psi/pi;
  del := arg(row)*180/pi;

  writeln('psi = ',psi,' del = ',del);

end;

{-----}

procedure FILM_THICKNESS;
const
  pi = 3.141592654;

var
  psi,del,phi0,lambda           :real;
  n0,n1,n2,dphi_lambda,row      :complex;
  thickness1,thickness2         :complex;
  A,B,C,D,E,F                  :complex;
  tempcnum                      :array [1..24] of complex;

begin
  n0.re := 1.0;
  n0.im := 0.0;
  n1.re := 1.46;

```

```

n1.im := 0.0;
n2.re := 3.85;
n2.im := 0.02;
lambda := 6328;

writeln('enter phi0');
readln(phi0);
phi0 := phi0*pi/180;

ABCDE(n0,n1,n2,phi0,A,B,C,D,E,F);

writeln('enter psi and del');
readln(psi,del);

psi := pi*psi/180;
del := pi*del/180;

row.re := (sin(psi)*cos(del))/cos(psi);
row.im := (sin(psi)*sin(del))/cos(psi);
writeln('from FILM_THICKNESS1 row = ',row.re,' + j ',row.im);

tempcnm[1] := mul(row,E);
tempcnm[2] := scmul(-i,tempcnm[1]);
tempcnm[3] := add(B,tempcnm[2]);
tempcnm[4] := mul(tempcnm[3],tempcnm[3]);           {sqr(B-pE)}

tempcnm[5] := mul(row,F);
tempcnm[6] := scmul(-i,tempcnm[5]);
tempcnm[7] := add(C,tempcnm[6]);                 {(C-pF)}

tempcnm[8] := mul(row,D);
tempcnm[9] := scmul(-i,tempcnm[8]);
tempcnm[10] := add(A,tempcnm[9]);                 {(A-pD)}

tempcnm[11] := mul(tempcnm[7],tempcnm[10]);
tempcnm[12] := scmul(-4,tempcnm[11]);
tempcnm[13] := add(tempcnm[4],tempcnm[12]);
tempcnm[14] := sq_rt(tempcnm[13]);
tempcnm[15] := scmul(-i,tempcnm[14]);
tempcnm[16] := scmul(-i,tempcnm[3]);

tempcnm[17] := add(tempcnm[16],tempcnm[14]);
tempcnm[18] := add(tempcnm[16],tempcnm[15]);

tempcnm[19] := dvd(tempcnm[17],tempcnm[7]);
tempcnm[20] := dvd(tempcnm[18],tempcnm[7]);

tempcnm[21] := scmul(1/2,tempcnm[19]);
tempcnm[22] := scmul(1/2,tempcnm[20]);

write('1x1 = ',mag(tempcnm[21]));
write('1x2 = ',mag(tempcnm[22]));

tempcnm[23].re := (2*pi - arg(tempcnm[21]))/(2*pi);
tempcnm[23].im := (ln(mag(tempcnm[21])))/(2*pi);
tempcnm[24].re := (2*pi - arg(tempcnm[22]))/(2*pi);
tempcnm[24].im := (ln(mag(tempcnm[22])))/(2*pi);

dphi_lambda := Dphi(phi0,lambda,n0,n1);

thickness1 := mul(dphi_lambda,tempcnm[23]);
thickness2 := mul(dphi_lambda,tempcnm[24]);

writeln('Dphi = ',dphi_lambda.re,' + j ',dphi_lambda.im);
writeln('thickness = ',thickness1.re,' + j ',thickness1.im);

```

```

write('thickness = ', thickness.re, ' + j ', thickness.im);
end;
-----}
procedure PL_INTERF_PSI_DEL;
const pi = 3.141592654;
var
  n0, n1, row                                :complex;
  cxsin0, cxsini, cxcos0, cxcos1             :complex;
  fresnel_rp, fresnel_rs                     :complex;
  refl_p, refl_s, del_rp, del_rs             :real;
  psi, del, phi0                             :real;
begin
  n0 := one;
  writeln('enter n1.re, n1.im and phi0');
  readln(n1.re, n1.im, phi0);

  phi0 := pi*phi0/180;

  cxsin0 := scmul(sin(phi0), n0);
  cxsini := dvd(cxsin0, n1);

  cxcos0 := cxcos(cxsin0);
  cxcos1 := cxcos(cxsini);

  fresnel_rp := rp(n0, cxcos0, n1, cxcos1);
  fresnel_rs := rs(n0, cxcos0, n1, cxcos1);

  del_rp := 360 - arg(fresnel_rp)*180/pi;
  del_rs := 360 - arg(fresnel_rs)*180/pi;

  refl_p := sqr(mag(fresnel_rp));
  refl_s := sqr(mag(fresnel_rs));

  row := dvd (fresnel_rp, fresnel_rs);

  del := arg(row);
  del := 180*del/pi;
  psi := arctan(mag(row));
  psi := 180*psi/pi;

  writeln('refl_p = ', refl_p, ' ', 'refl_s = ', refl_s);
  writeln('del_rp = ', del_rp, ' ', 'del_rs = ', del_rs);
  writeln('psi = ', psi, ' del = ', del);
end;
-----}

procedure PL_INTERF_N1;
const
  tot_cnum = 20;
  pi = 3.141592654;
var
  psi, del, phi0                             :real;
  n0, n1, row                                :complex;
  cnum                                         : array [1..tot_cnum] of complex;
begin
  n0 := one;

  writeln('enter psi, del, phi0');
  readln(psi, del, phi0);
  psi := pi*psi/180;
  del := pi*del/180;
  phi0 := pi*phi0/180;

```

```

row.re := (sin(psi)/cos(psi))*cos(del);
row.im := (sin(psi)/cos(psi))*sin(del);

cnum[1] := add(one,row);
cnum[2] := mul(cnum[1],cnum[1]);
cnum[3] := scmul(4,row);
cnum[4] := dvd(cnum[3],cnum[2]);
cnum[5] := scmul(-sqr(sin(phi0)),cnum[4]);
cnum[6] := add(one,cnum[5]);
cnum[7] := sq_rt(cnum[6]);
cnum[8] := scmul(sin(phi0)/cos(phi0),cnum[7]);

n1 := mul(n0,cnum[8]);
n1.re := abs(n1.re);

if abs(n1.im) < 1E-7 then n1.im := 0;
writeln('n1 = ',n1.re,' - j ',n1.im);
end;

{-----}

begin
  for i := 1 to 100 do
    begin
      writeln;
      writeln('option 0 -- end program');
      writeln('option 1 -- determine psi & del of a film');
      writeln('option 2 -- determine film thickness');
      writeln('option 3 -- determine psi & del for a planar interface');
      writeln('option 4 -- determine n1 for a planar interface');
      writeln;
      writeln('enter option number and hit (enter)');
      readln(option);
      if option = chr(48) then
        begin
          halt;
        end
      else if option = chr(49) then
        begin
          FILM_PSI_DEL;
        end

      else if option = chr(50) then
        begin
          FILM_THICKNESS;
        end
      else if option = chr(51) then
        begin
          PL_INTERF_PSI_DEL;
        end
      else if option = chr(52) then
        begin
          PL_INTERF_N1;
        end
      end;
    end;
  end;
end;
end;

```

APPENDIX B

Germanium thin films deposited by the
ionized-cluster beam method

Germanium thin films deposited by the
ionized-cluster beam method

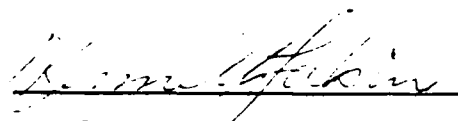
by

Jonathan Scott McCalmont

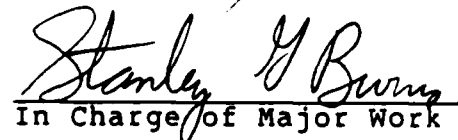
A Thesis Submitted to the
Graduate Faculty in Partial Fulfillment of the
Requirements for the Degree
MASTER OF SCIENCE

Department: Electrical Engineering and Computer Engineering
Major: Electrical Engineering

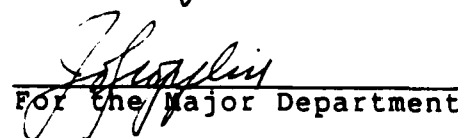
Approved:



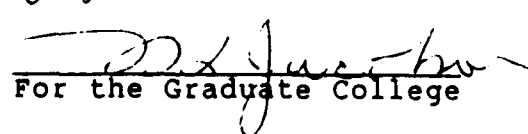
Dean



In Charge of Major Work



For the Major Department



For the Graduate College

Iowa State University
Ames, Iowa

1986

TABLE OF CONTENTS

	Page
CHAPTER I. INTRODUCTION	1
CHAPTER II. THEORY OF IONIZED-CLUSTER BEAM DEPOSITION	6
Cluster Generation	6
Ionization	13
Acceleration	13
Accelerating field	14
Effects of acceleration	14
CHAPTER III. COMPUTER ANALYSIS OF THE ACCELERATION ELECTRIC FIELD	17
Mathematical Theory	17
Outline of the Computer Programs	20
Computation Results	22
CHAPTER IV. EXPERIMENTAL IONIZED-CLUSTER BEAM DEPOSITION SYSTEM	29
Ion Source	29
Process Chamber	33
Substrate Handling Facilities	33
Process Monitors	34
CHAPTER V. EXPERIMENTAL PROCEDURE	36
Substrate Preparation	36
Choosing Deposition Parameters	36
System Operation	37
System Configurations	41

CHAPTER VI. DEPOSITION PARAMETERS AND CONDITIONS	42
Important Parameters	42
Average particle size	43
Energy per atom	44
Deposition Conditions	46
CHAPTER VII. CHARACTERIZATION OF DEPOSITED FILMS	50
Mechanical Characteristics	50
Electrical Characteristics	55
CHAPTER VIII. CONCLUSIONS AND RECOMMENDATIONS	62
REFERENCES	65
ACKNOWLEDGEMENTS	68
APPENDIX A. ALUMINUM AND GERMANIUM THIN FILMS DEPOSITED IN AN ULTRAHIGH-VACUUM IONIZED-CLUSTER BEAM SYSTEM	70
Abstract	70
Introduction	71
Experimental System	72
Experimental Procedure	78
Analysis and Results	80
Aluminum	80
Germanium	86
Conclusions	86
References	88
APPENDIX B. GERMANIUM THIN FILMS DEPOSITED BY THE IONIZED-CLUSTER BEAM TECHNIQUE	91
Summary Abstract	91
References	94

APPENDIX C. SOURCE CODE LISTINGS FOR THE FINITE- DIFFERENCE AND CONTOUR LINE PROGRAMS	95
APPENDIX D. PROCEDURES FOR SYSTEM OPERATION	101
Substrate Cleaning	101
Silicon	101
Gallium arsenide	101
Substrate Loading	102
Deposition Procedure	103

LIST OF TABLES

Table 1.1.	Semiconductor ICB applications	3
Table 4.1.	Source power supply capacities	31
Table 5.1.	Vapor pressure of germanium	38
Table 5.2.	Germanium vapor pressure coefficients	38
Table 6.1.	Deposition conditions	47
Table 6.2.	Particle size and average particle energy	49
Table 7.1.	Results of characterizations	51
Table A.1.	Vapor pressure coefficients	79
Table A.2.	Aluminum deposition conditions	82
Table A.3.	Aluminum film characteristics	82
Table A.4.	Germanium deposition conditions	87
Table B.1.	Deposition conditions and characteristics	92

LIST OF FIGURES

Figure 2.1.	Schematic ICB configuration	7
Figure 2.2.	Effect of cluster energy on the substrate	8
Figure 2.3.	Germanium vapor pressure curve	10
Figure 3.1.	Geometry of the acceleration region	23
Figure 3.2.	Equipotential lines for the acceleration region with a 4in mesh screen	24
Figure 3.3.	Equipotential lines for the acceleration region with a 2in mesh screen	25
Figure 3.4.	Equipotential lines for the acceleration region with a 1in mesh screen	26
Figure 3.5.	Equipotential lines for the acceleration region with a 0.5in mesh screen	27
Figure 4.1.	ICB source	30
Figure 4.2.	Source power supply interconnections	32
Figure 5.1.	Form for recording deposition conditions	40
Figure 7.1.	X-ray diffraction plot for a single-crystalline film	53
Figure 7.2.	X-ray diffraction plot for a polycrystalline film	54
Figure 7.3.	Buerger precession camera photograph for a single-crystalline film	56
Figure 7.4.	Indices for a Buerger precession camera photograph of a single-crystalline film	57
Figure 7.5.	Auger electron spectroscopy depth profile	58
Figure 7.6.	Resistivity of germanium as a function of doping concentration	60
Figure 7.7.	Solid solubility limit of aluminum in germanium	61

Figure A.1.	ICB system schematic diagram	73
Figure A.2.	Thin-film facility at Iowa State University	76
Figure A.3.	Cross-section of plugged crucible nozzle	81
Figure A.4.	Auger electron spectrometer map for aluminum	84
Figure A.5.	Auger electron spectrometer map for silicon	84
Figure A.6.	Element concentration versus depth for an aluminum film	85

CHAPTER I. INTRODUCTION

By providing a lattice-matching interface layer, epitaxial germanium on silicon combines the ease of silicon processing with the unique properties of gallium arsenide. Although gallium arsenide has promising applications in high-speed and opto-electronic devices, the superior mechanical and thermal properties of silicon have prevented gallium arsenide from becoming competitive with silicon. The epitaxy of gallium arsenide on silicon solves many of the problems inherent in gallium arsenide processing; silicon is lighter and less brittle than gallium arsenide, making it easier to handle, and silicon dissipates the heat generated by devices faster because it has a higher thermal conductivity than gallium arsenide [1].

Three problems have plagued the epitaxy of gallium arsenide on silicon. First, gallium arsenide is a ionic semiconductor while silicon is covalent. To obtain defect-free epitaxy, the film's first layer must be either all gallium or all arsenic. During growth, however, the gallium and arsenic atoms arrive at the surface randomly, precluding the formation of a monolayer of either atom. Second, the lattice constant of gallium arsenide is about 4% larger than that of silicon, causing defects in the deposited layer. Finally, the thermal expansion coefficients of gallium arsenide and silicon are different, leading to the generation

of stress in the epitaxial layer and in the substrate [1,2].

The techniques most frequently used to deposit gallium arsenide onto silicon are molecular beam epitaxy (MBE) and metal-organic chemical vapor deposition (CVD). A number of papers have reported progress toward the growth of device-quality gallium arsenide on silicon, usually involving a thick gallium arsenide buffer layer, a deliberately misoriented substrate, or a germanium buffer layer [1-3].

Despite a large (greater than 4%) lattice mismatch, epitaxial growth of germanium on silicon should occur easily because both are covalent semiconductors. Also, germanium has a thermal expansion coefficient between those of silicon and gallium arsenide [4]. Consequently, germanium is well-suited to be a buffer layer between silicon and gallium arsenide.

Previous efforts at depositing germanium onto silicon have used deposition techniques such as MBE [5], e-beam evaporation [6], CVD [6], ion beam sputtering [7], or ICB [8-10]. The first three techniques have resulted in epitaxy, but at a low (less than $1\text{\AA}/\text{s}$) deposition rate and with a substrate temperature as high as 450°C . The fourth technique has resulted in polycrystalline layers at a higher deposition rate ($5\text{--}7\text{ \AA}/\text{s}$) but with a substrate temperature of 450°C .

With this in mind, the ionized-cluster beam (ICB) technique was applied to the deposition of germanium films on primarily silicon substrates. The ICB technique is characterized by the ability to deposit high-quality films at

relatively low substrate temperatures. Because the ICB technique allows careful control of the average energy of the depositing particles, the optimum conditions for film formation are achievable [8].

The previous use of the ICB technique to deposit semiconductor films onto semiconductor substrates has resulted in epitaxial films at low substrate temperatures. Table 1.1 lists some previous results with this combination of film and substrate.

Table 1.1. Semiconductor ICB applications [8]

Film	Substrate	Comments
Si	(111) Si (100) Si	Low temperature (620°C) Epitaxial
GaAs	GaAs	Low temperature (550°C) Epitaxial
Ge	Si	Low temperature Epitaxial

Previous efforts at depositing germanium on silicon using ICB have resulted in epitaxial films. The results reported by Yamagishi et al., however, required high temperature annealing to achieve epitaxy [9], while the deposition apparatus of Kuiper et al. [10] is considerably more complex than the apparatus described by Takagi et al. [11].

The problem as initially faced was to build an ICB system to utilize a new ion source. The initial phase of the work involved completing the system and verifying its operation.

Thin films of aluminum were deposited and compared with previously published results and with other deposition techniques. Due to technical difficulties with the aluminum, the sequence of germanium depositions was begun.

There are two original contributions in the research performed and reported in this thesis. The design and construction of the electrostatic screen, discussed in Chapter III, is original work. Secondly, the doping of germanium with aluminum to facilitate the epitaxial formation of a thin film has not previously been reported. Both the acceleration screen and the aluminum doping are believed to be essential to obtain germanium epitaxy under the conditions reported.

Chapter II of this thesis begins by presenting background theory on the ICB deposition process. A computer analysis of the electric field in the ICB system is given in Chapter III. The experimental system used is described in Chapter IV, followed by an outline of the experimental procedure in Chapter V. Chapter VI contains a summary of the important conditions and parameters for deposition, as well as the conditions used for the germanium depositions. Chapter VII reports the results of the characterization of the germanium films. Finally, Chapter VIII includes an interpretation of the results, summarizes the research, and includes some recommendations for further study.

Included in the appendices are two papers generated as a result of this research. The first paper was presented at the

International Workshop on Ionized-Cluster Beam Technique in Tokyo, Japan on June 3, 1986, and covers the work leading up to the aluminum depositions [12]. The second paper was presented at the 33rd National Symposium of the American Vacuum Society in Baltimore, Maryland on October 30, 1986, and summarizes the germanium deposition results [13]. Also included in the appendices are the computer programs used for the electric field analysis and the step-by-step procedures used to deposit the germanium films.

CHAPTER II. THEORY OF IONIZED-CLUSTER BEAM DEPOSITION

The ICB technique uses a three-stage source to generate, ionize, and accelerate clusters. A schematic representation of a possible source configuration is shown in Figure 2.1. The cluster generation region is where the material to be deposited is formed into clusters. In the ionization region some of the clusters are given a single positive electronic charge. The acceleration region is used to impart a large kinetic energy to the ionized clusters. This kinetic energy is converted into thermal, sputtering, implantation, and migration energy when the cluster contacts the substrate, as depicted in Figure 2.2.

Cluster Generation

A cluster is a loosely-bound aggregate of up to several thousand atoms. Because a large percentage of its atoms are located on the surface, a cluster does not behave like a solid. Because it is loosely bound, a cluster does not behave like a liquid. A cluster is neither gaseous nor in the plasma phase. Consequently, clusters have been called "the fifth state of matter [14]."

The cluster generation for ICB deposition centers around a closed-top crucible. Typically the crucible is made of high-density graphite, but another material such as boron nitride could be used. The crucible has a small circular

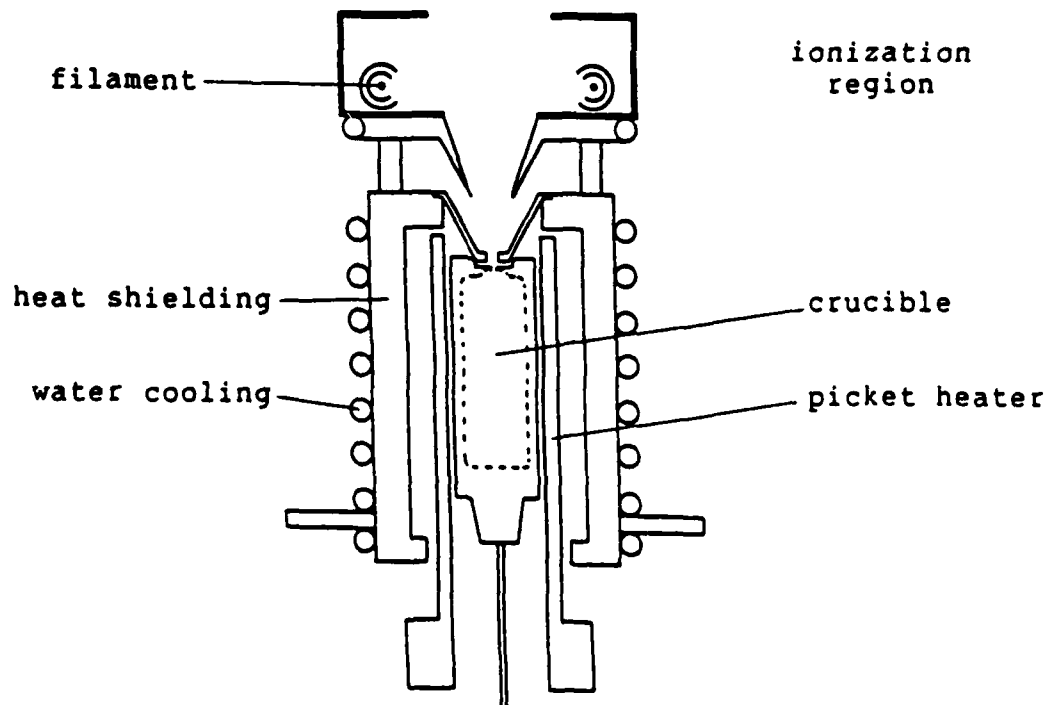
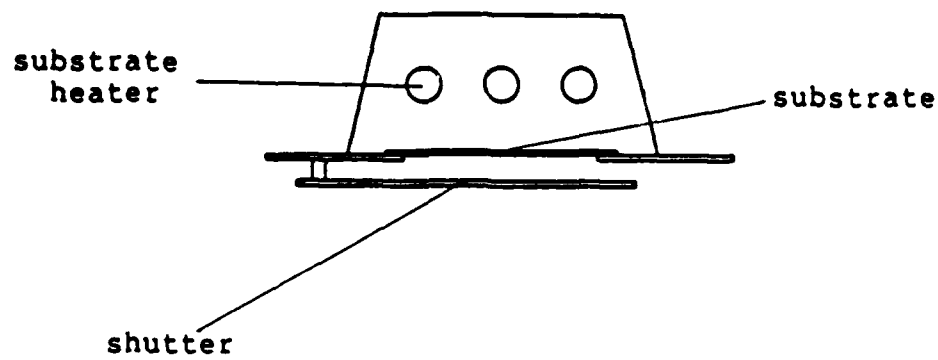


Figure 2.1. Schematic ICB configuration

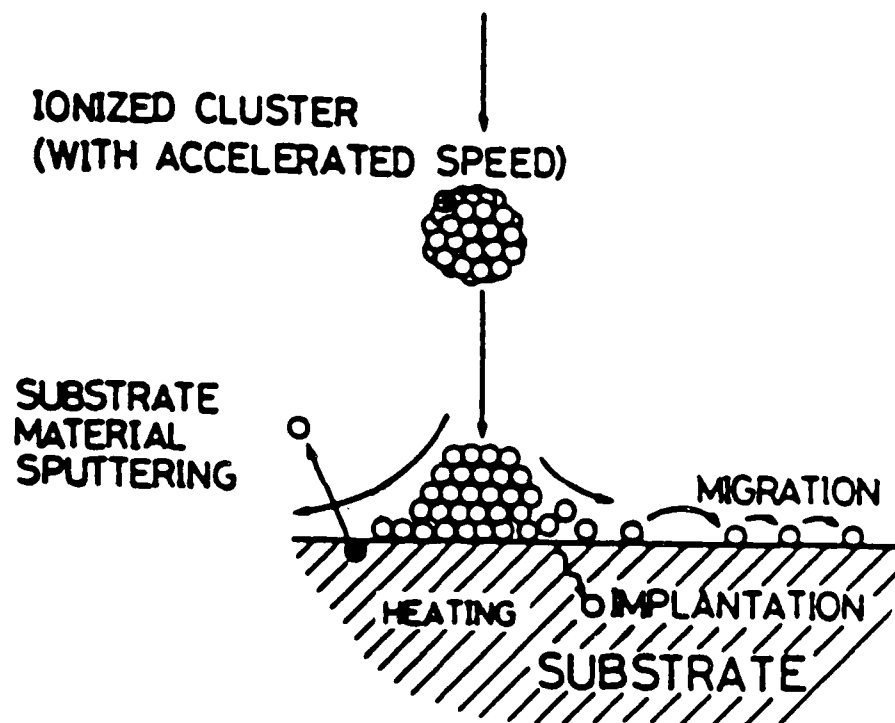


Figure 2.2. Effect of cluster energy on the substrate [15]

nozzle in the center of the top. A heater surrounds the crucible and provides even temperature control over the surface of the crucible.

Three methods of heating the crucible are possible: radiation, electron bombardment, and induction. Radiative heating is accomplished by surrounding the crucible with a filament or graphite picket heater. The heat emitted is absorbed by the crucible. Electron bombardment also uses a filament surrounding the crucible; however, the electrons emitted by the filament are accelerated into the crucible wall. This allows higher temperatures to be achieved than by radiative heat alone. Inductive heating uses an r.f. voltage applied to a coil surrounding the crucible to induce currents in the crucible wall, generating heat within the wall.

Because the crucible is enclosed, the pressure inside is the same as the vapor pressure of the material it contains. Curves of vapor pressure versus temperature have been determined for the elements; the curve for germanium is shown in Figure 2.3. These curves can be fitted to an equation of the form:

$$\log_{10} P = \frac{A}{T} + B \times \log_{10} T + C \times T + D \times T^2 + E \quad (2.1)$$

where T is the temperature in degrees Kelvin and P is the pressure in torr [16]. Using five data points from the vapor pressure curves, the coefficients A , B , C , D , and E can be determined. Cluster formation occurs when the pressure within

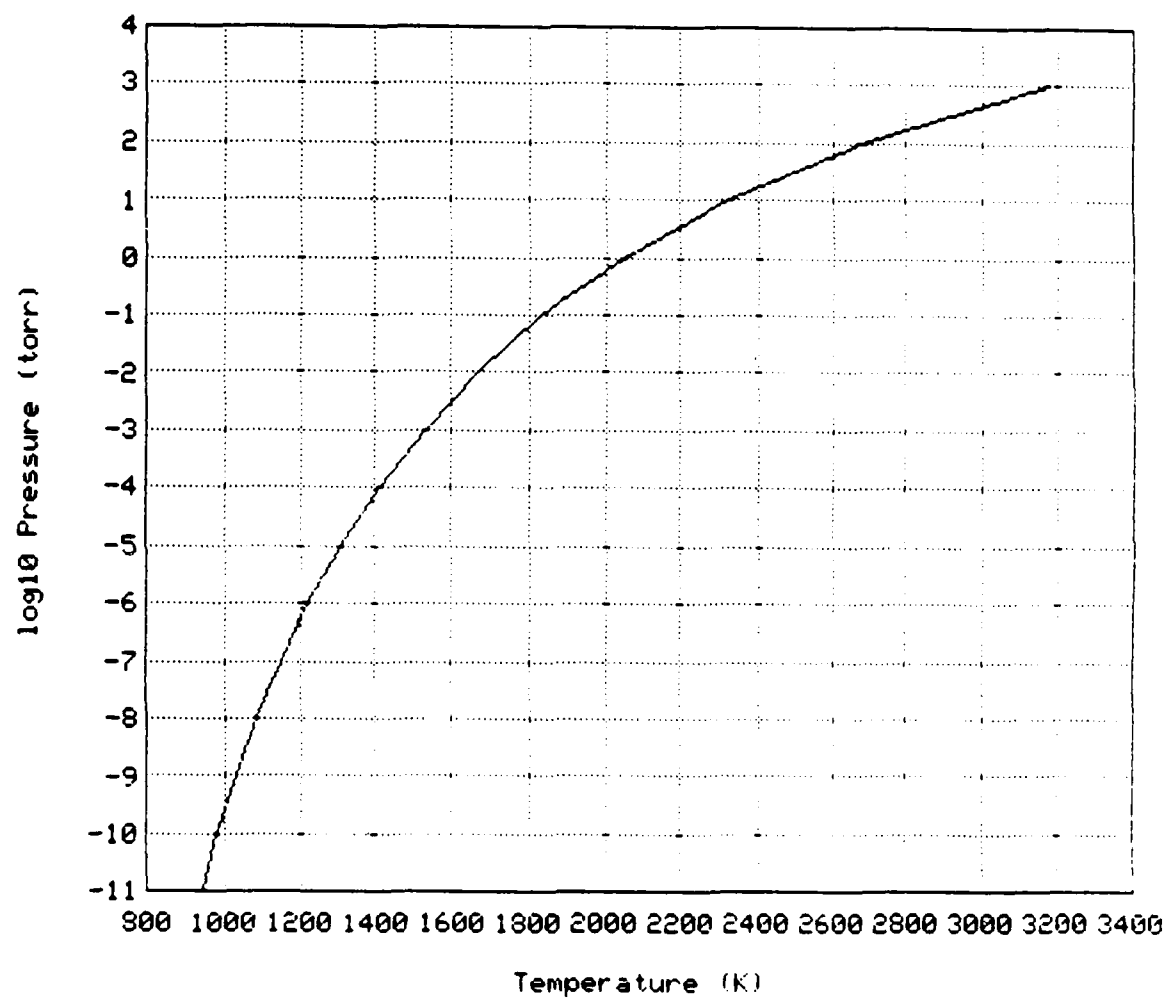


Figure 2.3. Germanium vapor pressure curve [16]

the crucible is of the order of several torr [17]; therefore, a suitable range for fitting equation 2.1 to the vapor pressure curves is 10^{-2} torr to 10^2 torr.

The formation mechanism of the clusters is a debatable topic. Two theories have been proposed--homogeneous nucleation and heterogeneous nucleation. Homogeneous nucleation is the condensation of the vaporized material upon itself, while heterogeneous nucleation requires some sort of impurity or interface, such as the wall of the crucible.

In the homogeneous nucleation theory, the vaporized material in the crucible moves into the vacuum region outside the crucible, forming a supersaturated jet beam that expands adiabatically, cools, and condenses into clusters. The condensation process occurs in a region about one nozzle diameter away from the crucible [18].

In the heterogeneous nucleation theory, the clusters form on the walls and in the nozzle of the crucible. As the material is heated, some atoms land on the walls. If the wall is too hot, the material immediately re-evaporates. If the conditions are right, however, the atom remains and acts as a nucleation site for further atoms. Each atom that arrives adds its heat of vaporization to the growing cluster. Eventually, the sum of the heats of vaporization gives the cluster enough energy to detach from the wall. Because the pressure in the crucible is higher than the pressure outside the crucible, there is a flow of material out the nozzle. The

detached cluster is swept out of the nozzle by this flow [19].

It should be noted that the heterogeneous theory points out a weakness of the homogenous theory. As the cluster is growing in the homogeneous theory, each arriving atom adds its heat of vaporization to the cluster. If this heat is not removed, the cluster will obtain enough energy to break apart. The only way to remove energy is through collisions with other particles, but the time involved in cluster growth is not sufficient to support the growth of clusters of the proper size [19]. By this argument, the heterogeneous nucleation theory seems to be the stronger of the two.

Further indication that heterogeneous nucleation is more likely than homogeneous nucleation comes from experimental data on cluster sources. The size of the clusters measured by Takagi et al. do not correspond to cluster sizes measured using nozzle-expansion sources. It is therefore unlikely that the clusters measured by Takagi et al. were formed by nozzle expansion; the clusters were formed before exiting the nozzle [10].

Finally, cluster formation requires a material that does not wet the walls of the crucible [20]. For a graphite crucible, suitable materials include copper, zinc, gallium, germanium, arsenic, selenium, silver, cadmium, tin, antimony, tellurium, gold, mercury, thallium, lead, bismuth, and polonium. Other materials, including organic materials, have been deposited using the ICB apparatus, but cluster formation

has not been demonstrated for many of these materials.

Ionization

After the cluster is formed, it travels upward into the ionization region at supersonic velocity. In the ionization region electrons are accelerated from a hot filament into the cluster beam. If an electron collides with a cluster, it will remove an additional electron from the cluster, giving the cluster a single positive electronic charge. Due to the weak binding forces of a cluster, it is presumed that double ionization will split a cluster because of the Coulombic repulsion of the charges. Only clusters with a single charge are likely.

The efficiency of electron bombardment for ionization is low; consequently, only a small percentage of the clusters become ionized. Therefore, the charge-to-mass ratio of the beam after ionization is low. This is an advantage, as the film may be deposited on an insulating substrate without the problem of substrate charging [11]. If the substrate becomes positively charged, future ionized clusters are repulsed.

Acceleration

The ionized clusters may be accelerated by an electric field created by having a d.c. voltage between the ionization region and the acceleration electrode. This electrode may be a separate part of the source, resulting in a short acceleration followed by a neutral drift to the substrate, or

it may be the substrate itself, resulting in acceleration the entire distance to the substrate. Acceleration is an important part of the ICB process because it allows the kinetic energy of the cluster beam to be controlled.

Accelerating field

One important consideration for the accelerating field is that the field be spatially uniform so that the cluster experiences an even acceleration force; otherwise, the cluster might be destroyed. To accomplish this, an electrostatic screen is placed around the accelerating region to change the shape of the electric field. A computer analysis of the electric field with such a screen was done and is discussed in Chapter III.

Effects of acceleration

Upon impacting the substrate, some of the kinetic energy of the accelerated clusters is transformed into thermal energy. This extra energy appears as an increased temperature of the substrate [11]. Although for many types of depositions an increased substrate temperature is necessary, in general this heating is not desired. ICB deposition is designed to eliminate much of the high temperature processing associated with thin-film deposition; unwanted substrate heating is minimized.

The second effect of acceleration is the sputtering of impurities from the substrate surface [11]. Some of the

energy of the incident particles is transferred to the surface atoms of the substrate, which gain enough energy to leave the surface. For materials such as silicon which form an oxide layer, this sputtering is important because it removes the oxide layer, allowing the deposited material to make direct contact to the substrate material. The sputtering also cleans other impurities from the surface, increasing the likelihood of epitaxial film formation.

The third effect of acceleration is shallow implantation [11]. Implantation occurs with the particles that have enough energy to bury themselves into the substrate, in particular the small accelerated particles such as monomers. These buried particles form a transitional layer between the substrate and the deposited film; this transitional layer can have important mechanical and electrical consequences. Mechanically, the transitional layer allows the deposited film to adjust to the crystal lattice of the substrate, increasing the likelihood of epitaxial growth. Electrically, the transitional layer provides a low resistance connection between the substrate material and the deposited material.

The last effect of acceleration is surface migration. Two theories exist. According to the first theory, the cluster breaks up into atoms after hitting the substrate. These adatoms have a large translational velocity and migrate across the surface of the substrate until they find a nucleation site. Other adatoms attach to the nucleation site,

forming islands that build up the deposited film [11]. The second theory proposes that the arriving clusters behave like molten droplets that remain in a small blob upon arriving at the substrate. In this model, there is little migration of the material being deposited [21].

CHAPTER III. COMPUTER ANALYSIS OF THE ACCELERATION ELECTRIC FIELD

A computer analysis was done to characterize the electric field in the acceleration region. This analysis was undertaken to determine the proper geometry and mesh of the electrostatic screen and to verify the effect of the screen. Two programs were written, one to solve for the potential distribution using the relaxation method and one to provide graphical output of the equipotential lines. The programs were written in Pascal; the source code listings are in Appendix C.

Mathematical Theory

The electric potential distribution in a region is satisfied by Poisson's equation:

$$\nabla^2 \phi = - \frac{\rho}{\epsilon} \quad (3.1)$$

where ϕ is the electric potential, ρ is the charge density, and ϵ is the permittivity. The operator ∇ is the Laplacian operator and is dependent on the coordinate system used. Laplace's equation, a special case of equation 3.1, arises when a region is free of charge and has a constant permittivity:

$$\nabla^2 \phi = 0. \quad (3.2)$$

For the acceleration region, the charge density is very low due to the low charge-to-mass ratio of the ion beam;

therefore, using Laplace's equation is reasonable for this analysis.

In cylindrical coordinates, (r, ϕ, z) , Laplace's equation is:

$$\frac{1}{r} \frac{\partial}{\partial r} \left(r \frac{\partial \phi}{\partial r} \right) + \frac{1}{r^2} \frac{\partial^2 \phi}{\partial \phi^2} + \frac{\partial^2 \phi}{\partial z^2} = 0. \quad (3.3)$$

If there is axial symmetry (no ϕ -dependence), and if the first term is expanded, equation 3.3 becomes

$$\frac{\partial^2 \phi}{\partial r^2} + \frac{1}{r} \frac{\partial \phi}{\partial r} + \frac{\partial^2 \phi}{\partial z^2} = 0 \quad (3.4)$$

To solve equation 3.4, finite-difference approximations are made for the derivatives. Expanding the potential (ϕ) using a Taylor series about the point (r, z) results in four equations:

$$\phi(r+h, z) = \phi(r, z) + h \frac{\partial \phi}{\partial r} + \frac{1}{2!} h^2 \frac{\partial^2 \phi}{\partial r^2} + \dots \quad (3.5a)$$

$$\phi(r-h, z) = \phi(r, z) - h \frac{\partial \phi}{\partial r} + \frac{1}{2!} h^2 \frac{\partial^2 \phi}{\partial r^2} - \dots \quad (3.5b)$$

$$\phi(r, z+h) = \phi(r, z) + h \frac{\partial \phi}{\partial z} + \frac{1}{2!} h^2 \frac{\partial^2 \phi}{\partial z^2} + \dots \quad (3.5c)$$

$$\phi(r, z-h) = \phi(r, z) - h \frac{\partial \phi}{\partial z} + \frac{1}{2!} h^2 \frac{\partial^2 \phi}{\partial z^2} - \dots$$

Terms with a third or higher derivative of the potential are neglected. Summing equation 3.5a and equation 3.5b

AD-A187 335

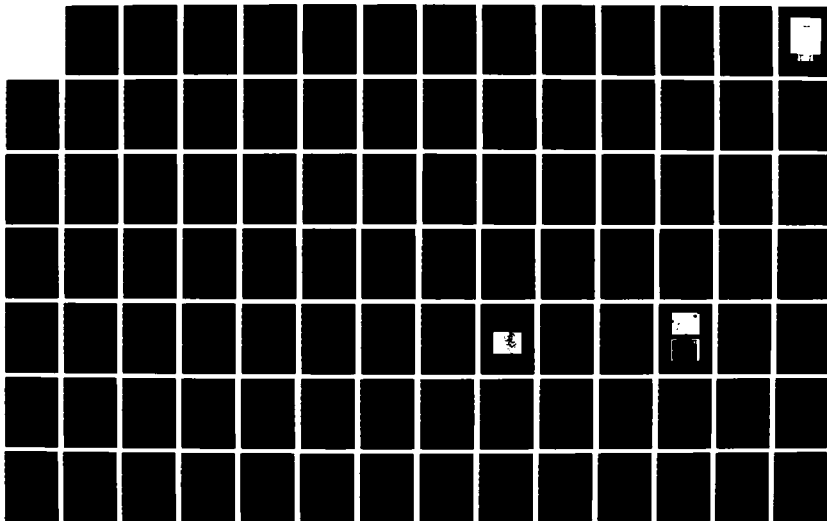
SYNTHESIS AND CHARACTERIZATION OF THIN FILMS(U) IOWA
STATE UNIV AMES MICROELECTRONICS RESEARCH CENTER
K H LAKIN 18 JUL 87 AFOSR-TR-87-1393 AFOSR-84-0388

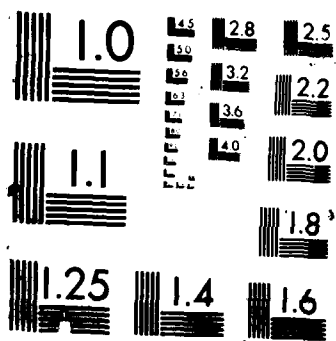
3/4

UNCLASSIFIED

F/G 13/8

NL





$$\phi(r+h,z) + \phi(r-h,z) = 2\phi(r,z) + h^2 \frac{\partial^2 \phi}{\partial r^2}. \quad (3.6)$$

Rearranging this leads to:

$$\frac{\partial^2 \phi}{\partial r^2} = \frac{\phi(r+h,z) + \phi(r-h,z) - 2\phi(r,z)}{h^2}. \quad (3.7)$$

Again using equations 3.5a and 3.5b only this time subtracting 3.5b from 3.5a leads to:

$$\phi(r+h,z) - \phi(r-h,z) = 2h \frac{\partial \phi}{\partial r} \quad (3.8)$$

or:

$$\frac{\partial \phi}{\partial r} = \frac{\phi(r+h,z) - \phi(r-h,z)}{2h}. \quad (3.9)$$

Similarly, adding equation 3.5c and equation 3.5d leads to:

$$\phi(r,z+h) + \phi(r,z-h) = 2\phi(r,z) + h^2 \frac{\partial^2 \phi}{\partial z^2} \quad (3.10)$$

which rearranges to give:

$$\frac{\partial^2 \phi}{\partial z^2} = \frac{\phi(r,z+h) + \phi(r,z-h) - 2\phi(r,z)}{h^2}. \quad (3.11)$$

Equations 3.7, 3.9, and 3.11 can be substituted into equation 3.4, resulting in:

$$\begin{aligned} \phi(r,z) = & \frac{\phi(r,z+h) + \phi(r+h,z) + \phi(r,z-h) + \phi(r-h,z)}{4} \\ & + h \frac{\phi(r+h,z) - \phi(r-h,z)}{8r}. \end{aligned} \quad (3.12)$$

This is the desired result--an equation that relates the

potential at a point to the potentials at neighboring points spaced a distance h away. Additionally, the equation is simple to solve for any region using a digital computer.

With equation 3.12 and a set of boundary conditions, the electric field in a region can be approximated. This method is easily programmed and works well where computation time considerations do not present a problem.

Outline of the Computer Programs

The first program solves equation 3.12 for a set of boundary conditions. Two two-dimensional arrays are defined, one with real-valued elements representing the potentials in the region and one with Boolean elements representing the existence of a boundary. A procedure initializes the arrays with the boundary conditions. The non-boundary elements are set to a potential of zero. Using zero for the initial solution at these points usually causes the algorithm to take longer to converge on the final solution, but the time lost is offset by the time saved in initializing the array--each element would have to be entered separately.

In the main loop of the program, repetitive passes are made through the array, using equation 3.12 to update the potential at each point. A temporary array is used, so that all of the updates are made using the values in the original array. A point located on a boundary is skipped so that its value does not change. A special boundary exists along the

center axis; the potential cannot be initialized explicitly. However, the first derivative of the potential with respect to r is zero due to the rotational symmetry. Consequently, a reflection of the point immediately next to the axis is used--the potential at $(-h, z)$ is the same as the potential at $(+h, z)$. Therefore, for $r=0$, equation 3.12 may be rewritten as:

$$\phi(0, z) = \frac{\phi(0, z+h) + 2\phi(+h, z) + \phi(0, z-h)}{4}. \quad (3.13)$$

During the updating process, a record is kept of the largest change made in any element. After the entire array has been updated, the maximum change is compared to an error tolerance. If the change is less than the tolerance, the main loop is exited; otherwise, the loop is repeated but with the original and the temporary arrays switched. After the main loop is exited, the array is output in a readable form. A standard text file was chosen as the output format, since it is easily read by either a person or a machine.

The second program presents the data from the first in graphical form. A useful picture is the lines of equal potential in the region, or the equipotential lines. The program reads the data from the text file into an array. An area of the display device is defined to correspond to the coordinates of each element in the array, so that the output will appear as a scaled drawing.

In the main loop the array is scanned twice, first

through the r-coordinates and then through the z-coordinates. The value of the potential at each element is checked to see if it compares to the desired equipotential line spacing. When a match is found, a dot is placed on the output device at the coordinates of the element. To provide a more detailed output, linear interpolation is made to estimate the potential between array elements if a match is not made to an element. After the array has been scanned in both directions, the output dots form a rough picture of the equipotential lines.

Computation Results

The boundary conditions for the region analyzed are shown in Figure 3.1. The source is a constant potential block at the bottom of the chamber. The chamber walls and substrate are at ground potential, while the source and screen are at the maximum acceleration voltage, 10kV.

The motivation for writing the computer programs was to aid the design of the screen and to verify its effect. After the relative geometry shown in Figure 3.1 was decided upon, information was needed to decide on a proper mesh for the screen. A solid screen was undesirable because it would block the source from view, so four meshes were tried: 4, 2, 1, and 0.5in. The graphical output for these four conditions is shown in Figures 3.2 through 3.5. The electric field between the source and the substrate is most evenly spaced for the 1in and 0.5in meshes. A 0.5in mesh screen was chosen because of

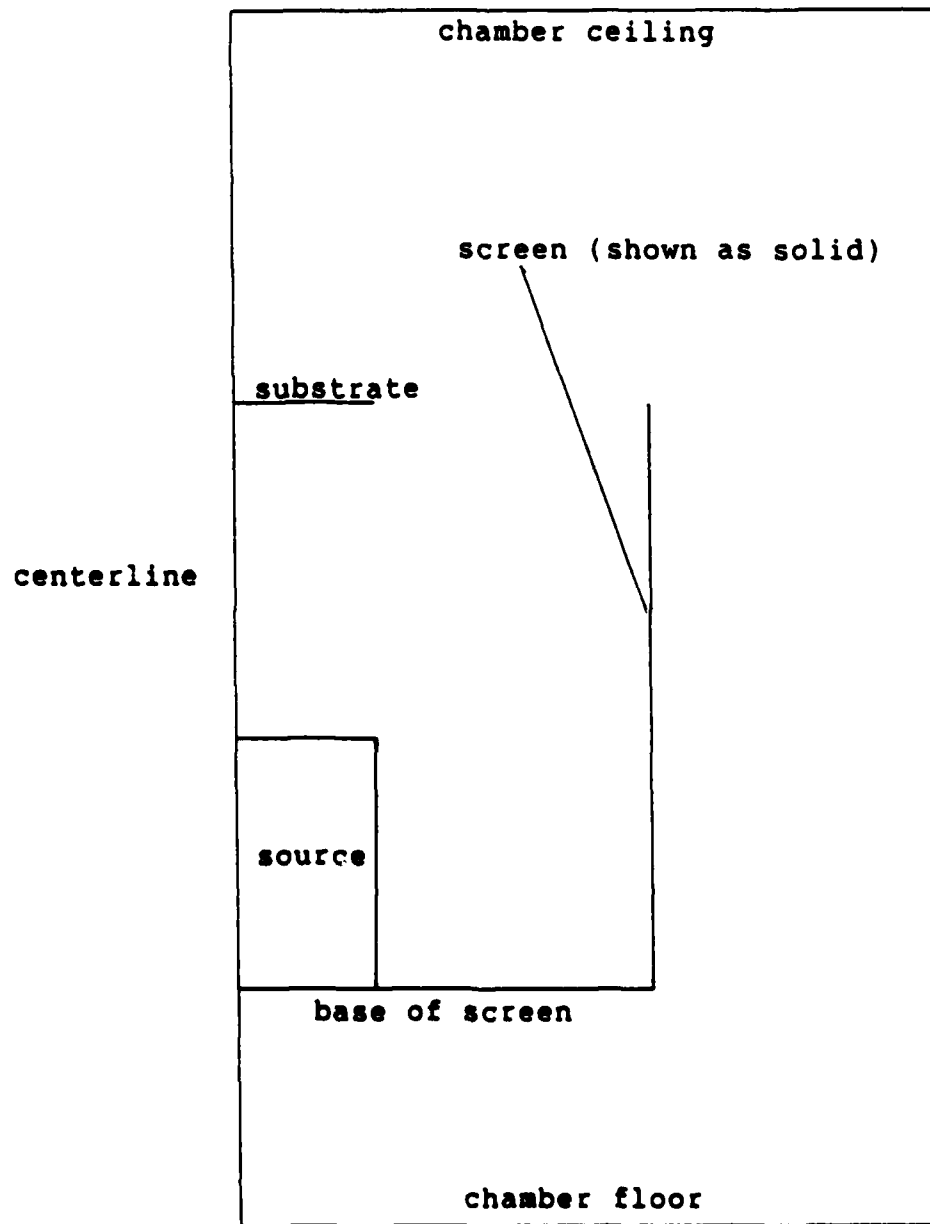


Figure 3.1. Geometry of the acceleration region

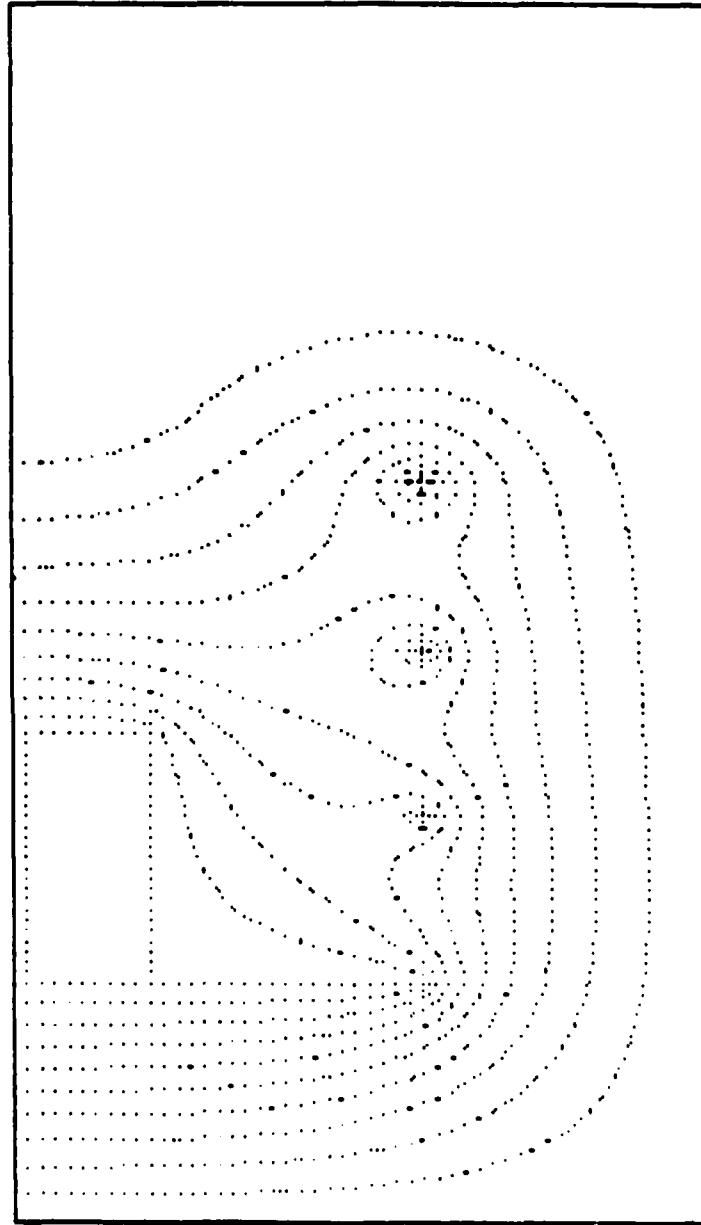


Figure 3.2. Equipotential lines for the acceleration region with a 4in mesh screen

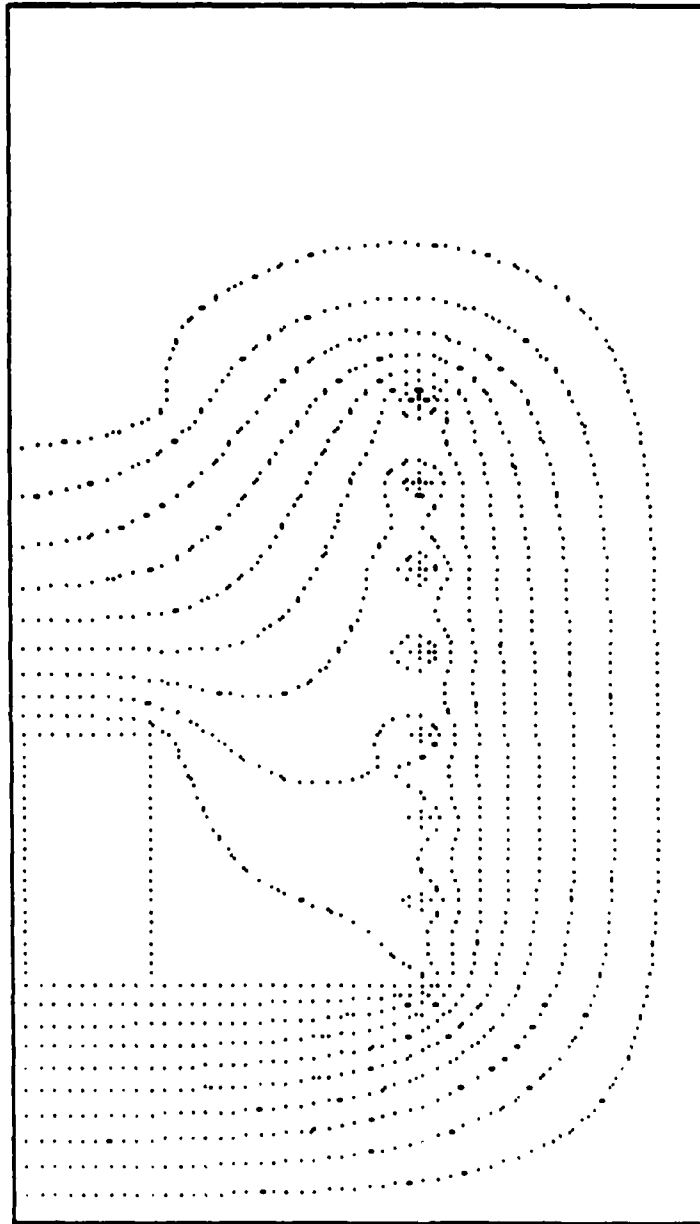


Figure 3.3. Equipotential lines for the acceleration region with a 2in mesh screen

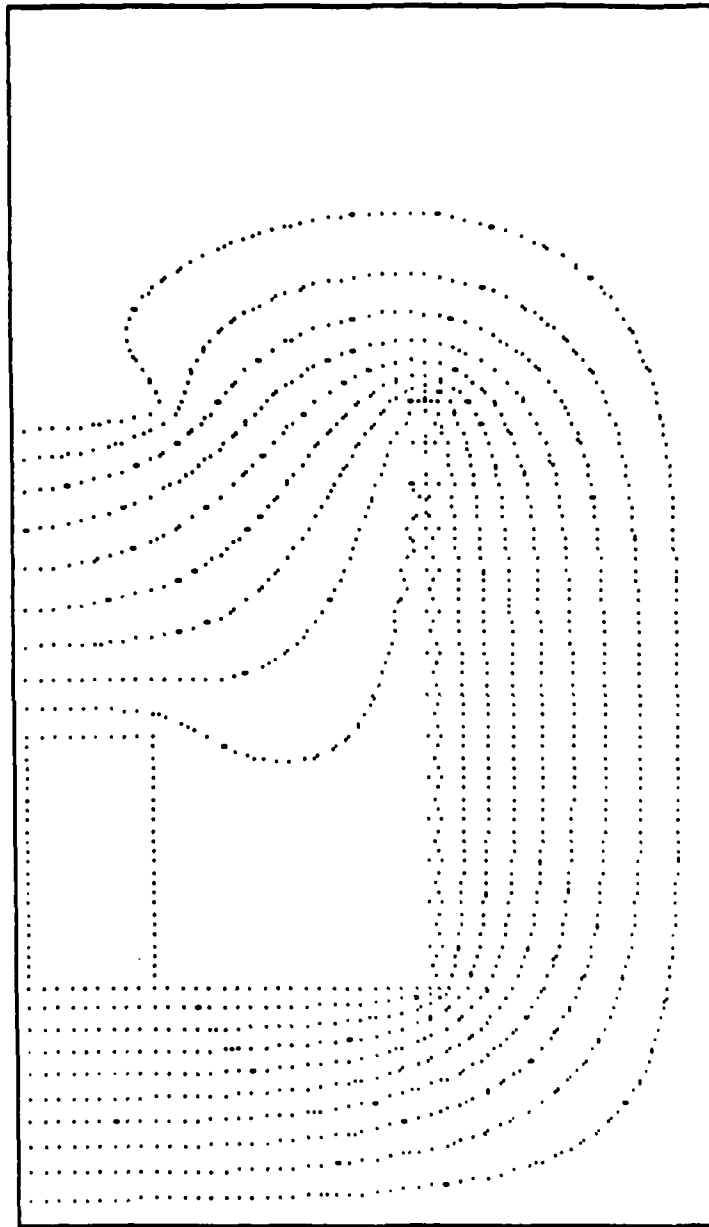


Figure 3.4. Equipotential lines for the acceleration region with a lin mesh screen

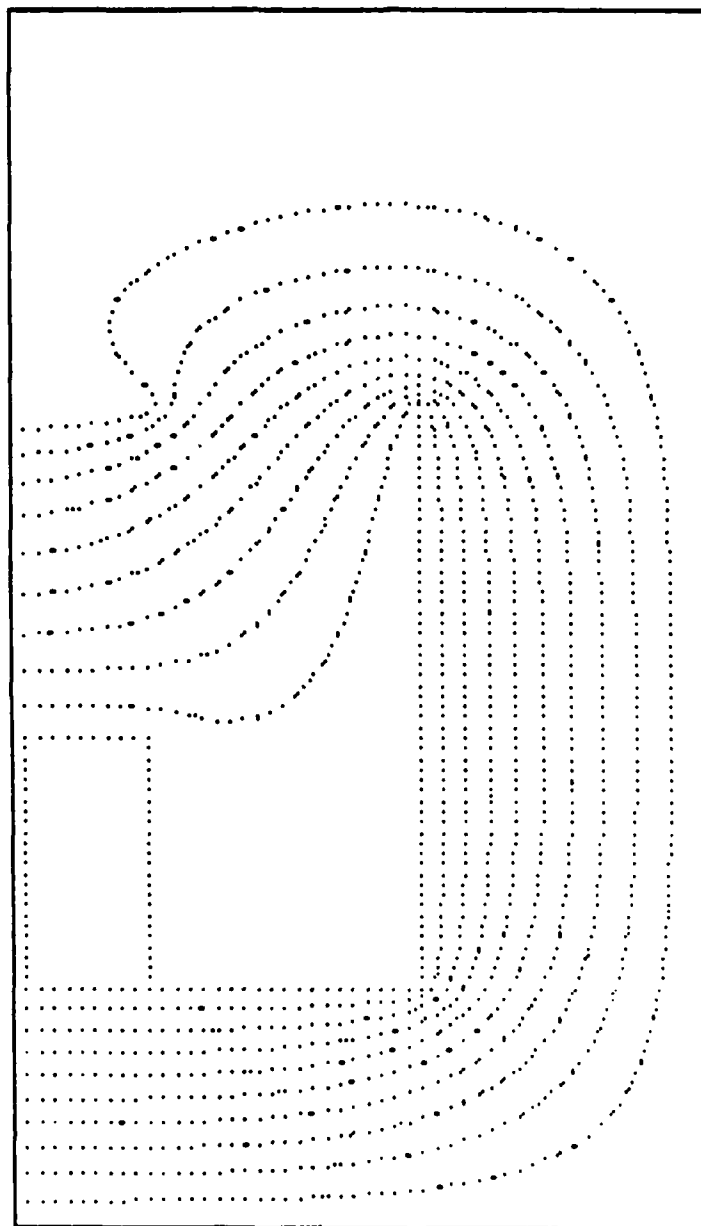


Figure 3.5. Equipotential lines for the acceleration region with a 0.5in mesh screen

an availability of materials--0.5in stainless-steel screening is commercially available.

The ionized clusters will tend to follow the electric field lines, or lines of electric force, which run perpendicular to the equipotential lines. By visually approximating the perpendiculars to the equipotential lines in Figure 3.5, it can be seen that the screen forces the ionized clusters toward the center of the substrate. This is an advantage as it increases the deposition rate and the acceleration effects.

CHAPTER IV. EXPERIMENTAL IONIZED-CLUSTER BEAM DEPOSITION SYSTEM

The ICB system used for the depositions is a combination of a commercially purchased ion source and a custom-built process chamber. The system is completed by the substrate handling facilities and the process monitors.

Ion Source

The ion source is mounted at the bottom of the process chamber on an eight-inch (outside diameter) UHV flange. The mounted source is pictured in Figure 4.1. The source was purchased from Eaton Corporation, Beverly, MA, and represents their second-generation design. Seven feed-throughs on the mounting flange permit electrical power to be applied to the source. The three feedthroughs for the acceleration and ionization are rated for high voltage and low current. The two crucible heater feedthroughs are rated for high voltage and high current. The source cooling feedthroughs are rated for high voltage.

The crucible heating region uses a graphite picket heater to radiatively heat the crucible. The heater is surrounded by multiple layers of molybdenum shielding, which is further surrounded by a water-cooled casing. Above the crucible, a graphite baffle provides heat shielding and prevents material from evaporating from the heating region and contaminating the film.

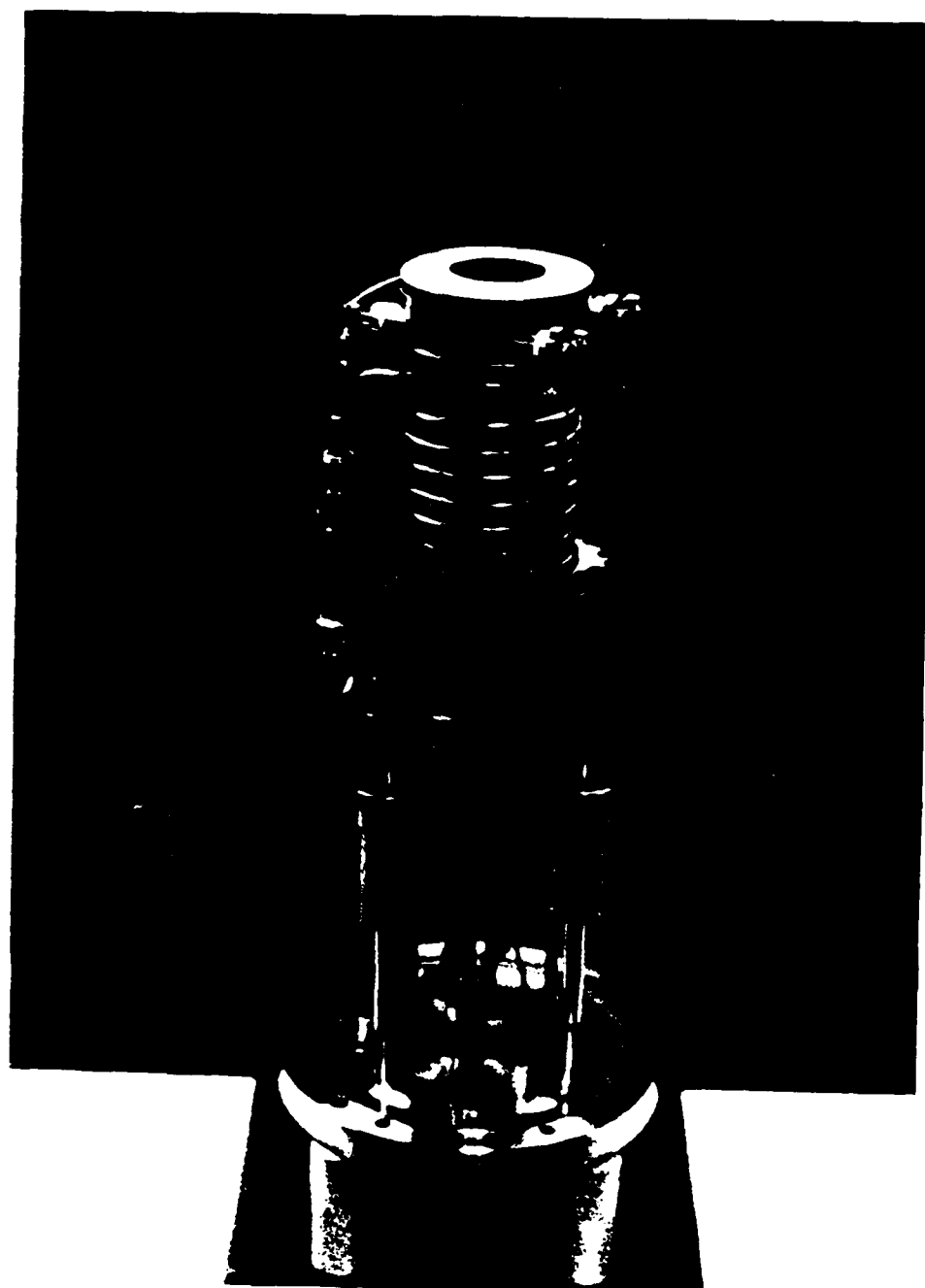


Figure 4.1. ICB source

The ionization region uses two tungsten filaments to emit electrons for electron bombardment. Surrounding each filament are two concentric cylinders with slots cut axially on the side facing the cluster beam. A negative voltage is placed on the filament and inner cylinder with respect to the outer cylinder so that the electrons are extracted and accelerated toward the cluster beam.

The acceleration region is the 25cm distance from the ionization region to the substrate. The source is biased at the positive acceleration voltage and the substrate is kept at ground potential.

Four separate power supplies are required to run the ICB system. A time-proportioning a.c. supply is used for the crucible heater. Two d.c. switching supplies are used to provide the high voltages for acceleration and ionization. A third d.c. switching supply provides the current for the ionization filament. The rated capacities for the supplies are given in Table 4.1.

Table 4.1. Source power supply capacities

Supply	Voltage	Current
Acceleration	10kV	10mA
Ionization Supply	500V	400mA
Ionization Filament	25V	25A
Crucible Heater	40V	150A

The power supply interconnections are shown in Figure 4.2. The crucible heater power supply is connected to the

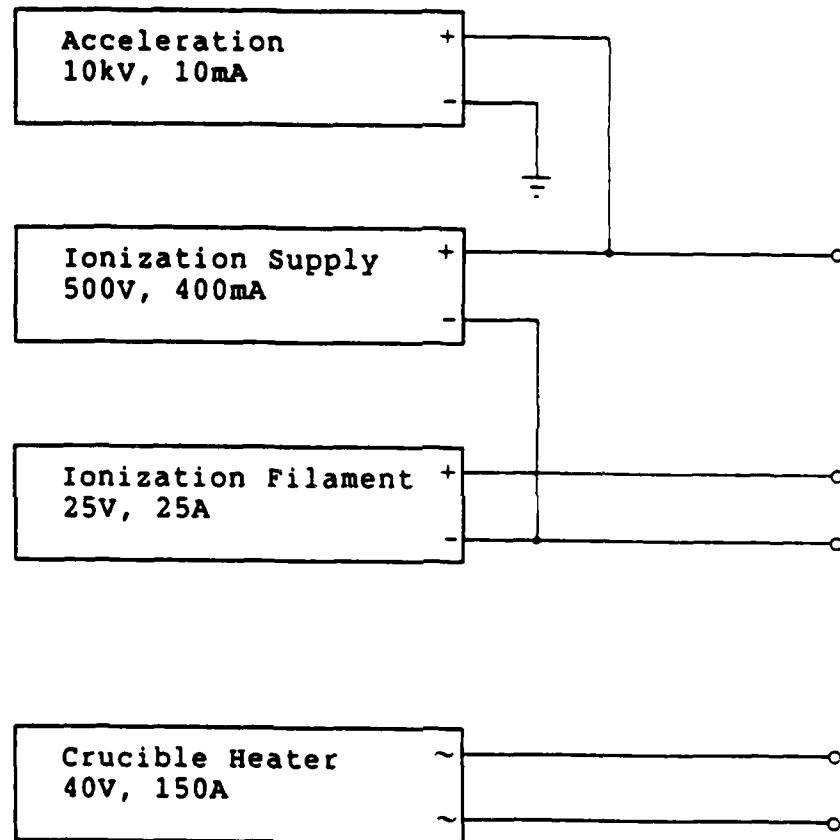


Figure 4.2. Source power supply interconnections

source using 15kV 2AWG cable; RG8A/U coaxial cable connects the ionization and acceleration supplies.

Process Chamber

The process chamber is a custom-built ultrahigh vacuum (UHV) chamber with a water-cooled exterior surface. The base pressure of the chamber is about 2×10^{-8} Pa. Two pumping systems are used--the primary pump is a 1000l/s turbomolecular pump, with additional pumping achieved through the use of a 2000l/s titanium sublimation pump (TSP). The TSP is mounted in a special chamber that is positioned perpendicular to the process chamber; the TSP chamber is cooled by a water jacket. The turbo pump is mounted on the lower side of the TSP chamber.

Mounted on the floor of the process chamber is the acceleration screen. A 0.0625in thick circular stainless-steel base 15in in diameter is supported above the chamber floor by four ceramic insulators. A 7in diameter hole in the center allows the source to pass through. The screen is constructed of heavy-gauge stainless-steel wire with a 0.5in mesh. The screen extends from the base to about 0.5in below the height of the substrate.

Substrate Handling Facilities

The substrate is held in a boat made from stainless-steel sheet metal. Within the process chamber the boat rests on a 0.0625in thick stainless-steel track that is supported by

threaded rods extending down from the ceiling of the process chamber. The track is fully adjustable for height and tilt. A stop on the track positions the boat so that the substrate is centered over the source; a three-inch diameter hole is cut in the track to expose the substrate to the cluster beam.

Three infrared quartz heating lamps are mounted above the substrate, providing a total heating power of 3600W. Behind the lamps is a reflector made of a single layer of molybdenum sheet metal. The entire heating assembly is built in a stainless-steel frame. A tube extends through the frame and the reflector to allow a thermocouple to be positioned on the back side of the substrate.

Below the substrate is a shutter designed to protect the substrate from the cluster beam but to leave the process monitor sensors exposed.

Separated from the process chamber by a gate valve is a high-vacuum chamber used to introduce the substrate without cycling the process chamber to atmosphere. A magnetically-coupled manipulator arm is used to move the substrate boat between the two vacuum chambers. The load lock is equipped with a 501/s turbomolecular pump.

Process Monitors

Two sensors are installed in the process chamber to monitor the vacuum--an ionization gauge and a residual gas analyzer (RGA). The ionization gauge gives an indication of

the total pressure, while the RGA uses an r.f. quadrupole mass filter to determine the partial pressures of the gases in the vacuum.

The characteristics of the cluster beam are monitored by two sensors. A Faraday cup is used to measure the current density of the ion beam, while a second sensor measures the accumulated thickness of deposited material. The Faraday cup is a cup-shaped cylinder enclosed in a grounded casing. The ions collected in the cup cause a current to flow from the cup to ground. The current density of the ion beam is calculated by dividing the current by the collection area, 0.71cm^2 . The Faraday cup sensor is mounted on the shutter to allow the sensor to be positioned in the center of the ion beam. The deposition rate sensor is mounted to the side of the substrate; this sensor is a quartz-crystal resonator. The shift in frequency of an oscillating circuit incorporating the resonator is calibrated into a thickness signal. By differentiating the thickness signal with respect to time, the average rate of deposition is also obtained.

The temperature of the substrate is monitored by a thermocouple positioned so that it rests on the back side of the substrate. A manipulator raises and lowers the thermocouple so that the substrate can be slid in and out. The signal from the thermocouple is used as feedback to a temperature controller that adjusts the power to the heating lamps, maintaining the substrate at a constant temperature.

CHAPTER V. EXPERIMENTAL PROCEDURE

The experimental procedure consisted of preparing the substrate, choosing the deposition parameters, and depositing the film. The changes made in the system are also described, with an explanation of how the operating procedure was altered after each change. A detailed listing of the steps used for substrate preparation and system operation is given in Appendix D, so only a brief description is given here.

Substrate Preparation

The substrates were cleaned using a standard cleaning procedure. Silicon substrates were cleaned in organic solvents followed by a weak hydrofluoric acid etch to remove any native oxides, while gallium arsenide substrates were cleaned in organic solvents followed by a planar etch [22]. The clean substrate was placed in vacuum as quickly as possible.

Choosing Deposition Parameters

The main parameters to be set during an ICB deposition are the acceleration voltage, the substrate temperature, the ionization voltage and current, and the crucible temperature. The deposition parameters are discussed more fully in Chapter VI.

Because of the limited number of depositions performed, the parameter values were adapted from previously reported

values and a limited number of theoretical calculations. Previous attempts by Yamagishi et al. to deposit germanium films using ICB deposition indicated that low acceleration voltages and substrate heating resulted in the best crystallinity of the deposited film [9]. For these depositions, higher acceleration voltages (2.4kV) without substrate heating were initially tried. Later attempts used lower voltages (0.5kV) and substrate heating. The ionization voltage and filament current were set to maximize the emission current, to ionize the highest percentage of the clusters possible.

To determine a suitable crucible temperature, the germanium vapor pressure curve (Figure 2.2) was fitted to an equation as described in Chapter II. The values used are listed in Table 5.1. The coefficients obtained for the equation are given in Table 5.2. Using these coefficients, the crucible temperature was chosen to be in the range 1775-1900°C (2048-2173K), corresponding to a germanium vapor pressure in the range 1-3torr. Initially the crucible temperature was adjusted until a certain rate of deposition was obtained; for later depositions, the crucible temperature was set without regard to the deposition rate.

System Operation

Despite the changes made in the system, the basic steps to perform a deposition remain relatively unchanged from the

Table 5.1. Vapor pressure of germanium [16]

Temperature (K)	Pressure (torr)
1670	0.01
1830	0.1
2050	1.0
2320	10.0
2680	100.0

Table 5.2. Germanium vapor pressure coefficients

Coefficient	Value
A	-5.06638668673 $\times 10^5$
B	-1.58059487121 $\times 10^3$
C	3.18516683619 $\times 10^{-1}$
D	-2.4434021124 $\times 10^{-5}$
E	4.93140675383 $\times 10^3$

first procedure used. Before anything is begun, it is important to check all the cooling systems--water cooling for the process chamber, ion source, and deposition monitor, and forced-air cooling for the ion source feed-throughs. After a substrate is in place in the process chamber, the substrate temperature controller is set to the desired temperature. This is done so that the substrate is as clean as possible; the heat treatment ensures that contaminants such as water will be minimized.

While the substrate is heating, the ion source is warmed up. The crucible heater is set directly to the desired current. Due to the large time constant of the picket heater the crucible warms up slowly, reaching an equilibrium temperature in about 15 minutes. The acceleration and

ionization supply voltages are also set directly to the desired voltage. After the ionization supply is set, the ionization filament can be adjusted for the desired emission current.

Once the system has reached equilibrium, the deposition conditions can be adjusted to obtain the desired parameters. Deposition rate, Faraday cup current, and ionization current are the most important parameters. After everything is as desired, the shutter is opened and the deposition begun. All the parameters are recorded; Figure 5.1 shows a form useful for this. The form has sufficient columns to allow the conditions to be recorded at the start and end of the deposition and at two intermediate times. This is important in case the conditions change, either by operator adjustment or by system instability.

After the deposition, the shutter is closed. The substrate heaters are shut off first, to prevent any undesired annealing of the film. The ion source is ramped down by first turning off the crucible heater; again, the time constant is large enough that the heater can be shut off without any delay. The ionization filament is shut off, followed by the ionization supply and the acceleration supply. The system is allowed to cool for several hours after which the cooling systems are shut off. The substrate can be removed at any time, but to minimize thermal stress it is best to leave it in the process chamber until it has cooled.

IONIZED CLUSTER BEAM DEPOSITION

Sample ID:		Material/Substrate:			
Date:		Operator:			
Acceleration	V	V			
	I	mA			
Ionization	V	V			
	I	mA			
Filament	V	V			
	I	A			
Crucible	P	kW			
	I	A			
	T	°C			
Substrate	T	°C			
Pressure		Pa			
Deposition Rate		Å/s			
Elapsed Time		m:s			
Thickness		Å			
Notes:					

Figure 5.1. Form for recording deposition conditions

System Configurations

During the sequence of depositions performed, several system configurations were used. Each configuration change was due either to a breakdown, such as a burned-out filament, or to an improvement, such as a better substrate thermocouple arrangement.

After three germanium depositions, the ionization filament was replaced. The new filament operated similarly to the original one. Prior to beginning the germanium depositions, the ion source had been used for aluminum depositions; after eight germanium depositions the source was partially cleaned, removing an accumulation of aluminum and germanium. After eight and ten depositions, the crucible nozzle was cleaned to remove deposits of germanium that had condensed in and around the nozzle, effectively plugging it. None of these changes affected the operating conditions. Finally, after twelve depositions, the substrate track was completely reworked to allow the Faraday cup to be attached to the shutter. This was done so that the ion current could be measured in the center of the ion beam; the change did not affect the operating conditions.

CHAPTER VI. DEPOSITION PARAMETERS AND CONDITIONS

The important parameters for ICB deposition are divided into information about the particles, the deposition conditions, and the system configuration [20]. With complete information about these parameters, it is theoretically possible to duplicate the conditions and reproduce the deposition. The first three sections of this chapter discuss these parameters; the last section summarizes the conditions for the germanium depositions.

Important Parameters

Of primary importance in ICB deposition are the particles. To totally characterize the deposition, information on the neutral flux, the ionized flux, the size distribution, and the energy of the particles must be known. Measuring these quantities, however, is not trivial. For example, a technique such as time-of-flight mass spectrometry can be used to determine the size distribution of the ionized particles, but this is not necessarily the size distribution of the neutral particles. Larger particles might be more likely to become ionized.

Using the data available with the present system, estimates of the average particle size and the energy per atom can be made. The first calculation requires the rate of deposition, the Faraday cup current, and an estimate of the

ionization percentage, while the second calculation requires the rate of deposition, the Faraday cup current, the crucible temperature, and the acceleration voltage.

Average particle size

The current density (A/cm^2) is the effective atomic charge for a particle in the cluster beam ($C/atom$) multiplied by the atomic flux at the substrate ($atoms/s \cdot cm^2$). The effective atomic charge is simply given by:

$$\text{effective atomic charge} = \frac{p}{n} q \quad (6.1)$$

where p is the ionization percentage, n is the average cluster size (atoms), and q is the electronic charge ($q=1.6 \times 10^{-19}C$). The atomic flux at the substrate is the rate of deposition divided by the volume of a single atom. The atomic volume (\AA^3) is calculated using the material density, d (g/cm^3), and the atomic mass, M (amu):

$$\begin{aligned} \text{atomic volume} = V &= \frac{1.661 \times 10^{-24} g}{\text{amu}} \times M \times \frac{1}{d} \times \frac{10^{24} \text{\AA}^3}{\text{cm}^3} \\ \text{or } V &= 1.661 \frac{M}{d} \end{aligned} \quad (6.2)$$

Therefore, the atomic flux is:

$$\text{atomic flux} = \frac{r}{V} \times \frac{10^{16} \text{\AA}^2}{\text{cm}^2} \quad (6.3)$$

where r is the deposition rate ($\text{\AA}/s$). Multiplying equation 6.1 and equation 6.3 gives the current density, J :

$$J = \frac{p}{n} q \frac{10^{16} \text{rd}}{1.661 \text{M}} \quad (6.4)$$

Rearranging leads to:

$$\frac{p}{n} = 1.661 \times 10^{-16} \frac{\text{JM}}{\text{rd}} \frac{1}{q} \quad (6.5)$$

which gives the ratio of the ionization percentage to the average particle size as a function of the Faraday cup current density and the rate of deposition.

Energy per atom

Let the energy of an un-ionized particle at the substrate be E_n and the energy of a singly ionized and accelerated particle be E_i . If the units are electron volts (eV) and the average particle size is n atoms, then:

$$E_i = E_n + \frac{v}{n} \quad (6.6)$$

where v is the acceleration voltage. The effective energy per particle arriving at the substrate is then the energy of the ionized particles multiplied by the percentage of ionized particles plus the energy of the un-ionized particles multiplied by the percentage of un-ionized particles, or:

$$E = pE_i + (1-p)E_n \quad (6.7)$$

where p is the ionization percentage. Substituting equation 6.6 into equation 6.7 leads to:

$$E = \frac{p}{n} v + E_n. \quad (6.8)$$

It is of note that this expression does not require the percentage of ionization to be known, only the ratio p/n . For molecular beams, the energy per particle is the thermal energy [10]:

$$E_n = \frac{3}{2} \frac{kT}{q}. \quad (6.9)$$

Substituting equations 6.5 and 6.9 into equation 6.8 gives the desired result:

$$E = \frac{p}{n} v + \frac{3}{2} \frac{kT}{q} \quad (6.10)$$

which relates the energy per atom at the substrate to the acceleration voltage, the crucible temperature, the Faraday cup current density and the deposition rate.

The energy per atom at the substrate is important because it affects the film growth condition. If a particle is too energetic, it will cause damage to the film or the substrate. If a particle is not energetic enough, it will not adhere strongly to the substrate. The optimum energy range is 0.1-100eV/atom [15].

The second set of important parameters are the deposition characteristics: the flux uniformity, the substrate area, the substrate temperature, and the film thickness. All of these are easily recorded or measured. The flux uniformity can be

determined by measuring the thickness variation over a large-area substrate. The substrate area is simple to calculate or measure. Care should be taken that the substrate temperature measurement accurately reflects the actual substrate temperature. The thickness of the deposited film is measured using a quartz crystal deposition monitor, with confirmation made by a stylus-type thickness profiler.

The third set of parameters are the system parameters. These parameters describe the physical setup of the deposition apparatus and the operating values for the ion source. The dimensions of the crucible nozzle, the crucible temperature, the ionization extraction voltage and emission current, and the source-to-substrate separation all fall under this category. All are easily measured.

Deposition Conditions

A sequence of 17 germanium depositions was made; conditions for each deposition are given in Table 6.1. As discussed in Chapter IV, the system configuration was changed several times. Because of these changes, it was impossible to optimize the deposition conditions.

Table 6.2 shows the ratio of the ionization percentage to the average particle size and the energy per atom (as discussed above) for the depositions made with the Faraday cup installed. The cluster size estimate is based on 5% ionization.

Table 6.1. Deposition conditions

ID#	Substrate	Acceleration	Ionization	Current	Crucible Temperature
		Voltage	Voltage		
		V	V	mA	°C
88	p-Si	2000	500	39	1800
89	GaAs	3000	500	40	1890
90	n-Si	500	500	40	1900
***** Ionization filament replaced					
91	n-Si	2500	500	41	1900
92	n-Si	500	500	41	1820
93	n-Si	0	500	40	1830
94	n-Si	500	500	40	1850
95	n-Si	1000	500	40	1900
***** Crucible nozzle plugged					
96	n-Si	500	500	40	1770
97	p-Si	500	500	40	1850
98					
***** Crucible nozzle plugged					
99	n-Si	2500	500	50	1775
100	n-Si	500	500	50	1795
***** Substrate track replaced					
101	n-Si	500	500	50	1825
102	n-Si	500	500	50	1830
103	n-Si	2000	290	25	1810
104	n-Si	3000	100	1	1825
105	n-Si	500	500	50	1825

Substrate Temperature	Rate of Deposition	Thickness	Faraday Cup Current	Cup Rate
°C	Å/s	Å	$\mu\text{A}/\text{cm}^2$	Å/s
	1.1	5000		
200	1.5	5100		
380	2.3	5000		
400	2.3	5000		
405	1.3	5000		
400	0.9	5000		
300	1.0	5229		
300	0.5	4547		
400	1.3	10760		
400	1.1	5002		
450	1.4	5000		
500	1.6	5100		
400	2.0	15600	0.45	2.5
400	2.0	4800	0.35	2.0
400	1.9	4800	3.00	1.9
495	2.5	4400	1.00	2.5
>550	2.8	6700	0.35	2.8

Table 6.2. Particle size and average particle energy

ID#	n/p (atoms)	n (atoms)	E (eV/atom)
101	394	20	1.50
102	406	20	1.47
103	45	2	44.7
104	177	9	17.1
105	568	28	1.12

The crucible used for the depositions was made of high-density graphite with a nozzle 1mm long by 1mm in diameter. Acceleration was over the entire 25cm source-to-substrate separation. The boat in which the silicon substrates were held exposed a 2.5in diameter opening to the ion beam, resulting in a substrate area of approximately 32cm². Due to its smaller size, the gallium arsenide substrate only exposed a 1in diameter circle to the ion beam, for a substrate area of 5cm².

CHAPTER VII. CHARACTERIZATION OF DEPOSITED FILMS

The germanium films were analyzed for both mechanical and electrical characteristics. Visual inspection, X-ray diffraction, and Auger electron spectroscopy were used to determine the mechanical characteristics, while four-point probe measurements were used to determine the electrical characteristics. The data collected for the film characteristics are presented in Table 7.1.

Mechanical Characteristics

The first observation that is made about any thin film is the surface condition. A shiny appearance indicates a smooth surface, while a hazy appearance indicates a rough surface. No conclusions could be made from these observations other than the surface condition did not indicate anything about the film quality, either mechanically or electrically.

To determine the crystalline structure, X-ray diffraction techniques were employed. Two techniques were used--a standard diffractometer technique and a special technique using a Buerger precession camera that gives an undistorted representation of the reciprocal space for both the film and the substrate [23,24].

A standard X-ray plot of 2θ is shown in Figure 7.1 for a single-crystalline sample. Figure 7.2 is a 2θ plot for a polycrystalline sample. This technique provides a measure of

Table 7.1. Results of characterizations

ID#	Surface	X-ray	Buerger X-ray	AES ^a		
				Al	C	O
88	smooth	amorphous				
89	smooth	(100)	(100) epitaxial			
90	rough	(100)	(100) epitaxial	11/9	2	
91	rough					
92	rough	(100)	(100) epitaxial	7/x	x	x
93	smooth	(100)	(100) epitaxial	10/2	2	2
94	smooth	poly		16/x	2	
95	rough		(100) preferred	21/4	1	x
96	rough		polycrystalline	x/x	2	
97	rough		polycrystalline		.1	.1
98						
99	rough					
100	rough					
101	smooth		polycrystalline	6/x	2	
102	smooth		polycrystalline			
103	smooth		polycrystalline	7/x	1	x
104	smooth					
105	smooth		(100) epitaxial			

^aMaximum percentage listed for aluminum, carbon, and oxygen. For aluminum, the form is surface/bulk. An "x" indicates the level is below the AES detection level.

Resistivity $\text{m}\Omega\cdot\text{cm}$	Doping Concentration cm^{-3}	Atomic % Dopant
0.32	3×10^{20}	0.7
0.32	3×10^{20}	0.7
0.38	2×10^{20}	0.5
0.46	1×10^{20}	0.2
0.82	5×10^{19}	0.1
0.42	1×10^{20}	0.3
50.5	1×10^{17}	0.0002
24.6	3×10^{17}	0.0007
1.3	2×10^{19}	0.05
1.3	2×10^{19}	0.05
1.1	2×10^{19}	0.05
1.2	2×10^{19}	0.05
0.66	7×10^{19}	0.2

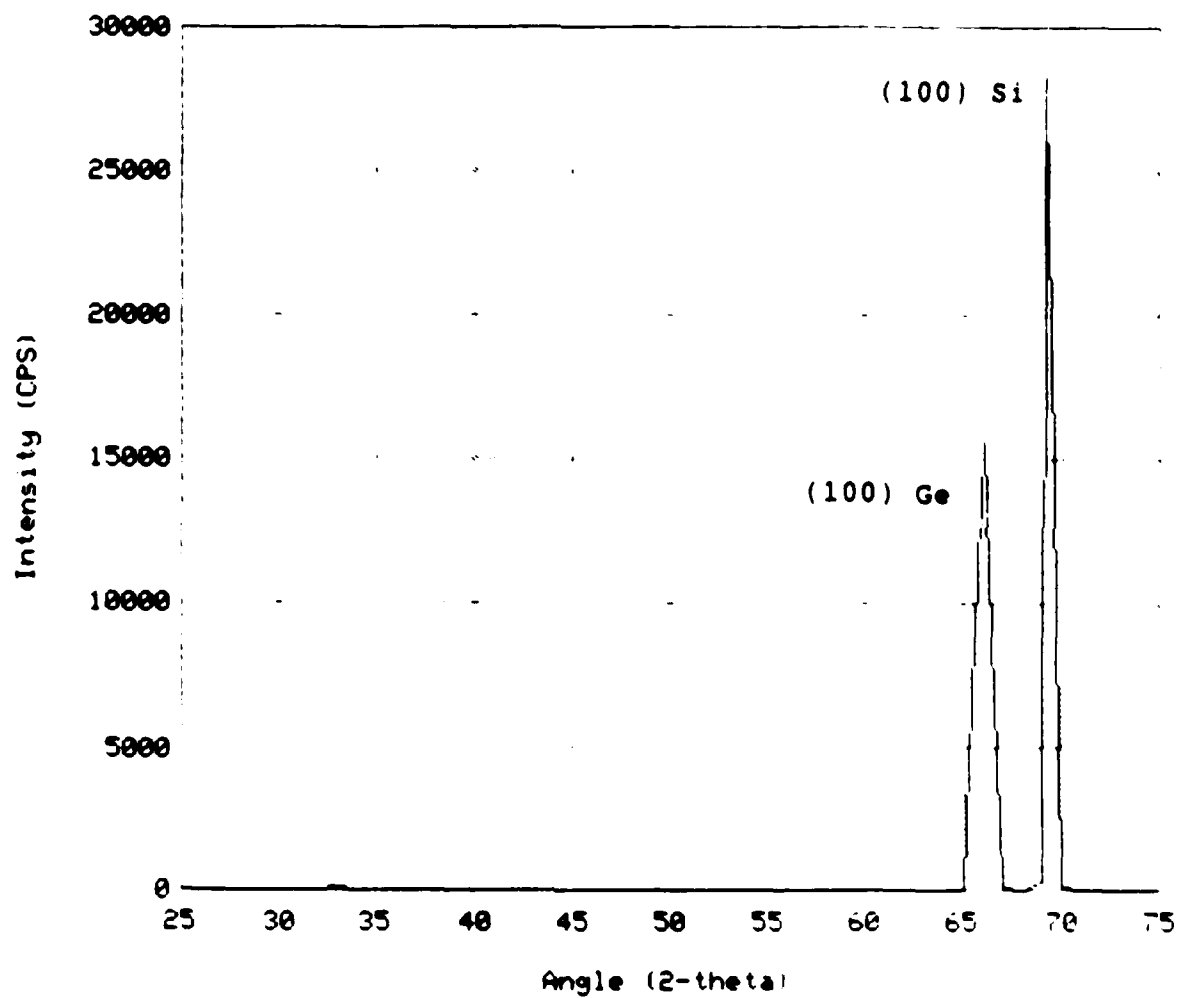


Figure 7.1. X-ray diffraction plot for a single-crystalline film

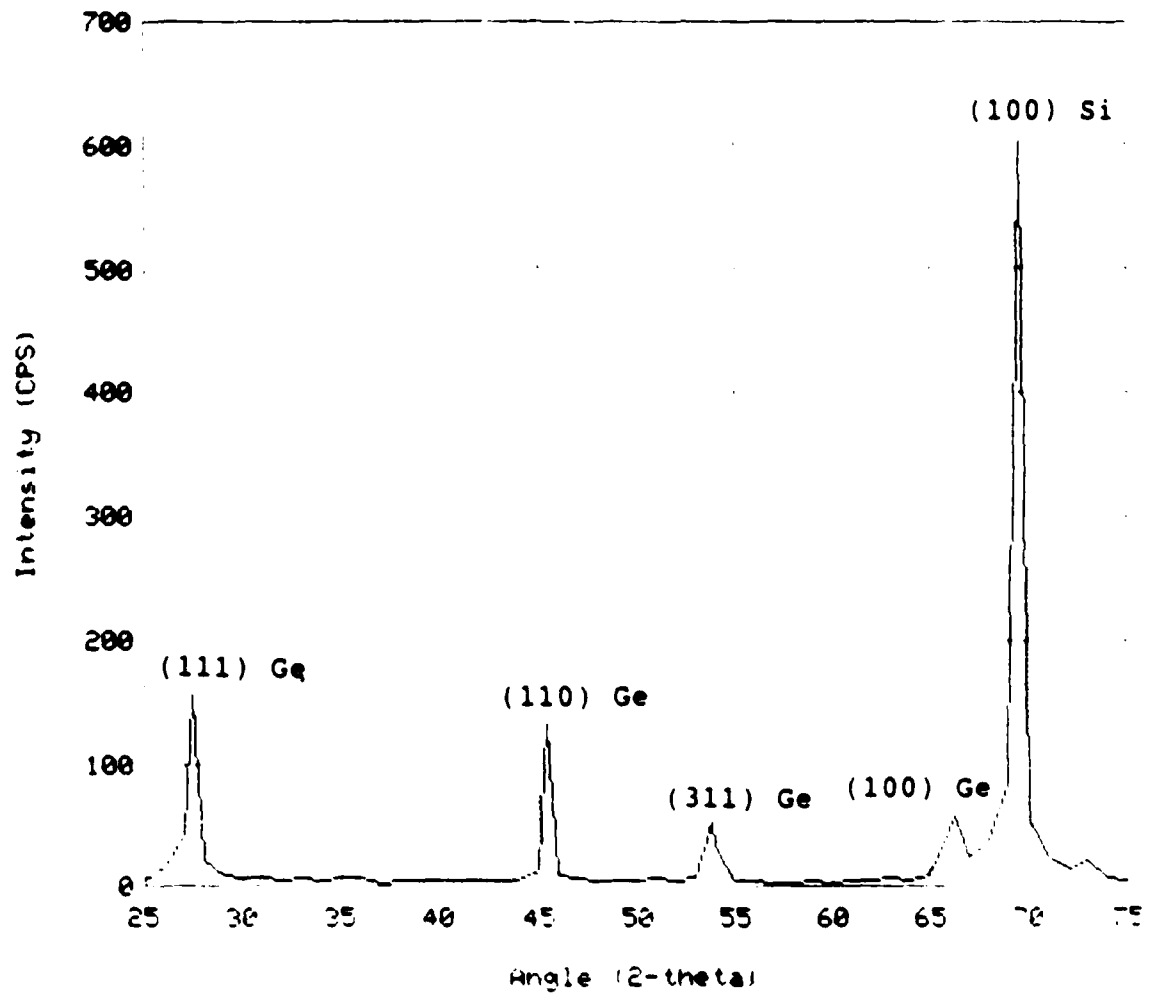


Figure 7.2. X-ray diffraction plot for a polycrystalline film

the crystallinity, in this case (100) orientation for the single-crystalline sample and (100), (110), (111), and (311) for the polycrystalline sample, but it does not provide information about the orientation of the film's lattice with respect to the substrate's lattice. For this information, the Buerger camera technique was invaluable. A picture resulting from this technique is shown in Figure 7.3; a diagram indexing the dots is shown in Figure 7.4. The double dots in the photograph are the lattice sites of atoms. The inner dot corresponds to a germanium atom, the outer to a silicon atom. For a polycrystalline sample, rings are observed instead of dots.

The impurity concentration of some of the films was measured using depth-profiling Auger electron spectroscopy (AES). A plot of the relative concentrations versus sputtering time (depth into the sample) is shown in Figure 7.5. The levels of oxygen and carbon are below the instrument's detection level, as is the aluminum trace. For the samples doped with aluminum there was typically 5-20% aluminum on the surface but less than 1% (the resolving capability of the AES instrument) in the bulk of the film.

Electrical Characteristics

The resistivities of the films were measured using the four-point probe technique and the data used to determine the doping concentrations. The doping concentrations were

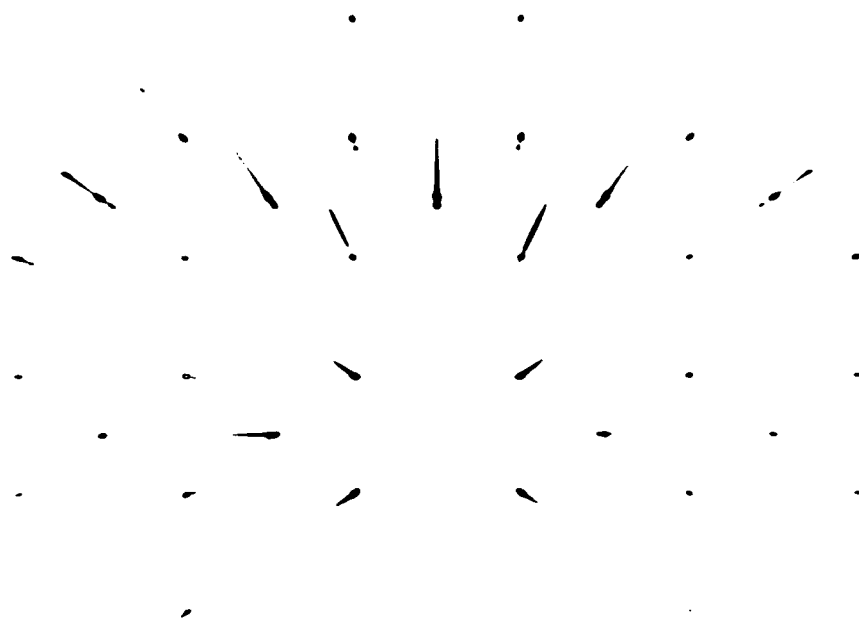


Figure 7.3. Buerger precession camera photograph for a single-crystalline film

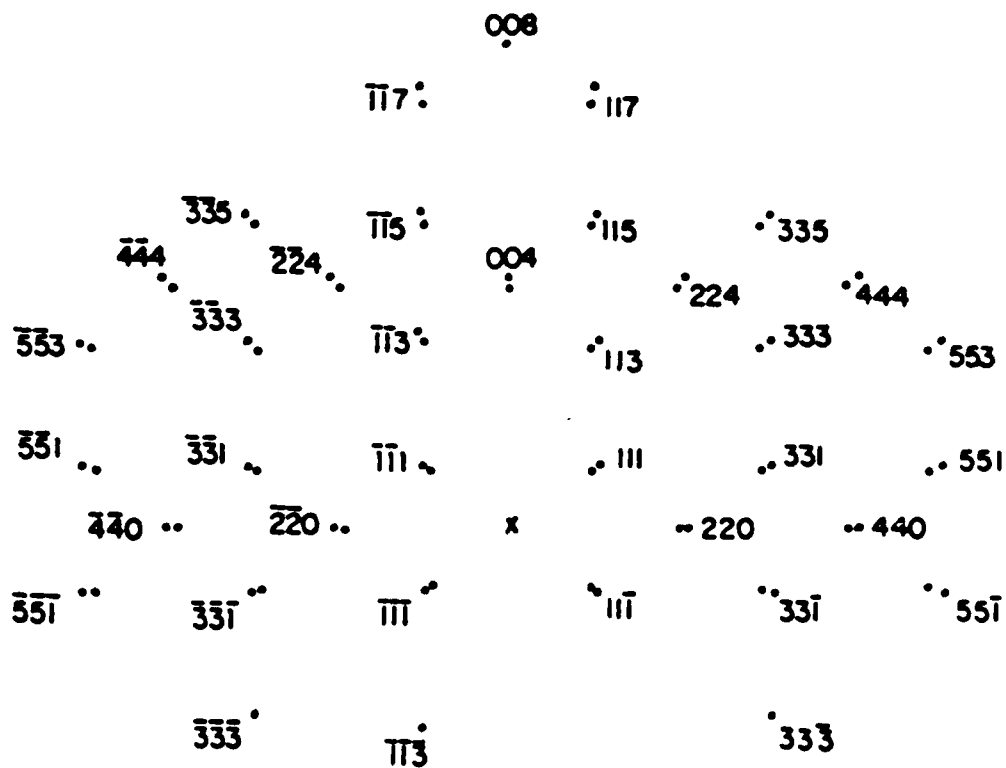


Figure 7.4. Indices for a Buerger precession camera photograph of a single-crystalline film

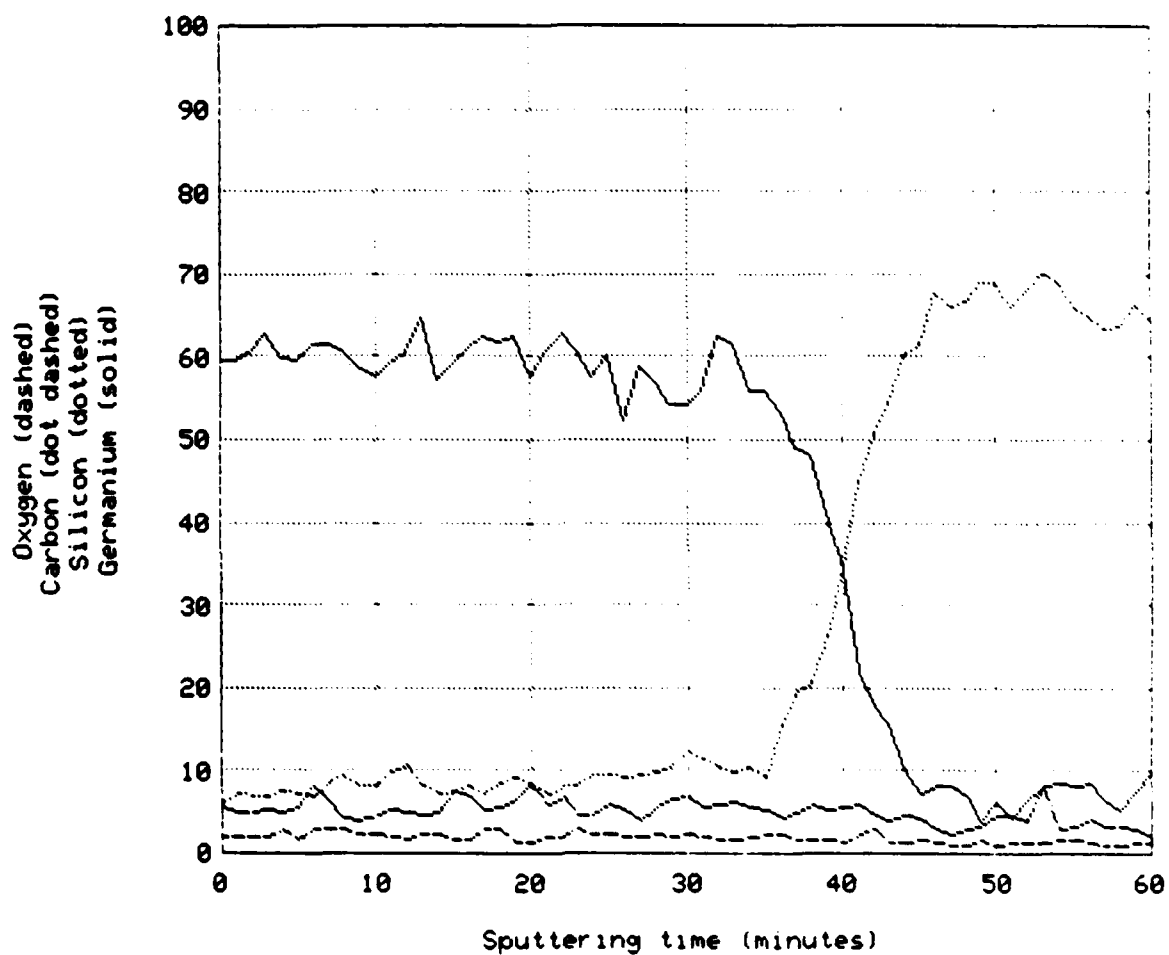


Figure 7.5. Auger electron spectroscopy depth profile

obtained using Figure 7.6, a plot of resistivity versus doping concentration. Assuming only one dopant, the atomic percentage of the dopant in the film is easily calculated from the doping concentration by using the density and the atomic mass of germanium. The density of atoms in germanium is:

$$\frac{5.35\text{g}}{\text{cm}^3} \times \frac{1 \text{ mole}}{72.59\text{g}} \times \frac{6.022 \times 10^{23} \text{atoms}}{1 \text{ mole}} = 4.44 \times 10^{22} \text{cm}^{-3}. \quad (7.1)$$

The atomic fraction of the dopant is then the ratio of the doping concentration to the density of germanium atoms:

$$\text{atomic fraction} = \frac{\text{doping concentration}}{4.44 \times 10^{22} \text{cm}^{-3}}. \quad (7.2)$$

The atomic percentage of dopant is the atomic fraction multiplied by 100.

As shown in Figure 7.7, the solid solubility limit of aluminum in germanium is less than 1 atomic percent. This corresponds in magnitude to the values obtained by measuring the resistivities of the germanium films. Considering the AES data that indicates a relatively high concentration of aluminum on the surface of the films, it is speculated that the aluminum only dopes the films up to the solid solubility limit; excess aluminum accumulates on the surface of the sample. In actuality, the germanium probably diffuses through the surface layer of aluminum after being deposited.

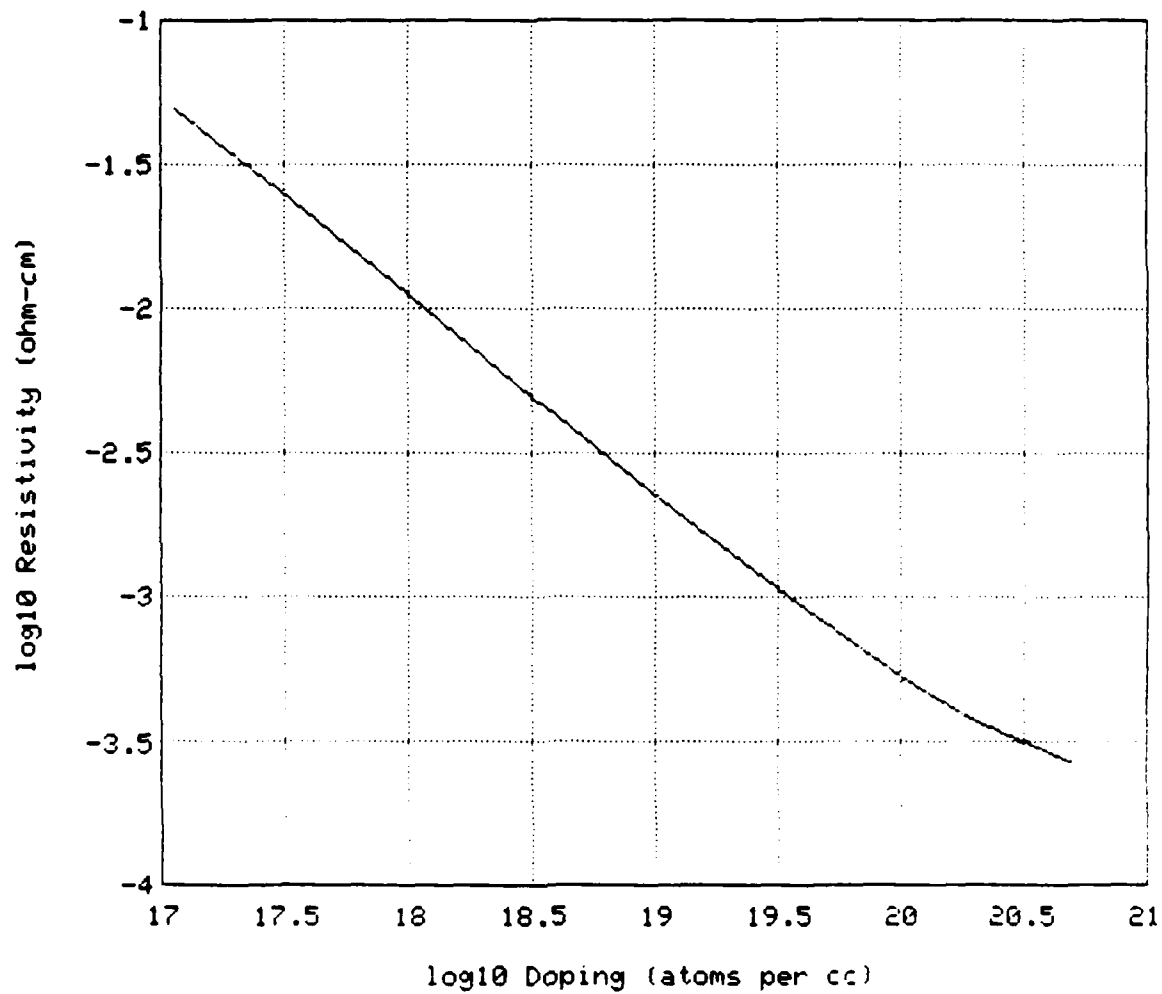


Figure 7.6. Resistivity of germanium as a function of doping concentration [25]

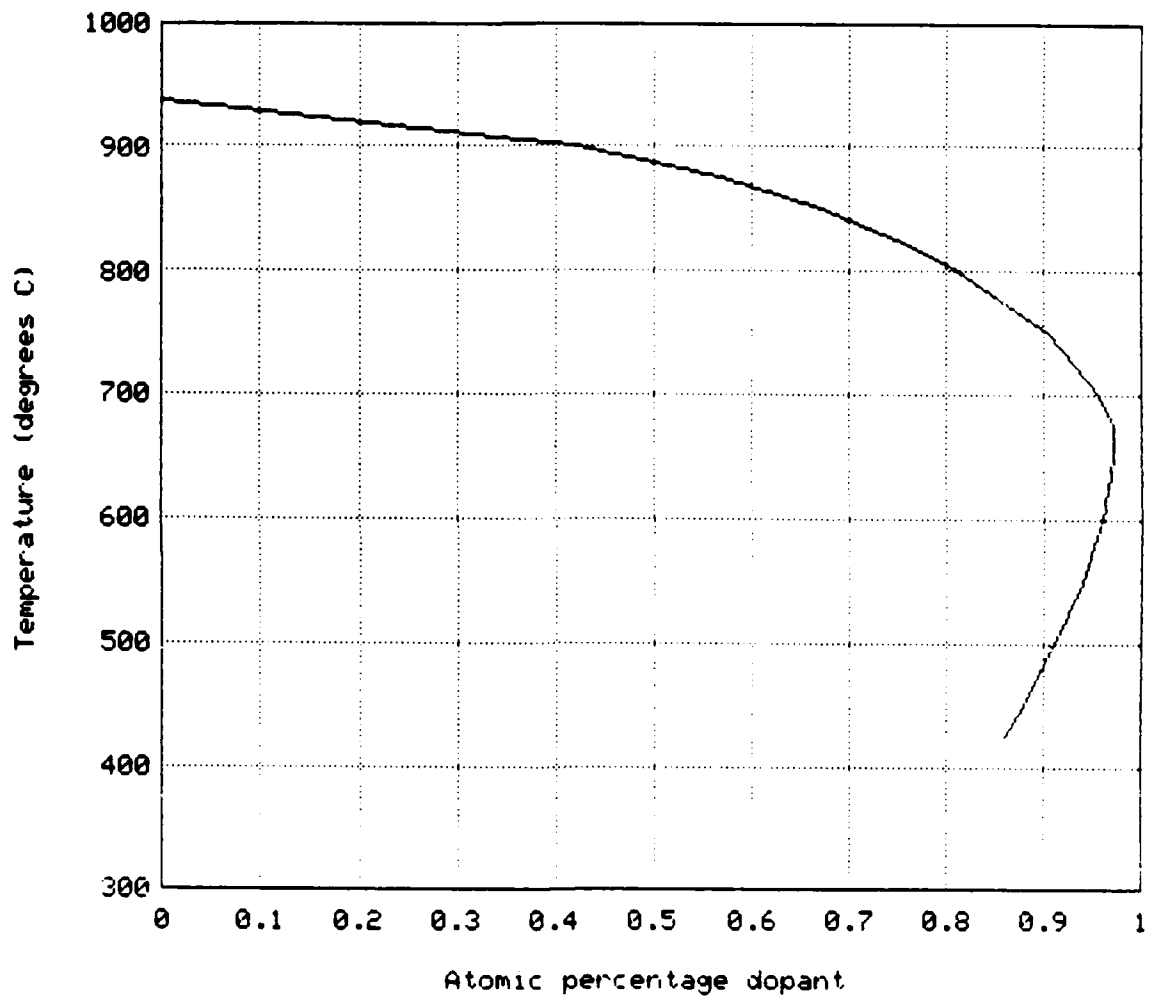


Figure 7.7. Solid solubility limit of aluminum in germanium [26]

CHAPTER VIII. CONCLUSIONS AND RECOMMENDATIONS

The film characteristics presented in Chapter VII indicate that epitaxial germanium films are possible using low substrate temperatures, if a small amount of aluminum is present in the film. The aluminum presumably changes the lattice parameter of the germanium, allowing it to match the lattice of the substrate.

Films numbered 101 and greater reflect an attempt to vary the amount of aluminum in the crucible with the germanium. Presumably, a certain percentage of aluminum is required to obtain epitaxy at a given substrate temperature. Another variable was introduced at the same time as the new crucible alloy--the substrate track was rebuilt to allow the Faraday cup to be mounted on the shutter. The temperature of a substrate is always difficult to measure, and there is little confidence that the temperature readings before the reworking are comparable to those after. An even more recent reworking configured the thermocouple to contact the back side of the substrate, but no depositions have been performed with this configuration.

The results, however, indicate that excellent films were obtained. The epitaxial films varied somewhat in quality, but represent some of the best germanium on silicon reported. In addition, film number 105 shows that epitaxy is achievable using an aluminum-germanium alloy (Al-Ge, affectionately

dubbed "algae") for the source material. Because of this, the results presented are an important and original contribution to thin-film technology.

To continue this research, more films need to be deposited with emphasis on developing a pattern in the deposition parameters. In particular, the substrate temperature, crucible temperature, and average energy per atom are considered important. No conclusions can be made about the data obtained using the Faraday cup at this point due to the lack of information about the films and the small data set. Further work also needs to be done to explore the role of the aluminum in obtaining epitaxy. A study of the quality of the crystallinity versus aluminum concentration would be interesting. A study of the role of the aluminum at the germanium-silicon interface would also be interesting; lattice-imaging techniques would be very useful for this.

To really develop the ICB technique to its fullest extent, further data should be collected on the deposition parameters. A time-of-flight mass spectrometer capable of measuring the cluster size distribution would provide more insight into the average energy per atom. A technique also needs to be developed to determine if the ionized-cluster size distribution is the same as that for un-ionized particles.

Finally, the theory needs to catch up with the practice. The ICB technique deposits high-quality films. The technique is currently useful, but to be fully developed, the formation

of clusters and the effect of acceleration need to be explored and explained.

REFERENCES

1. Robinson, Arthur L. "A Silicon Solution for Gallium Arsenide IC's." Science 232 (May 16, 1986), 826-828.
2. Uppal, Parvez N. and Kroemer, Herbert. "Molecular Beam Epitaxial Growth of GaAs on Si(211)." Journal of Applied Physics 58 (September 15, 1985), 2195-2203.
3. Neumann, D. A.; Zhu, Xiaomei; Zabel, H.; Henderson, T.; Fischer, R.; Masselink, W. T.; Klem, J.; Penk, C. K.; and Morkoc, H. "Structural Properties of GaAs on Si and Ge Substrates." Journal of Vacuum Science and Technology B 4 (March/April 1986), 642-644.
4. Sze, S. M. Physics of Semiconductor Devices. New York: Wiley-Interscience, 1981.
5. Hafich, M. J.; Gillenwater, R. L.; Robinson, G. Y.; and Sheldon, P. "Summary Abstract: Ge/Si Heterojunction Ohmic Contacts Formed by Molecular Beam Epitaxy." Journal of Vacuum Science and Technology B 4 (March/April 1986), 661.
6. Fletcher, Robert M.; Wagner, D. Ken; and Ballantyne, Joseph M. "Growth and Characterization of Epitaxial GaAs on Ge/Si Substrates." Thin Films and Interfaces II, pp. 417-422. Edited by J. E. E. Baglin, D. R. Campbell, and W. K. Chu. New York: North-Holland, 1984.
7. Windischmann, H.; Cavese, J. M.; Collins, R. W.; Harris, R. D.; and Gonzalez-Hernandez, J. "The Structure of Si and Ge Deposited by Ion Beam Sputtering." Thin Films: The Relationship of Structure to Properties, pp. 187-194. Edited by Carolyn Rubin Aita and K. S. SreeHarsha. Pittsburgh, PA: Materials Research Society, 1985.
8. Takagi, Toshinori. "Ionized-Cluster Beam Deposition and Epitaxy." Annual Report 1984 of the Takagi Research Laboratory (Kyoto, Japan: Kyoto University Department of Electronics), pp. 105-126.
9. Yamagishi, Chouho; Sano, Yoshiaki; Nonaka, Toshio; Ishida, Toshimasa; and Kaminishi, Katsuzo. "Crystallization of Germanium Films on Silicon by Ionized-Cluster Beam Deposition." Proceedings of the International Ion Engineering Congress, Kyoto, Japan, 1983, pp. 1209-1214.

10. Kuiper, A. E. T.; Thomas, G. E.; and Schouten, W. J. "Ion Cluster Beam Deposition of Silver and Germanium on Silicon." Journal of Crystal Growth 51 (1981), 17-40.
11. Takagi, Toshinori; Yamada, Isao; Matsubara, Kakuei; and Takaoka, Hiroshi. "Ionized-Cluster Beam Epitaxy." Journal of Crystal Growth 45 (1978), 318-325.
12. McCalmont, Jonathan S.; Shanks, Howard R.; and Lakin, Kenneth M. "Aluminum and Germanium Thin Films Deposited in a Ultrahigh-Vacuum Ionized-Cluster Beam System." Proceedings of the International Workshop on Ionized-Cluster Beam Technique, Tokyo, Japan, 1986, pp. 119-130.
13. McCalmont, Jonathan S.; Shanks, Howard R.; and Lakin, Kenneth M. "Thin Films of Germanium Deposited by the Ionized-Cluster Beam Technique." Submitted for publication, Journal of Vacuum Science and Technology B.
14. Stein, Gilbert D. "Atoms and Molecules in Small Aggregates: the Fifth State of Matter." The Physics Teacher 17 (November 1979), 503-512.
15. Yamada, Isao. "Some Important Characteristics in the Film Formation by ICB." Proceedings of the International Workshop on Ionized-Cluster Beam Technique, Tokyo, Japan, 1986, pp. 101-108.
16. Honig, Richard E. "Vapor Pressure Data for the Solid and Liquid Elements." RCA Review 23 (December 1962), 567-586.
17. Yamada, I.; Takaoka, H.; Inokawa, H.; Usui, H.; Cheng, C.; and Takagi, T. "Vaporized-Metal Cluster Formation and Effect of Kinetic Energy of Ionized Clusters on Film Formation." Thin Solid Films 92 (1982), 137-146.
18. Usui, H.; Ueda, T.; Yamada, I.; and Takagi, T. "Analysis of Vaporized Metal Cluster Formation by Classical Nucleation Theory." Proceedings of the 9th Symposium on Ion Sources and Ion-Assisted Technology, Tokyo, Japan, 1985, pp. 39-44.
19. Knauer, Wolfgang. Presentation given at the International Workshop on Ionized-Cluster Beam Technique, Tokyo, Japan, June 3, 1986.

20. Knauer, Wolfgang. Presentation given at the International Workshop on Ionized-Cluster Beam Technique, Kyoto, Japan, June 6, 1986.
21. Gspann, Jurgen. "On the Internal State of Free Clusters and Its Relation to Deposition." Proceedings of the International Workshop on Ionized-Cluster Beam Technique, Tokyo, Japan, 1986, pp. 109-116.
22. Chambers, Frank, AMOCO Research Center, Naperville, IL. Private communication.
23. Staudenmann, J. -L.; Horning, R. D.; and Knox, R. D. "Buerger Precession Camera and Overall Characterization of Thin Films and Flat Plate Crystals." Submitted for publication September 19, 1986, Journal of Applied Crystals.
24. Horning, R. D. and Staudenmann, J. -L. "Characterization of Thin Films, Epitaxial Layers, and Superlattices Using the Precession Camera." Physics Department, Iowa State University, Ames, IA.
25. Trumbore, F. A. and Tartaglia, A. A. "Resistivities and Hole Mobilities in Very Heavily Doped Germanium." Journal of Applied Physics 29 (October 1958), 1511.
26. Trumbore, F. A.; Porbansky, E. M.; and Tartaglia, A. A. "Solid Solubilities of Aluminum and Gallium in Germanium." Journal of the Physics and Chemistry of Solids 11 (1959), 239-245.

ACKNOWLEDGEMENTS

Most of all, I would like to thank my wife, Cindy, who has put up with a grumpy husband most of her married life.

A special thanks goes to my major professors, Ken Lakin and Stan Burns, and to Howard Shanks for the encouragement they have given me. Thanks also go to the staff of the Microelectronics Research Center, especially Kevin McCarron for his patient help, and Shirley Riney for occasionally letting me bump her off the computer so that I could print a file.

The assistance of several people is gratefully acknowledged: John Martin for X-ray analysis; Bob Horning for the precession X-ray measurements; and Al Bevolo, Ruth Shinar, and Linda Seaverson for the Auger analyses.

This work was done at the Microelectronics Research Center at Iowa State University.

Mom and Dad, I told you I'd finish this some day!

ALUMINUM AND GERMANIUM THIN FILMS DEPOSITED IN AN
ULTRAHIGH-VACUUM IONIZED-CLUSTER BEAM SYSTEM

Jonathan S. McCalmont, Howard R. Shanks, and Kenneth M. Lakin
Microelectronics Research Center
Iowa State University, Ames, IA 50010 U.S.A.

Presented at the
International Workshop on Ionized-Cluster Beam Technique
June 3-4, 1986
Tokyo, Japan

APPENDIX A. ALUMINUM AND GERMANIUM THIN FILMS DEPOSITED
IN AN ULTRAHIGH-VACUUM IONIZED-CLUSTER BEAM
SYSTEM

Abstract

Aluminum was deposited on (100) p-doped silicon using the ionized-cluster beam deposition method. Deposition was done at 1.0kV acceleration with a crucible temperature of 1700°C in a UHV chamber which can attain 2×10^{-8} Pa (1.5×10^{-10} torr) ultimate pressure. Pressure during deposition was 2.6×10^{-5} Pa (2×10^{-7} torr). The impurity concentrations and the interface characteristic of the films were analyzed by depth-profiling Auger electron spectroscopy, the crystal orientation by X-ray diffraction, and the electrical resistivity and the thickness variation by four-point probe measurements. The results indicated a (110) crystal orientation and no impurity concentration greater than 0.1%. The interface region consisted of an aluminum-silicon mixture about 500Å thick. For a film thickness of 5500Å the sheet resistance was $0.065 \Omega/\square$, corresponding to a resistivity of $3.6 \mu\Omega \cdot \text{cm}$, about 130% of the bulk value for aluminum. The thickness variation was 6% over the surface of a three-inch wafer. Also deposited were thin films of germanium on (100) n-doped silicon and (100) semi-insulating gallium arsenide substrates. Crucible temperatures were in the range 1850-1900°C. Analysis of these films is at present only qualitative, but suggests that a substrate temperature of 400°C and an acceleration voltage of

3.0kV are required for a good film, as determined by optical inspection.

Introduction

Ionized-cluster beam (ICB) deposition is a thin-film deposition technique first reported in 1972 by a group of researchers at Kyoto University in Japan [1]. The technique is characterized by the ability to deposit high-quality films at low substrate temperatures [2]. Metals, semiconductors, and insulators have successfully been deposited onto a variety of substrate types using the ICB process [3-7].

This paper describes an experimental ICB system recently installed and now in operation at Iowa State University. The system is unique because of its ability to operate in the ultrahigh vacuum region, because of its in situ sensors, and because of its inclusion in a unique thin-film deposition and analysis facility. With this facility, thin-films can be deposited and analyzed by several different techniques without exposing the substrate or film to non-vacuum conditions.

To test the operation of the ICB system attempts were made to reproduce some of the results reported by Takagi et al. Therefore, thin films of aluminum were deposited onto silicon. These films have been analyzed for crystal orientation, impurity concentration, film-substrate interface characteristics, thickness variation, and electrical properties. The results of these analyses are presented here.

In addition, thin films of germanium have been deposited onto silicon and gallium arsenide; the preliminary results of these depositions are also reported.

Experimental System

A schematic diagram of the ICB system is shown in Figure A.1. The ultrahigh-vacuum (UHV) chamber was custom-built. The chamber is a stainless-steel cylinder with removable end plates and a water-cooled exterior surface. The vacuum is maintained by a 1000 liter/second turbomolecular pump and a titanium sublimation pump. A base pressure of 2×10^{-8} Pa (1.5×10^{-10} torr) has been achieved with this system. Analysis of the vacuum with an r.f. quadrupole mass-analyzing spectrometer indicates that the residual gases are mainly hydrogen and water vapor.

The ionized-cluster source used in the system was purchased from Eaton Corporation, Beverly, MA, and represents their second-generation design. The casing of the heating section is water-cooled to minimize heat radiation from the source into the process chamber. Heating of the crucible is radiative, using a graphite picket heater. The heater is capable of dissipating 6kW, corresponding to a crucible temperature in excess of 2300°C. Ionization of the clusters is by electron bombardment. The source-to-substrate distance is 25cm. Acceleration of the ionized clusters is over this entire distance; the source is maintained at the acceleration

potential while the substrate is grounded. The geometry of the acceleration region was designed for linearity of the electric field.

In a departure from the Eaton design, the source is

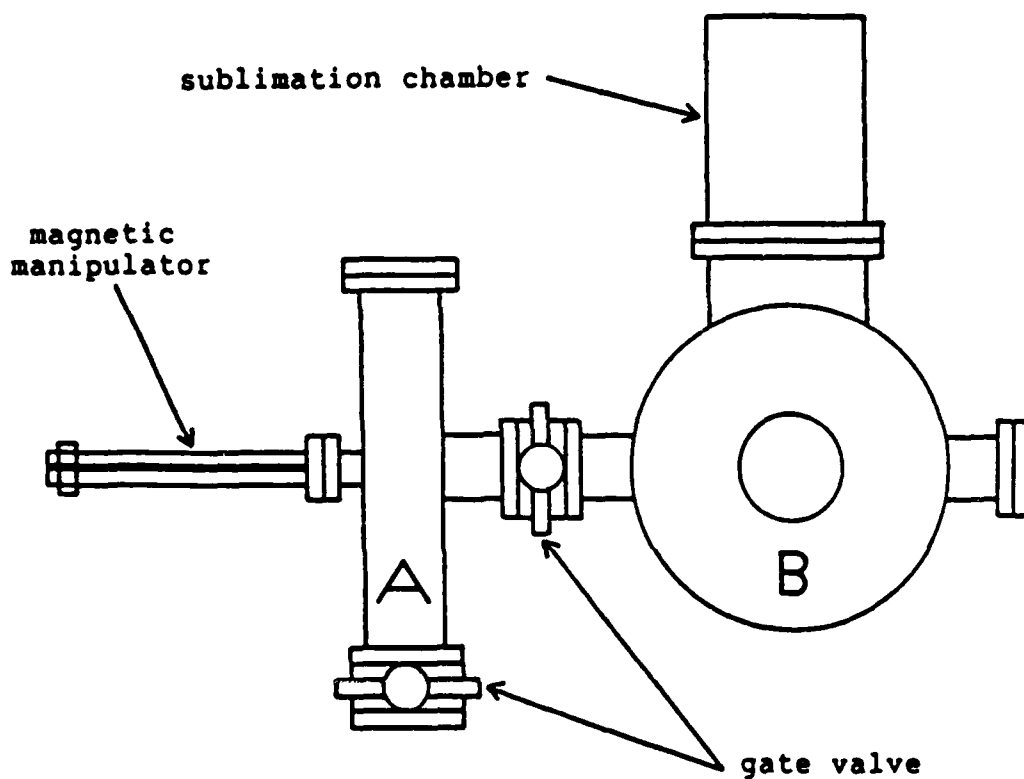


Figure A.1. ICB system schematic diagram

mounted on an eight-inch (outside diameter) UHV flange. This arrangement permits easy installation of the source into the high-vacuum chamber and allows interchangeability of sources. This not only lessens the down-time should a source fail, but also permits removal of one or more sources from the triple-source ICB now being constructed at Iowa State University while leaving the remaining sources operational. It also allows the use of alternative source designs, such as the inductively-heated source now being built at Iowa State University.

Sensors are installed in the ICB system to monitor and control the vacuum system and the deposition parameters. Vacuum monitoring is achieved through a residual-gas analyzer (RGA). The RGA has an r.f. quadrupole mass analyzer and an electron multiplier for maximum sensitivity. A deposition monitor provides information regarding the rate of deposition and the accumulated film thickness; its sensor is mounted next to the substrate. A Faraday cup is also mounted near the substrate to detect the current density of the incident ionized clusters. If an assumption is made regarding the percentage of ionization, an estimate of the average cluster size can be made using the Faraday cup current and the deposition rate. Finally, infrared heating lamps are mounted above the substrate and permit the substrate to be heated up to 500°C. Regulation of the substrate temperature is by a time-proportioning temperature controller.

Presently the ICB system is equipped with a high-vacuum load lock for the introduction of substrates without the loss of vacuum in the process chamber. The load lock is isolated from the process chamber and from the room by pneumatic gate valves. The load lock is equipped with a separate turbomolecular pump, capable of attaining a vacuum of 1×10^{-4} Pa (7.5×10^{-7} torr). Movement of the substrate transport-vehicle is by a magnetically-coupled manipulator arm.

The load lock, however, is only the first section of the transfer-tube system of the total thin-film facility. A diagram of the planned facility is given in Figure A.2. When completed, substrate preparation, thin-film deposition, and analysis will be integrated into a single ultrahigh-vacuum facility housed in a clean room. Each section of the transfer tube will be isolated by gate valves and will have a separate vacuum pump; substrates will be loaded into a transport vehicle that will be moved through the tube by remote-control manipulators.

The substrate preparation section of the facility will consist of a substrate loading area and a substrate cleaning system. The substrate loading area will be under a laminar-flow clean bench to reduce particulate contamination as much as possible. The substrate cleaning system will allow an atomically-clean substrate to be prepared by sputter etching. Since the entire transfer-tube system will be maintained at or below 10^{-8} Pa (10^{-10} torr), a substrate so cleaned will remain

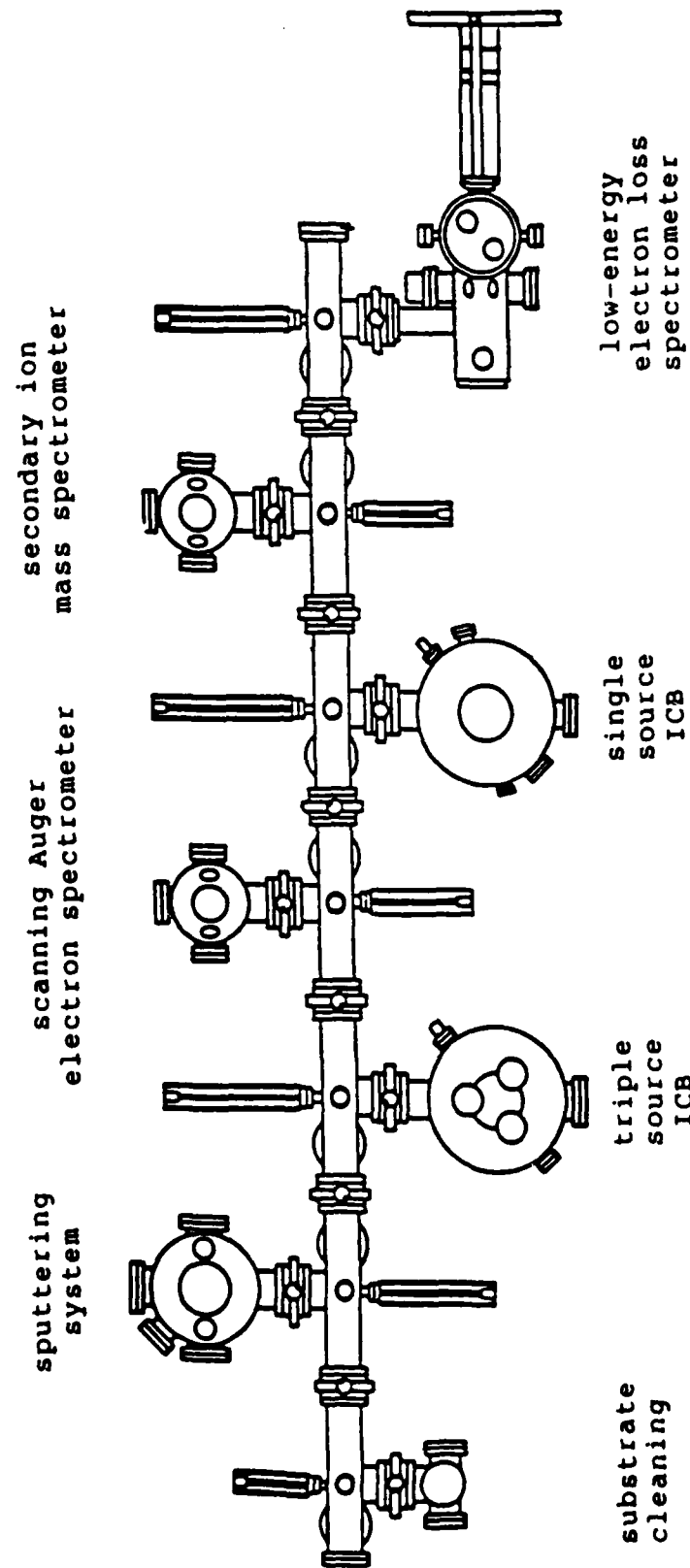


Figure A.2. Thin-film facility at Iowa State University

relatively free of native oxides or other contaminants.

Three deposition systems are planned for the facility: the ICB system, the triple-source ICB system, and a sputter-deposition system. The triple-source ICB system will have three completely independent sources and will be used to deposit compound materials; this system is under construction. The sputter-deposition system is operational and is currently being tested by d.c. magnetron sputtering of aluminum.

Finally, three separate analysis systems will be included. For surface analysis of thin films, the low-energy electron energy loss spectrometer will be used. The LEELS system is now operational and will be used to study the formation mechanisms of thin films. Because of the unique ultrahigh-vacuum transfer tube, a substrate can be moved into the LEELS analysis chamber without oxidizing the surface of the substrate or the film. Therefore, a very short deposition time may be used to form small nucleation regions on a substrate, which can then be safely moved into the LEELS system where the nucleation mechanisms can be studied. The depth-profiling Auger electron spectrometer is for compositional analysis of the deposited films. Because of its three-dimensional scanning ability, detailed information about the film content and the film-substrate interface region can be obtained. This system is also operational. Due to its high resolution, the secondary-ion mass spectrometer (SIMS) will be used for thin-film dopant analysis when it is

installed.

In addition to the separate analysis systems, several in situ analysis systems are planned for the ICB deposition systems. Work is being done on a high-speed ellipsometer that will allow real-time analysis of the film thickness and dielectric constant during deposition. Also planned is a reflection high-energy electron diffraction (RHEED) instrument for each of the ICB systems. This will allow crystallinity information to be obtained during deposition. Finally, a time-of-flight mass spectrometer is being designed to measure the cluster sizes during deposition. This should provide a greater understanding of the cluster formation mechanisms and the effect of cluster size on the deposited film.

Experimental Procedure

All of the films were deposited onto substrates with (100) crystal orientation. For the aluminum depositions, three-inch diameter p-doped silicon wafers with a resistivity in the range 0.1-30 Ω ·cm were used. The wafers were cleaned using a standard cleaning procedure consisting of an organic-solvent cleaning followed by an etch in 10% hydrofluoric acid (HF) to remove native oxides. Immediately after the HF etch, a wafer was placed into the transport vehicle in the load lock and pumped to high vacuum.

The procedure for the germanium depositions was very similar. For the depositions onto silicon, three-inch

diameter n-doped wafers with a resistivity in the range 5-9 Ω -cm were used. The preparation of the wafers was identical to the above procedure. The depositions onto gallium arsenide were onto one-fourth of a two-inch diameter wafer. The cleaning procedure for the gallium arsenide wafers consisted of the organic-solvent cleaning, followed by a three-minute planar etch [8]. Again, the substrate was immediately placed into the transport vehicle and pumped to high vacuum.

During depositions, the crucible was maintained at a constant temperature, corresponding to a pressure within the crucible of several torr. In the region of interest, the vapor pressure versus temperature curves can be fitted to a general equation of the form [9]:

$$\log_{10} p = \frac{A}{T} + B \log_{10} T + C \times T + D \times T^2 + E \quad (\text{A.1})$$

where p is the pressure in torr and T is the temperature in degrees Kelvin. Five data points were used to determine the coefficients A, B, C, D, and E, covering the region from 10⁻² torr to 10² torr. The coefficients for aluminum and germanium are given in Table A.1.

Table A.1. Vapor pressure coefficients

	Aluminum	Germanium	
A	-5.0366653535	-5.06638668673	$\times 10^5$
B	-1.85288160827	-1.58059487121	$\times 10^3$
C	4.38665343031	3.18516683619	$\times 10^{-1}$
D	-3.94690713839	-2.4434021124	$\times 10^{-5}$
E	5.64958363239	4.93140675383	$\times 10^3$

While depositing material, the chamber pressure was maintained as low as possible, but due to outgassing rose as high as 3×10^{-5} Pa (2×10^{-7} torr). Even at this pressure, however, the resulting film was free of impurities as measured by Auger electron spectroscopy. Difficulty was encountered in maintaining a lower pressure during depositions because of the frequent cycling of the vacuum chamber to atmospheric pressure. As will be noted below, problems with the crucible during the aluminum depositions led to the venting of the UHV chamber after every deposition.

The remaining parameters varied were the acceleration voltage and the substrate temperature. The acceleration voltage was varied from 0-1.0kV for the aluminum depositions and from 0.5-3.0kV for the germanium depositions. The substrate was not heated while depositing aluminum but due to the thermal heating effect of the energetic clusters and radiative heating from the ion source the substrate temperature typically rose to about 150°C. Three substrate temperatures were used during the germanium depositions: 183°C (maximum), 200°C, and 400°C.

Analysis and Results

Aluminum

Aluminum on silicon is of technological interest for metallization of semiconductor devices. However, due to difficulties encountered with molten aluminum in the graphite

crucible, few films of aluminum could be deposited. Molten aluminum is highly reactive with graphite, leading to the formation of aluminum carbide and the plugging of the crucible nozzle. Figure A.3 shows a polished cross-section of a plugged crucible nozzle at 50X magnification. The nozzle is filled mostly with aluminum, but grains of some other material are plain. These grains are believed to be aluminum carbide, formed by the reaction of the hot aluminum with the carbon walls of the crucible.



Figure A.3. Cross-section of plugged crucible nozzle

Growth conditions for the best aluminum film obtained are presented in Table A.2. Analysis was performed by four techniques. The crystalline orientation of the film was

determined by X-ray diffraction. Depth-profiling Auger electron spectroscopy was used to measure the impurity concentrations and to analyze the silicon-aluminum interface. A stylus thickness gauge was used to confirm the thickness data from the deposition monitor. The resistivity and thickness variation of the film were measured using a four-point probe. The thickness variation was determined by assuming a constant resistivity across the surface of the deposited film.

Table A.2: Aluminum deposition conditions

Acceleration Voltage	1.0 kV
Ionization Voltage	500 V
Ionization Current	100 mA
Crucible Temperature	1700 °C
Substrate Temperature (maximum)	155 °C
Deposition Rate	3.7 Å/s
Thickness	5500 Å

The results of the analysis for these deposition conditions are shown in Table A.3. The use of these deposition conditions resulted in an aluminum film with a smooth surface. Optical microscopy showed no surface roughness. The (110) crystal orientation of the aluminum film corresponds to the orientation observed by other researchers [10].

Table A.3. Aluminum film characteristics

Crystal Orientation	(110)
Impurity Concentration	< 0.1 %
Sheet Resistance	0.065 Ω/□
Resistivity	3.6 μΩ·cm
Thickness variation (3" wafer)	6 %

Of particular interest is the silicon-aluminum interface region of 500Å. This interface region is probably due to the shallow-implantation effect of the ICB technique [11]. Auger electron spectrometer maps of the interface are shown in Figure A.4 and Figure A.5. The darker regions correspond to the presence of the element being observed. Figure A.6 shows the aluminum and silicon concentrations versus depth (sputtering time) into the interface. The concentrations of oxygen and carbon are also shown. The peaks at 9 and 24 minutes are anomalies of the Auger system and are not significant. The interface region is important because it provides the high concentration of recombination centers necessary for ohmic contacts, but eliminates the need for high-temperature annealing which can lead to the Kirkendall effect [12].

Also of note is the low impurity concentration of the aluminum film. There were no impurities detectable by the Auger electron spectrometer. As seen in Figure A.6, the concentrations of oxygen and carbon, the two elements most likely to be found in the film, are below the detection limit of the Auger spectrometer, less than 0.1%. The low value of resistivity is also significant. The value indicated is about 130% the bulk value of resistivity for aluminum. This is important for low-resistance interconnections of devices.

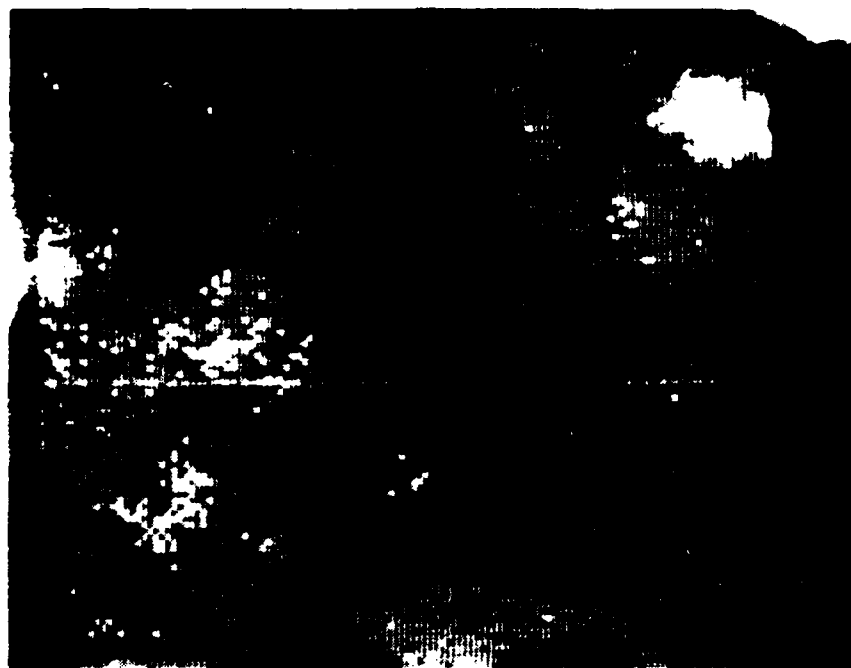


Figure A.4. Auger electron spectrometer map for aluminum



Figure A.5. Auger electron spectrometer map for silicon

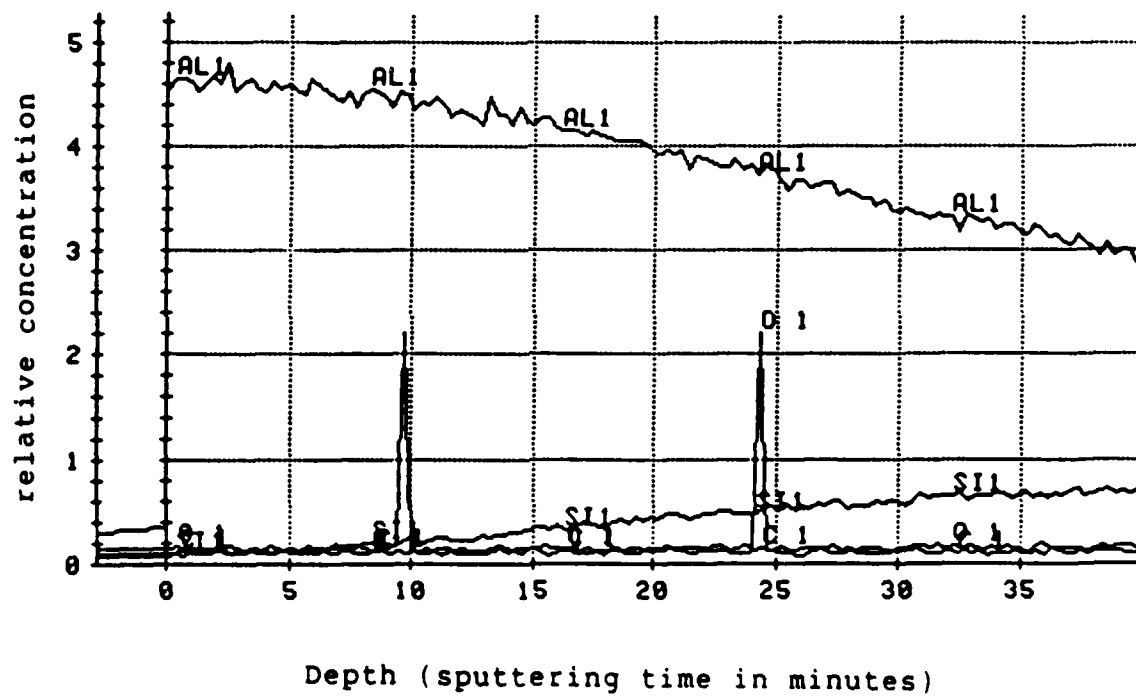


Figure A.6. Element concentration versus depth for an aluminum film

Germanium

Thin-films of germanium on silicon have technological interest as a lattice-matching intermediate layer between silicon and gallium arsenide. As previously mentioned, the practical interest in germanium deposition was due to difficulties encountered with aluminum in the graphite crucible. No problems have been encountered with germanium in the graphite crucible. After several depositions, the crucible lid was easily removed; no interaction of the germanium with the graphite could be observed.

Typical deposition conditions for germanium are given in Table A.4. Although complete analysis of the germanium films has not been undertaken yet, a few generalizations can be made. As determined by X-ray diffraction, films grown at the lower substrate temperatures (200°C or less) were amorphous. Films grown at the lower deposition rate were smooth-surfaced, while the films grown at the higher deposition rate were hazy due to surface roughness. For a film grown at the higher deposition rate and 0.5kV acceleration, Auger electron spectroscopy indicated an abrupt germanium-silicon interface. No difference has yet been observed between films grown on silicon or gallium arsenide substrates.

Conclusions

Further analysis of both sets of films is needed. The aluminum should be studied to determine time and temperature

Table A.4. Germanium deposition conditions

Acceleration Voltage	0.5-3.0 kV
Ionization Voltage	500 V
Ionization Current	40 mA
Crucible Temperature	1850-1900 °C
Substrate Temperature	200,400 °C
Deposition Rate	1-3 Å/s
Thickness	5000 Å

stability. In addition, tests should be made to see if the aluminum is epitaxial, as reported by Yamada et al. [10]. To continue deposition of aluminum, a non-graphite crucible will be obtained, probably one made of boron nitride. The germanium films are being studied to determine their potential as an intermediate layer between silicon and gallium arsenide. To be useful, the gallium arsenide would have to be able to be grown epitaxially.

The goal of the Iowa State University thin-film facility ionized-cluster beam deposition systems is to study the general low-temperature ion-assisted growth process. The combination of state-of-the-art analysis equipment and the ICB systems into a single ultrahigh-vacuum system will allow much to be learned about the mechanisms associated with these growth processes.

This work was sponsored by the Air Force Office of Scientific Research.

References

1. Yamada, Isao. "A Review of Ionized-Cluster Beam Technology." Proceedings of the International Ion Engineering Congress, Kyoto, Japan, 1983, pp. 1177-1192.
2. Takagi, Toshinori. "Development of New Materials by the Ionized-Cluster Beam Technique." Ion Implantation and Ion Beam Processing of Materials, pp. 501-511. Edited by G. K. Hubler, O. W. Holland, C. R. Clayton, and C. W. White. New York: North-Holland, 1984.
3. Theeten, J. B.; Madar, R.; Mircea-Roussel, A.; Rocher, A.; and Laurence, G. "Cadmium Telluride Layer Deposition Using the Ionized-Cluster Beam Technique." Journal of Crystal Growth 37 (1977), 317-328.
4. Inokawa, Hiroshi; Fukushima, Kazunori; Yamada, Isao; and Takagi, Toshinori. "Characteristics of Al Films Formed by Ionized-Cluster Beam Deposition." Proceedings of the Sixth Symposium on Ion Sources and Ion-Assisted Technology, Tokyo, Japan, 1982, pp. 355-358.
5. Usui, Hiroaki; Naemura, Masahiko; Yamada, Isao; and Takagi, Toshinori. "Organic Film Formation (Anthracene) by Ionized-Cluster Beam Deposition." Proceedings of the Sixth Symposium on Ion Sources and Ion-Assisted Technology, Tokyo, Japan, 1982, pp. 331-336.
6. Yamanishi, K.; Minowa, Y.; and Shuhara, A. "SiO₂ Films by Ionized-Cluster Beam." Proceedings of the International Ion Engineering Congress, Kyoto, Japan, 1983, pp. 1203-1207.
7. Kudo, J.; Morishita, T.; Iguchi, K.; Koba, M.; Awane, K. "New Ionized-Cluster Beam Deposition System and Its Application to Si Films." Proceedings of the International Ion Engineering Congress, Kyoto, Japan, 1983, pp. 1193-1196.
8. Frank Chambers, AMOCO Research Center, Naperville, IL. Private communication.
9. Honig, Richard E. "Vapor Pressure Data for the Solid and Liquid Elements." RCA Review 23 (December 1962), 567-586.
10. Yamada, I.; Inokawa; and Takagi, T. "Aluminum Epitaxy on Si(111) and Si(100) Using an Ionized-Cluster Beam." Thin Solid Films 124 (1985), 179-184.

11. Takagi, Toshinori; Yamada, Isao; Matsubara, Kakuei; and Takaoka, Hiroshi. "Ionized-Cluster Beam Epitaxy." Journal of Crystal Growth 45 (1978), 318-325.
12. Ghandhi, Sorab K. VLSI Fabrication Principles. New York: Wiley-Interscience, 1983.

GERMANIUM THIN FILMS DEPOSITED BY THE
IONIZED-CLUSTER BEAM TECHNIQUE

Jonathan S. McCalmont, Howard R. Shanks, and Kenneth M. Lakin
Microelectronics Research Center
Iowa State University, Ames, IA 50011

Presented at the
33rd National Symposium of the American Vacuum Society
October 26-31, 1986
Baltimore, MD

APPENDIX B. GERMANIUM THIN FILMS DEPOSITED BY THE IONIZED-CLUSTER BEAM TECHNIQUE

Summary Abstract

Thin films of germanium have been deposited on silicon substrates using the ionized-cluster beam (ICB) deposition technique. The deposition system consisted of an Eaton Corporation source mounted in an ultrahigh vacuum chamber. The crucible was made of high-density graphite with a nozzle 1mm long by 1mm in diameter. Acceleration of the ionized clusters was through the entire 25cm source-to-substrate separation. The substrates were (100) n-doped three-inch silicon wafers with a resistivity in the range 4-9 Ω ·cm.

Table B.1 summarizes the deposition conditions for five films. The first four films have a small amount (0.1-1.0 atomic percent) of aluminum mixed with the germanium; the fifth film was deposited with the aluminum source removed.

The films were analyzed by four techniques: visual inspection, X-ray diffraction, Auger electron spectroscopy, and four-point probe measurements. The results of these analyses are also summarized in Table B.1. Visual inspection was used to determine the surface condition; for deposition rates of 1.0 \AA /s or less, the surface of the films were smooth. The mechanical and electrical characteristics of the films, however, were not affected by the surface condition.

X-ray diffraction was used to determine the crystal

Table B.1. Deposition conditions and characteristics

Sample I.D.	1	2	3	4	5	
<u>Deposition Conditions</u>						
Acceleration Voltage	500	500	0	500	500	V
Ionization Voltage	500	500	500	500	500	V
Current	100	100	100	100	100	mA
Deposition Rate	2.3	1.3	0.9	1.0	1.3	Å/s
Substrate Temperature	380	405	400	300	400	°C
Thickness	5000	5000	5000	5000	10760	Å
<u>Characteristics</u>						
Surface Condition ^a	r	s-r	s	s	r	
AES Percent Aluminum		<1.0			<1.0	%
X-ray: Standard	(100)	(100)	(100)	poly		
Precession	epi	epi	epi		poly	
Resistivity	0.32	0.38	0.46	0.82	50.5	mΩ·cm
Atomic Percent Aluminum	0.7	0.5	0.2	0.1	10 ⁻⁴	%

^ar = rough, s = smooth.

structure. Two techniques were used--a standard diffractometer method and a new technique that uses a Buerger precession camera. The latter technique produces a photograph of the reciprocal space for both the substrate and the film [1,2]. The diffraction technique indicated the film orientation to be either (100) single crystalline or (100), (110), (111), and (311) oriented polycrystalline. Precession camera photographs taken of the single-crystalline films showed that they were epitaxial.

Depth-profiling Auger electron spectroscopy (AES) was used to determine the impurity concentrations in the films. The first four films showed less than 1 percent aluminum in the bulk of the film. The fifth sample showed no aluminum in the bulk. To further determine the doping concentrations, four-point probe measurements were made to determine the electrical resistivity. The aluminum-doped samples had resistivities in the range 0.3-0.8m Ω ·cm. The fifth sample had a much higher resistivity--50m Ω ·cm. Using data on heavily-doped germanium collected by Trumbore and Tartaglia [3], the resistivities were converted to doping concentrations, which were then used to calculate the atomic percentage of aluminum in the film. From these calculations, the first four samples are doped with 0.2-0.7% aluminum, whereas the fifth is only doped with 10⁻⁴% aluminum.

In summary, thin films of aluminum-doped germanium have been deposited on silicon using the ionized-cluster beam

technique. Substrate temperatures during deposition can be as low as 400°C to obtain epitaxy. The films have low resistivity.

Acknowledgement is made to J. T. Martin for the X-ray diffraction measurements, to R. D. Horning and J. -L. Staudenmann for the precession camera photographs, and to A. J. Bevolo, L. M. Seaverson, and R. Shinar for the AES data. This work was sponsored by the Air Force Office of Scientific Research.

References

1. R. D. Horning and J. -L. Staudenmann, submitted to Journal of Crystal Growth.
2. R. D. Horning and J. -L. Staudenmann, submitted to Applied Physics Letters.
3. Trumbore, F. A. and Tartaglia, A. A. "Resistivities and Hole Mobilities in Very Heavily Doped Germanium." Journal of Applied Physics 29 (October 1958), 1511.

APPENDIX C. SOURCE CODE LISTINGS FOR THE FINITE-DIFFERENCE
AND CONTOUR LINE PROGRAMS

```

1:D      0 SPAGES
2:D      0 program field(input, output);
3:D      1 const
4:D      1   h = 0.25;
5:D      1   error = 10;
6:D      1   max_r = 52;
7:D      1   max_z = 118;
8:D      1   accel = 10000;
9:D      1   title = 'ICB interior potentials with 0.5in mesh screen';
10:D     1 type
11:D     1   grid = array[1..max_z, 1..max_r] of integer;
12:D     1   ptr = ^grid;
13:D     1   word = string[40];
14:D     1 var
15:D     -42 1   filename : word;
16:D     -58 1   i, j, counter, change : integer;
17:D     -62 1   phi : ptr;
18:S
19:S
20:D      1 procedure init_boundary_conditions(var phi : ptr);
21:D      2 var
22:D      -8 2   i, j : integer;
23:C      2 begin
24:C      2   for i:=71 to 95 do
25:C      3     for j:=1 to 11 do
26:C      4       phi^[i,j] := accel;
27:C      2   for j:=12 to 31 do
28:C      3     phi^[95,j] := accel;
29:C      2   for i:=39 to 94 do
30:C      3     phi^[i,31] := accel;
31:C      2 end;
32:S
33:D      1 function boundary(i, j : integer) : boolean;
34:C      2 begin
35:C      3   if ( (i=1) or (i=118) or (j=52) or
36:C      3     ((i=39) and (j in [2..11])) or
37:C      3     ((i in [71..95]) and (j in [2..11])) or
38:C      3     ((i=95) and (j in [12..31])) or
39:C      3     ((i in [39..94]) and (j=31)) )
40:C      3   then
41:C      3     boundary := true
42:C      3   else
43:C      3     boundary := false;
44:C      2 end;
45:S
46:D      1 procedure finite_diff(var phi : ptr; i, j : integer; var change
1: integer);
47:D      2 var
48:D      -4 2   nphi : integer;
49:C      2 begin
50:C      2   if j=1 then
51:C      3     nphi := (phi^[i-1,j] + 2*phi^[i,j+1] + phi^[i+1,j]) div
4
52:C      3   else
53:C      3     nphi := (phi^[i-1,j] + phi^[i+1,j] + phi^[i,j-1] + phi^[
1,j+1]) div 4
54:C      3     + (phi^[i,j+1] - phi^[i,j-1]) div (8*(j-1));
55:C      2   if abs(nphi - phi^[i,j]) > change then
56:C      3     change := abs(nphi - phi^[i,j]);
57:C      2   phi^[i,j] := nphi;
58:C      2 end;
59:S
60:D      1 procedure update(change : integer; counter : integer);

```



```

61:C      2 begin
62:C      2   writeln(chr(12),chr(128),chr(140));
63:C      2   writeln; writeln('Extended run in progress.  Program runni
ng...');
64:C      2   writeln; writeln('See Scott McCalmont for more information
');
65:C      2   writeln; writeln; writeln;
66:C      2   writeln('Maximum change = ',change:10);
67:C      2   writeln; writeln('counter = ', counter:8);
68:C      2   writeln; writeln; writeln(title);
69:C      2   writeln('Output file = ', filename);
70:C      2 end;
71:S
72:D      1 procedure fileout(var filename : word; var counter : integer;
var phi : ptr);
73:D      2 var
74:D      2   outfile : text;
75:D      2   i, j : integer;
76:C      2 begin
77:C      2   rewrite(outfile,filename);
78:C      2   writeln(outfile, '! h = ',   h:5:3, '   counter = ', counte
r:8);
79:C      2   writeln(outfile, '! ', title);
80:C      2   for i:=1 to max_z do begin
81:C      3     for j:=1 to max_r do begin
82:C      4       write(outfile, phi^[i,j]:8);
83:C      4       if j mod 9 = 0 then
84:C      5         writeln(outfile);
85:C      4     end;
86:C      3     writeln(outfile);
87:C      3   end;
88:C      2   close(outfile, 'SAVE');
89:C      2 end;
90:S
91:S
92:C      1 begin
93:C      1   write(chr(12),'Output file: ');
94:C      1   readln(filename);
95:C      1   new(phi);
96:C      1   for i:=1 to max_z do
97:C      2     for j:=1 to max_r do
98:C      3       phi^[i,j] := 0;
99:C      1   init_boundary_conditions(phi);
100:C      1   counter := 0; change := -1;
101:C      1   update(change, counter);
102:C      1   repeat
103:C      2     change := 0;
104:C      2     counter := counter + 1;
105:C      2     for i:=2 to (max_z - 1) do
106:C      3       for j:=1 to (max_r - 1) do
107:C      4         if not boundary(i,j) then finite_diff(phi, i, j, c
hange);
108:C      2     update(change, counter);
109:C      2     if counter mod 100 = 0 then
110:C      3       fileout(filename, counter, phi);
111:C      2   until change < error;
112:C      1   fileout(filename, counter, phi);
113:C      1   writeln(chr(12));
114:C      1 end.

```

No errors. No warnings.

```

1:D      0 SPAGES
2:D      0 program contour_lines(input, output);
3:D      1 (* Scott McCalmont  3 May 1985 *)
4:D      1 (* revised 18 Nov 1985 *)
5:D      1 import
6:D      1   dgl_lib;
7:D      1 const
8:D      1   size = 200;
9:D      1   display = 3;
10:D     1 type
11:D     1   bigarray = array[1..size, 1..size] of real;
12:D     1   grid = ^bigarray;
13:D     1 var
14:D     -4 1   phi : grid;
15:D     -20 1   r1, r2, z1, z2 : integer;
16:D     -28 1   k : real;
17:D     -29 1   done : char;
18:S
19:D     1 procedure initialize(var a : grid);
20:D     2 var
21:D     -664 2   infile : text;
22:D     -686 2   name : string[20];
23:D     -768 2   words : string[80];
24:D     -788 2   rmax, zmax, i, j, error : integer;
25:C     2 begin
26:C     2   write('What is the grid size? (rmax zmax) ');
27:C     2   readln(rmax, zmax);
28:C     2   write('What is the input file? ');
29:C     2   readln(name);
30:C     2   reset(infile, name);
31:C     2   while infile^ = '!' do begin
32:C     3     readln(infile, words);
33:C     3     writeln(words);
34:C     3   end;
35:C     2   writeln('Reading in the data points...');
36:C     2   for i:=1 to zmax do
37:C     3     for j:=1 to rmax do
38:C     4       read(infile, a^[i,j]);
39:C     2   graphics_init;
40:C     2   display_init(display, 0, error);
41:C     2   if error <> 0 then
42:C     3     halt(1);
43:C     2   set_aspect(511,389);
44:C     2 end;
45:S
46:D     1 procedure window(var r1, r2, z1, z2 : integer);
47:C     2 begin
48:C     2   clear_display;
49:C     2   writeln(chr(12));
50:C     2   writeln('Enter viewing window coordinates:');
51:C     2   write('   radial: (rmin rmax) ');
52:C     2   readln(r1, r2);
53:C     2   write('   axial: (zmin zmax) ');
54:C     2   readln(z1, z2);
55:C     2   if (z2-z1) > (r2-r1) then
56:C     3     set_viewport(0.5-((r2-r1)/(2*(z2-z1))), 0.5+((r2-r1)/(2*(
z2-z1))), 0, 0.75)
57:C     3   else
58:C     3     set_viewport(0.125, 0.875, 0.375-((z2-z1)/(2*(r2-r1))),
59:C     3                               0.375+((z2-z1)/(2*(r2-r1))),
60:C     2   set_window(r1, r2, z2, z1);

```

```

61:C      2   move(r1,z1);
62:C      2   line(r1,z2); line(r2,z2); line(r2,z1); line(r1,z1);
63:C      2 end;
64:S
65:D      -24  1 procedure range(a1, a2, k : real; var min, max : real; var ok
: boolean);
66:C      2   begin
67:C      2     if a1 < a2 then begin
68:C      3       min := a1;
69:C      3       max := a2;
70:C      3       end
71:C      3     else begin
72:C      3       min := a2;
73:C      3       max := a1;
74:C      3     end;
75:C      2   min := k * (trunc(min/k) + 1);
76:C      2   if (min > max) or (a1 = a2) then
77:C      3     ok := false
78:C      3   else
79:C      3     ok := true;
80:C      2 end;
81:S
82:D      -8   1 procedure axial_scan(var a : grid; r1, r2, z1, z2 : integer; k
: real);
83:D      -8   2 var
84:D      -16  2     r, z : integer;
85:D      -48  2     min, max, g, p : real;
86:D      -49  2     ok : boolean;
87:C      2   begin
88:C      2     for r := r1 to r2 do
89:C      3       for z := z1 to z2-1 do begin
90:C      4         range(a^[z,r], a^[z+1,r], k, min, max, ok);
91:C      4         g := min;
92:C      4         if ok then repeat
93:C      6           p := z + ((g-a^[z,r]) / (a^[z+1,r]-a^[z,r]));
94:C      6           move(r,p);
95:C      6           line(r,p);
96:C      6           g := g + k;
97:C      6           until g > max;
98:C      4         end;
99:C      2 end;
100:S
101:D      -8   1 procedure radial_scan(var a : grid; r1, r2, z1, z2 : integer;
k : real);
102:D      -8   2 var
103:D      -16  2     r, z : integer;
104:D      -48  2     min, max, g, p : real;
105:D      -49  2     ok : boolean;
106:C      2   begin
107:C      2     for z := z1 to z2 do
108:C      3       for r := r1 to r2-1 do begin
109:C      4         range(a^[z,r], a^[z,r+1], k, min, max, ok);
110:C      4         g := min;
111:C      4         if ok then repeat
112:C      6           p := r + ((g-a^[z,r]) / (a^[z,r+1]-a^[z,r]));
113:C      6           move(p,z);
114:C      6           line(p,z);
115:C      6           g := g + k;
116:C      6           until g > max;
117:C      4         end;
118:C      2 end;
119:S
120:S

```

```

121:C      1 begin
122:C      1   new(phi);
123:C      1   initialize(phi);
124:C      1   repeat
125:C      2     window(r1, r2, z1, z2);
126:C      2     write('What is the contour line spacing? ');
127:C      2     readln(k);
128:C      2     axial_scan(phi, r1, r2, z1, z2, k);
129:C      2     radial_scan(phi, r1, r2, z1, z2, k);
130:C      2     write('Do you want another view? (Y/N) ');
131:C      2     readln(done);
132:C      2     until done in ['N', 'n'];
133:C      1   graphics_term;
134:C      1 end.

```

No errors. No warnings.

APPENDIX D. PROCEDURES FOR SYSTEM OPERATION

Substrate Cleaning

Silicon

- Store the 1,1,1-trichloroethane (TCA) in a Teflon bottle.
 - Use a separate glass petri dish for each organic solvent.
 - Dispose of all chemicals properly.
 - Substrate should not dry off during the procedure.
1. Rinse the substrate with TCA using a Teflon squirt bottle.
 2. Hot (boiling) TCA for about 10 minutes.
 3. Thoroughly rinse with acetone using a squirt bottle.
 4. Hot (boiling) acetone for about 5 minutes.
 5. Rinse with methanol using a squirt bottle.
 6. Hot methanol.
 7. Rinse in D.I. water (at least 10MΩ·cm) until water "sheets" on the wafer surface.
 8. Etch substrate in a weak hydrofluoric acid solution (about 10% HF) for 1 minute.
 9. Rinse in D.I. water.
 10. Blow dry with compressed N₂.

Gallium arsenide

- Store the 1,1,1-trichloroethane (TCA) in a Teflon bottle.
 - Use a separate Teflon beaker for each organic solvent.
 - Dispose of all chemicals properly.
 - Substrate should not dry off during the procedure.
1. Rinse the substrate with TCA using a Teflon squirt bottle.
 2. Hot (boiling) TCA for about 10 minutes.

3. Thoroughly rinse with acetone using a squirt bottle.
4. Hot (boiling) acetone for about 5 minutes.
5. Rinse with methanol using a squirt bottle.
6. Hot methanol.
7. Rinse in D.I. water (at least 10M Ω ·cm) until water "sheets" on the wafer surface.
8. Place the substrate in sulphuric acid.
9. Mix a 5:1:1 H₂SO₄:H₂O₂:H₂O solution and heat on the hotplate.
10. Etch the substrate for 3 minutes in the hot acid solution.
11. Thoroughly rinse in D.I. water.
12. Blow dry with compressed N₂.

Substrate Loading

1. Turn off the load lock ionization gauge and RGA filaments. Allow the filaments to cool for 5 minutes before venting.
2. Check that the substrate boat is in the load lock and that the gate valve separating the load lock from the process chamber is closed.
3. Close the valve to the turbo pump (located on the top of the load lock); turn the turbo pump off. Leave the fore pump running unless an extended shut-down is anticipated (longer than that required to load a substrate).
4. Check that the nitrogen pressure is at about 4psi. Open the venting valve.
5. Close the venting valve when the pressure of the nitrogen line reaches 0psi.
6. Open the gate valve separating the load lock from the room and prop it open.

7. Wearing polyethylene gloves, remove the substrate boat; place the substrate in the boat and replace the boat.
8. Remove the prop and close the gate valve.
9. Slowly open the valve to the turbo. It will still be spinning rapidly (up to 90000 r.p.m.) but will slow down quickly when opened to atmosphere.
10. Restart the turbo.
11. After the turbo reaches full speed the vacuum gauges can be turned on. Let the pressure reach the 10^{-7} torr range before continuing.
12. Open the gate valve to the process chamber.
13. Use the magnetic manipulator to slide the boat into the process chamber. Retract the manipulator and close the gate valve.
14. Check the substrate position and the operation of the shutter.

Deposition Procedure

1. Close the valve to the RGA (located directly above the sublimator chamber).
2. Check that the chamber cooling is on; the Ti-Ball should be on and in the stand-by mode.
3. Turn on the source water cooling, the feedthrough cooling (forced air), and deposition sensor water cooling.
4. Set the Ti-Ball to 0.01g/hr, continuous mode.
5. Turn on the high voltage power supply (HVPS) controller, the three HVPS circuit breakers, the deposition monitor, and the substrate temperature controller. The Fluke 1720A computer must be on for the deposition monitor to pass the RS-232 test.
6. Adjust the power supply setpoints to zero!

7. Set the temperature controller to the desired temperature. Verify that the heaters are working and that the shutter is closed. The current to the heaters can be controlled using the motor-driven autotransformer; adjustment is made using the buttons on the panel in the lower right side of the equipment rack.
8. Turn on the power supplies using the buttons on the HVPS controller. The LEDs on the front of each supply should be lit.
9. Adjust the HVPS outputs: acceleration to setpoint voltage; ionization supply to setpoint voltage; slowly ramp the ionization filament to 10A; crucible heater current to setpoint current. Slowly ramp the ionization filament to obtain the desired emission current.
10. Wait for the substrate temperature and crucible temperature to reach equilibrium.
11. Set the deposition monitor for the correct film. Film #2 is germanium. Put the CRT display on mode 8 (data display).
12. Start the deposition: Press "zero thickness", then "start" on the deposition monitor; open the shutter; record the deposition parameters.
13. Allow the desired thickness of material to be deposited. The RGA valve may be opened briefly to monitor the vacuum, but to reduce contamination of the sensor head, it should not be left open for an extended period.
14. After the desired thickness has been deposited, close the shutter and record the deposition parameters.
15. Turn the substrate heaters off. Turn the HVPS outputs off: crucible current to zero; slowly ramp the ionization filament current to zero; ionization supply and acceleration voltage to zero.
16. Leave the supply breakers on until the supplies cool. Leave the source and deposition monitor sensor cooling on for at least one hour to allow the system to cool.
17. Remove the substrate by reversing the loading procedure.

APPENDIX C

The deposition and characterization of
lithium niobate thin films

The deposition and characterization of
lithium niobate thin films

by

John Thomas Martin

A Thesis Submitted to the
Graduate Faculty in Partial Fulfillment of the
Requirements for the Degree of
MASTER OF SCIENCE

Department: Physics
Major: Applied Physics

Approved:

Th R Shanks

Bruce Harmon
In Charge of Major Work

David W. Lynch
For the Major Department

W. R. Linton
For the Graduate College

Iowa State University
Ames, Iowa

1986

TABLE OF CONTENTS

	Page
I. INTRODUCTION	1
II. LITHIUM NIOBATE SUMMARY	6
A. Crystal Structure	6
B. Physical Properties	9
III. SPUTTER DEPOSITION	16
A. Mechanisms	16
B. Lithium Niobate System	20
C. Thin Film Formation	23
D. Relevant Parameters	24
E. Deposition Procedure	29
IV. SAMPLE CHARACTERIZATION METHODS	31
A. Physical Appearance	31
B. Infrared Analysis	32
C. X-ray Diffraction	33
D. Auger Analysis	37
E. Network Analyzer Measurement	39
V. RESULTS AND DISCUSSION	45
A. Parameter Development	45
B. Characterization	61
VI. CONCLUSIONS	74
VII. REFERENCES	76
VIII. ACKNOWLEDGEMENTS	78
IX. APPENDIX	79

THE DEPOSITION AND CHARACTERIZATION OF LITHIUM NIOBATE THIN FILMS

I. INTRODUCTION

Lithium niobate (LiNbO_3) is a widely used dielectric material in integrated and guided wave optics. A ferroelectric crystal, lithium niobate exhibits large birefringent, pyroelectric, piezoelectric, electro-optic, elastic, photoelastic, and bulk photovoltaic effects. Lithium niobate is a synthetic material which does not exist in nature. Of the many important properties of LiNbO_3 , its piezoelectric properties were of primary interest for this investigation.

Lithium niobate was first discovered to be ferroelectric in 1949 (1). A ferroelectric material is one in which the relationship between the electric field and induced polarization is not linear, but rather shows a hysteresis loop. Lithium niobate is also piezoelectric since all ferroelectric crystals are piezoelectric, although the reverse is not true. Piezoelectric materials have the ability to convert mechanical energy into electrical energy or vice versa. This is done by inducing polarization with applied stress. The converse (or inverse) effect in piezoelectric crystals is a strain caused by an applied

electric field.

At present there are over 400 known piezoelectric materials. One of the most technically promising of these materials is lithium niobate, with piezoelectric coefficients several times larger than quartz (the best known and most utilized piezoelectric material). The first investigation of the piezoelectric effect in LiNbO_3 was done by Nassau et al. (2), on single crystals synthesized at Bell Telephone Laboratories in 1965. One year later this work led to a cornerstone series of five papers on lithium niobate (3-7). Also in 1966, the first determinations of the elastic and piezoelectric constants for lithium niobate single crystals were made at Bell Labs (8) and the Electrical Communications Laboratory in Tokyo (9).

In order to investigate the piezoelectric response in lithium niobate, the material must be in single crystal form, or at least in a highly oriented polycrystalline state. Single crystals of LiNbO_3 have been produced using the Czochralski method of pulling the crystal from a melt (2,10). Often an electric field is applied during or after growth to pole the material. The boule of single crystal LiNbO_3 is then usually sliced into thin wafers. More recently it has become desirable to develop single crystal LiNbO_3 on a substrate of another material for waveguide or transducer applications. This has led to various attempts

to grow single crystalline LiNbO_3 in thin film form.

Attempts to produce LiNbO_3 by direct vacuum evaporation were not successful. A successful method for producing single crystal films, epitaxial-growth-by-melting, was reported in 1973 (11). Chemical vapor deposition has also been used successfully (12). Other methods such as rapid quenching (13) only produced amorphous material. By far, however, the majority of attempts to produce thin film lithium niobate have been by various methods of sputtering.

One of the first attempts to sputter LiNbO_3 for thin film transducer application was partly successful. In 1968, Bell Laboratories produced amorphous and polycrystalline LiNbO_3 through diode sputtering (14). Although single crystal thin films were not produced, piezoelectric response was still noted in the highly oriented polycrystalline films, with the piezoelectric coupling factor being about one half that of single crystal LiNbO_3 . In 1974, the Electrochemical Laboratory, in Tokyo, reported producing single crystal LiNbO_3 thin films by r.f. sputtering (15). However, these films were only intended to be used as optical waveguides, and as such were only deposited to a thickness of 1800 Angstroms, far too thin to be used for transducers or resonators. Most attempts to sputter lithium niobate have been done to study its properties in the amorphous state. The feasibility of using r.f. sputtering

to deposit single crystal lithium niobate thick enough for resonator or transducer application is unknown. This was the main goal of this investigation.

The objective of this work was to deposit LiNbO_3 onto substrates using an r.f. planar magnetron high vacuum sputtering system, from a target of LiNbO_3 . Sputtering parameters would then be adjusted to determine the optimal conditions for producing the best quality films. Those films would then be characterized to determine their quality and suitability for use in piezoelectric applications. This leads to the secondary goal of this research--to test the resulting films for piezoelectric response. This was to be done by using the best films obtained to construct composite resonators following the construction of Lakin and Wang (16).

The composite resonator is constructed by depositing a piezoelectric material, in this case lithium niobate, onto a thin membrane of silicon supported by the bulk of the silicon wafer. The piezoelectric material is usually a micron or more thick, and the membrane several times that. Both the top and the bottom of this construction are metallized, with the top being patterned to a known area. The piezoelectric film excites acoustic waves in the composite structure. Using a network analyzer for measurements, this structure can be used to determine if the

sputtered lithium niobate is showing any piezoelectric activity. If it is, the "coupling coefficient" can be determined. This structure can also be used to determine the relative dielectric constant of the film at various frequencies.

A summary of the crystalline and physical properties of lithium niobate is given in Chapter II. Chapter III concerns the deposition technique. General mechanisms of sputtering and thin film formation are given along with specifics concerning the sputtering apparatus, parameters, and procedures used for the deposition of LiNbO_3 for this investigation. Sample characterization methods are described in Chapter IV. Chapter V details the experimental procedure for the development of the parameter optimization, and describes the sample characterization results during and as a result of the optimization attempts. Chapter VI then summarizes the results and the potential of this method of depositing LiNbO_3 for practical transducer or resonator application.

II. LITHIUM NIOBATE SUMMARY

A. Crystal Structure

The structure of lithium niobate below its ferroelectric Curie temperature of approximately 1210°C contains planar sheets of oxygen atoms arranged in a distorted hexagonal closed-packed arrangement. The interstitial sites formed in this arrangement are filled one third by lithium atoms and one third by niobium atoms, while one third remains vacant. Considered in the $+c$ direction, these follow the order of Nb, empty, Li, Nb, empty, Li,... (5). This is depicted in Figure 1. Above the Curie temperature, lithium niobate is in the paraelectric phase. Here the lithium atom lies in a oxygen plane, while the niobium atoms are equally spaced between oxygen planes. These positions result in the phase being non-polar (7). This is shown in Figure 2. As the crystal is cooled from its Curie temperature, elastic forces in the crystal force the lithium and niobium ions into the positions of Figure 1. This shift of ions relative to the oxygen octahedral results in a charge separation causing spontaneous polarization. Therefore, at temperatures below 1210°C, LiNbO_3 is known as a displaced ferroelectric.

Referring to its ferroelectric phase for the rest of this description, LiNbO_3 is a member of the trigonal crystal

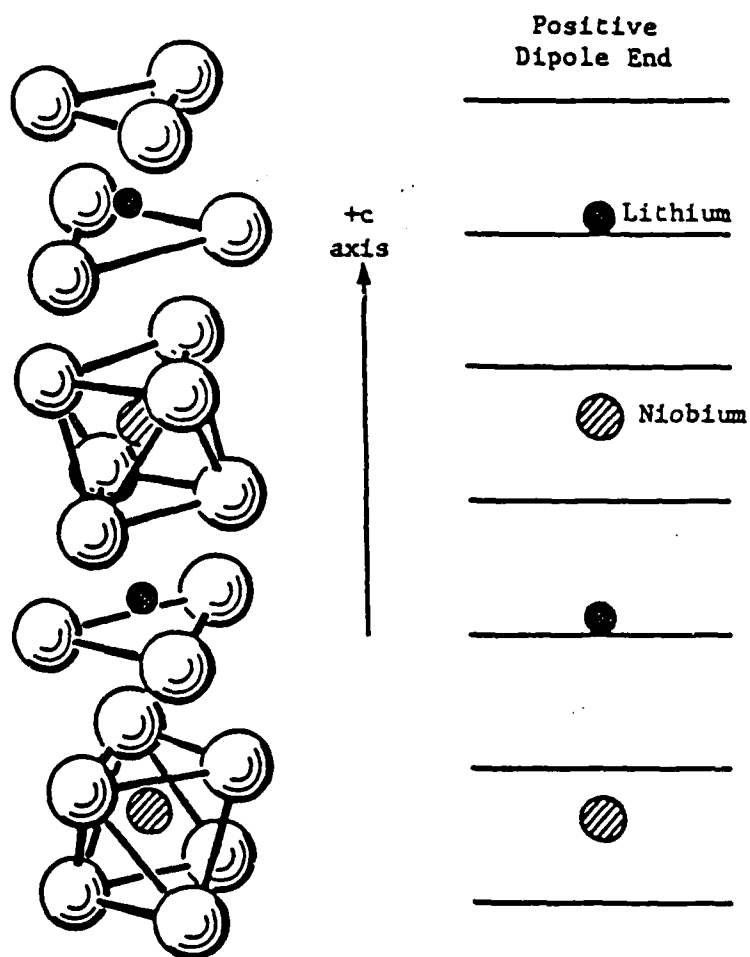


Figure 1. The arrangement of lithium and niobium atoms with respect to the oxygen planes of lithium niobate in the ferroelectric phase

AD-A187 335

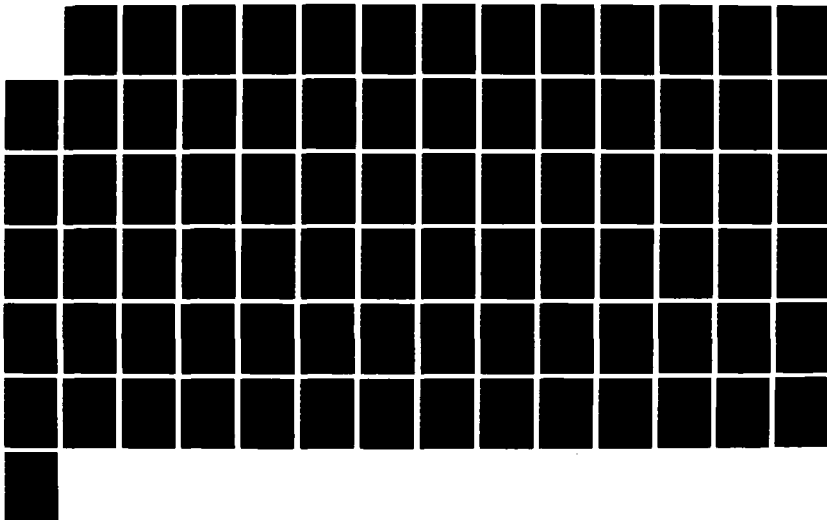
SYNTHESIS AND CHARACTERIZATION OF THIN FILMS(U) IOWA
STATE UNIV AMES MICROELECTRONICS RESEARCH CENTER
K H LAKIN 18 JUL 87 AFOSR-TR-87-1393 AFOSR-84-0388

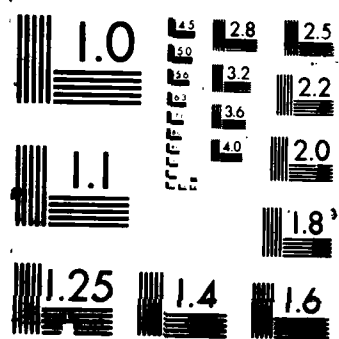
4/4

UNCLASSIFIED

F/G 13/8

NL





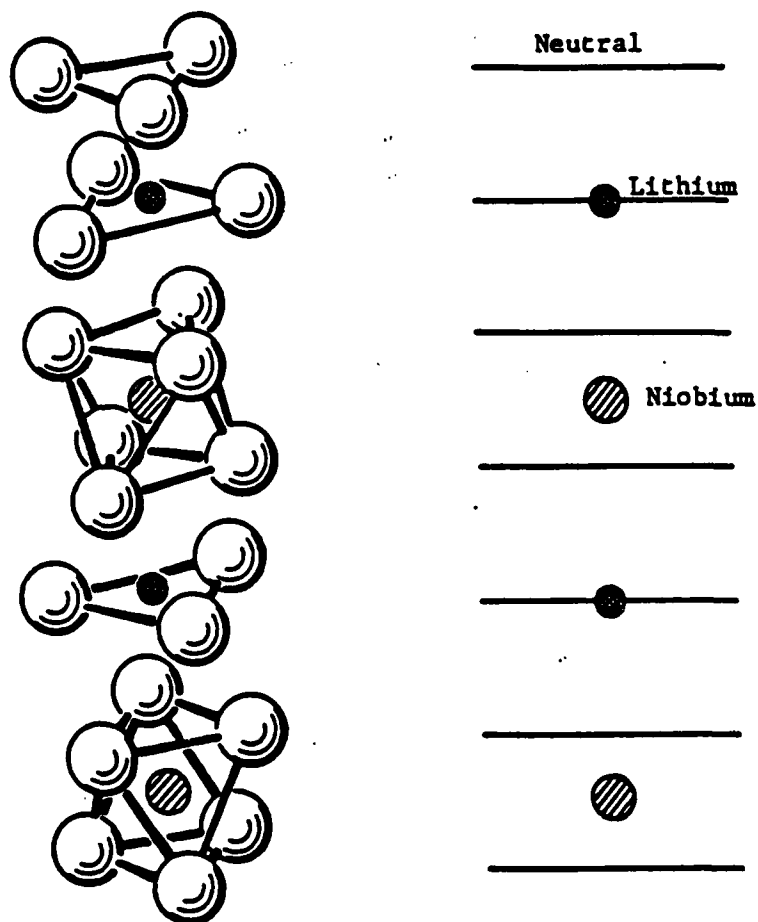


Figure 2. The arrangement of lithium and niobium atoms with respect to the oxygen plane of lithium niobate in the paraelectric phase

system. It exhibits three-fold rotation about its c-axis, and exhibits mirror symmetry about three planes 60° apart along the c-axis. Thus, LiNbO_3 is considered a member of the $3m$ point group (17). Two unit cells can be chosen to structurally describe LiNbO_3 , hexagonal and rhombohedral. The rhombohedral unit cell has parameters $a_R = 5.148 \text{ \AA}$ and $\alpha = 55.867^\circ$, while the more commonly referenced hexagonal unit cell has parameters $a_H = 5.148 \text{ \AA}$ and $c = 13.863 \text{ \AA}$ (5). The hexagonal unit cell with axis lengths and interatomic spacings indicated is seen in Figure 3.

B. Physical Properties

In describing the physical properties of lithium niobate in tensor form, a cartesian system is used rather than a rhombohedral or a hexagonal coordinate system. The z-axis (or x_3 -axis) is chosen parallel to the c-axis while the x-axis is chosen to be along any of the equivalent a_H -axes. The y-axis is then chosen to form a right-handed coordinate system. Using this system, slices of single crystal LiNbO_3 are referred to as being x-cut, y-cut, or z-cut, corresponding respectively to the x, y, or z direction being normal to the surface. Many important properties are described using tensor notation, including the pyroelectric effect, permittivity, the piezoelectric effect, the converse piezoelectric effect, the electro-optic

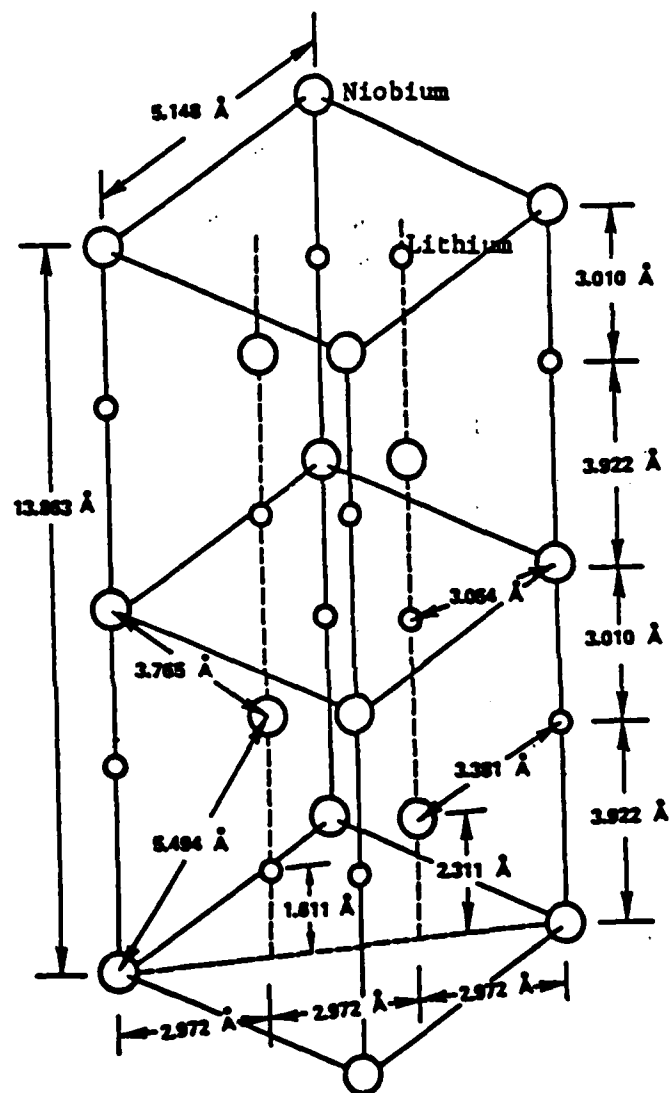


Figure 3. Hexagonal unit cell of lithium niobate

effect, elasticity, the photoelastic effect, and the photovoltaic effect. Of primary interest here are permittivity and piezoelectricity.

The permittivity is involved in the relationship between electric flux density (D) and electric field (E). In tensor form it is written as

$$D_i = \sum_j \epsilon_{ij} E_j, \quad (1)$$

where $i, j = 1, 2, 3$. The second-rank permittivity tensor has the diagonal elements non-zero for materials such as lithium niobate. Also, because of the symmetry about the c-axis in lithium niobate, the permittivity would be the same in the plane perpendicular to the c-axis for any electric field direction. The result is that the permittivity tensor can be expressed as,

$$\epsilon_{ij} = \begin{bmatrix} \epsilon_{11} & 0 & 0 \\ 0 & \epsilon_{11} & 0 \\ 0 & 0 & \epsilon_{33} \end{bmatrix}. \quad (2)$$

The dielectric constant, or more accurately, the relative permittivity, is the permittivity normalized in terms of the permittivity of vacuum (ϵ_0).

The relative permittivity of lithium niobate has been shown to change with frequency (4). Below the mechanical resonance, the crystal is considered to be in a mechanically free (unclamped) state. Here the stress (T) in the crystal

is zero, and the relative permittivity (ϵ^T/ϵ_0) is fairly constant. Above the mechanical resonance, the crystal is considered to be in a clamped state. Here the strain (S) in the crystal is zero, and the relative permittivity (ϵ^S/ϵ_0) is also fairly constant, but not with the same value as ϵ^T/ϵ_0 . Accepted values for the relative permittivity are

$$\begin{aligned}\epsilon_{11}^T/\epsilon_0 &= 84 & \epsilon_{33}^T/\epsilon_0 &= 30 \\ \epsilon_{11}^S/\epsilon_0 &= 44 & \epsilon_{33}^S/\epsilon_0 &= 29 \quad (8).\end{aligned}$$

The variation with frequency is shown in Figure 4.

The second main area of interest is piezoelectricity. As stated previously, the direct piezoelectric effect is induced polarization from applied stress. This relationship, in tensor notation, is

$$P_i = \sum_{j,k} d_{ijk} \sigma_{jk}, \quad (3)$$

with $i, j, k = 1, 2, 3$ representing x, y, z . P_i is the induced polarization vector. Here, σ_{jk} is the second-rank stress tensor, and d_{ijk} is the third-rank piezoelectric tensor. The stress tensor is symmetrical, $\sigma_{jk} = \sigma_{kj}$. This dictates that the piezoelectric tensor contains 18 independent variables, so it can be written as a 3×6 matrix, with the jk subscripts reduced to a single subscript:

$$\begin{aligned}11 &\rightarrow 1 & 23, 32 &\rightarrow 4 \\ 22 &\rightarrow 2 & 13, 31 &\rightarrow 5 \\ 33 &\rightarrow 3 & 12, 21 &\rightarrow 6.\end{aligned} \quad (4)$$

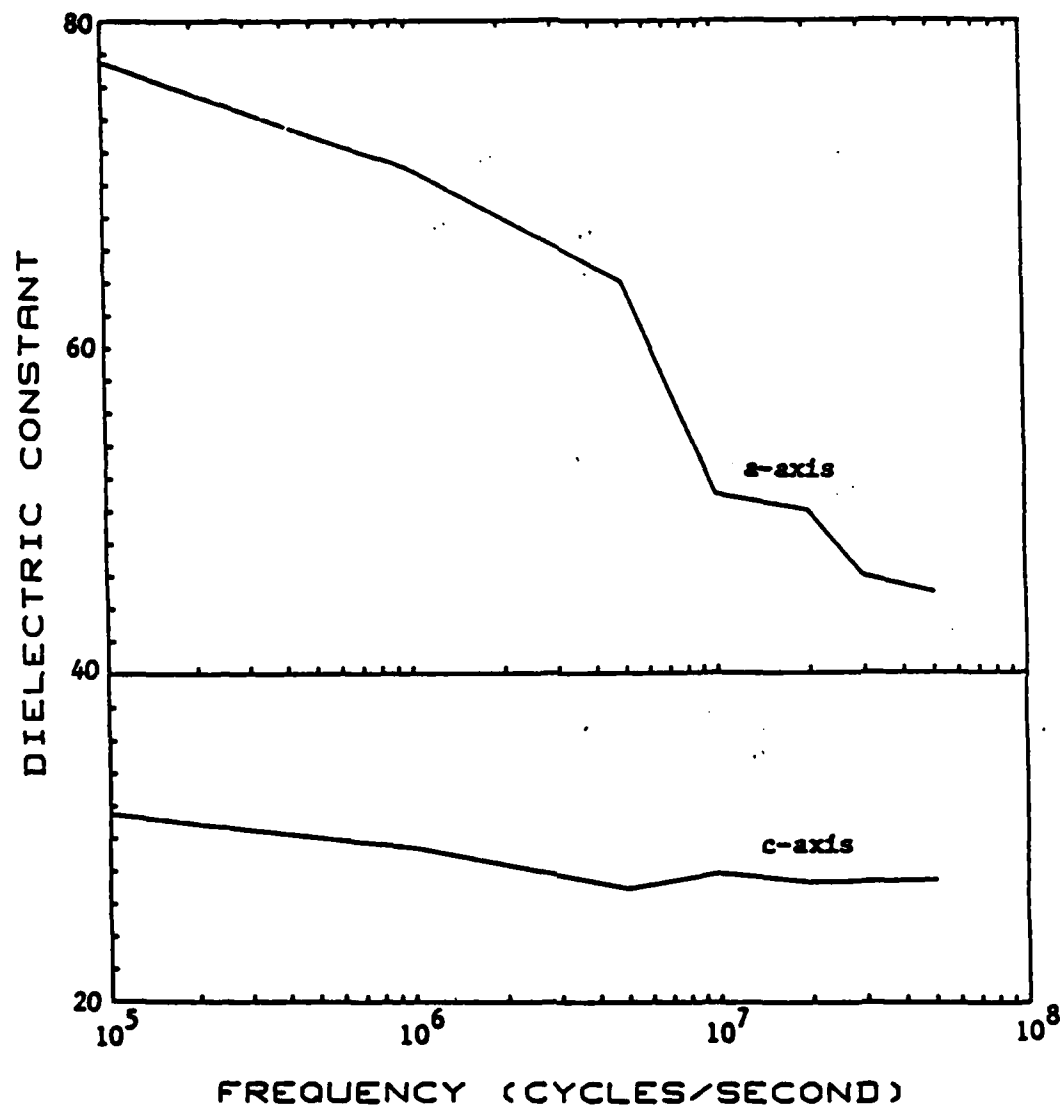


Figure 4. Dielectric constant as a function of frequency after Nassau et al. (4)

The tensors describing lithium niobate must have at least the symmetry of the 3m point group. When the reduced notation and the symmetries are applied to the piezoelectric tensor, the result is

$$d_{ijk} = \begin{bmatrix} 0 & 0 & 0 & 0 & d_{15} & -2d_{22} \\ -d_{22} & d_{22} & 0 & d_{15} & 0 & 0 \\ d_{31} & d_{31} & d_{33} & 0 & 0 & 0 \end{bmatrix}. \quad (5)$$

Therefore, only four independent coefficients, d_{15} , d_{22} , d_{31} , and d_{33} , are needed to describe the piezoelectric effect in lithium niobate. Accepted values for these coefficients are

$$d_{15} = 6.8 \times 10^{-11} \text{ Coulombs/Newton}$$

$$d_{22} = 2.1 \times 10^{-11} \text{ C/N}$$

$$d_{31} = -0.1 \times 10^{-11} \text{ C/N}$$

$$d_{33} = 0.6 \times 10^{-11} \text{ C/N (8).}$$

The converse piezoelectric effect is a strain resulting from an applied electric field. The coefficients that connect this strain and electric field are identical to those connecting the polarization and stress in the direct effect. Thus the relation, in tensor form is

$$S_{jk} = \sum_i d_{ijk} E_i \quad (6)$$

where S_{jk} is the second rank stress tensor.

The ability of piezoelectric materials to convert mechanical energy to electrical energy or vice versa is

expressed by an electromechanical coupling coefficient K .

This is defined equivalently as

$$K^2 = \frac{\text{mechanical energy converted into electrical energy}}{\text{mechanical energy input}}$$

for the direct effect, or

$$K^2 = \frac{\text{electrical energy converted into mechanical energy}}{\text{electrical energy input}}$$

for the converse effect.

To determine the coupling coefficient of the LiNbO_3 thin films produced in this investigation, the composite resonator construction was used. In a resonator configuration, K^2 can be determined from the series and parallel resonant frequencies, using

$$K^2 = \phi_s / \tan \phi_s \quad (7)$$

where $\phi_s = (1/2)\pi(f_s/f_p)$. In a thin film composite resonator, the same formula is used to define an effective coupling coefficient.

III. SPUTTER DEPOSITION

A. Mechanisms

Sputter deposition is the formation of a deposit (thin film) by the condensation of atoms or molecules formed by sputtering. Sputtering is the ejection of atoms from a surface by momentum transfer from high energy particles bombarding the surface. Sputtering is one of the most common thin film deposition methods. There are several unique advantages to sputter deposition including uniform coating of surfaces, a constant deposition rate, good adhesion of film to substrate, ability to deposit alloys and compounds as well as elements, and the ability to reactively sputter elements to produce compounds. While some materials, such as gold and aluminum, are very easy to sputter, others such as active semiconductor, ferromagnetic, or ferroelectric films can be extremely difficult. Lithium niobate is one of the latter.

A schematic of a basic sputtering system is shown in Figure 5. The important components include a vacuum chamber, a source of sputtering material (the target), a substrate for the sputtered material to deposit on, a source of gas, usually argon, to derive the high energy particles from, and a power supply to form an electric field from the target to the substrate region. The argon gas is injected

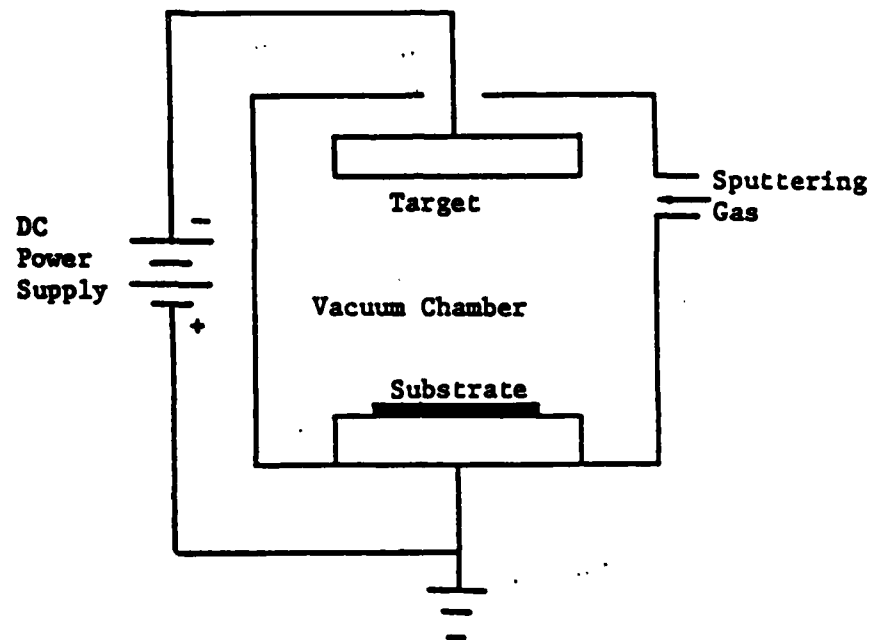


Figure 5. Schematic of a basic DC sputtering system

into the chamber at a certain flow rate. The electric field then acts to accelerate electrons into the argon atoms. The atoms are ionized, forming Ar^+ and more electrons, creating a plasma. The Ar^+ particles are then accelerated by the electric field into the target. Upon contact with the target several things could happen. The incident particle could simply be reflected from the surface, probably neutralized in the process. The impact could lead to a series of collisions within the target material, known as collision cascade, possibly imbedding the incident ion or ejecting a target atom (18). This ejected atom is considered a sputtered atom. Secondary electrons can also be ejected in this process. These are then used to sustain the plasma. The atoms of the target material which are sputtered tend to scatter in random directions, some striking and condensing on the substrate. When repeated again and again this results in a thin film coating.

Sputtering systems using r.f. power supplies, such as the one used in this investigation, are often needed when the target material is insulating. If an insulating target is used in a DC system the constant bombardment by positive ions would build up a positive charge on the target, thereby reducing the electric field and the ability of more positive ions to contact the surface. If an r.f. power supply is used, the alternating field causes the target surface to be

alternately bombarded with positive ions and electrons, avoiding charge build-up. Due to the large velocity difference between electrons and positive ions bombarding the surface, the target will charge up more slowly due to ion bombardment than due to electron bombardment. The result of this, plus the alternating field, is a self bias (or a DC offset) resulting in almost continuous bombardment of the target by positive ions. Another advantage of r.f. sputtering is the reduction of possible arcing. Since the applied field is sustained in one direction for less than one cycle, it is much more difficult for arcing to occur. Most r.f. sputtering systems operate at the FCC allowed frequency of 13.56 MHz.

Another feature of many sputtering systems is a magnetron assembly in the target holder. The magnetic fields produced are intended to make more efficient use of the ionization effect of the electrons. The electrons are trapped near the target as a result of the magnetic fields, increasing their ionization effect in that area, while reducing the possibly damaging effects of electron bombardment of the substrate.

When sputtering a multicomponent film, such as lithium niobate, it is likely that the target can be sputtered in both a molecular species form and in atomic form (18). Since it is not sputtered in a completely molecular form, it

is quite likely that the resulting stoichiometry of the thin film would be different than that of the target material. The resultant material is usually lacking in the gaseous element. When sputtering an oxide, such as lithium niobate, it is often found that the thin film is lacking in oxygen. This can be compensated for by adding several percent of the deficient element, such as oxygen, to the sputtering gas. With oxygen, the plasma environment provides opportunity for energetic electrons to disassociate the molecular oxygen into its chemically more active form. This is a form of reactive sputtering. Although reactive sputtering usually involves the deposition of a compound different from the target material by chemical combination with an element in the gas phase, this is still reactive sputtering for compensation purposes.

B. Lithium Niobate Sputtering System

The sputtering apparatus used to produce the LiNbO_3 samples for this research is an r.f. planar magnetron system. The vacuum system was built by NRC Equipment Corporation, but it has been extensively modified. A collar from a CVC Products vacuum system has been added to allow for the introduction of r.f. power from the side. The matching network, needed to provide optimum power dissipation in the plasma and to reduce reflected power, is

also from CVC. The vacuum chamber itself, along with the target assembly, is water cooled.

Within the sputtering system, the target assembly rests on the bottom of the chamber, thus allowing for a sputter-up configuration. The assembly is designed to hold an eight inch diameter sputtering target. Above the target, a large stainless steel plate is positioned. The substrate holder rests within a four inch hole in the center of this plate. The vertical position of the plate is adjustable to allow variation of the separation between the target and the substrate. The substrates are held onto the substrate holder by means of a thin stainless steel plate which screws into the holder. Mounted directly onto the back of the substrate holder is a resistive type heater. This permits the variation of the substrate temperature up to 750°C. A stainless steel shutter is available to protect the substrates during the presputter period. Presputtering is used to clean the target of contaminants formed there when exposed to atmosphere. The shutter also has adjustable vertical positioning.

The r.f. generator provided with this system, is a 13.56 MHz generator made by Plasma-Therm Inc. Although the generator is capable of power output of up to 3 kilowatts, it was never used at greater than 750 watts. Even at that power, the target can become heated to the point of glowing.

The DC bias voltage produced in this system varied from 200 volts to 600 volts, depending on the parameter settings.

The pumping system for the chamber consists of an oil diffusion pump backed up by a belt-driven mechanical pump. A liquid nitrogen cold trap and a water-cooled baffle are provided above the diffusion pump to prevent the backstreaming of oil into the chamber. The mechanical pump operates continuously to maintain a vacuum in the region below the main chamber, separated from the chamber by the main throttle valve.

The sputtering gases to be used for the sputtering process are introduced through the collar at the base of the chamber. The flow of the gases is regulated by means of a NUPRO toggle valve followed by a NUPRO needle valve in each gas line. To backfill the chamber with nitrogen following the sputtering runs, a third gas line in the chamber base is provided.

To monitor the pressure of the system, two ion gauges, two thermocouple gauges, a pirani gauge, and a capacitance manometer are provided. The ion gauges are positioned directly below the main throttle valve and midway up the chamber. One of the thermocouple gauges is located in the foreline, between the diffusion pump and the mechanical pump, while the other is located in the chamber roughing line. The pirani gauge and the capacitance manometer are

both located in the collar at the base of the chamber. The ion gauge controller is a MKS Type 290 Controller. The thermocouple gauges are controlled by a NRC 720 Controller. The pirani gauge meter is a CVC GP-310, and the capacitance manometer was manufactured by MKS. The substrate temperature was monitored by a thermocouple connected to a Temp-Tender Pyrometer.

The materials used in this sputtering apparatus were a lithium niobate target and gases of argon and oxygen. The target was manufactured by Cerac, Inc. and was composed of 99.9% pure powdered lithium niobate sintered into a disc 8.030 inches in diameter and 0.300 inches in thickness. The gases were high purity Ar and O₂ from Matheson.

C. Thin Film Formation

During the sputter deposition process, the sputtered material arrives at the substrate surface in atomic or molecular form. These atoms, or molecules, diffuse around the substrate in a manner dependent on the binding energy of the particles to the substrate. This is influenced by the nature of the substrate and the substrate temperature. As atoms join to form doublets and triplets, a process called nucleation, quasi-stable islands are formed. Eventually these islands coalesce to form a continuous film (18). If the substrate is a single crystalline material, the islands

will have an orientation determined by the substrate crystal structure, so that coalescence could lead to a single crystal film.

Heating the substrate increases the mobility of the sputtered atoms on it. With greater mobility, these atoms stand a better chance of finding a position of low energy in the growing film. This is consistent with crystal growth. Crystal growth is also enhanced by low deposition rates, since it takes time to find a low energy position.

In order for these two processes to work well together--the substrate determining the initial structure of the film, and atoms seeking positions of low energy within that film--it is important that the crystal structure of the substrate closely coincide with the natural crystal structure of the growing film, particularly as far as lattice parameters are concerned. This growth process is called epitaxy, and the ability to closely match lattice parameters of the substrate and film is vital.

D. Relevant Parameters

In order to successfully and reproducibly sputter a thin film, Mattox (19) lists the following variable parameters which need to be empirically established and kept constant:

System geometry.

Initial system vacuum.
Substrate/target distance.
Target and system preconditioning.
Substrate/target geometry.
Sputtering gas purity (in chamber).
Sputtering gas pressure.
Sputtering gas flow rate.
Target voltage and current.
Target temperature.
System gas throughput.
Substrate bias.
Substrate temperature.
Sputtering time.
Surface conditioning of target.
Cleanliness of vacuum target.
Exact procedure used for deposition.

For the deposition of LiNbO_3 in the vacuum system already described, some of these parameters are not variable, others are not applicable, and others are not monitorable, while several important parameters are not listed here. The most important factors to consider in the deposition of lithium niobate in the available system are the following:

Type of substrate.
Temperature of substrate.
Radio-frequency sputtering power.

Target-substrate separation.

Sputtering pressure.

Oxygen percentage of sputtering gas.

Each of these will now be examined in terms of their importance, possible choices in relation to the available system, and results of past attempts at varying these parameters to sputter-deposit lithium niobate.

The importance of substrate choice for the growth of single crystal films has already been pointed out. The crystal lattice parameters of LiNbO_3 were given in Chapter II as $a_H = 5.148 \text{ \AA}$ and $c = 13.863 \text{ \AA}$. In order to truly aid in the thin film crystal growth, a substrate of similar parameters should be used. Sapphire has been chosen as an excellent choice for a substrate (15), with parameters $a_H = 4.758 \text{ \AA}$ and $c_H = 12.991 \text{ \AA}$ (20). Single crystal lithium tantalate (LiTaO_3) has also been used as another excellent choice, with parameters $a_H = 5.154 \text{ \AA}$ and $c_H = 13.784 \text{ \AA}$ (21). Several researchers have used glass as a substrate, but that almost always resulted in an amorphous film (22,23,24,25). For economic reasons a possible choice is (111) oriented silicon. This can be considered to have possible matching parameters of $a = 7.681 \text{ \AA}$ and $c = 10.959 \text{ \AA}$. This is not as good of a match, but the crystals are less expensive than sapphire or lithium tantalate. Another point which must be considered is that in order for these films to eventually be

used as the piezoelectric material in the composite resonator described in the Introduction, they must be deposited on (100) silicon, to be able to form the membrane. This is a very poor lattice match along the c-axis, since (100) silicon is cubic with $a = 5.43095 \text{ \AA}$ (26).

The temperature of the substrate is important in determining when epitaxial growth might take place. Researchers who have attempted to deposit LiNbO_3 in single crystal or polycrystalline form have reported the need for a substrate temperature in the range of 325°C to 500°C (15,21,27). This temperature is dependent on the deposition rate, because for each deposition rate there is an epitaxial temperature, above which single crystals can possibly be grown. This deposition rate is determined mainly by the radio-frequency sputtering power and the target-substrate separation.

As stated previously, a slow deposition rate is one of the factors in determining crystal growth. Unfortunately, since the sputtering power is related to the total target size, it is difficult to make comparisons between the system used in this investigation and reported sputtering attempts in regard to applied sputtering power and target-substrate separation because of different target sizes or other unreported information.

The sputtering pressures used in past attempts to

sputter single crystal or polycrystalline LiNbO_3 have been in the range of 10 - 20 mtorr (15,21,26). However, if these were the optimal pressure values was not made clear. Only one of these attempts (15) utilized r.f. sputtering, which allows for a plasma to be sustained at lower pressures.

The last of the important variable parameters is the oxygen percentage of the sputtering gas. The importance of utilizing oxygen for compensation reactive sputtering to restore the proper stoichiometry in LiNbO_3 has already been pointed out. The amount of oxygen reportably needed to achieve this has been extremely variable in past attempts to deposit LiNbO_3 . Everything from 5% - 10% reported by Foster (26) in 1968, to 60% reported by Okada (21) in 1975, has been used.

E. Deposition Procedure

For the production of the samples used in this investigation, the substrate wafers were cleaned according to the following procedure:

Hot Trichloroethane	(10 min).
Acetone	(2 min).
Methanol	(2 min).
10% Hydrofluoric acid	(2 min).
Deionized water rinse	(5 min).

The hydrofluoric acid step was omitted when the substrate used was an oxide (sapphire). The cleaned substrate was then mounted to the substrate holder-heater assembly and

placed in the sputtering chamber. The shutter was interposed between the substrate and the target, and the heater was connected to its controller. The chamber was then roughed out by the mechanical pump alone to a pressure of 0.15 - 0.20 torr. At this point the main throttle valve was opened, and the diffusion pump was allowed to pump the chamber down to approximately 1×10^{-6} torr.

The argon and oxygen were then injected at the appropriate ratio with the chamber pressure monitored by the capacitance manometer. The pressure above the diffusion pump was also monitored by the ion gauge located there, to prevent the pressure there from approaching the diffusion pump oil backstreaming region of about 5×10^{-4} torr. The main valve was then throttled off and the pressure in the chamber allowed to rise to the 10 - 20 mtorr range needed to ignite the plasma. The r.f. generator was then turned on and the plasma ignited.

At this point the substrate heater was turned on and the temperature controller set to the desired temperature. Meanwhile the main throttle valve was slowly opened, allowing the chamber pressure to drop to the desired level. As the pressure dropped to the desired level and the plasma stabilized, the matching network needed periodic adjustment to prevent large amounts of reflected power. This time for plasma stabilization was also needed for the temperature of

the substrate to rise and stabilize at the desired value. This usually required an hour, and also served as an excellent presputter time for cleaning contaminants from the target.

When everything had stabilized, the shutter was opened and material was deposited on the substrate for the desired time, after which the r.f. power was turned off. The substrate was usually allowed to cool down in vacuum, then removed from the system following nitrogen backfilling. The sample was then ready for analysis. In all, this procedure, or a close variation, was used to produce 155 samples for this investigation.

IV. SAMPLE CHARACTERIZATION METHODS

A. Physical Appearance

The first means of characterizing the LiNbO_3 films produced in this investigation was by optical microscopy. This was primarily to check the uniformity and smoothness of the sputtered films. Most of the films were thin enough that they exhibited an interference color based on the thickness. Olympus Vanox microscopes were used for this aspect of the characterization. One of the microscopes is equipped with a Nomarski interference contrast feature which helped determine the surface roughness of the samples. Another purpose the microscopes served was as a means of determining the thickness of the thin films. A sodium lamp could be used as the light source for the microscopes. Since the edges of the sputtered films sloped down to the substrate gradually, rather than being sharp steps, light and dark interference fringes could be observed along the edges of the films when viewed with the sodium lamp. Using $2nd = m\lambda$, with the wavelength of sodium light being 5889 Å, and taking n to be the average of the ordinary ($n^o = 2.305$) and extraordinary ($n^e = 2.212$) indices of refraction of lithium niobate (28) at the wavelength of sodium light, then the thickness of the films per fringe is determined to be 1305 Å.

Another method for determining the thickness of the films was to use a Tencor Instruments Alpha-Step surface profiler. This uses a stylus moved across the surface of the substrate and film to determine the film depth. However, the accuracy of this instrument was not very good, and often in doubt, so it was used for depth measurement only periodically as a check against the method of counting fringes. The fringe counting method proved quite accurate despite the fact that if the deposited film was not exactly LiNbO_3 , the chosen values for the refractive indices would be incorrect. The Alpha-Step profiler was valuable though, as a tool for determining the surface roughness quantitatively. The Nomarski microscope allows only qualitative evaluation of surface roughness.

B. Infrared Analysis

To assist in the determination of the degree of crystallinity of the films produced, infrared transmission spectra were taken for several of the samples. The scans were made and the resulting curves were then compared with the results of Nassau et al. (29) seen in Figure 6. The range of the wavenumbers in the reference scan is greater than in the scans taken for this research, but it is enough to easily distinguish whether a sample more closely resembles the glass (amorphous) or the crystalline state.

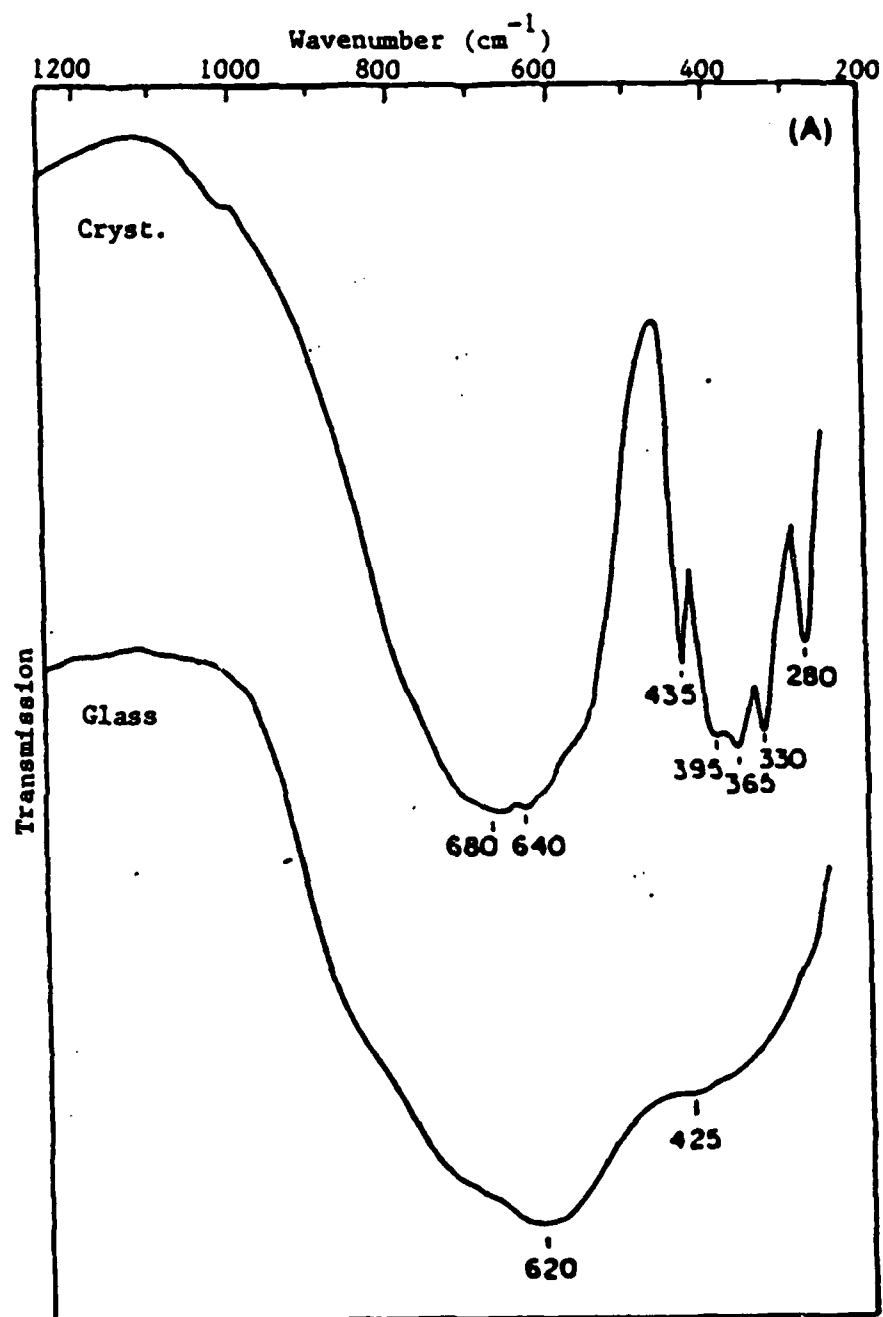


Figure 6. Infrared scans of LiNbO_3 after Nassau et al. (29)

The broad absorption band in the region $900 - 300 \text{ cm}^{-1}$ is due to the vibration of NbO_6 units within the material. A representative infrared scan is seen in Figure 7.

C. X-ray Diffraction

X-ray diffraction was used to determine the degree of crystallization and the orientation of the crystal structure. A single crystal material would display a peak on an x-ray diffraction pattern corresponding to the surface plane. A polycrystalline material would show many such peaks. An x-ray pattern of a powdered polycrystalline sample of lithium niobate is seen in Figure 8 for reference. Because of the applied electric field which is present during the sputtering process, it is expected that the lithium niobate would grow orienting itself with its c-axis normal to the substrate. Thus the final thin film should appear as a z-cut of LiNbO_3 when x-rayed, if it is a single crystal. Of course a peak from the single crystal substrate structure would also be present in the pattern. The (006) peak in the diffraction pattern corresponds to the c-axis of lithium niobate. In the powdered polycrystalline LiNbO_3 diffraction pattern, the (006) peak is only 4% of the strongest peak (012).

In order for the films produced in this investigation to have a chance of displaying a piezoelectric effect, the

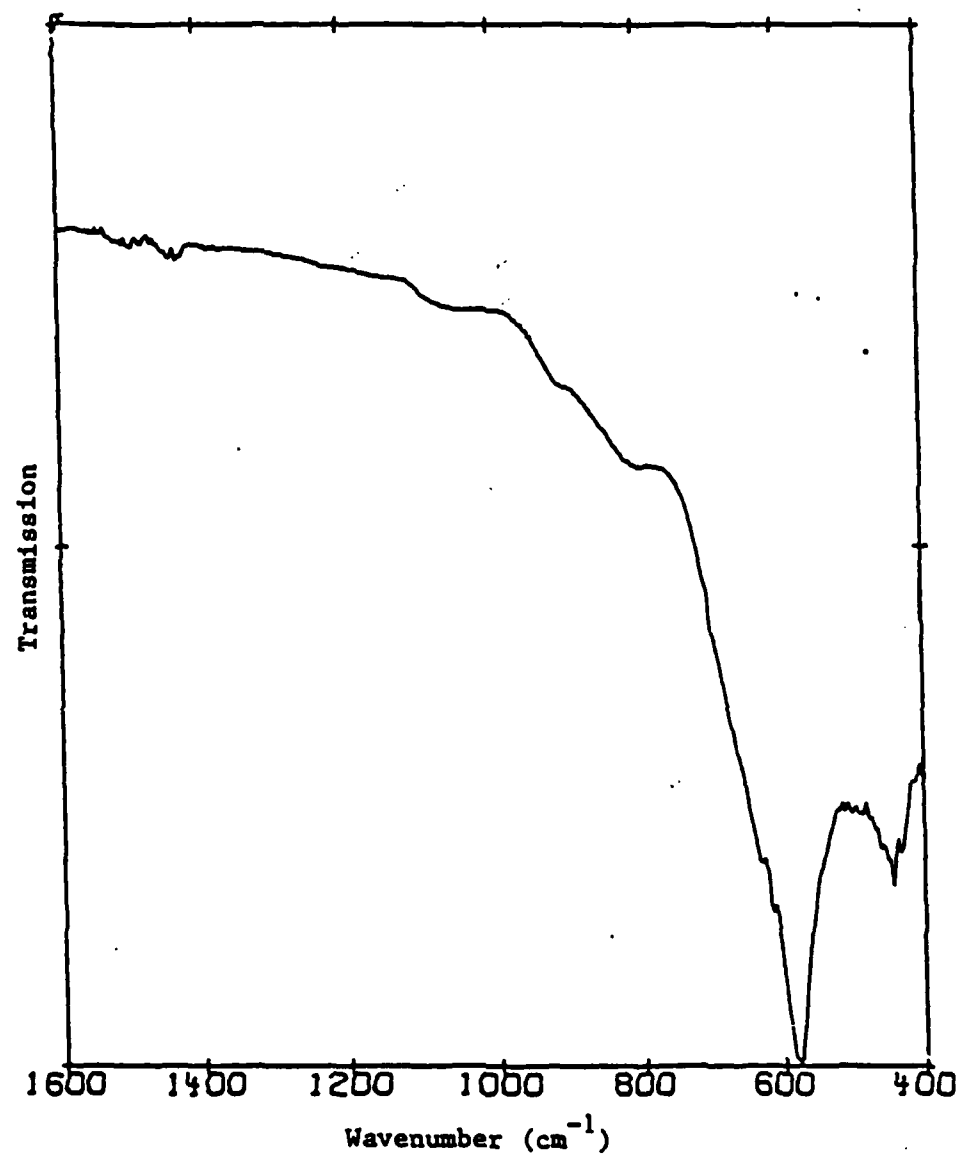


Figure 7. Infrared scan of sample LiNbO₃:49

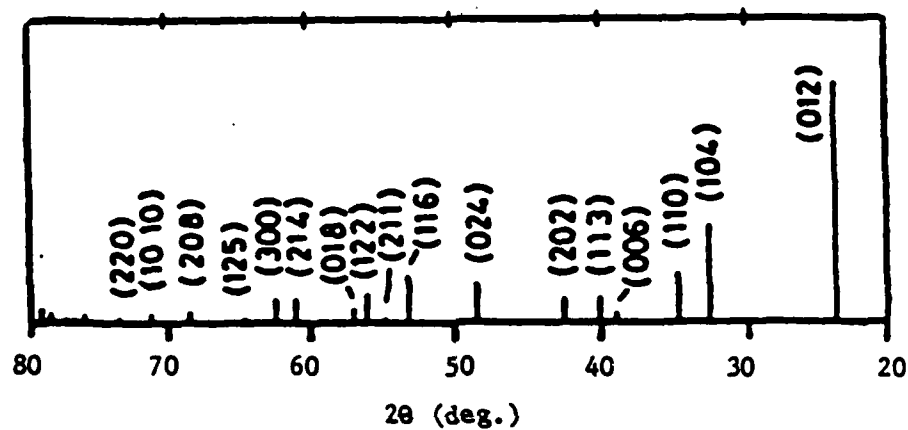


Figure 8. X-ray diffraction pattern of polycrystalline LiNbO_3

x-ray pattern should reveal only a prominent (006) peak. Polycrystalline material could also exhibit a piezoelectric effect if it is highly oriented. Thus if other peaks are present, as they would be in a polycrystalline material, they must be small in intensity compared to the (006) peak.

The x-ray equipment used to make these measurements was a Rigaku Geigerflex. A representative x-ray diffraction pattern appears in Figure 9.

D. Auger Analysis

A few of the samples in this investigation were examined using Auger electron spectroscopy. This involves the analysis of outer shell electrons ejected from a material with energy gained by another electron, as that electron fills a core level vacancy caused by ionization. This analysis determines the elements and their concentrations present in the material. For the samples in this investigation, Auger analysis could determine if the lithium, niobium, and oxygen were present with the proper stoichiometry. Impurity elements present could also be identified and measured.

Carbon is the impurity most commonly found in sputtered films. Oxygen and nitrogen are also common impurities in sputtered films, but in LiNbO_3 oxygen would not be an impurity. The most common problem found with the

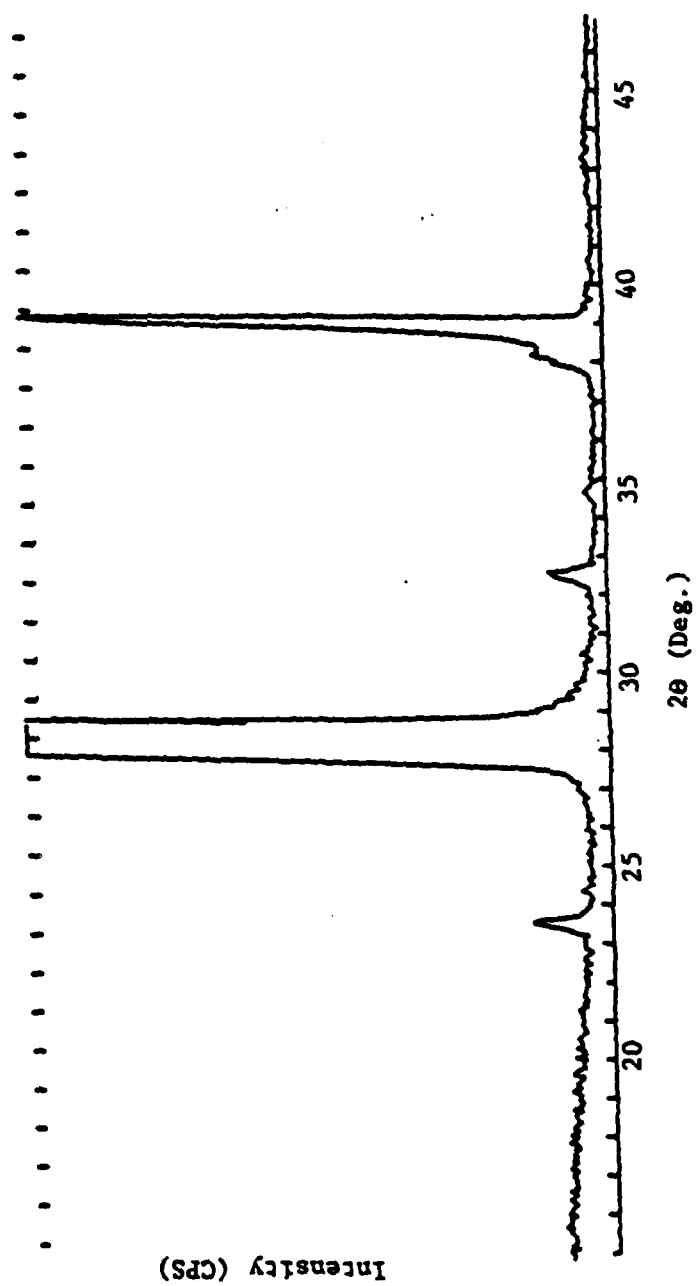


Figure 9. X-ray diffraction pattern of sample $\text{LiNbO}_3:61$

stoichiometry of sputtered LiNbO_3 films is a lack of oxygen. The Auger examinations were done in two Perkin-Elmer Auger systems. A representative element concentration depth profile from Auger analysis appears in Figure 10.

E. Network Analyzer Measurements

A Hewlett-Packard 8505A Network Analyzer and a Hewlett-Packard 8510T Network Analyzer were used to determine the dielectric constant (relative permittivity) and the piezoelectric response of the sputtered lithium niobate films. To make these measurements, LiNbO_3 films were deposited onto membranes of (100) silicon to form composite resonators, as described in the Introduction. The top metallization pad was a $400\text{ }\mu\text{m} \times 400\text{ }\mu\text{m}$ pad of aluminum. This metallization pattern was also used on films deposited on silicon without membranes to determine the dielectric constant of the LiNbO_3 films from two sources--structures with and without membranes.

The relative permittivity of the films was determined by taking reflection coefficient measurements of the aluminum pattern samples using the network analyzer. Capacitive reactance (X_C) values can be determined from the Smith Chart at various frequencies, an example of which can be seen in Figure 11. The relative permittivity can be determined from the capacitive reactance, the frequency, the

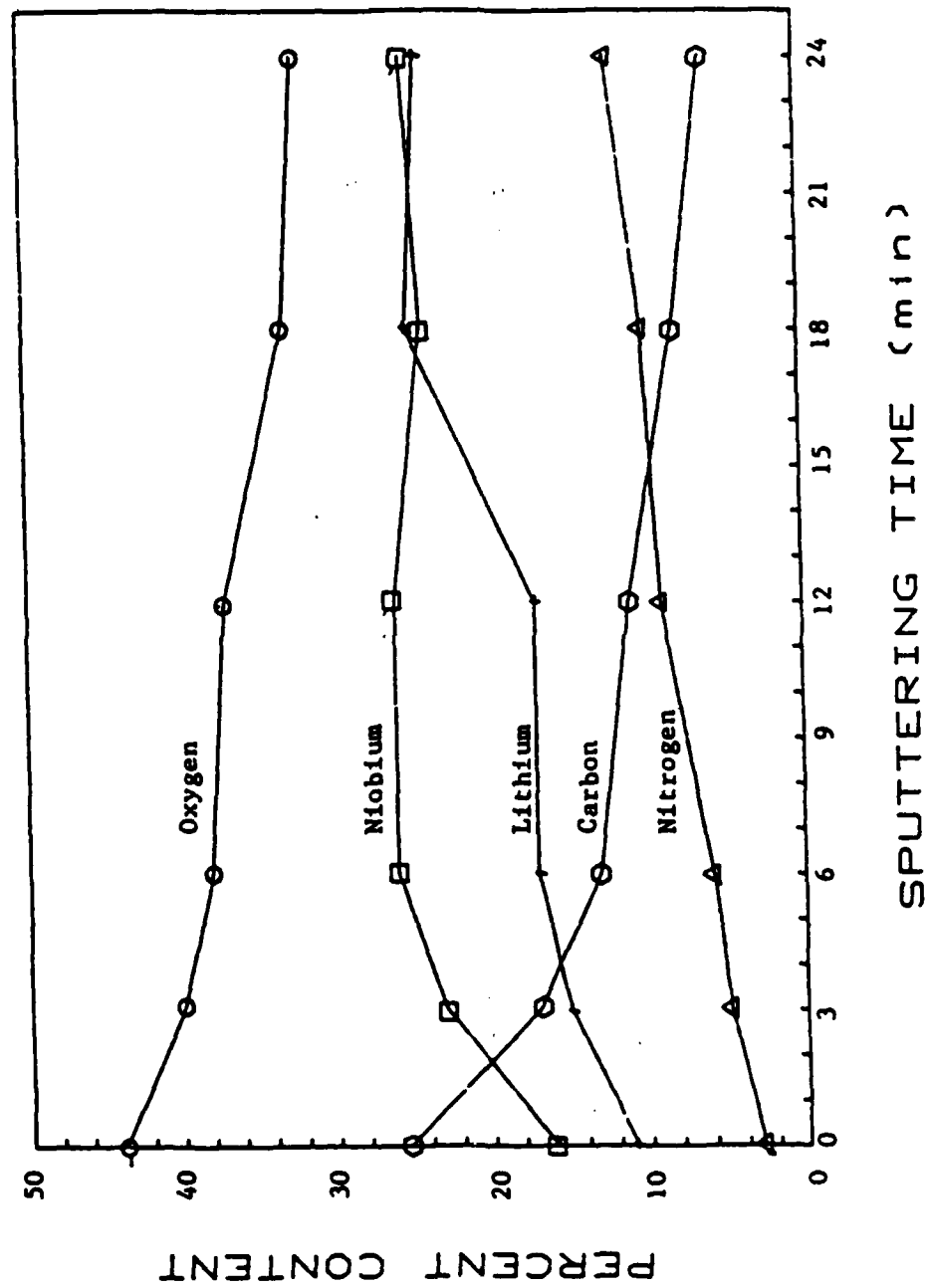


Figure 10. Auger analysis depth profile of sample $\text{LiNbO}_3:81$

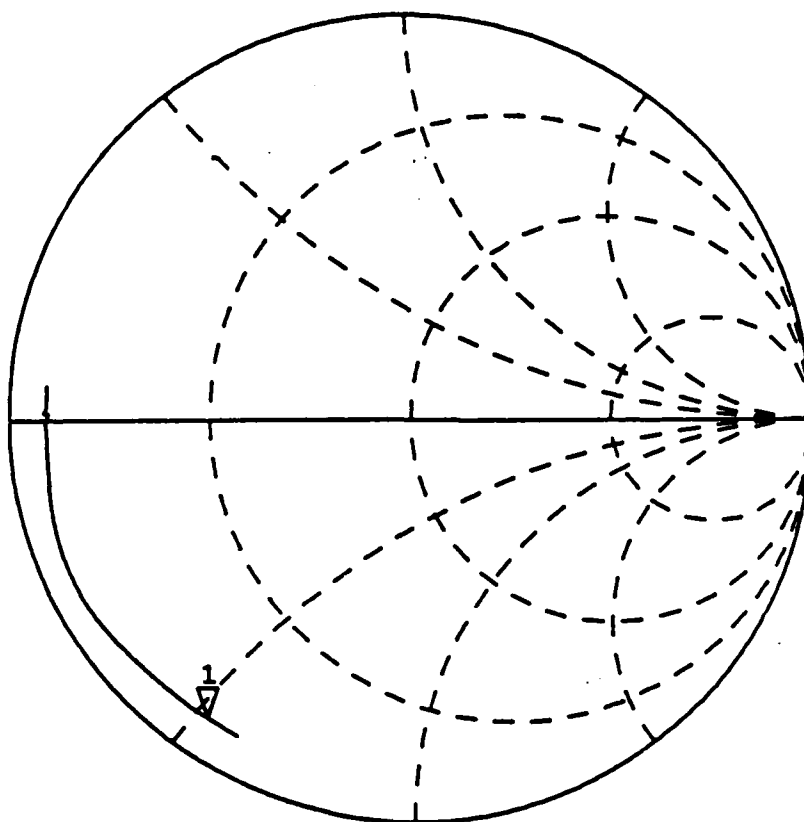


Figure 11. Smith Chart capacitive reactance measurement of sample $\text{LiNbO}_3:139$

thickness of the film, and the area of the metal pad.

Capacitive reactance can be expressed by

$$X_C = 1/\omega C = 1/2\pi f C. \quad (8)$$

The capacitance is

$$C = \epsilon_0 \epsilon_r A/d. \quad (9)$$

Therefore,

$$X_C = \frac{d}{2\pi f \epsilon_0 \epsilon_r A} \quad (10)$$

or

$$\epsilon_r = \frac{d}{2\pi f \epsilon_0 X_C A}. \quad (11)$$

The dielectric constant measurements in this investigation were made at low frequencies (10 - 50 MHz), well below the resonant frequency for films of the thickness sputtered here. Since it has been shown that the thin films produced appear as z-cut LiNbO_3 , if properly oriented the expected relative permittivity is $\epsilon_{33}^T/\epsilon_0 = 30$.

The resonant frequency of a z-cut thin film lithium niobate resonator is determined as follows. The wave velocity for a longitudinal mode propagating in the z direction is 7.33059×10^3 m/s (30). For the fundamental resonance, the frequency is given by $f = v/2d$. Thus for a one micron thick piece of z-cut lithium niobate, a frequency of 3.67 GHz would be expected. If the one micron layer of lithium niobate were on top of a layer of silicon several

times that thickness, the wave excited by the lithium niobate would propagate through the thicker silicon layer, reducing the frequency to a more easily measurable value. The coupling coefficient in this composite resonator can be determined from the formula defined in Chapter II,

$$K_{EFF}^2 = \phi_s / \tan \phi_s \quad (7)$$

where $\phi_s = (1/2)\pi(f_s/f_p)$. The parallel and series resonance frequencies can be determined from the electrical impedance (Z) of the composite resonator. The series resonance is defined as the minimum of Z , and the parallel resonance is defined as the maximum of Z . This relationship is sketched in Figure 12.

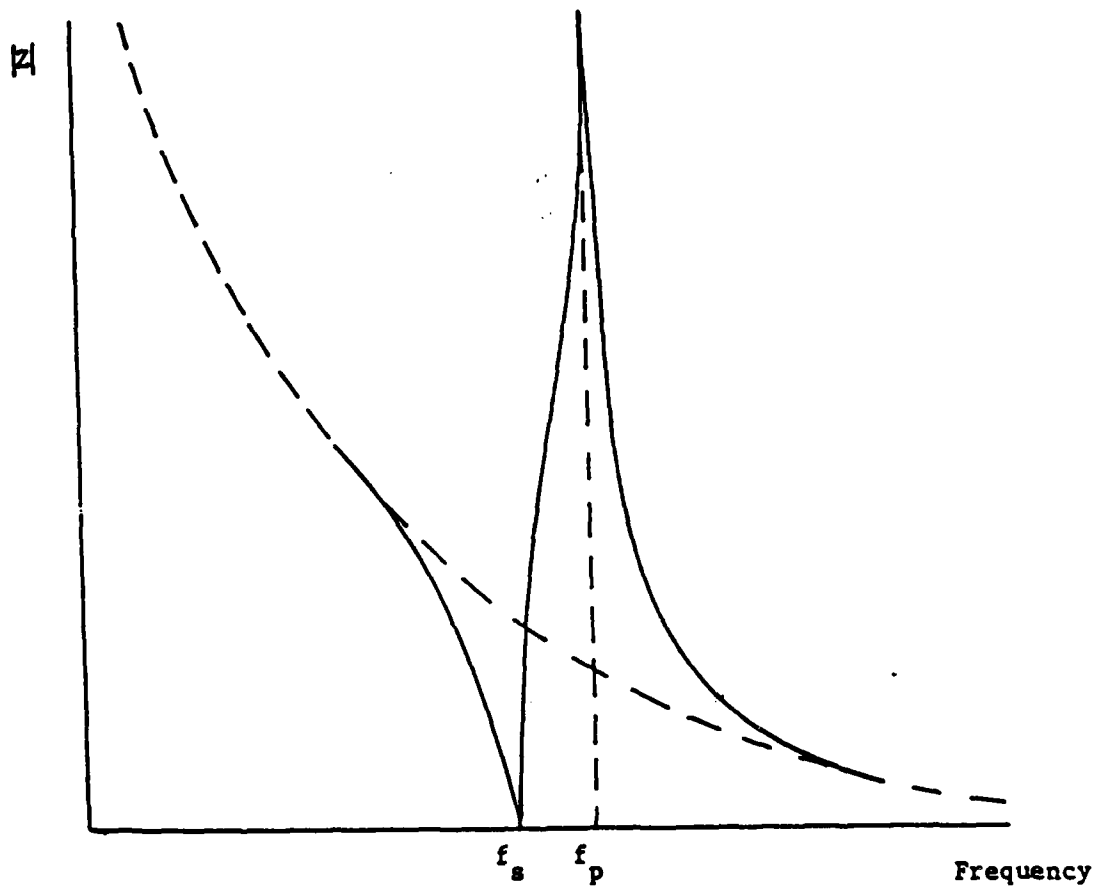


Figure 12. Relationship of series resonance and parallel resonance frequencies to electrical impedance

V. RESULTS AND DISCUSSION

A. Parameter Development

In determining the optimal parameter values for the r.f. sputtering of lithium niobate for this research, it was not always a case of determining the parameter values that would produce the best quality films. This was especially true for the choice of a substrate and the choice of applied r.f. power. As was previously pointed out, choosing a substrate with a good lattice match would be of little value in using the film in a composite resonator. Also, substrate cost is an additional consideration. Therefore, most of the samples in this investigation were deposited on either (100) or (111) silicon, and the remaining parameters were varied to produce the best quality films on the silicon. The applied r.f. power also had a constraint placed on it which possibly prevented the determination of the actual optimal value. It was impractical in the unautomated sputtering system used in this research to deposit for an extended period of time. A deposition rate of less than 1000 Å/hour could not be used very often. Since the applied power is directly related to the deposition rate, r.f. power values of less than 250 watts had to be avoided. This was unfortunate since it has been suggested that deposition rates on the order of less than 500 Å/hour are needed for

single crystal LiNbO_3 films (15,21).

The remaining four variables also had constraints placed on them, although these constraints probably did not affect the optimization of the parameter values. The separation between the target and the substrate could not be less than 4 cm, since below that value the plasma would not ignite easily. The separation could not be more than 10 cm, since the deposition rate would become too low for practical sputtering. It was stated in Chapter IV that the sputtering power could not be used higher than 750 watts because of overheating problems. The sputtering pressure had limits of approximately 0.5 mtorr and 25 mtorr. Below 0.5 mtorr the plasma could go out, and above 25 mtorr stability in the plasma and stability in maintaining a constant pressure could be problems. The substrate temperature had limits of approximately 200°C and 750°C. The lower limit was set by the heating of the substrate by the plasma, while the upper limit was set by the maximum ability of the resistive heater. The ratio of argon to oxygen gas had no restrictions. This information is summarized in Table 1.

Optimization of the parameters was a matter of varying one parameter while attempting to hold the others constant. Difficulties arose when more than one parameter influenced a film growth property. For example, both the applied power and the target-substrate separation would influence the

Table 1. Range of permissible parameter variations

Parameter	Range
Type of substrate	---
Temperature of substrate	200°C - 750°C
Radio-frequency sputtering power	250 watts - 270 watts
Target-substrate separation	4 cm - 10 cm
Sputtering pressure	0.5 mtorr - 25 mtorr
Oxygen percentage of sputtering gas	0% - 100%

deposition rate. One separation would result in one optimal applied power setting, while another separation would result in a different optimal applied power setting. In this respect, the optimal parameter values obtained in this research were only optimal relative to each other.

To begin this optimization procedure, initial values for some of the parameters were taken from similar attempts by others to sputter deposit LiNbO_3 . A temperature of approximately 500°C was indicated (15,21), as was an oxygen content of about 40% (15). An initial sputtering pressure of 1 mtorr to 3 mtorr was chosen after several initial sputtering runs were done for qualitative assessment.

The determination of the quality of the lithium niobate films was based on the degree of crystallization and the crystal orientation. X-ray measurements were best suited for this determination. Throughout most of the x-ray measurements made in this investigation, three peaks of lithium niobate dominated the patterns. The (006), (012), and (104) peaks were most consistently present in the patterns. Intensity data were taken of the three peaks in the diffraction patterns, with the intent of finding parameter settings which most enhanced the (006) peak, while reducing or eliminating the (012) and (104) peaks. This defined the highest quality films producible.

The first parameter to be determined was the sputtering

power. The target-substrate separation was arbitrarily set and the other parameters were set as given above. X-ray patterns at 500 watts and 700 watts showed distinctly lithium niobate polycrystalline peaks but with poor orientation. At both power settings the (006) peak was smaller than the (012) or (104) peaks. An example of this can be seen in Figure 13. In the pattern of the 700 watt sputtering, the (006) peak was barely visible. This is consistent with high deposition rates resulting in poorer crystal structure. Setting the r.f. power at 300 watts resulted in the (006) peak being the dominant peak, and since much below this power setting resulted in an impractical deposition rate, 300 watts was chosen as the optimal r.f. sputtering power for the system used in this research.

The next parameter to be determined was the target-substrate separation. X-ray patterns taken of samples with a separation of 10 cm revealed the (006) peak was no longer the dominant peak. X-ray patterns of samples with the separation from 4 cm to 6 cm displayed a dominant (006) peak, but also displayed numerous other peaks not associated with LiNbO_3 . These can be seen in Figure 14. Diffraction patterns of films produced using a target-substrate separation of 8 cm showed a dominant (006) peak and few or no peaks not belonging to LiNbO_3 . Therefore, 8 cm was

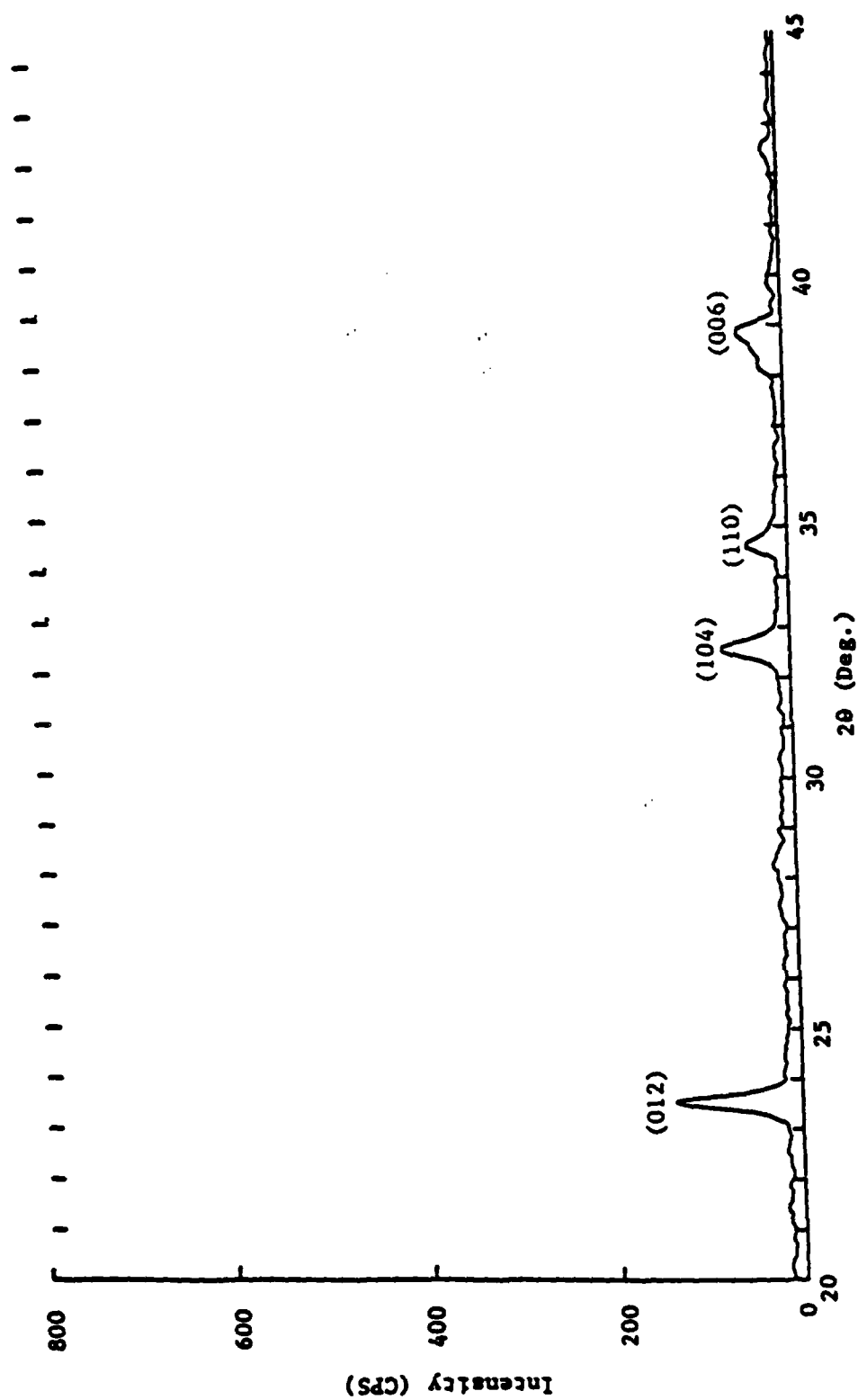


Figure 13. X-ray diffraction pattern of sample $\text{LiNbO}_3:128$. High r.f. power setting resulted in an insignificant (006) peak

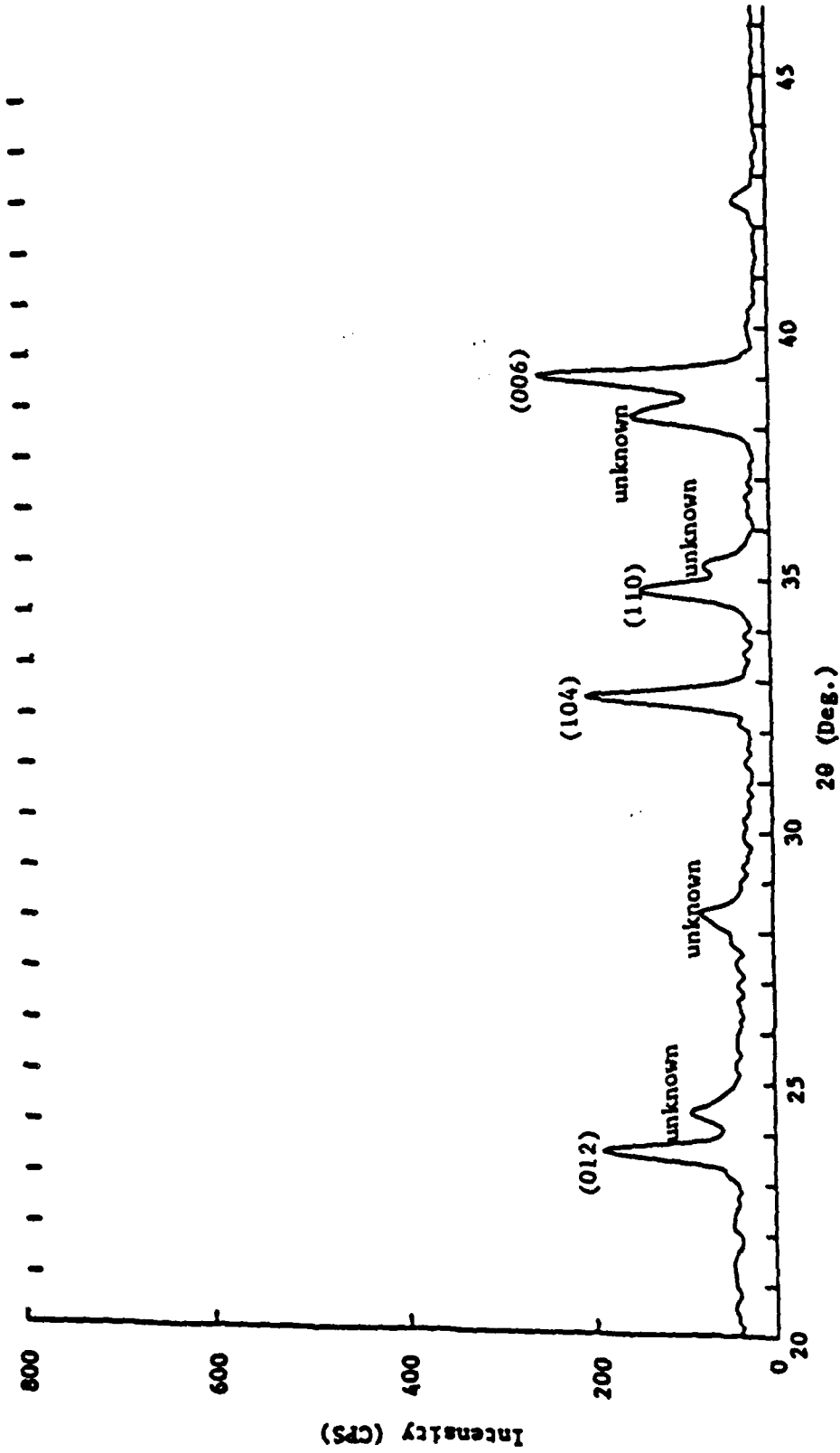


Figure 14. X-ray diffraction pattern of sample $\text{LiNbO}_3:124$. Small target-substrate separations resulted in numerous peaks not associated with LiNbO_3

chosen as the optimal target-substrate separation associated with an applied r.f. power of 300 watts. These two parameters, combined with the area of the target, resulted in a power density of 0.12 watts/cm^3 .

The next parameter to be optimized was the sputtering pressure. With the applied power and the target-substrate separation held at their determined values, and the substrate temperature and oxygen content being approximately 500°C and 40%, respectively, the sputtering pressure was varied from 1 mtorr to 20 mtorr. A portion of the x-ray results can be seen in Figure 15. For this figure, the amplitudes of the three peaks, (006), (012), and (104) were measured as a function of pressure. The intent was to determine a pressure that maximized the (006) peak, and minimized the others. These criteria were only met at 3 mtorr. Below that value, all three peaks dropped off rapidly. Above 3 mtorr, the amplitude of the (006) peak dropped off, while the amplitudes of the other peaks increased. Thus, a sputtering of 3 mtorr was determined as the optimal pressure associated with an applied power of 300 watts and a target-substrate separation of 8 cm.

The optimal oxygen content was determined next. Using the same procedure as was used to determine the sputtering pressure, the amplitudes of the diffraction peaks were plotted as a function of percent oxygen content in Figure

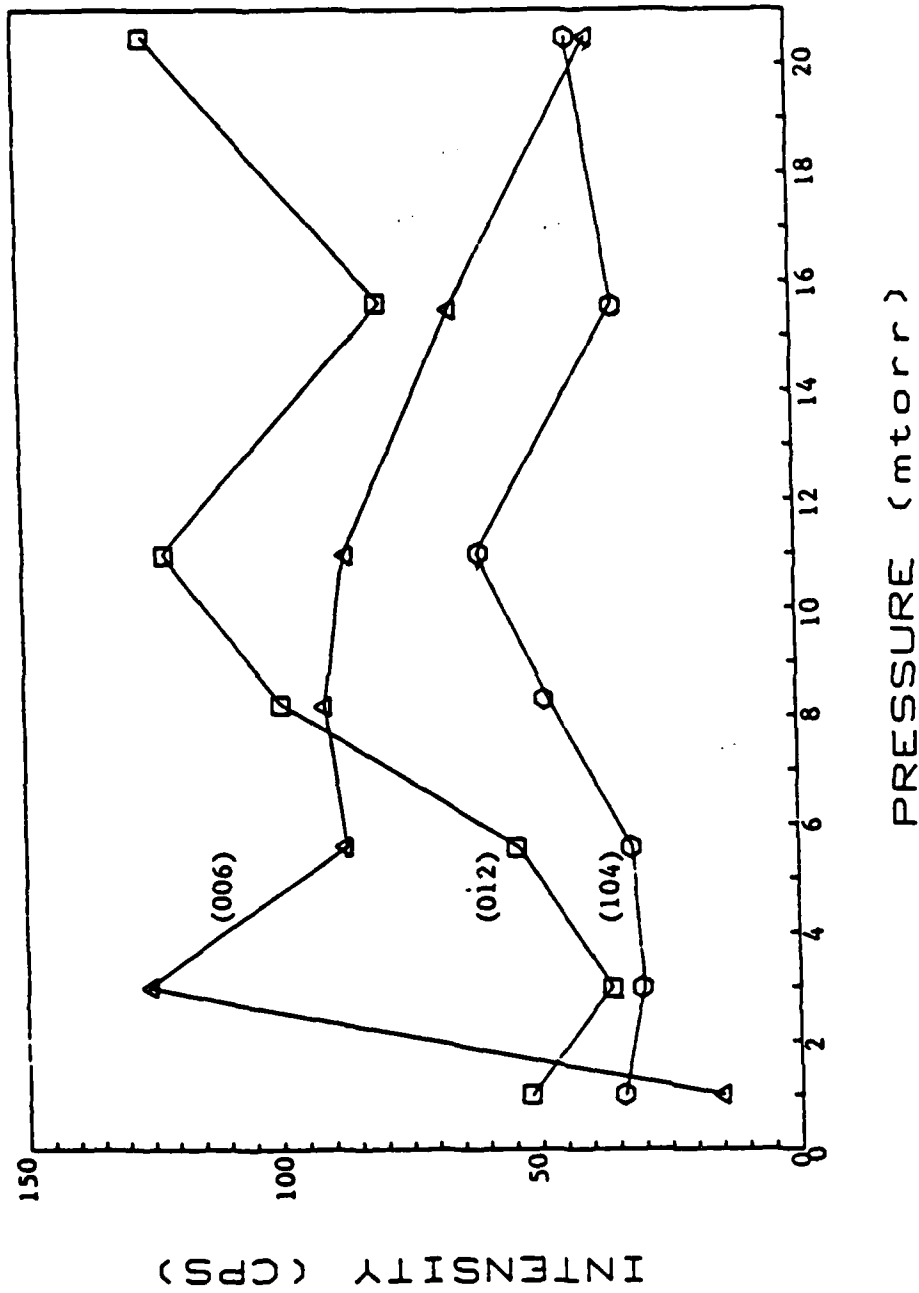


Figure 15. X-ray diffraction results of variation in sputtering pressure. The (006) peak is maximized, while the others are minimized at 3 mtorr

16. This plot indicated a desirable oxygen content of 50%. Although anything between 40% O₂ to 60% O₂ appeared favorable. Above 60% oxygen all peaks dropped off in intensity quickly. Below 40%, the intensity of the (006) peak dropped off until it fell below the intensities of the (012) and (104) peaks at approximately 20% O₂. The x-ray diffraction patterns used to produce Figure 16 can be seen in the Appendix. The optimal oxygen content associated with a sputtering pressure of 3 mtorr, an applied r.f. power of 300 watts, and a target-substrate separation of 8 cm, was determined to be approximately 50%.

The last parameter to be determined was the substrate temperature. The other parameters were kept as determined and the temperature was varied. Once again a peak intensity plot was developed. This is presented in Figure 17. The lithium niobate remained completely amorphous until a small (006) peak appeared near 250°C. The other two peaks did not appear until higher temperatures. The (006) peak intensity quickly increased as the temperature increased. The other two peaks also quickly increased with temperature. Although the most intense (006) peak occurred at the highest temperatures, this was not chosen as the optimal temperature since the (012) peak was also very intense at those temperatures, and peaks not associated with LiNbO₃ occurred after 600°C. One of the extraneous peaks became a dominant

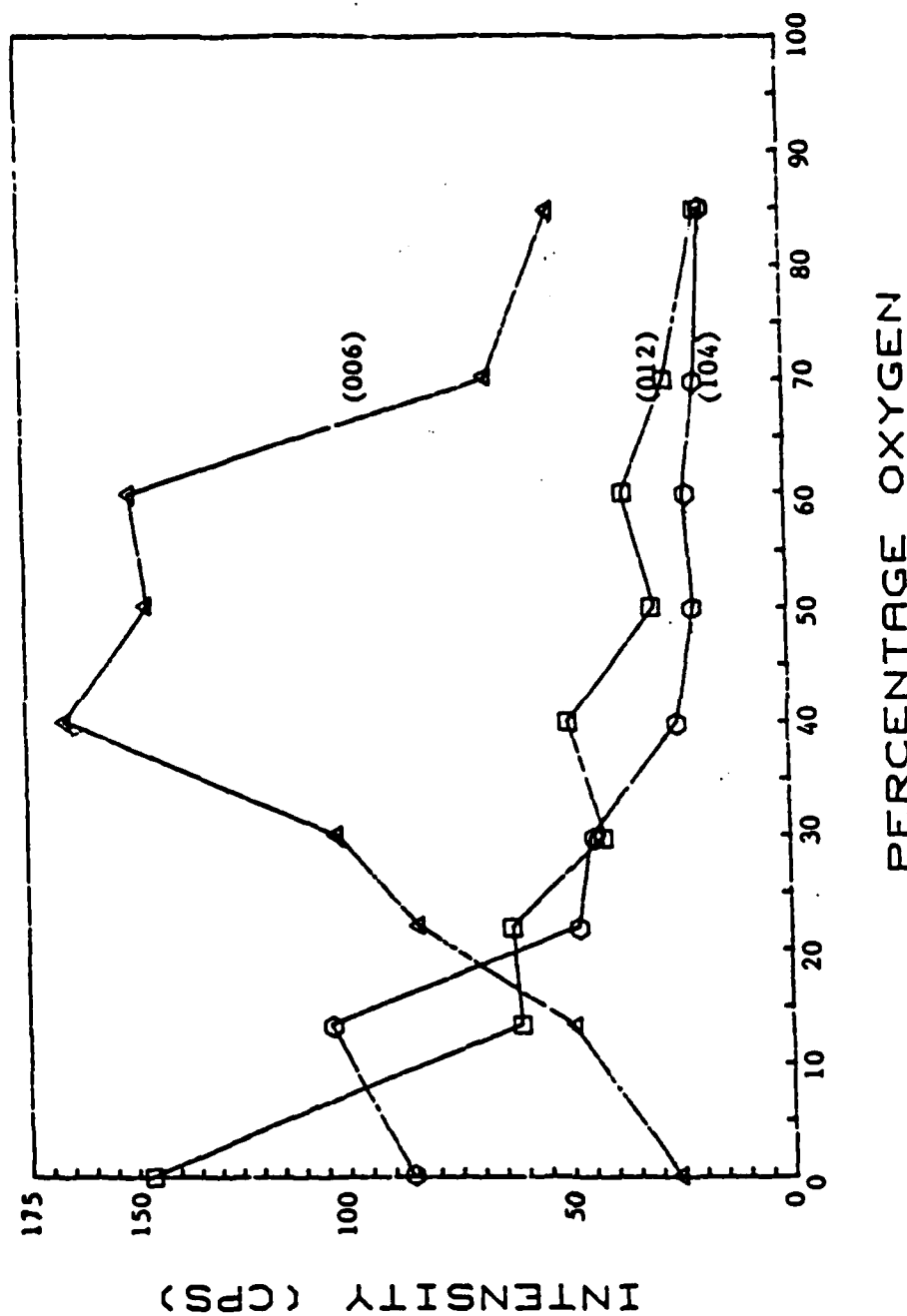


Figure 16. X-ray diffraction results of variation in oxygen content of sputtering gas. Optimal content is 50%

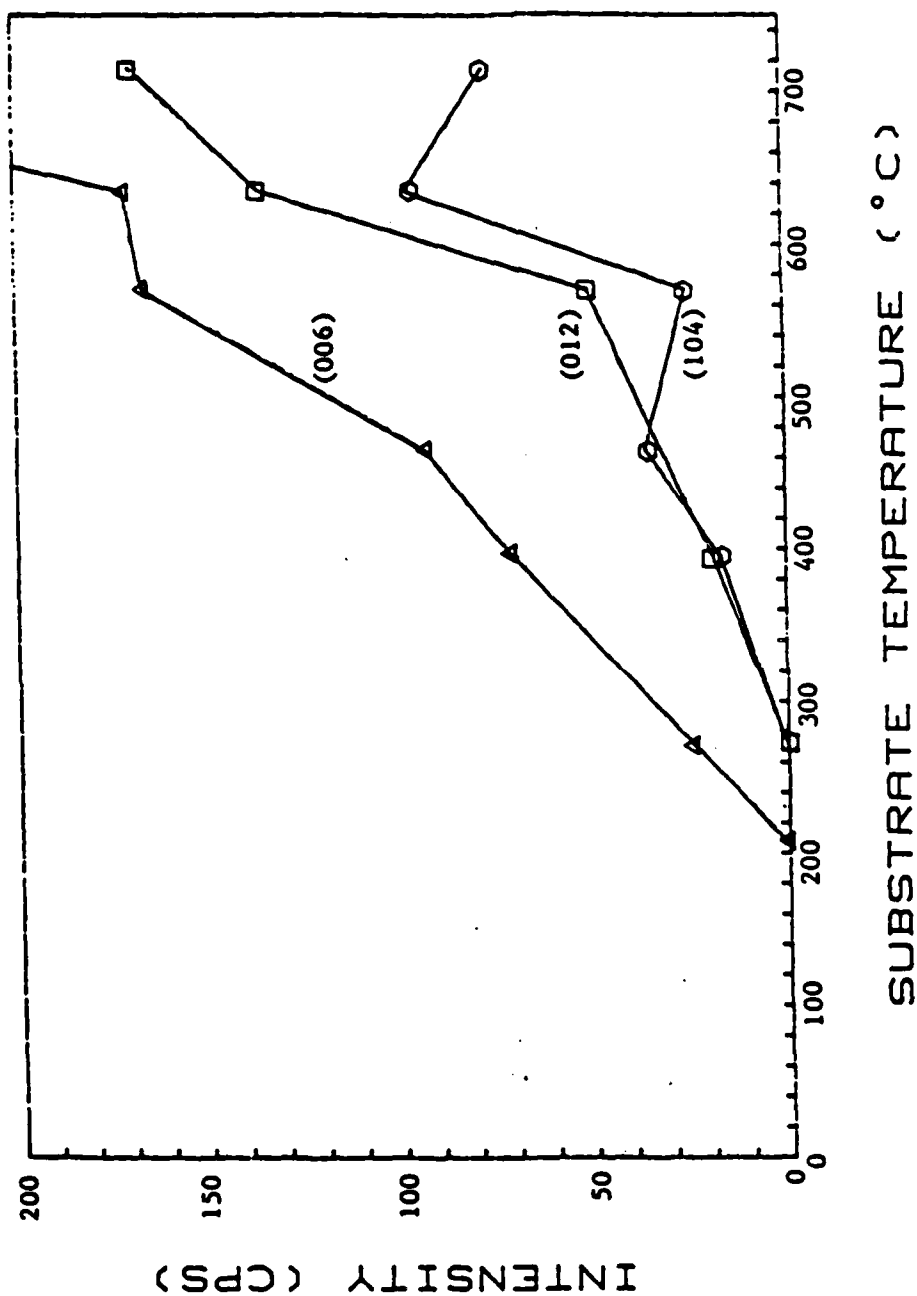


Figure 17. X-ray diffraction results of variation in substrate temperature. Peaks not associated with LiNbO_3 occurred at temperatures above 600°C

peak at high temperatures. Only around 550°C - 600°C was the (006) peak most dominant with no non-LiNbO₃ peaks present. Thus, the optimal temperature associated with an oxygen content of 50% in the sputtering gas, using a sputtering pressure of 3 mtorr, with applied r.f. power of 300 watts, and a target-substrate separation of 8 cm, was determined to be between 550°C and 600°C.

This entire optimization procedure was constantly being modified with slight variations in an attempt to achieve perfect films. The numbers presented here represent the parameter values ultimately achieved after many such permutations.

These resultant parameters, summarized in Table 2, were then used to produce films on substrates of (100) silicon, (111) silicon, and basal-plane sapphire. X-ray diffraction measurements were then taken of these samples. The results are presented in Figure 18. This figure shows that while the use of (111) oriented silicon seemed to have improved the crystallinity of the films slightly, compared to those films on (100) silicon, the sapphire substrate, with its excellent lattice match, made a radical improvement in the crystalline quality of the film. The x-ray pattern of the film deposited on the basal-cut sapphire substrate can be seen in Figure 19.

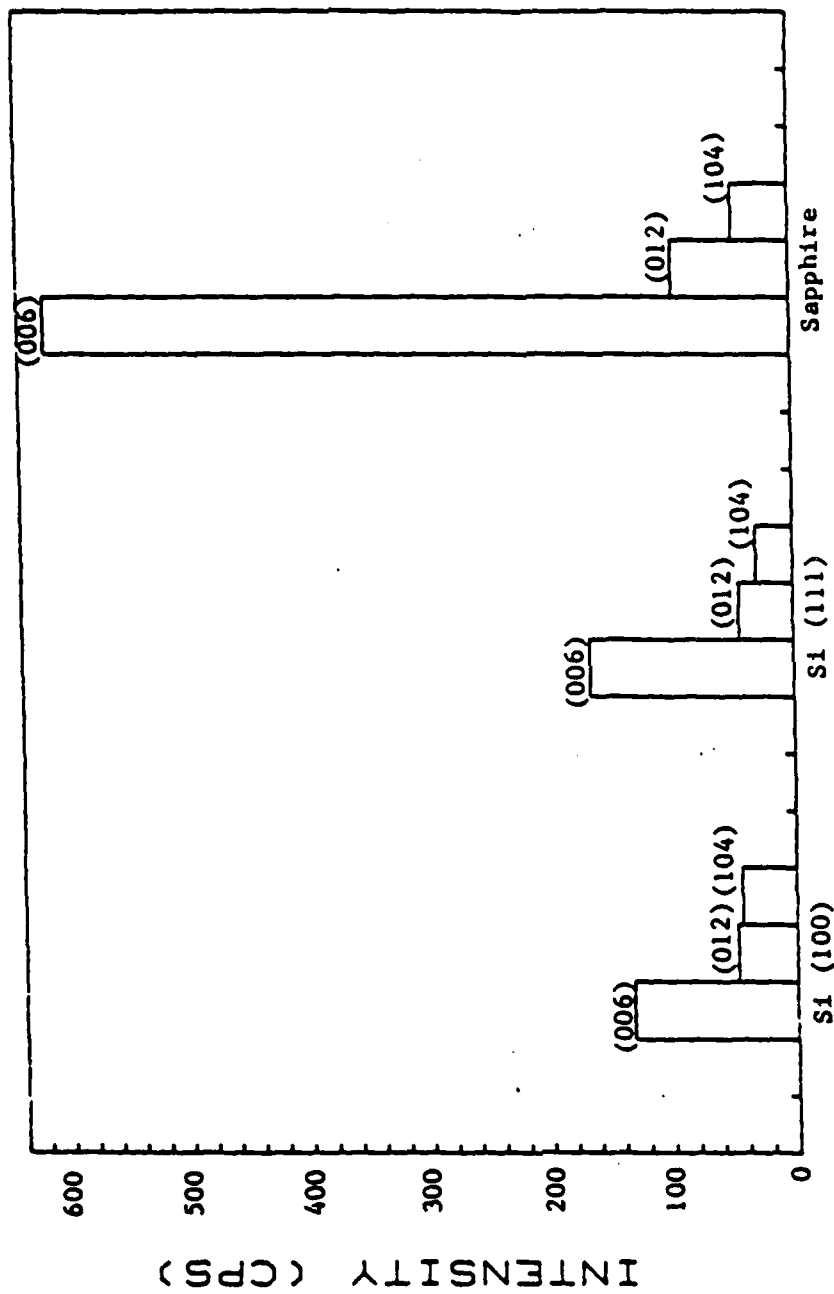


Figure 18. X-ray diffraction peak intensities of films on (100) silicon, (111) silicon, and basal-cut sapphire

Table 2. Optimal parameter values determined

Parameter	Optimal Value
Type of substrate	Sapphire
Temperature of substrate	550°C - 600°C
Radio-frequency sputtering power	300 watts
Target-substrate separation	8 cm
Sputtering pressure	3 mtorr
Oxygen percentage of sputtering gas	50%

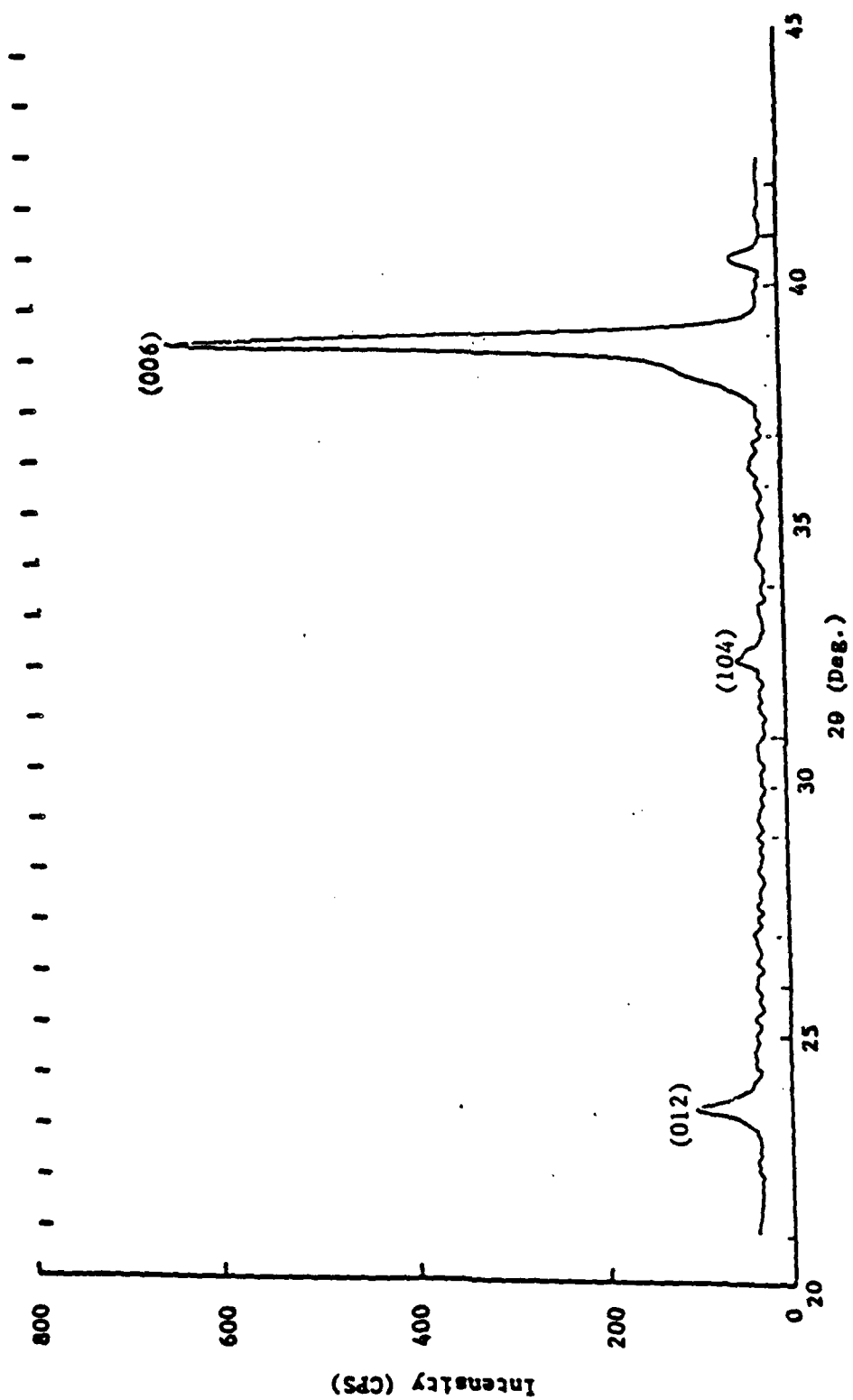


Figure 19. X-ray diffraction pattern of sample LiNbO₃:153 on basal plane sapphire

B. Characterization

The physical appearance of the films produced in this investigation were marked by a high degree of surface roughness. The thicker the films, the rougher the surface became. This is illustrated, using surface profiles from the Tencor Alpha-Step, in Figure 20. This was a feature of all the crystalline films produced in this investigation. The amorphous films however, those produced at low substrate temperatures, exhibited remarkably smooth surfaces. This surface roughness of the crystalline films presents a major problem for the possible use of sputtered LiNbO_3 thin films as resonator material. Films of greater than one micron are needed, and the surfaces must be very smooth for wave reflection. This research indicates that this is not likely with LiNbO_3 sputtered as it was here. This surface roughness feature of sputtered LiNbO_3 was also noted by Nunomura et al. (31).

Thickness measurements were made of the samples during the optimization procedures described in the last section. The results are given here. The variation of temperature and the variation of pressure resulted in very little detectable change in film thickness, except for a slight increase noted with increasingly amorphous material. Variation of r.f. power, oxygen content of the sputtering gas, and target-substrate separation, on the other hand

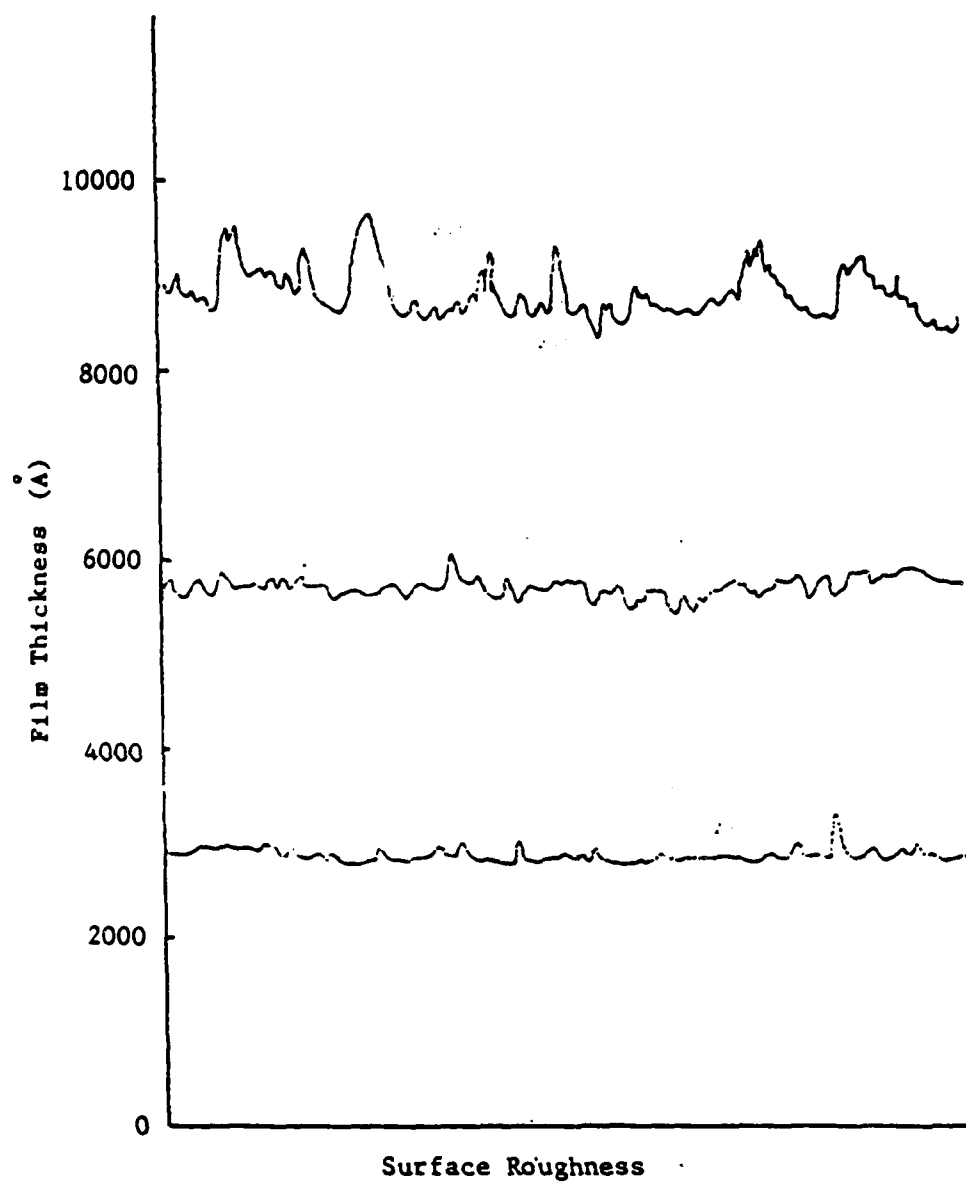


Figure 20. Surface roughness of LiNbO_3 films with increasing thickness

resulted in distinct thickness changes. The relationship between film thickness and target-substrate separation was reasonably linear over the range investigated, while the relationships between film thickness and oxygen percentage of the gas, and film thickness and applied r.f. power are shown in Figure 21 and Figure 22, respectively.

Infrared transmission spectra were obtained for many of the samples early in the investigation. These scans however, revealed little in the way of useful quantitative data. All of the scans produced look remarkably similar, revealing a crystalline structure, but giving no information on the degree of crystallization, or crystalline orientation. An infrared scan taken of a latter film produced using the optimized parameters is seen in Figure 23. This figure depicts somewhat more defined peaks than earlier attempts.

X-ray diffraction provided the information on crystal structure that IR analysis could not, and many of the results were presented in the last section. What must be pointed out is that despite the optimization of the sputtering parameters, the resulting films were still polycrystalline. While the polycrystalline films were oriented with the c-axis normal to the plane of the substrate, the orientation was not that strong.

Auger analysis on early samples in this investigation

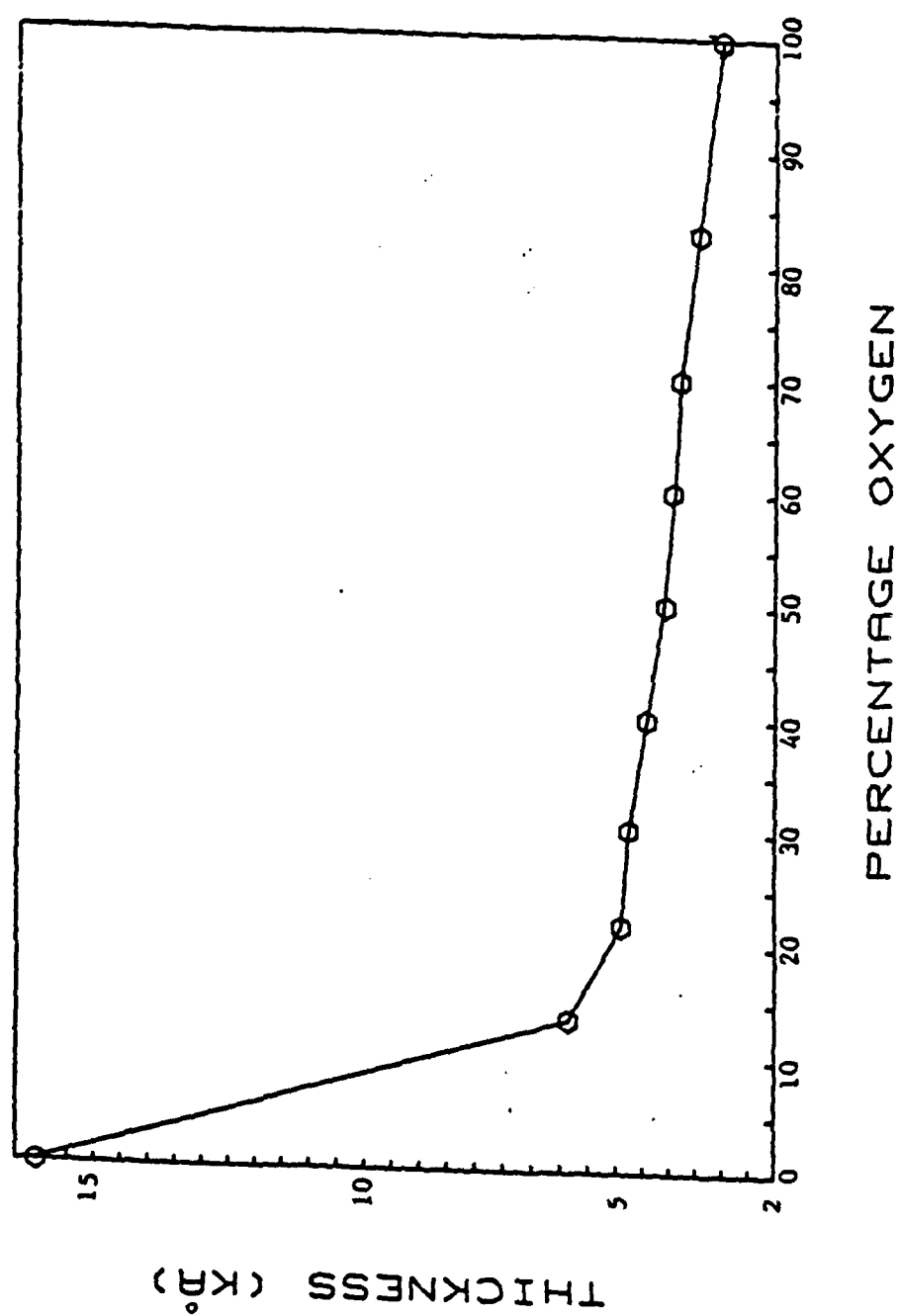


Figure 21. Thickness measurements of LiNbO_3 sputtered films as a function of oxygen content of sputtering gas

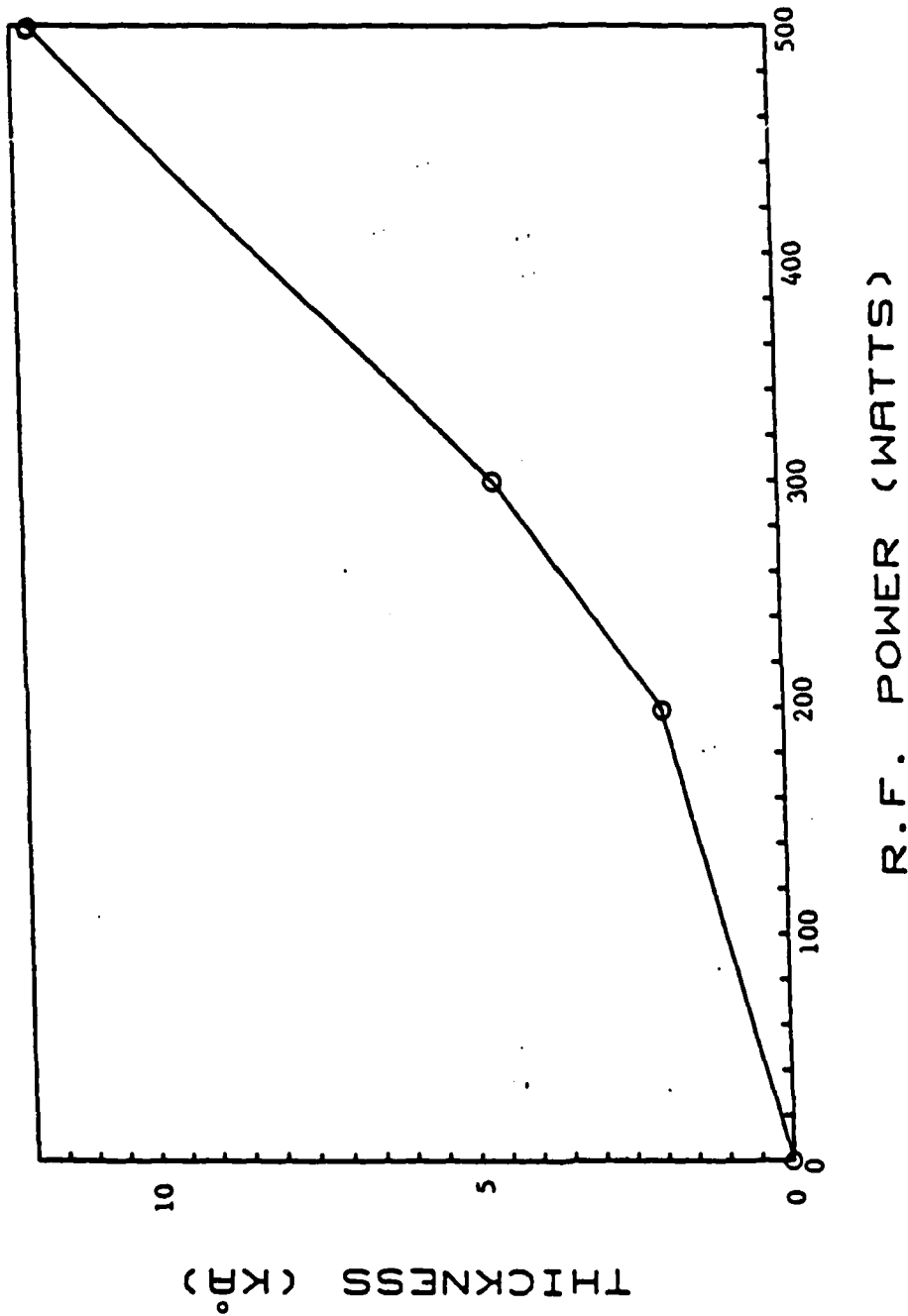


Figure 22. Thickness measurements of LiNbO₃ sputtered films as a function of applied r.f. sputtering power

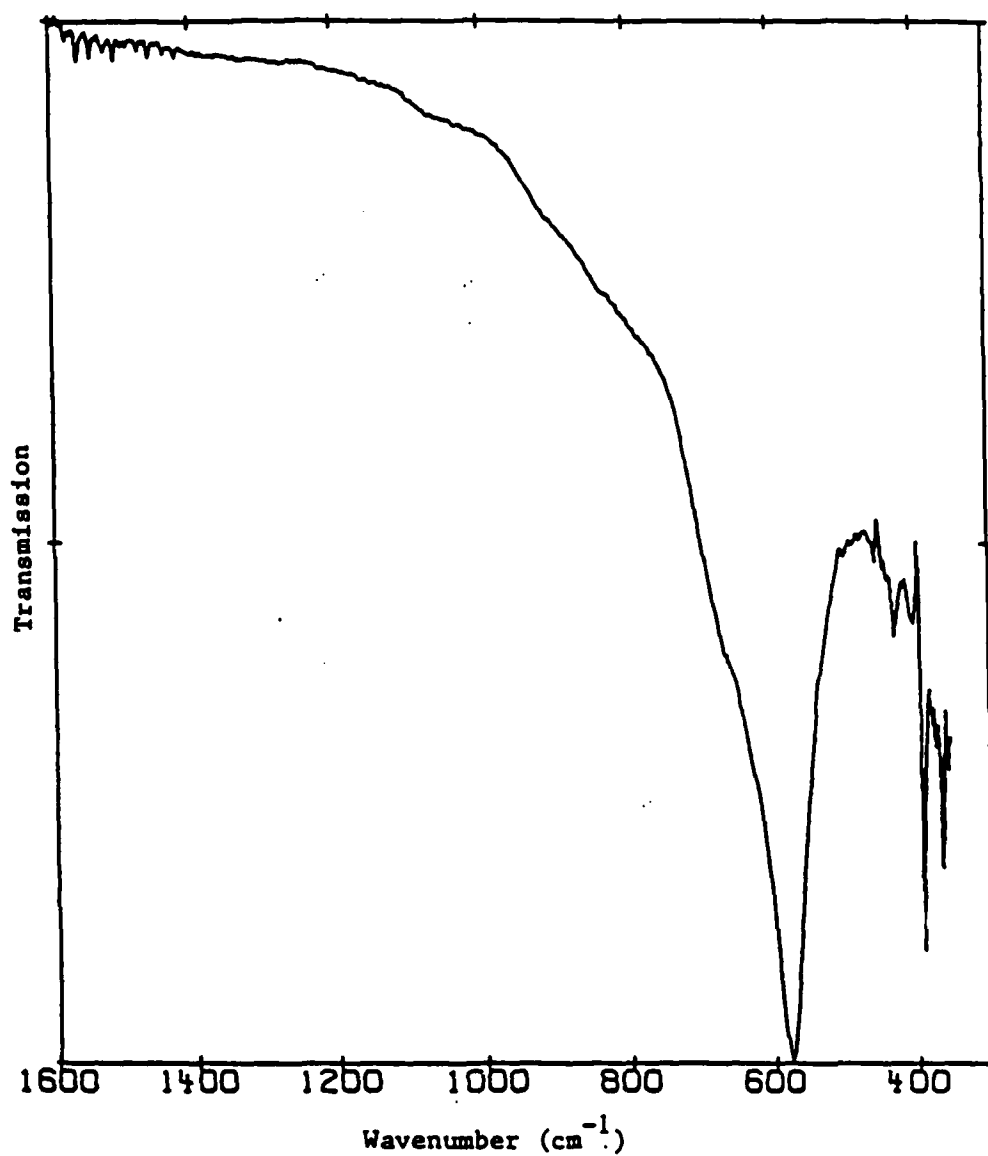


Figure 23. Infrared scan of LiNbO₃:152, produced using the optimized parameters

(Figure 10) appeared to indicate high levels of carbon and nitrogen contamination, and rather poor stoichiometry of the film itself. Auger analysis performed after the complete optimization procedure were much improved. As indicated in Figures 24 and 25, the sputtered LiNbO_3 films appeared almost identical to the bulk LiNbO_3 crystal used as a reference. Figure 24 compares the lithium and niobium content of the film with the reference, while Figure 25 does the same with the oxygen content. The plots appear virtually the same. The contaminant (nitrogen and carbon) content in the films was nearly nonexistent. Figure 26 is a depth profile of the film showing little or no change in the composition of the film until contact with the substrate.

The network analyzer was used to determine dielectric constant numbers and to observe piezoelectric response. Relative permittivity values were determined from thin films deposited on membranes of silicon, as the composite resonator would be constructed, and on normal silicon wafers. Surprisingly, the results differed greatly. Measurements were taken during the parameter optimization described in the last section, with the intent of observing relative permittivity changes with parameter changes. This was difficult because of uncertainties in the numbers used to determine the relative permittivity. However, for the measurements taken on wafers without membranes, trends were

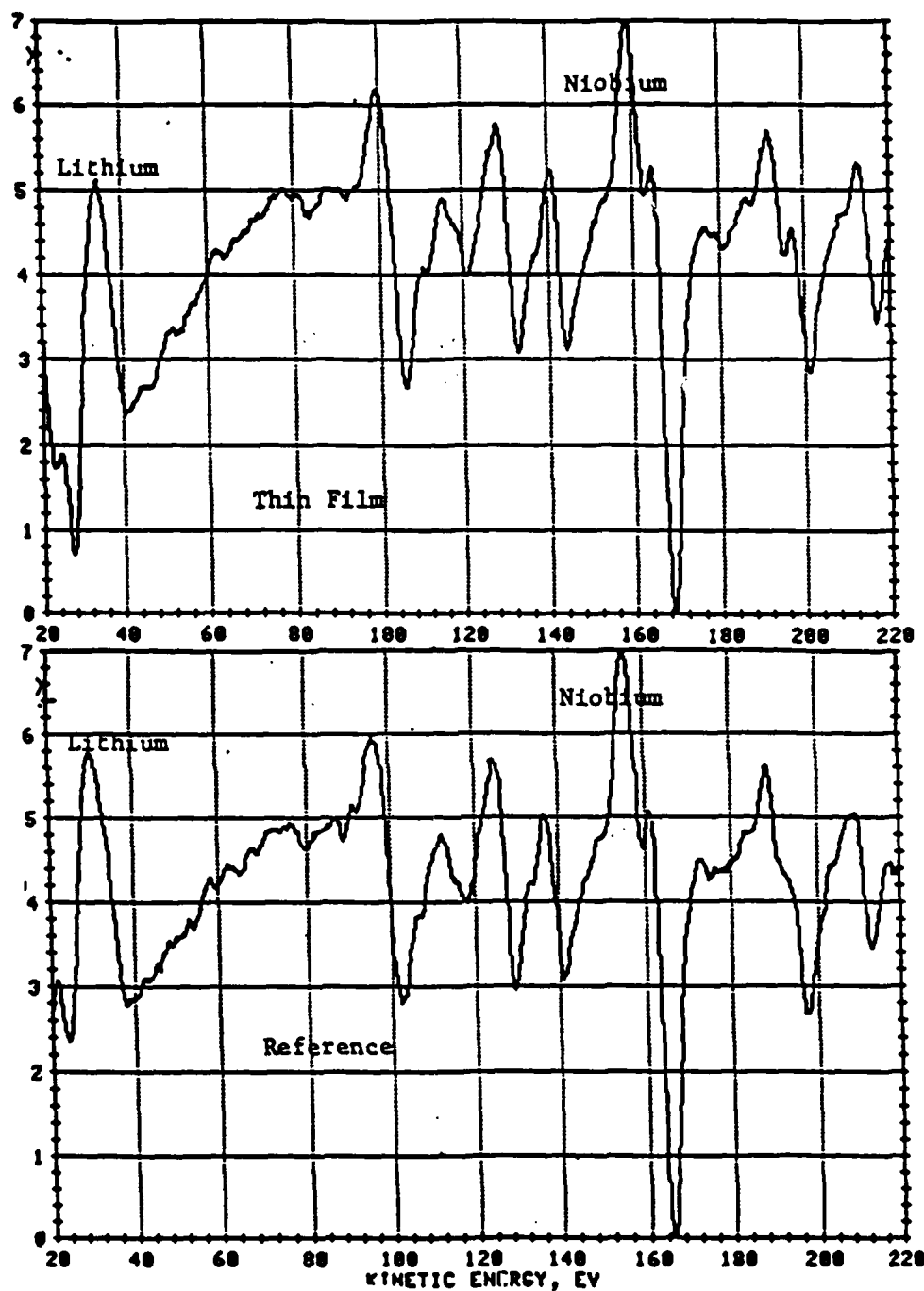


Figure 24. Auger pattern of $\text{LiNbO}_3:152$ (top) compared to bulk single crystalline sample (bottom). Lithium and niobium contents are shown as being nearly identical

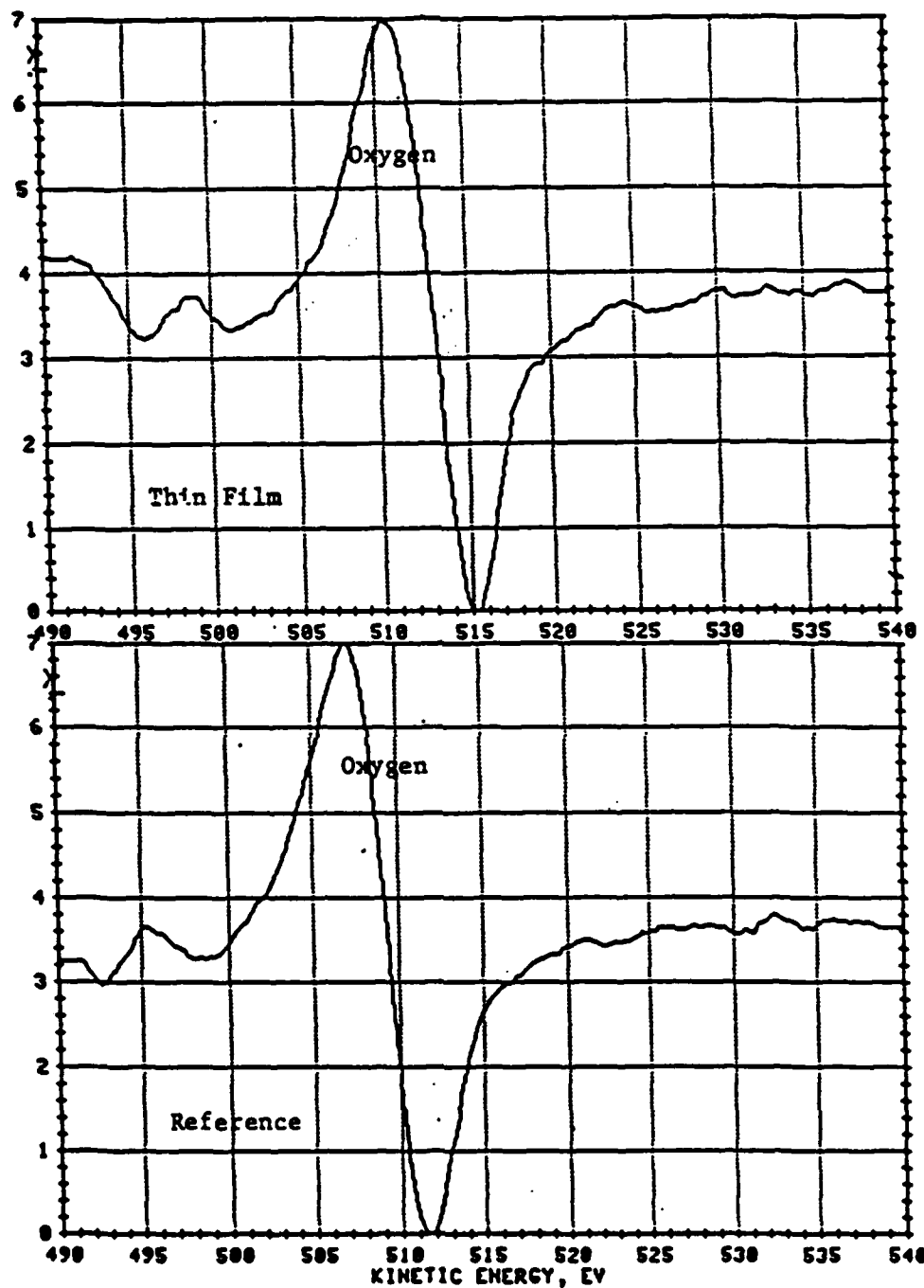


Figure 25. Auger pattern of $\text{LiNbO}_3:152$ (top) compared to bulk single crystalline sample (bottom). Oxygen contents are shown as being nearly identical

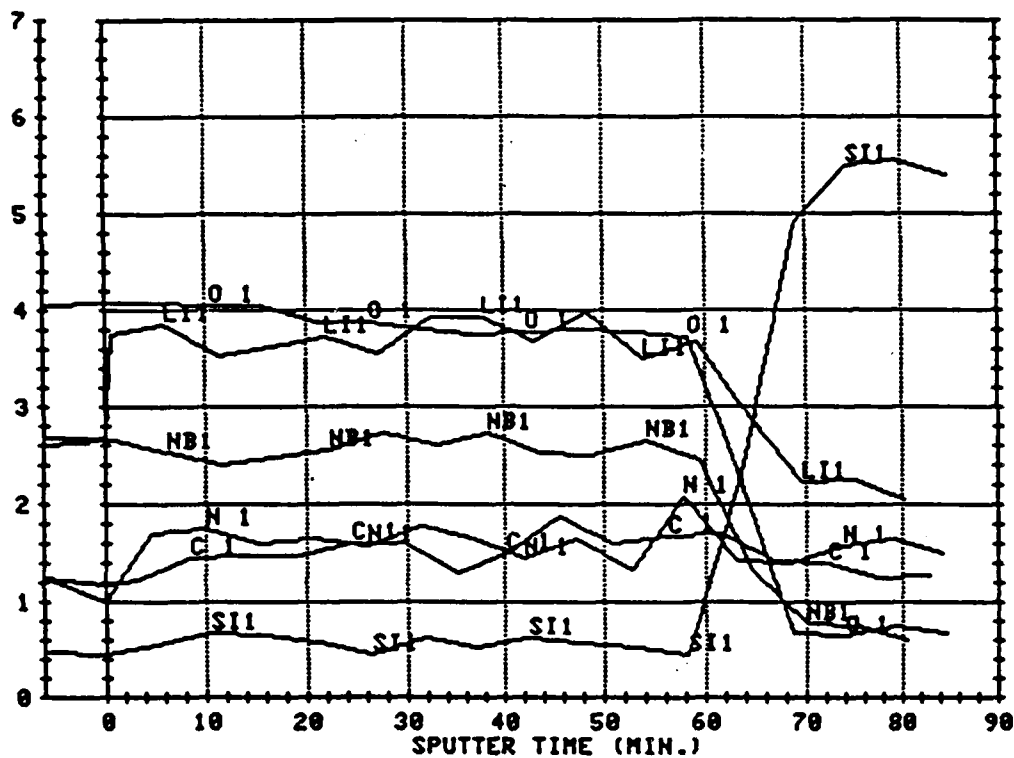


Figure 26. Depth profile of LiNbO₃:152 from Auger analysis. The stoichiometry of the film was constant from surface to substrate

noticeable. The more highly oriented and less amorphous a film, the lower its relative permittivity. This is most apparent in the variation of O_2 content in the gas seen in Figure 27 (lower part of plot). Unfortunately, the relative permittivity at the optimal parameter value (50% oxygen content) was only 50% of the expected value of $\epsilon_{33}^T/\epsilon_0 = 30$.

The relative permittivity measurements taken on the samples produced on membranes revealed much higher numbers, some exceeding 150. Trends noticeable in the films without membranes were totally absent in those with membranes. This can be seen in the upper portion of Figure 27. Since the membranes were formed from a p+ silicon layer, relative permittivity measurements were made on films sputtered on p+ layers without the membranes to check what caused the problem, the p+ layer or the membrane. The results showed the same problem existed on the samples having p+ layers without membranes. This odd behavior of the films deposited on p+ silicon layers is discouraging for the possible use of these films for composite resonators.

Samples were checked for piezoelectric response on the Network Analyzer throughout this investigation, both during and as a result of the parameter optimization procedure. Never has any response been noted. Several explanations for this have already been alluded to. They include:

- Surface roughness. The deposited films showed a

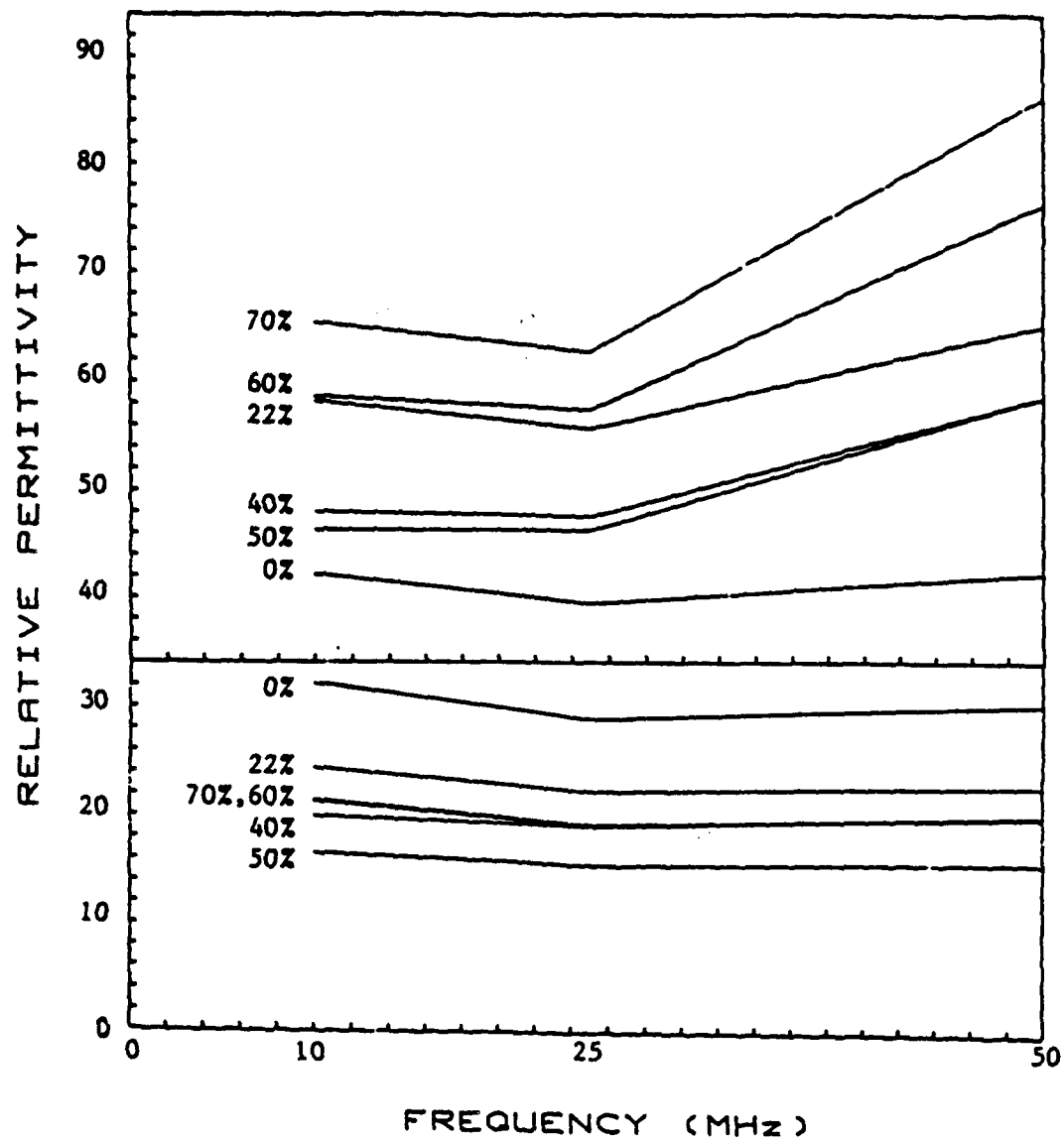


Figure 27. Relative permittivity values as a function of frequency for LiNbO_3 films sputtered using different oxygen concentrations in the sputtering gas

tendency to develop extremely rough surfaces as they were made thicker. Films only one micron thick had surface irregularities of 1000 Å or more. Resonators demand smooth surfaces for wave reflection. Because of this roughness, most measurements in this investigation had to be done on film samples less than 5000 Å thick.

-Crystal orientation. Although the films produced showed a marked orientation along the c-axis of LiNbO_3 , it was possibly not oriented strongly enough.

-Odd behavior of the relative permittivity when the films were deposited on p+ silicon layers. Since the piezoelectric measurements were made on p+ membranes, flaws in those films would inhibit response.

Another possibility is that the films were not poled. When LiNbO_3 single crystals are grown by the Czochralski method, often a strong electric field is applied to pole the crystals. It is possible that the electric field provided by the DC offset of the sputtering system used was not strong enough to adequately pole the deposited material. This explanation is extremely plausible, and could also explain the relative permittivity of the optimized samples being lower than the relative permittivity of bulk single crystal lithium niobate. Any or all of these could result in no piezoelectric response being observed in the sputtered films.

VI. CONCLUSIONS

Lithium niobate films were sputter deposited and analyzed to determine their suitability for transducer or resonator material. A set of sputtering parameters was determined as being the most relevant variables in the r.f. sputter deposition of LiNbO_3 thin films. The parameters were then optimized with respect to each other to obtain the best quality (in regard to crystallinity) thin films. The optimized parameters were:

An applied radio-frequency power of 300 watts.

A target-substrate separation of 8 cm.

A sputtering pressure of 3 mtorr.

An oxygen content of 50% in the sputtering gas.

A substrate temperature of 550°C - 600°C .

A sapphire substrate.

With these optimized parameters in effect, the resulting films were deposited with a deposition rate of approximately $1300 \text{ \AA}/\text{hour}$. The DC bias during the deposition was around 350 volts. Infrared scans of the films revealed a definite LiNbO_3 crystalline curve with distinctive peaks (Figure 23). X-ray diffraction patterns demonstrated that the films were highly oriented polycrystalline LiNbO_3 (Figure 19). Auger electron spectroscopy on these films indicated an almost identical

stoichiometry as bulk single crystal LiNbO_3 , with little contamination (Figures 24 and 25). The relative permittivity of these films was determined to be 15 - 16. No piezoelectric effect was observed using the composite resonator structure.

Several possible explanations were supplied concerning this lack of piezoelectric response. While LiNbO_3 deposited on p+ membranes appears unsuitable for use as a composite resonator, very possibly due to the p+ membrane, sputtered LiNbO_3 could be used for other piezoelectric devices which require thinner films and do not demand a substrate with a poor lattice match or p+ doping. SAW devices on sapphire would be an example.

Further work could be done on what was begun here. A better sputtering system (more automated) could be used so that slower deposition rates, and thus possibly better films could be produced. An applied DC bias could be added to the sputtering system so as to more likely pole the sputtered films. Another possibility would be to try an entirely different method of sputtering lithium niobate, such as completely reactive sputtering.

VII. REFERENCES

1. B. T. Matthias and J. P. Remeika, Phys. Rev. 76, 1886 (1949).
2. K. Nassau, E. G. Spenser, and P. V. Lenzo, Appl. Phys. Lett. 7, No. 3, 67 (1965).
3. K. Nassau, H. J. Levinstein, and G. M. Laioco, J. Chem. Phys. Solids 27, 983 (1966).
4. K. Nassau, H. J. Levinstein, and G. M. Loiacono, J. Chem. Phys. Solids 27, 989 (1966).
5. S. C. Abrahams, J. M. Reddy, and J. L. Bernstein, J. Chem. Phys. Solids 27, 997 (1966).
6. S. C. Abrahams, W. C. Hamilton, and J. M. Reddy, J. Chem. Phys. Solids 27, 1013 (1966).
7. S. C. Abrahams, W. C. Hamilton, and J. M. Reddy, J. Chem. Phys. Solids 27, 1019 (1966).
8. A. W. Warner, M. Onoe, and G. A. Coquin, J. Acoust. Soc. Amer., 1223 (1967).
9. T. Yamada, N. Niizeki, and H. Toyoda, Jap. J. Appl. Phys. 6, No. 2, 151 (1967).
10. J. R. Curruthers, G. E. Peterson, M. Grasso, and P. M. Bridenbach, J. Appl. Phys. 42, No. 5, 1846 (1971).
11. S. Miyazama, Appl. Phys. Lett. 23, No. 4, 198 (1973).
12. B. J. Curtis and H. R. Brunner, Mater. Res. Bull. 10, 515 (1975).
13. A. M. Glass, K. Nassua, and T. J. Negran, J. Appl. Phys. 49, No. 9, 4804 (1974).
14. N. F. Foster, Commun., 420 (1968).
15. S. Takada, M. Ohnishi, H. Hayakawa, and N. Mikoshiba, Appl. Phys. Lett. 24, No. 10, 490 (1974).
16. K. M. Lakin and J. S. Wang, Appl. Phys. Lett. 38, No. 3, 125 (1981).

17. R. S. Weis and T. K. Gaylord, Appl. Phys. A 37, 191 (1985).
18. B. Chapman, Glow Discharge Processes (John Wiley & Sons, New York, 1981), P. 184.
19. D. M. Mattox, Sputter Deposition and Ion-Plating Technology (American Vacuum Society, New York, 1973), p. 40.
20. M. A. Jeppensen, J. Opt. Soc. Am. 48, 629 (1958).
21. A. Okada, Ferroelectrics 14, 739 (1976).
22. T. Mitsuya and K. Waso, Jap. J. Appl. Phys. 20, No. 1, L48 (1981).
23. M. Kitabatake, K. Waso, and T. Mitsuya, J. Appl. Phys. 56, No. 6., 1780 (1984).
24. G. Griffel, S. Ruschin, A. Hardy, M. Itzkovitz, and N. Croitoru, Thin Solid Films 126, 185 (1985).
25. P. R. Meck and L. Holand, Vacuum 34, No. 3-4, 411 (1984).
26. S. M. Sze, Physics of Semiconductor Devices (John Wiley & Sons, New York, 1981), P. 848.
27. N. F. Foster, Communications, 421 (1968).
28. G. D. Boyd, W. L. Bond, and H. L. Carter, J. Appl. Phys. 38, No. 4, 194 (1967).
29. K. Nassau, C. A. Wang, and M. Grasso, J. Amer. Ceram. Soc. 62, No. 9-10, 503 (1979).
30. E. G. Spencer, P. V. Lenzo, and H. A. Ballman, Proc. IEEE 55, 2074 (1967).
31. K. Nunomura, A. Ishitani, T. Matsubara, and I. Hayashi, J. Cryst. Growth 45, 355 (1978).

VIII. ACKNOWLEDGEMENTS

I would like to express my thanks to H. R. Shanks, my major professor, who provided help and guidance numerous times before and during my graduate career. Thanks also goes to Dr. K. M. Lakin and the rest of the MRC for providing an interesting atmosphere for this project. For technical assistance, thanks goes to Dr. A. J. Bevolo and Dr. L. M. Seaverson for the Auger work, to P. Klavins for assistance with the x-ray measurements, and to O. M. Sevde for help with numerous technical problems. For help with the actual production of this thesis, I would like to thank Dr. P. A. Basore for the use of his ColorWriter program, and J. S. McCalmont for Spudgraph.

IX. APPENDIX

X-ray diffraction patterns of LiNbO_3 thin films produced at various concentrations of oxygen in the sputtering gas are shown in Figures 28 - 36.

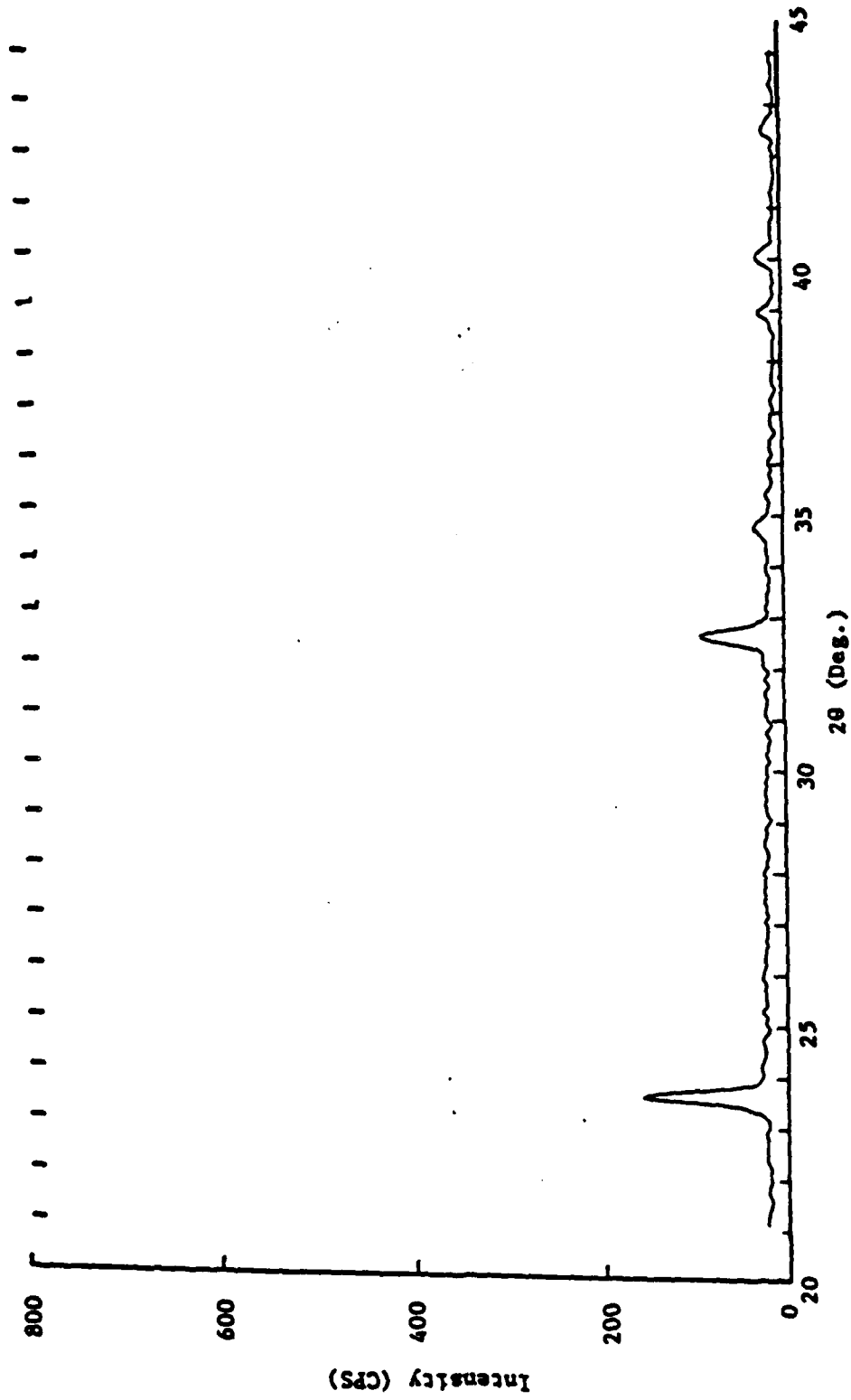


Figure 28. X-ray diffraction pattern of sample $\text{LiNbO}_3:137$ sputtered using a gas of 0% oxygen

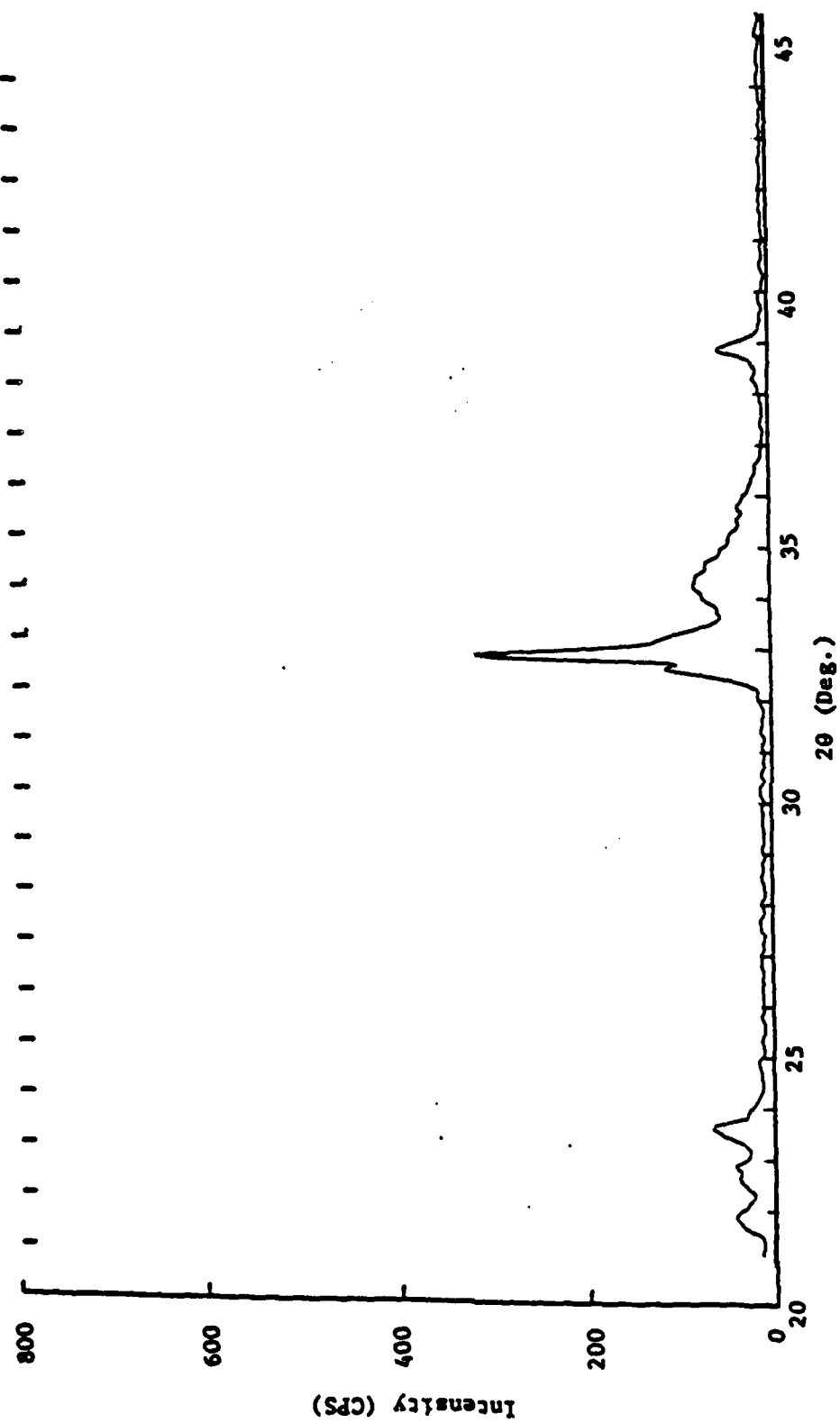


Figure 29. X-ray diffraction pattern of sample $\text{LiNbO}_3:138$ sputtered using a gas of 13.4% oxygen

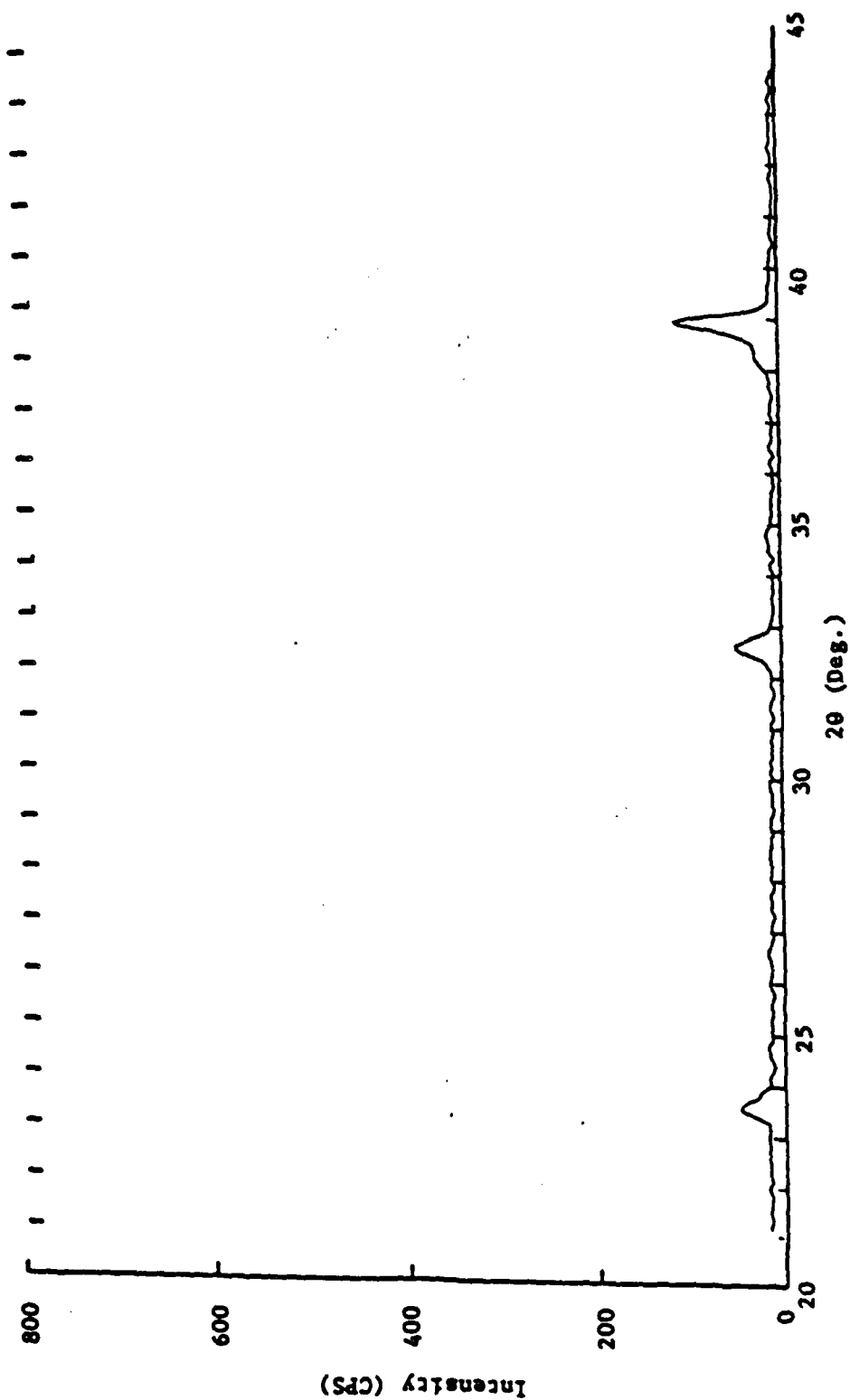


Figure 30. X-ray diffraction pattern of sample $\text{LiNbO}_3:139$ sputtered using a gas of 22% oxygen

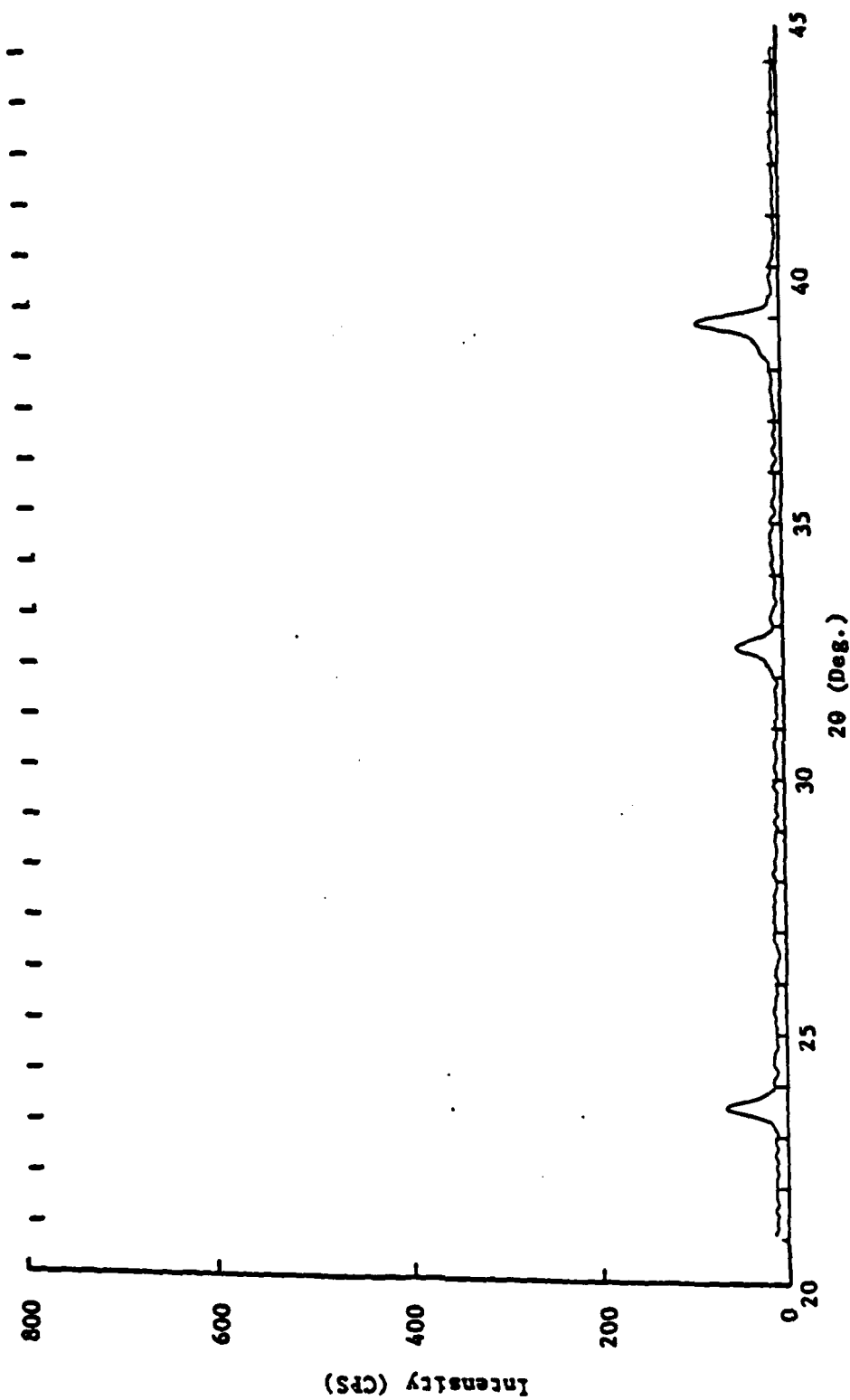


Figure 31. X-ray diffraction pattern of sample $\text{LiNbO}_3:140$ sputtered using a gas of 30% oxygen

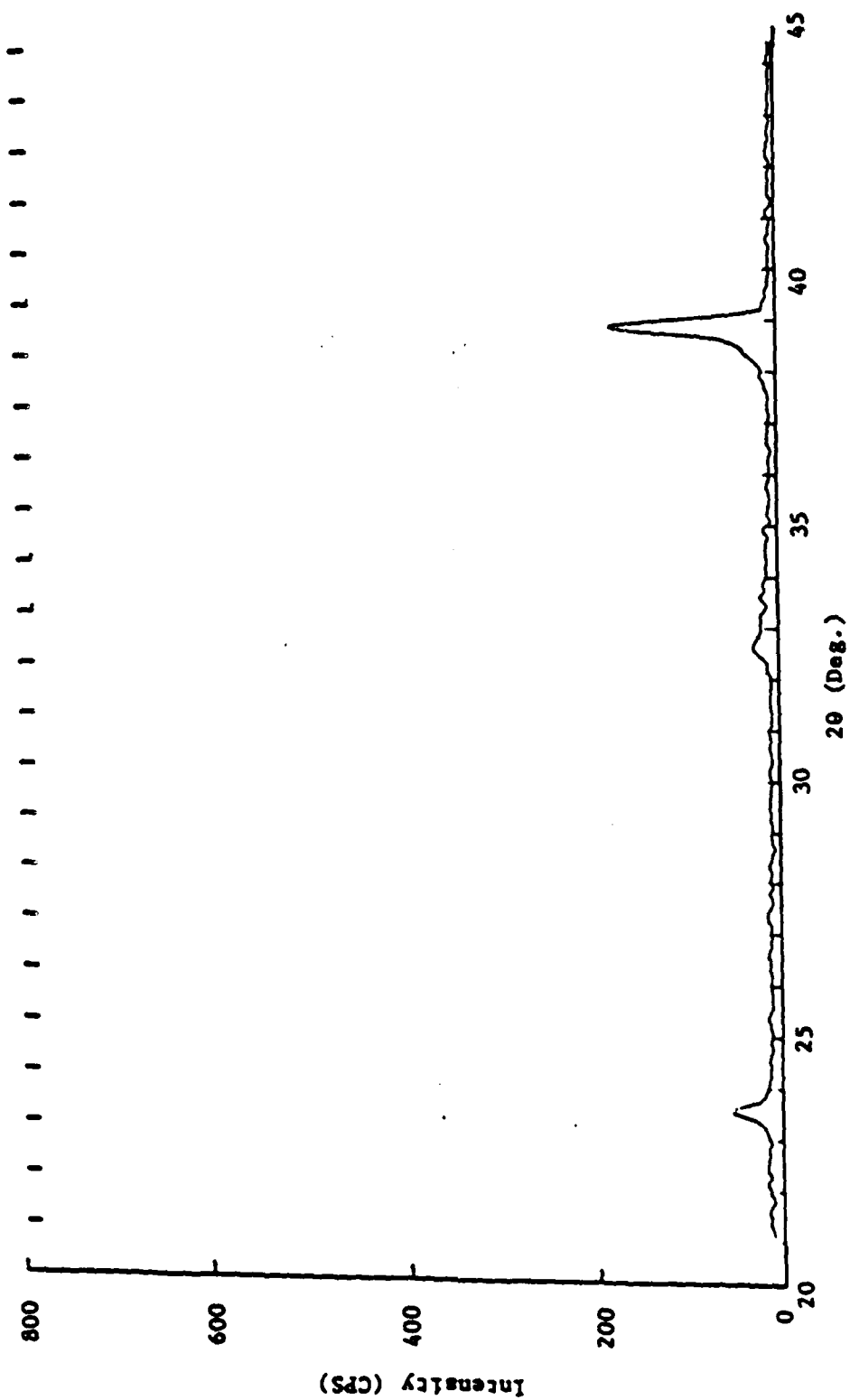


Figure 32. X-ray diffraction pattern of sample $\text{LiNbO}_3:141$ sputtered using a gas of 40% oxygen

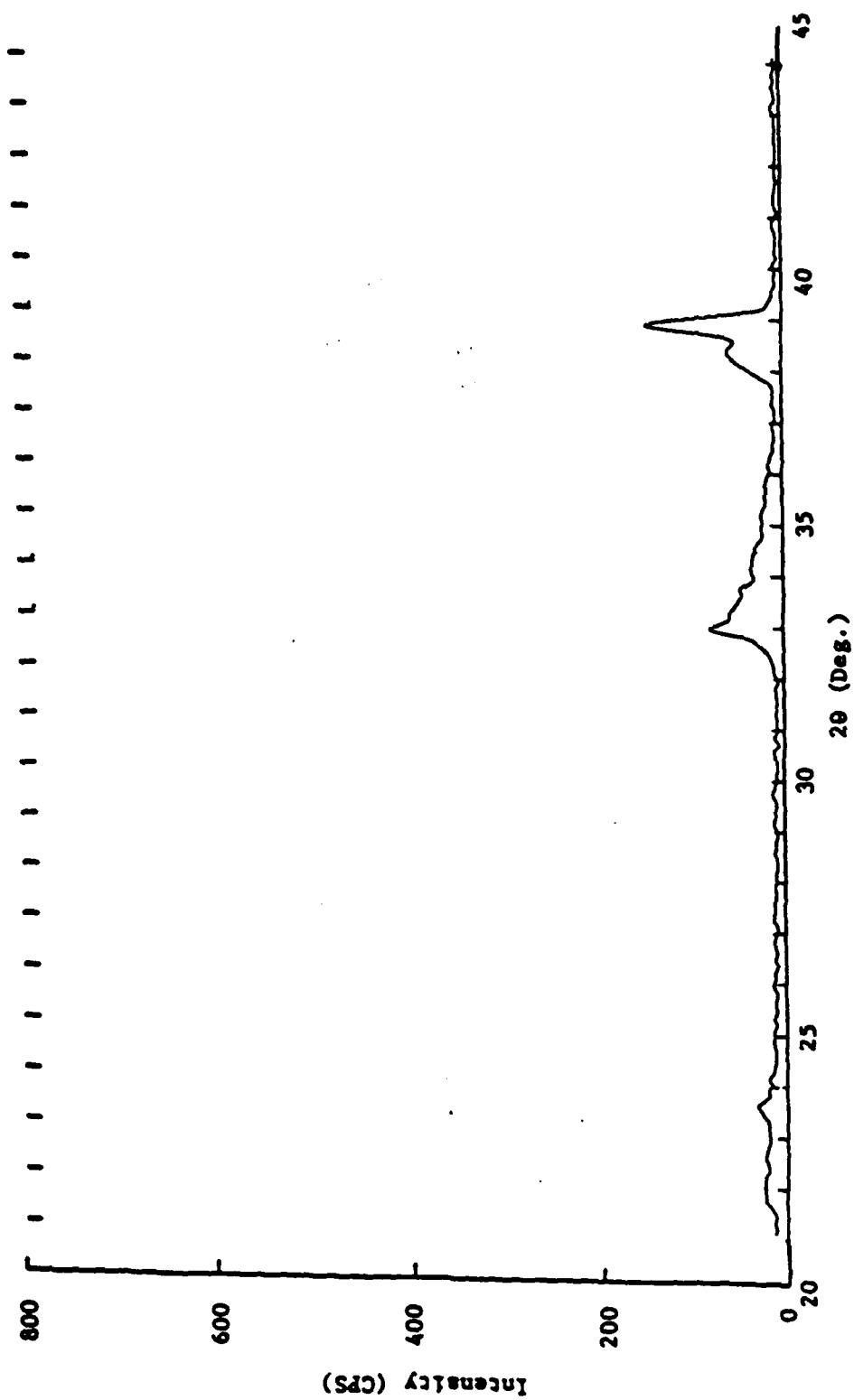


Figure 33. X-ray diffraction pattern of sample $\text{LiNbO}_3:142$ sputtered using a gas of 50% oxygen

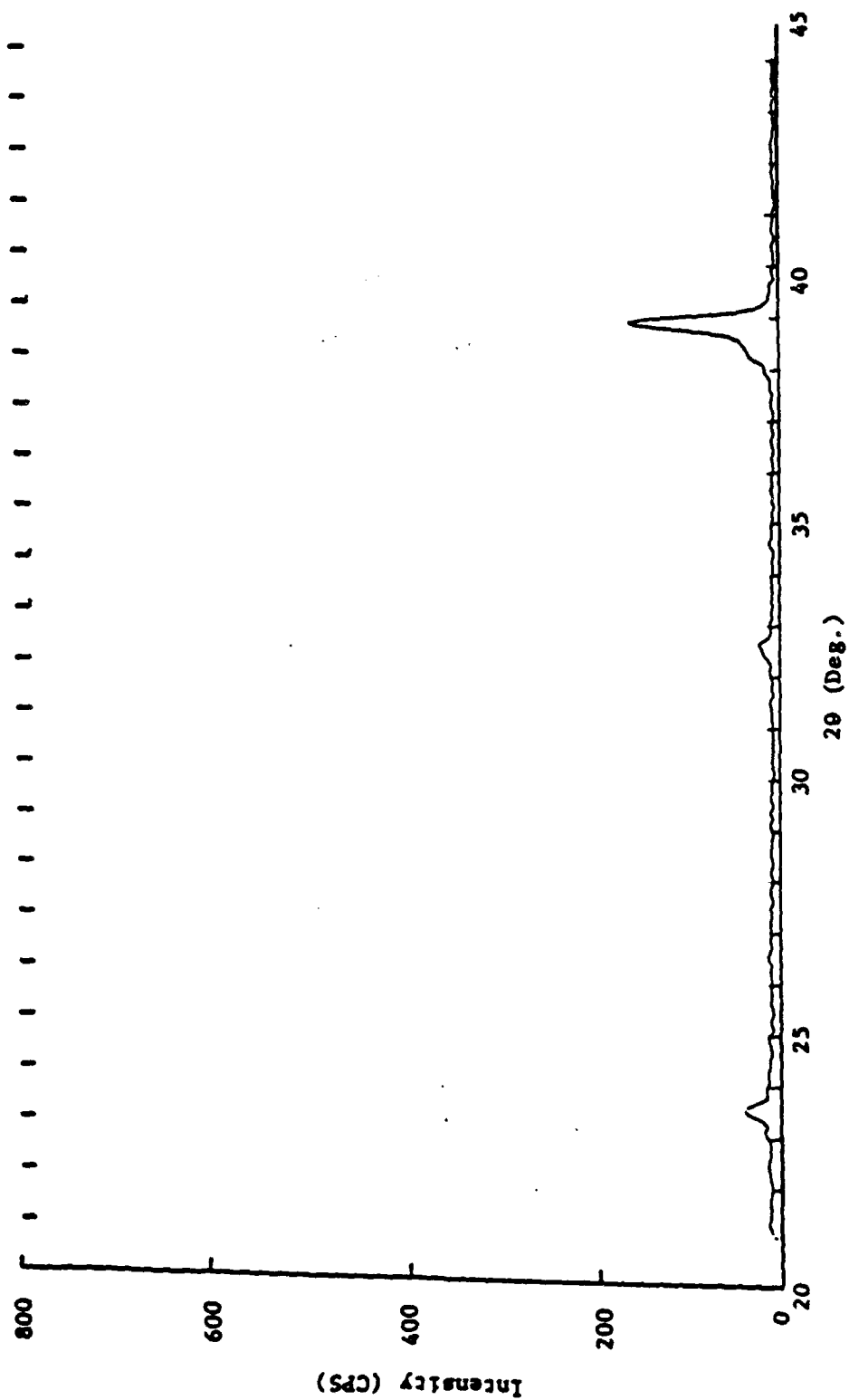


Figure 34. X-ray diffraction pattern of sample $\text{LiNbO}_3:143$ sputtered using a gas of 60% oxygen

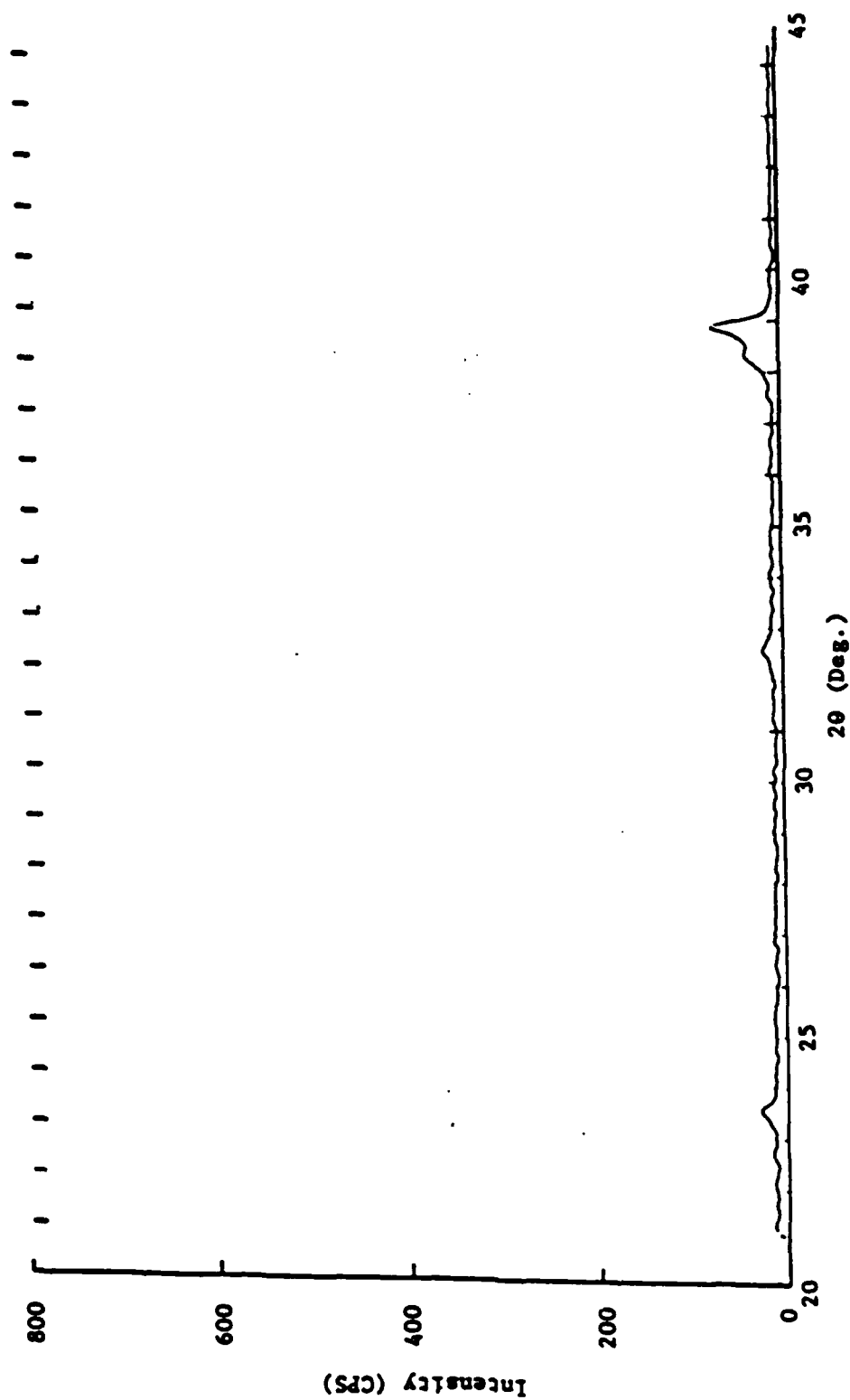


Figure 35. X-ray diffraction pattern of sample $\text{LiNbO}_3:144$ sputtered using a gas of 70% oxygen

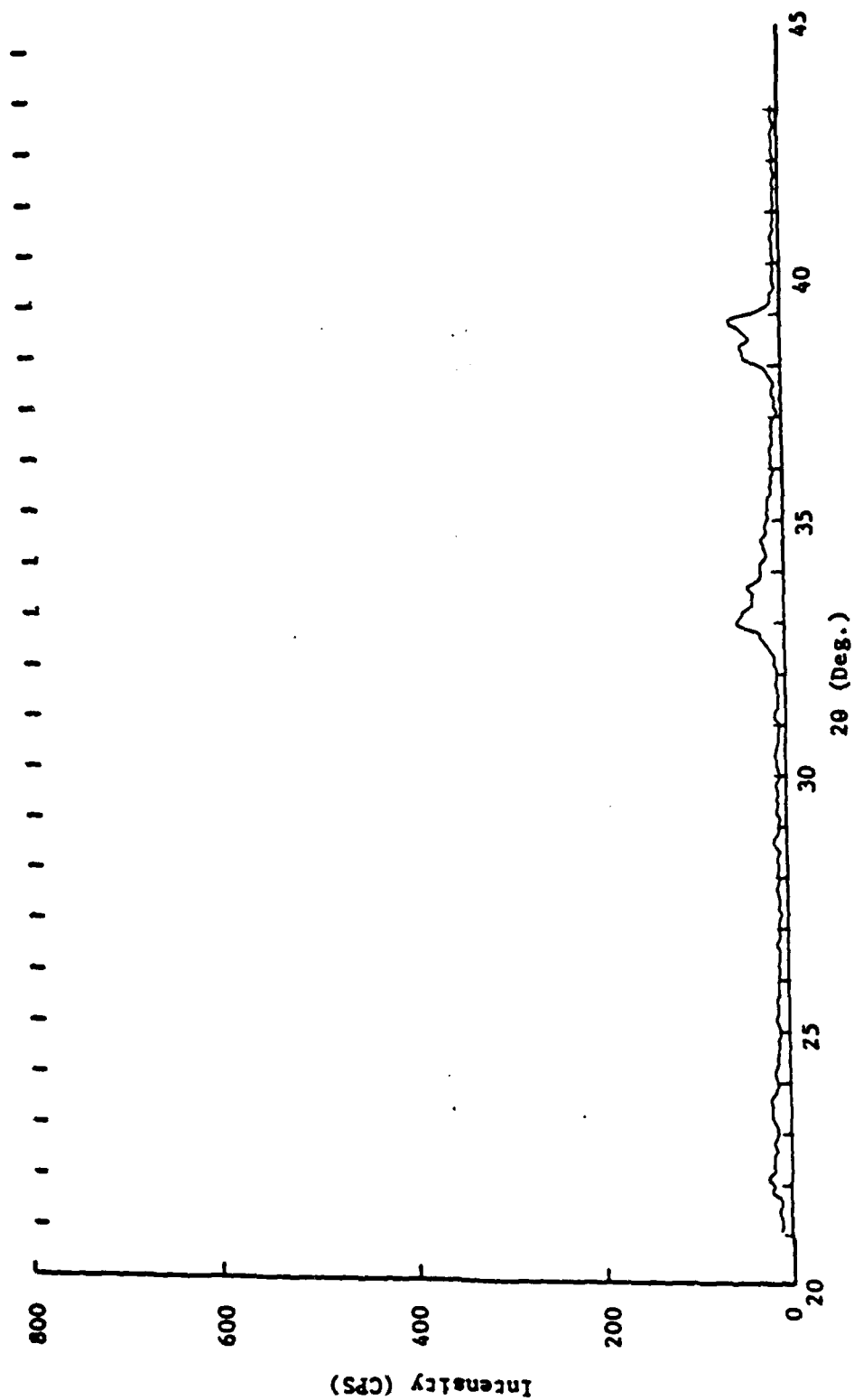


Figure 36. X-ray diffraction pattern of sample $\text{LiNbO}_3:145$ sputtered using a gas of 85% oxygen

END

DATE

FILMED

FEB.

1988